

# CVD-Grown Graphene in High Magnetic Fields

Von der Fakultät für Mathematik, Informatik und  
Naturwissenschaften der RWTH Aachen University  
zur Erlangung des akademischen Grades eines Doktors  
der Naturwissenschaften genehmigte Dissertation

vorgelegt von

Hans-Michael Schmitz, M.Sc.  
aus Bad Münstereifel

Berichter: Universitätsprofessor Dr. Christoph Stampfer  
Universitätsprofessor Dr. Markus Morgenstern

Tag der mündlichen Prüfung: 16. Januar 2024

Diese Dissertation ist auf den Internetseiten  
der Universitätsbibliothek online verfügbar.



# Abstract

The chemical vapor deposition (CVD) on metal catalyst surfaces is the most promising candidate to enable scalable growth of the two-dimensional (2D) carbon allotrope graphene (Gr), thereby opening the door to applications on industrial scales not realizable by the tape exfoliation techniques commonly applied to cleave micrometer sized Gr flakes from bulk graphite crystals. However, the widely employed wet methods to transfer CVD-grown Gr (CVD-Gr) onto arbitrary substrates were demonstrated to degrade its structural and electronic quality precluding industrial harvesting of its various fascinating properties and even casting doubts over the intrinsic quality of CVD-Gr and its suitability for high-quality (HQ) applications.

This thesis aims to prove the equality of the intrinsic capabilities of CVD-Gr and the exfoliated reference material by employing and improving the recently introduced dry-transfer method for CVD-Gr, which allows a direct pick-up from the metal growth substrate and subsequent encapsulation in other 2D-materials, thus avoiding the quality degradation associated with wet transfers. Electronic transport devices patterned from such heterostructures were characterized in temperature-dependent magneto-transport measurements in a high magnetic field laboratory. Quantum Hall effect (QHE) measurements reveal a clear formation of Landau levels (LLs) that is overlaid upon increasing magnetic field and decreasing temperature by symmetry-broken LLs and, finally, by a series of clearly pronounced fractional quantum Hall states with composite fermion filling factors up to  $\nu^* = 4$  and activation gaps well comparable with those observed in similar devices based on exfoliated graphene (Ex-Gr). These data prove for the first time that the quantum mobilities of CVD-Gr match those of Ex-Gr if a suitable transfer method is applied. Discarding fears of intrinsic differences to Ex-Gr, the CVD-Gr devices could be used as a HQ references within a set of other graphene devices hosting varying level of disorder. In a series of further high magnetic fields measurements, the crucial role of long range disorder for the manifestation of the QHE at room temperature (RT) could be clarified, as an increasingly pronounced effect was observed with increasing disorder level and the QHE vanishing in the HQ CVD-Gr devices well below 150 K at 30 T. In a similar study on the device set, a transition of the predominant scattering mechanism in the RTQHE regime from an extrinsic, disorder-mediated to an intrinsic, electron-phonon mediated scattering mechanism with decreasing disorder level could be revealed.



# Zusammenfassung

Die chemische Gasphasenabscheidung auf metallischen Katalysatoroberflächen ist der aussichtsreichste Kandidat, um ein skalierbares Wachstum des zweidimensionalen (2D) Kohlenstoff-Allotrops Graphen (Gr) zu ermöglichen und dadurch die Tür für Anwendungen auf industriellen Skalen zu öffnen, die mit den gewöhnlich angewandten Exfolierungstechniken zum Abspalten Mikrometer-großer Gr Flocken von Graphitkristallen nicht realisierbar sind. Es wurde jedoch nachgewiesen, dass die häufig angewandten nass-chemischen Methoden zum Transfer von CVD-gewachsenem Gr (CVD-Gr) auf beliebige Substrate dessen strukturelle und elektronische Qualität verringern und so die industrielle Anwendbarkeit seiner vielen faszinierenden Eigenschaften verhindern und sogar Zweifel an die intrinsische Qualität von CVD-Gr und seiner Eignung für hoch-qualitative (HQ) Anwendungen aufkommen liessen.

Das Ziel dieser Arbeit ist es, die intrinsische Gleichwertigkeit von CVD-Gr und exfolierten Referenzmaterial zu beweisen, indem eine kürzlich eingeführte trockene Transfermethode angewandt und verbessert wird, um CVD-Gr direkt von seinem metallischen Wachstumssubstrat hochzuheben und anschließend in anderen 2D-Materialien zu enkapsulieren, wodurch die mit nassen Transfermethoden assoziierten Qualitätsminderungen vermieden werden. Aus solchen Heterostrukturen gebaute elektronische Transportproben wurden in temperaturabhängigen Magnetotransportmessungen in einem Hochfeldlabor untersucht. Quantum Hall Effekt (QHE) Messungen enthüllen eine saubere Formierung von Landau Levels (LL), die bei steigenden magnetischen Feldern und fallenden Temperaturen überlagert werden durch symmetrie-gebrochene LL und schließlich durch eine Serie klar ausgeprägter fraktionaler Quantum Hall Zustände mit Komposit-Fermionen Füllfaktoren bis zu  $\nu^* = 4$ , sowie Aktivierungsenergien, die sehr gut mit denen in exfolierten Gr (Ex-Gr) Proben vergleichbar sind. The Daten beweisen erstmalig, dass die Quantenmobilitäten von CVD-Gr mit denen von Ex-Gr übereinstimmen, sofern eine geeignete Transfermethode angewandt wird. Dies erlaubt es, die CVD-Gr Proben als HQ Referenz in einem Ensemble weiterer Graphen Proben zu nutzen, die variierende Level an Unordnung aufweisen. In einer Serie weiterer Hochmagnetfeldmessungen konnte die wichtige Rolle von langreichweitiger Unordnung für die Manifestation des QHE bei Raumtemperatur (RT) geklärt werden, da ein zunehmend ausgeprägter Effekt mit zunehmendem Unordnungslevel nachgewiesen wurde und der QHE in unseren HQ CVD-Gr Proben bei 30 T sogar bereits unter 150 K verschwand. In einer ähnlichen Studie mit dem selben Probenensemble wurde ein Übergang des vorherrschenden Streumechanismus im RTQHE Regime von einem extrinsischen, Unordnungs-dominierten, zu einem intrinsischen, Elektron-Phonon-dominierten Streumechanismus mit abnehmenden Unordnungslevel enthüllt.

# Contents

<b>1</b>	<b>Introduction</b>	<b>1</b>
<b>2</b>	<b>Graphene: Structural and Electronic Properties</b>	<b>5</b>
2.1	Graphene Lattice . . . . .	5
2.2	Electronic Band Structure . . . . .	6
2.3	Density of States and Ambipolar Electronic Transport in Graphene . .	10
2.4	Hexagonal Boron Nitride . . . . .	14
2.5	Raman Spectrum of Monolayer Graphene . . . . .	15
2.6	Summary . . . . .	19
<b>3</b>	<b>Quantum Hall Effect I: Landau Quantization</b>	<b>21</b>
3.1	Classical Hall Effect . . . . .	22
3.2	Landau Level Quantization . . . . .	24
3.3	Degeneracy-Lifting and the Ground-State of Graphene . . . . .	28
3.4	Fractional Quantum Hall States . . . . .	31
3.5	Discovery of the Integer Quantum Hall Effect . . . . .	35
3.6	Summary . . . . .	40
<b>4</b>	<b>Quantum Hall Effect II: Microscopic Pictures</b>	<b>43</b>
4.1	The Conventional Picture . . . . .	44
4.2	Many-Body Screening Picture . . . . .	59
4.3	Summary . . . . .	73
<b>5</b>	<b>Chemical Vapor Deposition</b>	<b>77</b>
5.1	Typical Gr-CVD Setups and Processes . . . . .	78
5.2	Growth Mechanisms and Kinetics . . . . .	79

5.3	Growth Reactors . . . . .	82
5.4	Catalyst Metal Foils . . . . .	83
5.5	Transfer Methods . . . . .	91
5.6	Copper Oxidation . . . . .	93
5.7	CVD Growth of hBN and Bilayer Graphene . . . . .	95
5.8	Summary . . . . .	97
<b>6</b>	<b>Fabrication of High Quality CVD Graphene Devices</b>	<b>99</b>
6.1	Introduction . . . . .	99
6.2	Exfoliation of 2D Materials . . . . .	100
6.3	CVD Growth of Monolayer Graphene Crystals . . . . .	102
6.4	Forced Interface Oxidation . . . . .	105
6.5	Dry-Transfer of CVD Graphene . . . . .	109
6.6	Stack Refining by PC Stacking . . . . .	111
6.7	Device Patterning . . . . .	117
6.8	Graphite-Gated CVD-Graphene Devices . . . . .	122
6.9	Changes in our CVD System . . . . .	122
6.10	Summary . . . . .	123
<b>7</b>	<b>Measurement Systems</b>	<b>125</b>
7.1	VTI System . . . . .	125
7.2	HFML Systems . . . . .	126
7.3	Single Shot $^3\text{He}$ Cryostat . . . . .	128
7.4	Flow Cryostat . . . . .	129
7.5	Measurement Set-Ups . . . . .	130
<b>8</b>	<b>Fractional Quantum Hall Effect in CVD-grown Graphene</b>	<b>131</b>
8.1	Introduction . . . . .	131
8.2	Low-Temperature Magneto-Transport Measurements . . . . .	133
8.3	High Field Measurements . . . . .	133
8.4	Activation Gap Measurements . . . . .	136
8.5	Summary . . . . .	137
<b>9</b>	<b>Room Temperature Quantum Hall Effect in Graphene</b>	<b>139</b>
9.1	Introduction . . . . .	140

9.2	The Role of Disorder in the Temperature-Induced Breakdown of the QHE . . . . .	141
9.3	Role of Electron-Phonon Mediated Scattering in the QHE at RT . . .	151
9.4	Summary . . . . .	158
<b>10</b>	<b>Summary and Outlook</b>	<b>161</b>
10.1	Summary . . . . .	161
10.2	Outlook . . . . .	163
	<b>Appendices</b>	<b>167</b>
A	Fabrication Details . . . . .	167
B	Supplementary Material RTQHE . . . . .	170
B.1	Activation of the Interaction-Mediated Landau Levels . . . . .	170
B.2	Plateau Overshoots on the Bulk Side . . . . .	171
C	List of samples . . . . .	173
	<b>Publications</b>	<b>174</b>
	<b>List of Figures</b>	<b>176</b>
	<b>Bibliography</b>	<b>178</b>
	<b>Acknowledgments</b>	<b>207</b>
	<b>Curriculum Vitae</b>	<b>210</b>



# List of Abbreviations

<b>2DES</b>	2-dimensional electron system	<b>LPCVD</b>	Low pressure CVD
<b>APCVD</b>	Atmospheric pressure CVD	<b>MFC</b>	Mass flow controller
<b>BLG</b>	Bilayer Gr	<b>MOSFET</b>	Metal organic field effect transistor
<b>BZ</b>	Brillouin zone	<b>MPE</b>	Microwave plasma enhanced
<b>c2DES</b>	Conventional 2DES with parabolic dispersion	<b>NNH</b>	Nearest neighbor hopping
<b>CAF</b>	Canted antiferromagnetism	<b>PC</b>	Poly(bisphenol A carbonate)
<b>CDW</b>	Charge density wave	<b>PL</b>	Photoluminescence
<b>CF</b>	Composite fermion	<b>PMMA</b>	Poly(methyl methacrylate)
<b>CNP</b>	Charge neutrality point	<b>PVA</b>	Poly(vinyl alcohol)
<b>CS</b>	Compressible strip	<b>QHE</b>	Quantum Hall effect
<b>CSG</b>	Chklovskii Shklovskii Glazman	<b>RIE</b>	Reactive ion etching
<b>CVD</b>	Chemical vapor deposition	<b>RT</b>	Room temperature
<b>CVD-Gr</b>	CVD-grown graphene	<b>SB</b>	Step bunching
<b>DFT</b>	Density functional theory	<b>SC</b>	Single-crystal
<b>DOS</b>	Density of states	<b>SCBA</b>	self consistent Born approximation
<b>E-S</b>	Efros-Shklovskii	<b>SdH</b>	Shubnikov de-Haas
<b>EBL</b>	Electron beam lithography	<b>TFA</b>	Thomas-Fermi approximation
<b>Ex-Gr</b>	Exfoliation-derived Gr	<b>TFPA</b>	Thomas-Fermi Poisson approximation
<b>FQHE</b>	Fractional quantum Hall effect	<b>TMD</b>	Transition-metal dichalcogenide
<b>FWHM</b>	Full width at half maximum	<b>VRH</b>	Variable range hopping
<b>Gr</b>	Graphene	<b>VTI</b>	Variable temperature insert
<b>HP</b>	Hall plateau		
<b>hBN</b>	hexagonal boron nitride		
<b>HFML</b>	High field magnet laboratory		
<b>IPA</b>	Isopropyl alcohol		
<b>IQHE</b>	Integer quantum Hall effect		
<b>IS</b>	Incompressible strip		
<b>KD</b>	Kekule distortion		
<b>LL</b>	Landau level		



# Chapter 1

## Introduction

A fundamental consequence of *human action* is that a lowering of the *time preference*<sup>1</sup> of the individuals within a free society under the division of labor in an unhampered market economy results in a continued lengthening of the production period, induced by a shift of capital towards higher stages of production [1]. The availability new of capital from increased investments allows the practical implementation of new recipes and technologies (i.e. *innovations*), that would have remained in the shelf of unrealized possibilities otherwise, and, thereby, facilitates the prosperous progression of economy and society<sup>2</sup>. In this context, the ultimate *end of fundamental research* in the natural sciences lies in the discovery and development of novel technologies and knowledge, that, if made accessible to the common public, become *unlimited* factors of production and are eventually realized by the allocation of invested capital [2, 3]. Seeking to attain this end, researchers are generally faced with a nearly infinite variety of disciplines and topics open for investigation and it is important to realize that objective valuation schemes upon which a specific topic might be chosen cannot exit. On the contrary, the valuation of research topics, just like all ends of human

---

<sup>1</sup>Time preference reflects the degree to which an individual prefers the present attainment of the ends of his action over a future attainment everything else being equal. In the economic context, a lowering of time preference results in a reduced spending on consumption and an increased spending on investments and cash holdings. It is a vital aspect of the *austrian school of economics* known by its most popular fellows Ludwig von Mises (1881-1973) and his students Murray N. Rothbard (1926-1995) and Friedrich A. von Hayek (1899-1992), the latter of was honored with the Nobel prize in economics in 1974.

<sup>2</sup>As writes Rothbard in [2], p. 963:

In practice, since resources need capital to find and develop them, since technological improvement can be applied to production only via capital investment, since entrepreneurial skills act only through investments, and since an increased labor supply is relatively independent of short-run economic considerations and can backfire in Malthusian fashion by lowering per capita output, the *only* viable way to growth is through increased saving and investment.

action, is determined by their subjective *marginal utility* on the ordinal value scales of individuals pursuing or funding them [1], and it is generally irrelevant whether a topic is investigated with an application as a factor of production already in mind or on a purely academic, rather self-related basis. Furthermore, possible utilization of new theories and results might be concealed by the veil of uncertainty that always lies on the future. In fact, history has seen many examples of new technologies applying research that was once regarded as purely abstract (e.g. the concept of relativistic time dilation applied in the GPS technology). The above made considerations highlight the important role of *ideas* governing action in a society, as they influence both the degree of time preference of individuals as well their subjective valuations of ends to be persuaded by e.g. by research [1]. The predominant ideas in a society can be multi-fold and even partially opposing each other. Over the last decades, the western societies were largely driven by a lasting desire for enhanced interconnection and digitalization, requiring increasingly powerful computers and related smart technologies, while on the other hand, the idea of sustainability and a decreased carbon footprint of the society became ever more dominating, calling for more energy efficient *green* technologies and processes.

These predominant ideas are the reason why the two-dimensional (2D) carbon allotrope *graphene* (Gr) has, since its rediscovery in 2004 by Novoselov and Geim<sup>3</sup> [4], attracted a phenomenal interest, both in the spheres of fundamental research, as well as in various branches of industry aiming both to establish more powerful as well as more sustainable technologies and has opened the door to an entirely new research field investigating the rich zoo of 2D materials [5, 6]. Furthermore, owing to the fascinating electronic, mechanic and optic properties of Gr, this research field makes prime example of a topic investigated with concrete applications in mind, as well as a testbed for delicate solid state physics concepts.

This thesis marks important advancements both on the way to scalable resource-efficient applications of Gr in future technologies and products as well as for understanding the mechanisms of interaction driven effects under the exotic conditions of high magnetic fields up to 35 T and elevated temperatures up to 300 K. From the early days on, the method used to obtain Gr crystals with tens of microns of diameter was the mechanical exfoliation from bulk graphite - a method which lacks both scalability and reproducibility. Hence, the industry as well as the fundamental research community were seeking for reliable methods to produce Gr of high quality on larger scale. Over the years, the most promising candidate to achieve this goal became the *chemical vapor deposition* (CVD) of Gr on the surface of metal foils [7]. Due to the

---

<sup>3</sup>Kostya Novoselov (\*1974) and Andre Geim (\*1958) were the first to obtain individual graphene sheets from tape exfoliation of natural graphite on wafer substrates [4] - However, monolayers of graphite were already deposited on metal surfaces several decades earlier (see Chapter 5). For their groundbreaking experiments regarding graphene Novoselov and Geim were honored with the Nobel prize in physics in 2010.

---

surface limited nature of this growth process, monolayer graphene (MLG) can be obtained on arbitrary scales (see Chapter 5) on copper foils. However, as the metal growth catalysts are not suitable for the exploitation of the outstanding electronic properties of Gr, processes have to be applied to transfer the 2D sheets onto arbitrary substrates. Commonly used methods involve carrier polymers, wet etching of the metal catalyst as well as several solvents, all of which were shown to contaminate the transferred Gr (see Chapter 5 for details and references). Consequently, the structural and electronic properties of such *wet-transferred* CVD-grown Gr (CVD-Gr) are repeatedly reported to be inferior to exfoliation-derived Gr (Ex-Gr) up to the point, where considerable parts of the research community feared, that even the intrinsic quality of the as-grown CVD-Gr might be inferior to that of Ex-Gr. This changed only in 2015, when we adapted a *dry-transfer* method for CVD-Gr, that relies only on the van-der-Waals forces between Gr and another 2D material (in this case hexagonal boron nitride (hBN)) prepared on a transfer stamp to directly pick up the CVD-Gr from the Cu foil and fabricate it into hBN/CVD-Gr/hBN heterostructures [8]. Electronic transport devices patterned into such heterostructures were shown to reproducibly achieve high charge carrier mobilities and low residual charge carrier fluctuations, both comparable to the best heterostructures based on Ex-Gr as well as record breaking ballistic mean free paths exceeding  $28\text{ }\mu\text{m}$  [9]. Indicating that the transfer method is the predominant factor in determining the final material quality, a strong case was therefore made in defense of the intrinsic quality of CVD-Gr. Yet still, doubts remained whether CVD-Gr capabilities of CVD-Gr also extended to the top notch category of quality, which is commonly seen in the observation of fragile, disorder-sensitive, interaction-mediated phenomena like the *fractional quantum Hall effect* (FQHE), which were already reported in Ex-Gr devices [10, 11].

These doubts mark the starting point of this thesis, which aims first of all to provide the ultimate proof of the intrinsic equality of CVD-Gr and Ex-Gr via the successful measurement of the FQHE in a CVD-Gr heterostructure. To achieve highest possible device performances, the dry-transfer method, as well as the subsequent fabrication steps and processes were improved significantly during the course of this work. The devices obtained from these processes were characterized in multiple measurement stays in the High Field Magnetic Laboratory (HFML) in Nijmegen, finally revealing well pronounced fractional quantum Hall states. Attaining this end marks an important step on the way for Gr to high quality applications and further legitimizes the use of CVD-Gr devices together with Ex-Gr devices in comparative studies, some of which are also part of this work and focus on the manifestation of *quantum Hall effect* (QHE) at *room temperature* (RT) and the predominant scattering mechanisms in this regime.

This thesis is structured in order to cover all relevant background information in the beginning, followed by a description of the processes and process optimiza-

tions necessary for device fabrication, while the actual transport experiments on the heterostructures and their evaluations are presented in the last part. Chapter 2 elaborates the basic structural and electronic properties of Gr, hBN, as well as of their corresponding Raman scattering characteristics. This is followed by a detailed review of the physics governing the electronic transport in two-dimensional electron systems (2DES) in the presence of perpendicular magnetic fields in Chapter 3, from the classical Hall effect over Landau level quantization in 2DES and in Gr up to the initial discovery of the integer quantum Hall effect. As the QHE cannot be derived directly from the Landau quantization, but instead requires microscopic pictures in order to be understood, the two predominant microscopic pictures of the QHE known today are reviewed in Chapter 4 with an emphasis on the role of temperature and sample disorder. The detailed elaborations in Chapters 3 and 4 are vital to accurately interpret the transport data obtained from the high magnetic field measurements. Similarly, in order to better understand the CVD of Gr and the dry-transfer process and to judge their perspectives for future industrial realization, a detailed review of the fundamental principles of Gr CVD together with a summary of the state-of-the-art in this research field is given in Chapter 5. After establishing all necessary background information, Chapter 6 covers all process and process optimizations for the fabrication of highest quality CVD-Gr heterostructures - from the exfoliation of 2D materials, over the CVD growth of MLG on the inside of Cu enclosures and the subsequent dry-transfer and stacking to quality refinement processes and device patterning. Chapter 7 briefly covers all measurement systems and set-ups used to characterize the transport devices within our own labs, as well as in the high magnetic field facility. The successful measurements of the FQHE in our CVD-Gr devices and hence the proof of the intrinsic equality to Ex-Gr is presented in Chapter 8. This followed by a study of an ensemble of Gr transport devices with varying degrees of sample disorder, allowing the investigation of the role of disorder for the manifestation of QHE at room temperature as well as of the role of electron-phonon mediated scattering in this regime. Chapter 10 contains a summary of the results and advancements of this thesis, as well as an outlook on meaningful future measurements in the field of quantum Hall physics in Gr, as well as on the perspectives of our dry-transfer for scalable applications.

## Chapter 2

# Graphene: Structural and Electronic Properties

The fascinating structural, electronic and optical properties of monolayer graphene (MLG) arise from the 2-dimensional crystal lattice structure of constituent carbon atoms. In this chapter, the prominent electronic properties of graphene will be derived from its crystal lattice and electronic band structure, followed by a brief description of hexagonal boron-nitride and the Raman spectra of both 2D materials.

### 2.1 Graphene Lattice

A carbon atom has six electrons, two of which form a closed  $1s^2$  shell and the other four filling  $2s$  and  $2p$  orbitals. For the carbon allotrope graphene (Gr), or likewise graphite, which consists of multiple stacked-up Gr layers, the carbon atoms are arranged in a single layer in  $sp^2$ -hybridization, in which the  $2s$ -orbital and both  $2p_x$  and  $2p_y$  orbitals form three hybrid orbitals separated by  $120^\circ$  angles resulting in a hexagonal crystal [12, 13]. Such a honeycomb lattice is described by two triangular sublattices, referred to as A and B in the remainder of this chapter. Each atom on a given sublattice is surrounded by three next neighbours from the opposite sublattice only (a bipartite lattice) and many of the extraordinary electronic properties of Gr are related to its two-fold sublattice structure. In a coordinate system defined as shown in Fig. 2.1(a), the vectors pointing from an atom on the A sublattice to the three next neighbours on the B sublattice can be written as

$$\vec{r}_1 = a \begin{pmatrix} 1 \\ 0 \end{pmatrix}, \quad \vec{r}_2 = a \begin{pmatrix} -\frac{1}{2} \\ -\frac{\sqrt{3}}{2} \end{pmatrix}, \quad \vec{r}_3 = a \begin{pmatrix} -\frac{1}{2} \\ \frac{\sqrt{3}}{2} \end{pmatrix}, \quad (2.1)$$



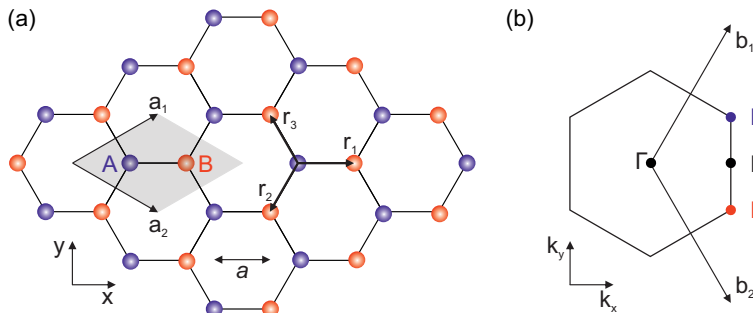


Figure 2.1: **(a)** Schematic of the hexagonal Gr lattice consisting of the A (blue) and B (red) sublattices, together with the corresponding unit cell shown in shaded gray. **(b)** The first Brillouin zone of the Gr lattice, together with the high symmetry points  $\Gamma$ ,  $K$ ,  $K'$ , and  $M$  marked in different colors.

where  $a \approx 1.42 \text{ \AA}$  is the nearest-neighbour distance between two atoms. A unit cell of the hexagonal lattice contains two neighbored atoms - one located on the A sublattice and one on the B sublattice. The unit cell, as well as the location of the next atoms on a given sublattice is defined by the lattice vectors

$$\vec{a}_1 = \sqrt{3}a \begin{pmatrix} \frac{\sqrt{3}}{2} \\ \frac{1}{2} \end{pmatrix}, \quad \vec{a}_2 = \sqrt{3}a \begin{pmatrix} \frac{\sqrt{3}}{2} \\ -\frac{1}{2} \end{pmatrix}. \quad (2.2)$$

The lattice constant of Gr can then be denoted as  $a_0 = |\vec{a}_{1,2}| = \sqrt{3}a \approx 2.46 \text{ \AA}$ . In the reciprocal space, the Gr lattice is of hexagonal nature as well with the corresponding reciprocal lattice vectors

$$\vec{b}_1 = \frac{4\pi}{3a} \begin{pmatrix} -\frac{\sqrt{3}}{2} \\ \frac{1}{2} \end{pmatrix}, \quad \vec{b}_2 = \frac{4\pi}{3a} \begin{pmatrix} +\frac{\sqrt{3}}{2} \\ \frac{1}{2} \end{pmatrix}. \quad (2.3)$$

The points of high symmetry in  $k$ -space are  $\Gamma$  in the center,  $M$  in the middle between two neighbouring atoms, and two  $K$  points at the corners of the Brillouin zone. These  $K$  points are in-equivalent and will therefore be denoted as  $K$  and  $K'$ . A schematic of the first Brillouin zone with all relevant symmetry points is shown in Fig. 2.1(b). Our next task is to derive the electronic band structure of Gr.

## 2.2 Electronic Band Structure

The formerly mentioned  $sp^2$ -hybrid orbitals form so-called  $\sigma$ -bonds arising from overlapping orbitals between the neighbouring atoms. The strong in-plane binding forces

of these bonds result in the outstanding mechanical properties of Gr [14, 15]. However, they do not contribute to electronic transport or optical processes in the low energy regime as a large gap separates the bonding and the anti-bonding counterparts. Instead, the electronic properties are mainly determined by the remaining  $p_z$ -orbitals, which are oriented perpendicular to the crystal plane. The  $p_z$ -orbitals at the atom sites overlap and thereby create delocalized  $\pi$ -bands, which are located closely around the Fermi energy. A tight binding calculation of the bands was first reported by P. R. Wallace in 1947 [16] and enhanced roughly a decade later<sup>1</sup> [19, 20] and later again in the context of carbon nanotubes [21, 22]. Wallace assumed that the  $\pi$ -bands satisfy Bloch's theorem [23] - which means that the  $p_z$ -orbitals of the  $N$  carbon atoms form a basis, where each wave function is an energy eigenstate of the system and can be written as  $\psi(\vec{r}) = e^{i\vec{k}\vec{r}} \cdot u(\vec{r})$ , where  $u$  is invariant under the translation of lattice vector  $\vec{R}_i = n_i\vec{a}_1 + m_i\vec{a}_2$  for integer  $n_i, m_i$ , such that  $u_k(\vec{x}) = u_k(\vec{x} + \vec{R}_i)$ . When locating the origin in the A sublattice of our Gr system, the A and B wave functions then become

$$\begin{aligned}\psi_A(\vec{r}) &= \frac{1}{\sqrt{N}} \sum_{i=1}^N e^{i\vec{k}\cdot\vec{R}_i} u(\vec{r} - \vec{R}_i), \\ \psi_B(\vec{r}) &= \frac{1}{\sqrt{N}} \sum_{i=1}^N e^{i\vec{k}\cdot\vec{R}_i} u(\vec{r} - \vec{R}_i - \vec{r}_1)\end{aligned}\tag{2.4}$$

and the total wave function  $\Psi(\vec{r})$  of the system is a linear combination of both sublattice wave functions

$$\Psi(\vec{r}) = \alpha\psi_A(\vec{r}) + \beta\psi_B(\vec{r}).\tag{2.5}$$

The Gr Hamiltonian is represented by a sum over the individual atomic potentials  $V_0(\vec{r})$  of all carbon atoms such that

$$H = \frac{\vec{p}^2}{2m} + \sum_{i=1}^N (V_0(\vec{r} - \vec{R}_i) + V_0(\vec{r} - \vec{R}_i - \vec{r}_1)).\tag{2.6}$$

In the following, we will only consider nearest-neighbour hopping and assume that the overlap integral of adjacent  $p_z$ -orbitals as well as the orbital energy  $\epsilon_0 = \langle u(\vec{r}) | H | u(\vec{r}) \rangle$  are zero [24], which reduces the eigenvalue problem to

$$\begin{pmatrix} \epsilon_0 & -\gamma_0 f(\vec{k}) \\ -\gamma_0 f^*(\vec{k}) & \epsilon_0 \end{pmatrix} \begin{pmatrix} \alpha \\ \beta \end{pmatrix} = E \begin{pmatrix} \alpha \\ \beta \end{pmatrix},\tag{2.7}$$

where  $\gamma_0 \langle u(\vec{r} - \vec{r}_1) | H | u(\vec{r}) \rangle$  is the nearest neighbor hopping energy and  $f(\vec{k}) = \sum_{l=1}^3 e^{i\vec{k}\cdot\vec{r}_l}$ . It can be calculated numerically using density-functional-theory (DFT) to

<sup>1</sup>All these early works treat the graphite band structure rather than Gr as an isolated crystal. This is due to the fact, that for a long time it was believed, that individual Gr layers could not exist due to their thermodynamic instability following the Mermin-Wagner-Theorem [17, 18]

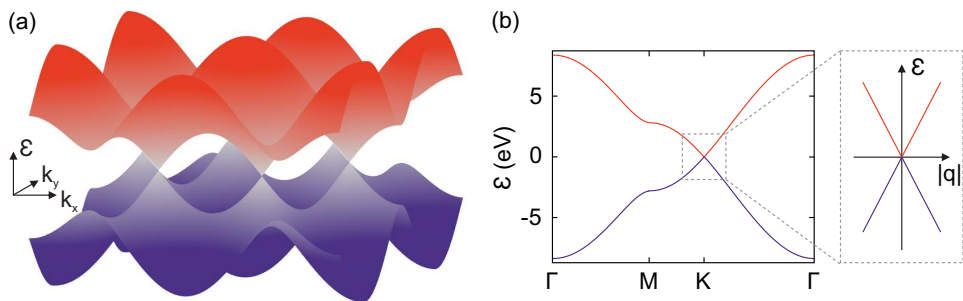


Figure 2.2: **(a)** Electronic band structure of monolayer Gr obtained by tight binding calculation, where the conduction band ( $\pi^*$ ) and the valence band ( $\pi$ ) are shaded in red and blue. **(b)** Line cut through **(a)** along symmetry points of the first Brillouin zone (BZ) together with a magnification of the linear dispersion at  $K$ . This figure is partially inspired by [25].

$\gamma_0 \approx -3.033$  eV [21].

For this simple case we can now calculate the eigenvalues  $\epsilon(\vec{k})$ , which take the form

$$\epsilon_{\pm} = \pm \gamma_0 |f(\vec{k})| = \pm \gamma_0 \sqrt{3 + 2 \cos(\sqrt{3} k_y a) + 4 \cos\left(\frac{\sqrt{3}}{2} k_y a\right) \cos\left(\frac{3}{2} k_x a\right)}. \quad (2.8)$$

We thus obtain a bonding ( $\pi$ ) and an anti-bonding ( $\pi^*$ ) band, as shown in Fig. 2.2(a). Both bands touch at the  $K$  and  $K'$  points, which are also called the Dirac<sup>2</sup> points and the largest separation is found at the  $\Gamma$ -point with  $6\gamma_0 \approx 18$  eV [13]. In the absence of external doping, the  $\pi$  band is filled up, while the ( $\pi^*$ ) band is empty, implying that the Fermi energy is situated directly at the Dirac points. Therefore, to understand transport phenomena in Gr, the considered energy range is usually limited to the dispersion around the  $K$ -points and facilitates an expansion of the Hamiltonian for low energies.

Such an expansion can be done by introducing a small  $\vec{q}$  around the  $K$  points such that

$$\vec{k} = \vec{K} + \vec{q} \quad \text{with} \quad \vec{K}^{(\prime)} = \frac{2\pi}{3a} \begin{pmatrix} 1 \\ (-) \frac{1}{\sqrt{3}} \end{pmatrix}, \quad (2.9)$$

<sup>2</sup>Named after the English theoretical physicist Paul Adrien Maurice Dirac (1902-1984). Being one of the founding fathers of quantum physics he was awarded with the Nobel prize in physics in 1933. Among his most significant contributions is the introduction of the Dirac equation in 1928, within which he combined for the first time the special theory of relativity with quantum mechanics. Gr is prominent for hosting relativistic fermions, described by the Dirac equation (see further below).

and, consequently,

$$f(\vec{K} + \vec{q}) = \sum_{l=1}^3 e^{i(\vec{K} + \vec{q}) \cdot \vec{r}_l} \approx \sum_{l=1}^3 e^{i\vec{K} \cdot \vec{r}_l} (1 + i\vec{q} \cdot \vec{r}_l). \quad (2.10)$$

This gives us an expression of the Hamiltonian around the  $K$  points:

$$H = \hbar v_F \begin{pmatrix} 0 & \alpha'(q_x - iq_y) \\ \alpha'^*(q_x + iq_y) & 0 \end{pmatrix}, \quad (2.11)$$

where  $\alpha' = e^{i5/6\pi}$  is a phase factor that can be tuned to one by rotating the basis functions [12] and  $v_F = \sqrt{3}\gamma_0 a / (2\hbar) \approx c/300 \approx 10^6$  m/s is the Fermi velocity. By using the Pauli matrices  $\vec{\sigma} = (\sigma_x, \sigma_y)$  the Hamiltonian around the  $K$ -points can be further simplified to the form of a Dirac-Weyl Hamiltonian

$$H_K = v_F \hbar \vec{\sigma} \cdot \vec{q}, \quad (2.12)$$

and thereby to a linear dispersion relation (as shown in the close-up of Fig. 2.2(b))

$$\epsilon_K(\vec{q}) = \pm v_F \hbar |\vec{q}|. \quad (2.13)$$

The Hamiltonian and the linear dispersion closely resemble those of massless Dirac fermions like neutrinos and contrasts itself from the parabolic dispersion in conventional two-dimensional electron systems (2DES). The speed of light  $c$  in the expression for neutrinos is replaced in the case of Gr by  $v_F$ .

In comparison with a relativistic particle, the vector  $(\alpha, \beta)$  acts formally equivalent to the real spin and is therefore called the *pseudo-spin* vector. It is directly locked to the direction of  $\vec{q}$ , depending on which  $\pi$ -band and which  $K$ -point is considered, implying that the wave functions are of a chiral nature. The conservation of the pseudo-spin further implies that direct back-scattering of carriers is forbidden within one valley and only becomes possible via intra-valley scattering, which requires a large momentum transfer that cannot be facilitated by simple scattering centers like defects or Coulomb scatterers [26]. Furthermore, it was realized that so-called Klein<sup>3</sup> tunneling, which describes the tunneling of Dirac fermions in the context of the Klein paradox [27, 28]. The latter effect is nicely summarized by Katsnelson in Chapter 4.3 of [12]:

In conventional terms of solid-state physics, Klein tunneling is nothing other than tunneling through a p-n-p (or n-p-n) junction when electrons are transformed into holes and then back to electrons (or vice versa). ... for massless Dirac fermions the transmission at normal incidence is always 100 % irrespective of the height and width of the potential barrier. From the point of view of applications, this is very bad news: if one just

---

<sup>3</sup>Named after the Swedish theoretical physicist Oskar Klein (1894-1977).

copies the construction of a silicon transistor it will not work, since it is impossible to lock it. The gap opening is necessary. The good news is, that due to the Klein paradox, the unavoidable inhomogeneities of the electron density in graphene do not lead to localization, and, moreover, their effect on the electron mobility is not very great.

This has far-reaching consequences for the electronic transport in Gr crystals, resulting in high charge carrier mobilities up to room temperature [29, 30]. A comprehensive discussion of the limitations of the carrier transport in Gr can be found in [31]. When the eigenfunctions are rotated adiabatically around the  $K$ -points on a closed path that forms the boundary of a surface  $\mathcal{S}$ , they pick up a phase of

$$\gamma = \int_{\mathcal{S}} d\vec{S} \cdot \vec{\Omega}(\vec{k}), \quad (2.14)$$

which is called the Berry<sup>4</sup> phase and  $\vec{\Omega}(\vec{k})$  the Berry curvature - a gauge-invariant local manifestation of the geometric properties of the wavefunctions in  $k$ -space [32–34]. In Gr, the Berry phase integral around the  $K^{(\prime)}$  point yields  $\gamma = \frac{(-)}{(+)}\pi$  for electrons and  $\gamma = \frac{(+)}{(-)}\pi$  for holes [35]. The Berry phase will become important for the unique high-field magneto-transport characteristics of Gr, as described in Chapter 3.

## 2.3 Density of States and Ambipolar Electronic Transport in Graphene

The massless nature of the charge carriers in Gr owes up for many of its unique electronic transport properties. As such electronic transport measurements constitute the greatest part of the data shown and discussed in this work, it is mandatory to elaborate the underlying mechanisms in detail. In the following, we will depict the density of states as well as the ambipolar field effect and the diffusive transport regime in Gr. A detailed description of the transport phenomena within magnetic fields is provided in Chapters 3 and 4.

The number of available states per energy interval  $d\epsilon$  per unit area of Gr is called the density of states (DOS) [36]. A single state in Gr occupies the area  $(2\pi)/A$  in the  $k$ -space, where  $A$  is the Gr sheet area. When we now imagine a ring of radius  $k$

---

<sup>4</sup>The Berry-phase is named after the British mathematical physicist Michael Berry (\*1941), who, apart from his great contributions in many fields of quantum mechanics and optics, was together with Andre Geim, awarded with the IG Nobel prize in 2000 for their work on the "The Physics of Flying Frogs". The experimental part of the latter consisted in the levitation of a frog in very high magnetic fields in the facilities of the high magnetic field laboratory (HFML) in Nijmegen. The present author feels honored to have measured Gr transport devices within the same high magnetic field laboratory.

and width  $dk$  in the  $k$ -plane, the number of states in that ring becomes  $dN = \frac{2kA}{\pi}dk$ . Now using Eq. (2.13), we obtain  $k = \frac{|\epsilon|}{\hbar v_F}$  and  $\frac{d\epsilon}{dk} = \hbar v_F$  and the DOS of Gr takes the form

$$D(\epsilon) = \frac{1}{A} \frac{dN}{d\epsilon} = \frac{1}{A} \frac{dN}{dk} \frac{dk}{d\epsilon} = \frac{2|\epsilon|}{\pi \hbar^2 v_F^2}. \quad (2.15)$$

In GR the DOS increases linearly with energy  $\epsilon$  around the  $K$ -points, which once again is in stark contrast to the constant DOS in parabolically dispersing 2DES [36]. We can now use the DOS to derive an expression for the Fermi energy  $E_F$  as function of the charge carrier density  $n$ , which is the number of carriers per area unit. By identifying a change in the charge carrier density as  $dn = \frac{dN}{A}$ , we get  $dn = \frac{2|\epsilon|d\epsilon}{\pi \hbar^2 v_F^2}$ . Once again using the Gr dispersion Eq. (2.13) and  $d\epsilon = \hbar v_F dk$  we obtain  $dn = \frac{2}{\pi} k dk$ . Integrating both sides of this equation yields

$$\int_0^n dn = \frac{2}{\pi} \int_0^{k_F} k dk. \quad (2.16)$$

And hence we get expressions for the Fermi wavevector  $k_F$  and the Fermi energy  $E_F$  as function of  $n$

$$k_F(n) = \sqrt{\pi|n|} \quad E_F(n) = \text{sign}(n) \hbar v_F \sqrt{\pi|n|}. \quad (2.17)$$

An important consequence of the massless nature of the charge carriers is, that the usual concept of the effective mass breaks down and the cyclotron mass approach must be applied [36, 37]. The cyclotron mass is defined as

$$m^* = \frac{1}{2\pi} \left[ \frac{\partial A(\epsilon)}{\partial \epsilon} \right]_{\epsilon=E_F}, \quad (2.18)$$

where  $A(\epsilon) = \pi k(\epsilon)^2 = \frac{\pi \epsilon^2}{(\hbar v_F)^2}$  is area enclosed by an orbit in  $k$ -space. This gives a cyclotron mass that depends on the square-root of  $n$  as

$$m^* = \frac{\hbar k_F}{v_F} = \frac{E_F}{v_F} = \frac{\hbar}{v_F} \sqrt{\pi n}. \quad (2.19)$$

In ideal undoped Gr where  $n = 0$ ,  $E_F$  should be situated at zero energy where the band  $\pi$  and  $\pi^*$  band touch at the  $K$ -points. This singular point, where neither electrons nor holes govern the transport in Gr is called the *charge neutrality point* (CNP). However, in real Gr crystals, there is always a finite level of doping  $n_0$  present, which offsets the Fermi level. Furthermore, due to inhomogeneities caused by charge disorder or nanometer-scale strain variations, a residual amount of charge carrier fluctuations  $n^*$  is present at zero energy, which precludes a complete absence of charge carriers [29, 38]. Both  $n_0$  and  $n^*$  are measures of the structural and electronic quality of a Gr crystal and can be determined in transport or Raman spectroscopy measurements.

The charge carrier density  $n$  in a Gr device can be altered via the electric field effect. To this extend, a conductive material acting as gate is brought close to the Gr layer, spaced by an insulating barrier. In the devices considered for this thesis, highly doped Si wafers with 300 nm thick SiO<sub>2</sub> dielectrics were used both as a substrate and back gate electrode. In order to fabricate close or local gates, hexagonal boron nitride (hBN) crystals (see section (2.4)) can be used as thin dielectric layers together with metallic or graphitic gate materials. Such advanced gating techniques lead to tremendous improvements in device tunability [39] in MLG as well as to great breakthroughs in the field of bilayer graphene (BLG) including quantum dots [40–47].

An electrostatic gate voltage  $V_{\text{BG}}$  is applied between the gate and the Gr device creating an electric field, which leads to the accumulation of charge carriers both in the Gr and on the gate surface analogue to the situation on a plate capacitor<sup>5</sup>. The charge carrier density induced in the Gr bulk by  $V_{\text{BG}}$  depends on the dielectric properties of the insulation layer and its thickness  $d$  as

$$n = \frac{\epsilon_0 \epsilon_r}{ed} (V_{\text{BG}} - V_0), \quad (2.20)$$

where  $e$  is the electron charge,  $\epsilon_0 = 8.85 \times 10^{-12}$  F/m is the vacuum permittivity,  $\epsilon_r$  is the dielectric constant. The pre-factor in Eq. (2.20) is called the gate lever arm  $\alpha = \frac{\epsilon_0 \epsilon_r}{ed}$ . The voltage  $V_0$  is required to compensate the offset charge carrier density  $n_0 = \alpha \cdot V_0$ . The relation in Eq. (2.20) holds for a wide range of carrier densities and since Gr is a semi-metal without a band gap, the system can be continuously tuned from electron to hole conduction. As discussed above, at the CNP, a minimum of charge carriers remains always present, resulting in a minimal conductance  $G$  and likewise maximum resistance  $R$ , while for increasing  $|n|$  we expect  $G$  to rise and  $R$  to fall. This behavior is called the *ambipolar* field effect in Gr. A typical Gr field effect transistor measurement is shown in Fig. 2.3(a), where the resistance  $R$  as function of the applied back gate voltage  $V_{\text{BG}}$  is plotted, while Fig. 2.3(b) shows the corresponding conductivity  $\sigma$  as function of the charge carrier density  $n$ .

The observed electronic transport behaviour at zero magnetic field at a given carrier density  $n$  now depends on the governing transport regime and, therefore, on the predominant scattering mechanism. Most of the Gr devices, that were measured in this thesis are in the *diffusive* transport regime, which means that the mean free path  $l_{\text{mfp}}$  that a charge carrier travels between two scattering events, as well as the Fermi wavelength  $\lambda_F = 2\pi/k_F$  (which is a measure of the mean spacing of the charge carriers in the system) are much smaller than the transport channel dimensions, namely its width  $w$  and length  $l$

---

<sup>5</sup>As the plates of our virtual capacitor are not infinitely large, the field lines will necessarily adverse from a purely vertical direction at the edges, creating the so-called gating or edge effect. The influence of these stray fields becomes important for all edge-sensitive effects e.g. the screening induced (in)compressible landscapes formed in large magnetic fields (see Chapter 4.2)

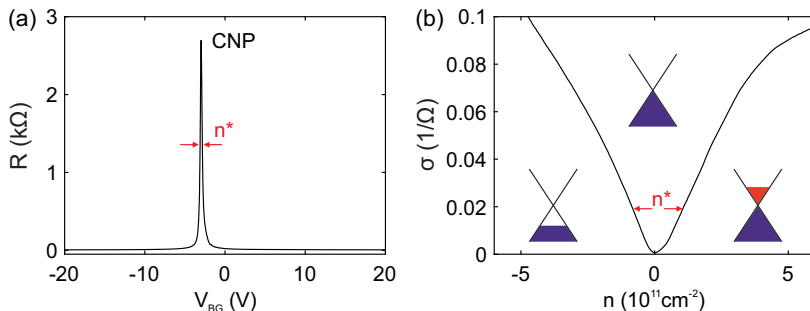


Figure 2.3: **(a)** Four-terminal resistance  $R$  of a Gr transport device as a function of the applied back gate voltage  $V_{BG}$  at a temperature of 100 K. The device shows slight p-doping as the CNP resides on the negative gate voltage side. **(b)** Conductivity  $\sigma$  as a function of the charge carrier density  $n$  calculated using the back gate lever arm  $\alpha_{BG}$ . The residual level of charge carrier fluctuations  $n^* \approx 2 \cdot 10^{10} \text{ cm}^{-2}$  is highlighted in **(a)** and **(b)** by red arrows.

$$l_{\text{mfp}}, \lambda_F \ll w, l. \quad (2.21)$$

As  $\lambda_F$  grows with decreasing  $n$  we would expect a breakdown of the diffusive transport near charge neutrality, however, due to the residual disorder present, corresponding effects like quantum interference are usually not observed and it is justified to apply the semi-classical Drude-Boltzmann transport model [12, 13]. The conductivity  $\sigma$  of a rectangular shaped device can then be expressed as

$$\sigma(n) = ne\mu = \frac{1}{\rho} = \frac{l}{w} \frac{1}{R}, \quad (2.22)$$

where  $\mu$  is the charge carrier mobility and  $\rho$  the resistivity. When the shape of a devices channel is adversing from a rectangular shape, the conductivity can still be extracted using the van-der-Pauw methods [24, 48]. In a device of arbitrary shape with four point-like contacts P, Q, R, S, at its edges, the resistance is measured in two configurations (by injecting a current from contact P to contact Q, while measuring at the voltage drop between contact R and contact S the resistance  $R_{PQ,RS}$  is measured). For the resistivity and likewise conductivity then follows

$$\rho = \frac{1}{\sigma} = \frac{\pi}{\ln 2} \frac{R_{PQ,RS} + R_{QR,SP}}{2} f \left( \frac{R_{PQ,RS}}{R_{QR,SP}} \right), \quad (2.23)$$

with the implicitly defined function

$$\frac{x-1}{x+1} = \frac{f}{\ln 2} \text{acosh} \left( \frac{1}{2} \exp \left( \frac{\ln 2}{f} \right) \right). \quad (2.24)$$



Now, while the carrier mobilities are related to the scattering time  $\tau$  and the effective mass  $m^*$  as  $\mu = \frac{e\tau}{m^*}$  conventional 2DES, the absence of  $\frac{1}{m^*} \propto \frac{\partial^2 E}{\partial k^2}$  due to the linear dispersion in Gr requires the cyclotron mass definition of  $m^*$  in Eq. (2.19) such that we can write

$$\mu_{\text{Gr}} = \frac{e\tau v_{\text{F}}^2}{E_{\text{F}}}. \quad (2.25)$$

The scattering time  $\tau$  in the above equations consists of the inversely added scattering times of all scattering processes present. The measurement of  $\sigma$  for varying  $n$  therefore contains valuable information on the transport regime and the dominant scattering mechanisms. Fits to the linear parts of the conductivity trace as function of carrier density yield the charge carrier mobilities of both electrons and holes, while an evaluation of the CNP-region in a log-log plot yields the charge carrier fluctuations  $n^*$ .

When  $l_{\text{mfp}}$  increases upon decreasing scattering events and finally becomes comparable to the device dimensions, the transport enters a *ballistic* regime, where the electrons travel in straight trajectories through the field free system (electron billiard). The mobility, which is needed for a channel of length  $l = l_{\text{mfp}}$  to become ballistic at a given threshold carrier density  $n_{\text{th}}$  can be written as [9]

$$\mu = \frac{2e\sqrt{\pi}l_{\text{mfp}}}{h\sqrt{n_{\text{th}}}}. \quad (2.26)$$

This expression can be used to estimate a lower threshold for carrier mobilities in devices that show an onset of ballistic transport at  $n_{\text{th}}$ .

When the Fermi wavelength  $\lambda_{\text{F}}$  increases compared to  $l_{\text{mfp}}$ , the phase properties of the charge carrier wave functions become increasingly important and enable interference and localization effects. This regime is called the mesoscopic<sup>6</sup> transport regime. A comprehensive summary of the relevant physics in that regime can be found in Chapter 1 of Ref. [50].

## 2.4 Hexagonal Boron Nitride

Hexagonal boron nitride (hBN) is a layered material, where each basal plane has a hexagonal lattice structure analogue to Gr layers within a graphite crystal and the individual layers are bound vertically by van-der-Waals<sup>7</sup> forces here as well. A schematic of the crystal structure of hBN is shown in Fig. 2.4. In this case, each of

<sup>6</sup>The term *mesoscopics* was introduced by van Kampen in 1981 [49].

<sup>7</sup>Named after Johannes Diderik van der Waals (1837-1923), a Dutch physicist awarded the Nobel Prize in Physics in 1910 for his significant contributions to the study of intermolecular forces and the behavior of gases and liquids. He introduced the concept of "van-der-Waals forces" to describe the weak intermolecular forces between atoms and molecules, which give rise to various physical phenomena. The discovery of Gr and other 2D materials has sparked renewed interest in the study of van-der-Waals forces and their impact on the properties and behavior of layered materials.

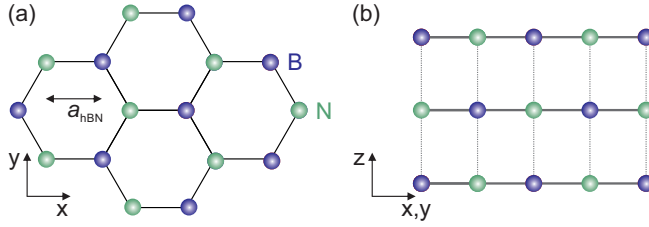


Figure 2.4: **(a)** The lattice structure of hBN, with boron (B) and nitrogen (N) atoms forming the two sublattices. **(b)** In bulk hBN crystals, the sublattices are vertically shifted, creating a vertical alternation of atom types.

the two sublattices are occupied exclusively by boron or nitrogen atoms. The nearest neighbour distance  $a_{\text{hBN}} = 1.44 \text{ \AA}$  is very similar to that of Gr (1.7 % larger), however due to different on-site potentials of both sublattices caused by the stacking order, hBN crystals are insulators with a band gap of 6.4 eV [51–53]. In the out-of-plane direction, hBN has a dielectric constant  $\epsilon_{\text{hBN}} = 3.4$  which is comparable to that of  $\text{SiO}_2$ , while in other cases like for the calculation of the effective Bohr radius in Gr (see Chapter 4.2) an averaged value of  $\epsilon_{\text{hBN}} = 5$  should be used [54–56]. The closely matching lattice constant, together with its flat surface, the absence of dangling bonds and the strongly insulating properties make hBN an ideal material for the integration with Gr as a substrate or by a full encapsulation [57–60]. Such hetero-stacking was successfully applied to achieve high mobility devices [57] and to measure delicate phenomena like the fractional quantum Hall effect [61–63] or superconducting phases in twisted bilayer Gr [64]. As the aim of this thesis is to fabricate CVD-Gr magnetotransport devices of the highest quality, hBN crystals were employed to dry-transfer and stack them into hBN/CVD-Gr/hBN heterostructures as described in Chapter 6.

## 2.5 Raman Spectrum of Monolayer Graphene

Raman spectroscopy<sup>8</sup> is a versatile tool for the fast and non-invasive study of structural properties of molecules and solids and of special importance for 2D materials like Gr as it allows to access spatially resolved information on the number of layers [66–68] as well as on local strain [38, 69–73] and doping [74–77]. Comprehensive summaries of most Raman related effects in Gr can be found in the PhD theses of Neumann, Reichardt and Sonntag [78–80]. In this work, micro-Raman spectroscopy is used at different steps of the device fabrication in order to monitor the composition, structural quality and homogeneity of Gr-based heterostructures and to monitor the

<sup>8</sup>Named after the Indian physicist C. V. Raman (1888-1970), who discovered the effect of Raman scattering in 1928 [65] and was awarded with the 1930 Nobel prize in physics for its discovery. In fact, he was the first Asian who ever received a Nobel prize in any branch of science.

oxidation of Cu/Gr interfaces.

A Raman scattering process in Gr consists of incident photons on the carbon lattice which then excite an electron-hole pair, followed by the emission or absorption of phonons and finally its recombination under the emission of an outgoing photon. Purely elastic scattering processes imply momentum conservation and, therefore, the wavevectors  $k_{\text{in}}$  and  $k_{\text{out}}$  of the incident and outgoing photons together with the sum of the wavevectors of the phonons created or involved  $K_{\text{phonons}}$  have to fulfill

$$k_{\text{in}} = K_{\text{phonons}} + k_{\text{out}}. \quad (2.27)$$

When  $k_{\text{in}}$  is known and the energy distribution of  $k_{\text{out}}$  is measured, information can be gained on the vibrational lattice modes in Gr. Experimentally, a given sample is usually illuminated with a laser of known wavelength  $\lambda_{\text{in}}$  in a special Raman-microscope and analyzes the outgoing light by a spectrometer after passing it through a grating. For a typical Raman spectrum, the count of emitted photons with  $\lambda_{\text{out}}$  is plotted against the so-called Raman shift

$$\Delta \frac{1}{\lambda} = \frac{1}{\lambda_{\text{in}}} - \frac{1}{\lambda_{\text{out}}}. \quad (2.28)$$

The analysis of the peaks in the spectra in terms of the positions  $\omega_{\text{peak}}$  and widths  $\Gamma_{\text{peak}}$  yields crucial information. In this work, for the characterization of heterostructures a green laser with  $\lambda_{\text{in}} = 532$  nm is used, while for the monitoring of Gr on Cu substrates a blue laser with  $\lambda_{\text{in}} = 457$  nm is employed to avoid the broad photo-luminescence peaks of the Cu surface within the studied spectral range (see Chapter 6).

Understanding the Raman spectrum of Gr starts by understanding its phonon dispersion. As there are two carbon atoms in the lattice unit cell, we have in total six possible in-equivalent phonon modes. These modes are either acoustic (A) or optical (O) with respect to the bond direction either longitudinal (L) or transverse (T). Four of the six modes are in-plane modes (iLA, iLO, iTA, iTO) and two are out of plane (oTA, oTO). Schematic illustrations of these phonon modes are shown in Fig. 2.5(a). The dispersions of these modes can be accessed via DFT calculations [81] and are plotted in Fig. 2.5(b). The selection rules that result from the crystal symmetry do not allow all of these phonon modes to be Raman active, but only the iLO and iTO modes [82]. For the simplest one-phonon Raman scattering process, the relevant  $k$ -range is further limited to the vicinity of the  $\Gamma$  point, as the incident photons have negligible wavevectors.

The main constituents of the Raman spectrum of Gr are the G-peak, the 2D-peak and the D-peak. A typical Raman spectrum of an hBN/Gr/hBN heterostructure is shown in Fig. 2.6(a). In the following we will briefly discuss the scattering mechanisms

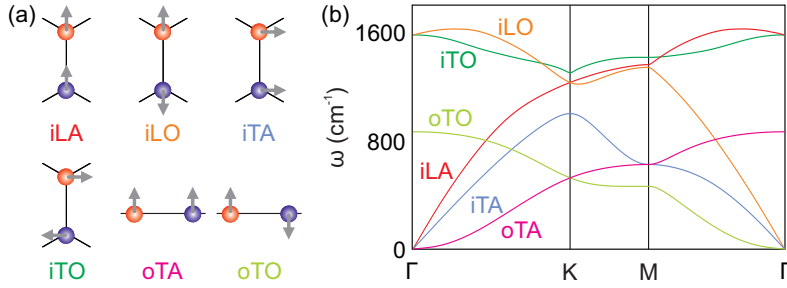


Figure 2.5: **(a)** Sketches of the six phonon modes of MLG: in-plane (i), out of plan (o), longitudinal (L), transverse (T), acoustic (A) and optical (O). **(b)** Corresponding frequency dispersions of the phonon modes shown in **(a)**. The panels are adapted from [31, 81].

behind each peak and what kind of information can be gained.

The G-peak is characteristic feature that is present in all graphitic materials and was hence named accordingly. It is created when an incident photon excites an electron, which then emits iTO/iLO phonons at the  $\Gamma$ -point and subsequently falls back into its initial state under the emission of an outgoing photon. A schematic illustration of this process is shown in Fig. 2.6(b). The wavelength difference between the in- and outgoing photons then determine the G-peak position [66, 67]

$$\omega_G = \Delta \frac{1}{\lambda_G} \approx 1585 \text{ cm}^{-1}. \quad (2.29)$$

The 2D-peak is the result of a second order Raman scattering process [83]. The incoming photon excites an electron-hole pair to valence band states, which then undergoes an inter valley scattering (e.g. from the  $K$  to the  $K'$  valley) under the emission of an iTO phonon near the  $K$ -point. Subsequently, the electron-hole pair falls back to the conduction band under the emission of a photon and is scattered back to its original valley repeating the emission of an iTO phonon near the  $K$  point. Each of the emitted iTO phonons causes a shift of  $\Delta \frac{1}{\lambda} = 1350 \text{ cm}^{-1}$  [81] and hence, the 2D peak position is located at roughly twice this shift, where the derivation stems from additional scattering processes connecting the outer band edges of the  $K$  and  $K'$  valley [84] and one obtains

$$\omega_{2D} = \Delta \frac{1}{\lambda_{2D}} \approx 2680 \text{ cm}^{-1}. \quad (2.30)$$

The 2D-peak scattering process can happen either on the inner or on the outer sides of respective to the  $K$  and  $K'$  points as illustrated in Fig. 2.6(c).

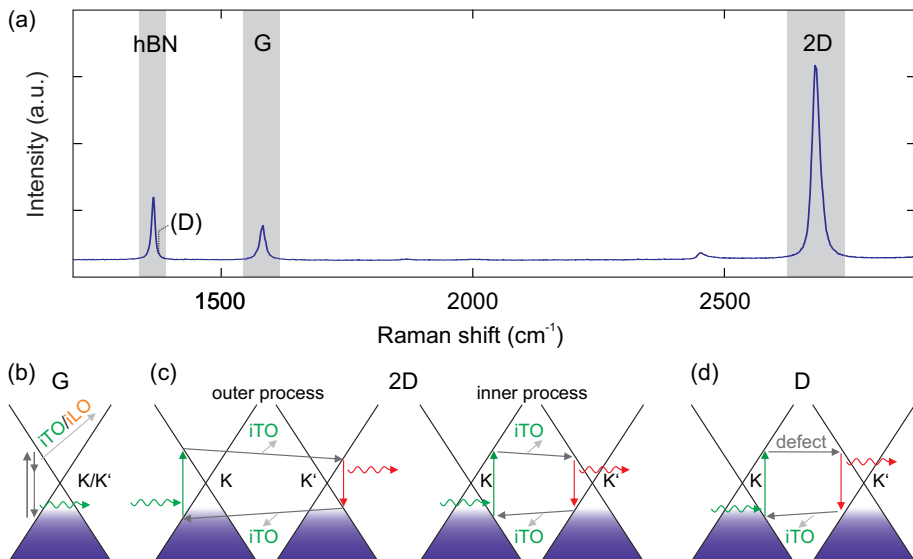


Figure 2.6: **(a)** Raman spectrum of an hBN/Gr/hBN heterostructure, with the G, 2D and hBN peaks highlighted in gray. The absence of the D peak is due to the high structural quality. **(b)-(d)** Schematic illustrations of the Raman scattering processes for the G-, 2D-, and D-peak, with wavy lines representing incoming or outgoing photons and light gray arrows indicating emitted phonons.

The Gr D-peak is created similarly to the 2D-peak (see Fig. 2.6(d)), with the important difference, that an inelastic scattering event replaces the one of the elastic inter-valley scattering processes and hence only one iTO phonon is emitted at the  $K$ -points, such that the D-peak position is located at [66, 67]

$$\omega_D = \Delta \frac{1}{\lambda_D} \approx 1350 \text{ cm}^{-1}. \quad (2.31)$$

The D-peak is therefore highly dependent on sharp local defects in the Gr lattice, which is why it is also interpreted as a defect peak and its intensity as measure of the amount of defects present in a Gr crystal, where the D-peak is fully absent in high quality Gr devices [8].

As hBN hosts a very similar lattice structure to Gr, and therefore hosts a first-order scattering peak that manifests similarly to the G-peak and is located at [85, 86]

$$\omega_{\text{hBN}} = \Delta \frac{1}{\lambda_{\text{hBN}}} \approx 1365 \text{ cm}^{-1}. \quad (2.32)$$

The other Gr peaks show no counterparts in the hBN spectrum, due to the vastly different band structure. As the hBN-peak is situated very close to the Gr D-peak,

one of them sometimes appears as a shoulder to the other and they are easily confused in low quality heterostructures.

All the above mentioned peak positions are given for  $\lambda_{\text{in}} = 532$  nm and one should keep in mind, that the positions eventually disperse upon changing the incident phonon energy. The positions further depend on the dispersion of the involved phonons and are therefore sensible to strain and doping of the Gr crystal lattice, where the strain effect can be straight forwardly understood by the reduced overlap of the bonding  $\text{sp}^2$ -orbitals that results in the softening of the phonon modes [69, 70]. The shift  $\delta\omega$  of the Raman frequency  $\omega_0$  with applied strain  $\delta\epsilon$  is characterized by the so-called Grüneisen<sup>9</sup> parameter [87]

$$\gamma = \frac{1}{2\omega_0} \frac{\delta\omega}{\delta\epsilon}. \quad (2.33)$$

The Grüneisen parameter allows us to relate the relative shift of G-peak and the 2D-peak in the presence of strain as [73]

$$\delta\omega_{2\text{D},\text{strain}} = 2.2 \times \delta\omega_{\text{G},\text{strain}}. \quad (2.34)$$

The doping-related frequency shift can be analyzed in a similar way and is based on the breakdown of the adiabatic Born-Oppenheimer approximation (see Refs. [75, 88] for details) and leads to

$$\delta\omega_{2\text{D},\text{doping}} = 0.7 \times \delta\omega_{\text{G},\text{doping}}. \quad (2.35)$$

Both relations together allow us to correlate the G-peak position to the 2D-peak position and subsequently separate strain and doping in a vector decomposition approach that was first reported in [73]. This analysis can be applied to get a statistical and spatial measure of the strain and doping distribution in a Gr heterostructure.

Concerning the peak widths, we will only discuss  $\Gamma_{2\text{D}}$ , as it is of the greatest relevance for device fabrication. Neumann et al. found, that the 2D-peak width, while being insensitive to changes in doping, is most likely broadened by random strain variations on the order of the laser spot size ( $\approx 500$  nm) [38]. As these random strain variations also impact the transport properties of Gr devices (see above), the evaluation of  $\Gamma_{2\text{D}}$  in terms of spatial mappings and histograms gives valuable information on the structural and the (to be expected) electronic quality of a device. The best Gr heterostructures usually host  $\Gamma_{2\text{D}} < 20 \text{ cm}^{-1}$  while Gr on bare  $\text{SiO}_2$  shows  $\Gamma_{2\text{D}} > 30 \text{ cm}^{-1}$  [8, 89].

## 2.6 Summary

In this chapter, the crystal lattice and band structure of MLG were derived, followed by a compilation of the most important consequences of the linear dispersion around

---

<sup>9</sup>Named after the German physicist Eduard August Grüneisen (1877-1949).

the  $K$ -points and basic transport properties in the diffusive regime. Finally, we discussed the Raman spectrum and the constituting mechanisms and applications of its significant peaks. The quantities and relations elaborated in this chapter will be crucial for the remainder of this thesis. In the next two chapters we will focus on the effects of (large) magnetic fields on 2DES like the one in Gr in detail, as it is of great importance for the understanding and interpretation of the results obtained in Chapters 8 and 9.

## Chapter 3

# Quantum Hall Effect I: Landau Quantization

In the previous chapter, the basic electronic properties and transport characteristics of Gr were elaborated. The main goal of this thesis is to test and explore the properties of CVD-Gr in the realm of large magnetic fields - a realm in which over the last decades, a zoo of increasingly complex physical phenomena has been reported in experiments and unified by theory. It is instructive to work out a detailed summary of the underlying physics of magneto-transport phenomena together with a history of thought in this field, as the knowledge of its recent advancements failed to percolate efficiently through the research communities<sup>1</sup> and only few works can be found in literature, that accurately compile such information.

In this chapter, we will first recap the classical Hall effect within the Drude framework for a two-dimensional electron system in presence of a low perpendicular magnetic field, followed by a semi-classical derivation of the condensation of its DOS into Landau level in higher magnetic fields. This is followed by a description of the modifications to such an energy spectrum in the case of strong interaction in the context of degeneracy lifting and the nature of the ground state of Gr as well as correlation effects leading to the formation of fractional quantum Hall states. Afterwards, a brief historic review of quantized magneto-transport measurements and accompanying the theory is drawn that resulted in the unexpected discovery of the integer quantum Hall effect (IQHE). It will become clear, that in order to explain aspects of the IQHE, further assumptions within a microscopic model have to be made and the discussion

---

<sup>1</sup>In fact, the microscopic pictures of the QHE (see Chapter 4) are vital example of the phenomenon, that the percolation of information in the research community, contrary to naive expectations, is not as efficient as e.g. the information percolation in the capital markets, where new data are immediately prized in. Although convincing theoretical and experimental works in this area of QHE physics exist, a paradigm change did not occur so far.



of such models is presented in Chapter 4.

### 3.1 Classical Hall Effect

The influence of an external magnetic field on a current carrying medium, as mediated by the Lorentz force, is well known since the end of the 19-th century as the classical *Hall-effect*<sup>2</sup> and has since then become an important part of any high schools physics curriculum. 2DES like Gr with a tunable charge carrier density  $n$  are restricted to in-plane directions and thus we will consider a 2DES in the xy-plane with a magnetic field  $B$  perpendicular to it in the z-direction in our following considerations. Hall measurements are ideally performed on device shaped in a so-called *Hall-bar* geometry (see Fig. 3.1). A bias voltage  $V_{DS}$  is applied between the *source* (S) and the *drain* (D) electrodes, driving a current  $I_x$  along the x-direction of the Hall bar. Respective to the current, the x-direction is also called *longitudinal* direction, while the y-direction is referred to as the *transverse* direction. A subset of electrodes between S and D allows to measure longitudinal ( $V_x$ ) as well as transverse ( $V_y$ ) voltage drops across the channel and, together with the current, the longitudinal resistance  $R_{xx} = V_x/I_x$  and the transverse resistance  $R_{xy} = V_y/I_x$  can be obtained, which is also called the Hall-resistance.

The transport in such a system in the presence of a low perpendicular magnetic field  $B = B_z$  can be described within the framework of the Drude<sup>3</sup> theory [24, 90–92]. The magnetic field forces free charge carriers to move on circular orbits (also called *cyclotron orbits*) and in a realistic conductor this motion is superimposed by scattering events. Together with the effective mass  $m^*$  and the scattering rate  $\tau$  one can express the classical equation of motion for a Drude electron as

$$m^* \frac{d\vec{v}_D}{dt} + \frac{m^*}{\tau} \vec{v}_D = -e(\vec{E} + (\vec{v}_D \times \vec{B})). \quad (3.1)$$

In stationary conditions the first term is zero and, therefore, the application of an electric field  $\vec{E}$  in the longitudinal in-plane direction leads to a *Hall-drift* with the velocity  $\vec{v}_D = \vec{E} \times \vec{B}/B^2 = -E/B$  in the transverse direction. By substituting  $\vec{v}_D$  with the current density  $\vec{j} = -en\vec{v}_D$ , the equation of motion Eq. (3.1) takes the simple form  $\vec{j} = \bar{\sigma} \cdot \vec{E}$ , which formally resembles Ohm's law with the important difference, that the conductivity caused in a perpendicular field is not a scalar quantity anymore, but a tensor of rank two (i.e. a  $2 \times 2$  matrix), such that

$$\begin{pmatrix} j_x \\ j_y \end{pmatrix} = \frac{en\mu}{1 + (\mu B)^2} \begin{pmatrix} 1 & \mu B \\ -\mu B & 1 \end{pmatrix} \cdot \begin{pmatrix} E_x \\ E_y \end{pmatrix}, \quad (3.2)$$

---

<sup>2</sup>Named after the American physicist Edwin Hall (1855-1938), who discovered the effect in 1879.

<sup>3</sup>Named after the German physicist Paul Drude (1863-1906).

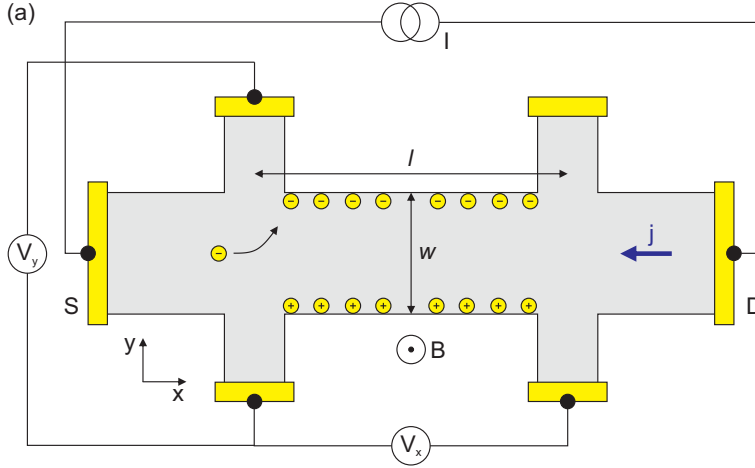


Figure 3.1: **(a)** Schematic illustration of a typical Hall bar device. A current density  $j$  is driven between the source (S) and drain (D) contacts, and the longitudinal ( $V_x$ ) and transverse ( $V_y$ ) voltage drop across the channel of dimensions  $l \times w$  is probed in a four-terminal configuration. The perpendicular magnetic field  $B$  induces a Lorentz force, leading to an accumulation of charges at the channel edges and thereby to a Hall voltage  $V_y$ .

where  $\mu = e\tau/m^*$  (or Eq. (2.25) for Gr) is the charge carrier mobility. The equation of motion can alternatively be expressed via the resistivity  $\bar{\rho}$  as  $\vec{E} = \bar{\rho} \cdot \vec{j}$ . For both tensors, the respective diagonal elements are equal (i.e.  $\sigma_{xx} = \sigma_{yy}$ ) and the off-diagonal ones are anti-symmetric (i.e.  $\sigma_{xy} = -\sigma_{yx}$ ). The resistivity can be obtained from the conductivity by the tensor inversion  $\bar{\rho} = \bar{\sigma}^{-1}$  as

$$\begin{pmatrix} \rho_{xx} & \rho_{xy} \\ -\rho_{xy} & \rho_{yy} \end{pmatrix} = \frac{1}{\sigma_{xx}^2 + \sigma_{xy}^2} \begin{pmatrix} \sigma_{xx} & \sigma_{xy} \\ -\sigma_{xy} & \sigma_{yy} \end{pmatrix}. \quad (3.3)$$

Once the current flow is restricted to longitudinal channel direction ( $j_y = 0$ ), as is the case for a typical Hall bar measurement, the relation Eq. (3.2) is simplified to  $j_x = ne\mu E_x$  and we can write the longitudinal and transverse conductivity components  $\sigma_{xx}$  and  $\sigma_{xy}$  as

$$\sigma_{xx} = n \cdot e \cdot \mu \quad \sigma_{xy} = \frac{\rho_{xy}}{\rho_{xy}^2 + \rho_{yy}^2}, \quad (3.4)$$

and the longitudinal and transverse resistivity  $\rho_{xx}$  and  $\rho_{xy}$  as

$$\rho_{xx} = \frac{1}{(n \cdot e \cdot \mu)} \quad \rho_{xy} = \frac{B}{(n \cdot e)}. \quad (3.5)$$

For a homogeneous channel of the dimensions  $l \times w$  in length and width, the measurable quantities are then given by

$$R_{xx} = \frac{l}{w} \cdot \rho_{xx} = \frac{l}{w} \cdot \frac{1}{e \cdot n \cdot \mu} \quad R_{xy} = \rho_{xy} = \frac{B}{e \cdot n}. \quad (3.6)$$

As the Hall resistance  $R_{xy}$  depends linearly on the magnetic field, it can be used either in Hall sensors to measure magnetic fields or to determine the charge carrier concentration  $n$  and carrier type within a 2DES and thereby e.g. can be used to determine the gate lever  $\alpha_{BG}$  of our Gr transport devices. Once  $n$  is known,  $R_{xx}$  can be used to extract the charge carrier mobility of a device. In a system without scattering, the considerations given above indicate that  $\rho_{xx} = R_{xx} = 0$ , which will become important later on.

## 3.2 Landau Level Quantization

As mentioned above, a magnetic field forces the charge carrier trajectories in the 2DES onto closed cyclotron orbits (see Fig. 3.2). In the quantum limit, which is reached for larger magnetic fields (typically  $B > 1$  T, depending on the charge carrier mobility  $\mu$ ), this results in a quantization of the eigenenergies into discrete levels that are usually called Landau levels<sup>4</sup> (LL). A Bloch electron on a closed orbit accumulates a phase of  $N$  multiples of  $2\pi$  plus an additional constant arising due to the lattice symmetry [12, 90, 93], such that

$$\oint \vec{k} d\vec{r} = 2\pi(N + \frac{1}{2} - \frac{\gamma}{2\pi}), \quad (3.7)$$

where  $\gamma$  is the Berry phase, which in Gr is  $\pm\pi$  depending on carrier type and valley (see Chapter 2.2), while in conventional 2DES like GaAs/Al<sub>x</sub>Ga<sub>1-x</sub>As-heterostructures it is zero [94]. These different values will result in fundamentally different energy spectra for both material systems, as will be derived in the following. In 1952 the Nobel laureate Lars Onsager (1903-1976) was the first to use Eq. (3.7) to determine the quantized cyclotron orbits of charge carriers in solids [95].

Within a lattice, the equation of motion for a Bloch electron in a magnetic field  $B$  is given by

$$\hbar \dot{\vec{k}} = -e\dot{\vec{r}} \times \vec{B}. \quad (3.8)$$

Using the equation of motion to calculate the magnetic flux through the area enclosed by the cyclotron orbit results in

$$\frac{1}{2} \vec{B} \oint \vec{r} \times d\vec{r} = \phi_0(N + \frac{1}{2} - \frac{\gamma}{2\pi}), \quad (3.9)$$

---

<sup>4</sup>Named after the Soviet physicist Lev Davidovich Landau (1908-1968), who in 1962 was awarded with the Nobel prize in physics for his development of a mathematical theory of superfluidity in liquid helium.

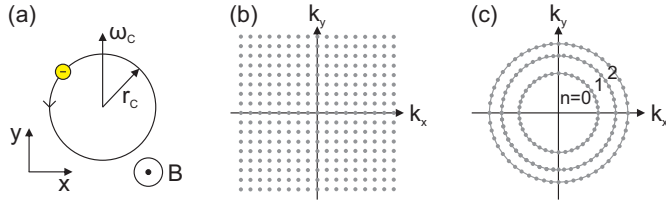


Figure 3.2: **(a)** In two dimensions, a perpendicular magnetic field forces the charge carriers onto cyclotron orbits with radius  $r_c$  and cyclotron frequency  $\omega_c$ . This results in quantization of the momentum space, where the allowed momentum values are discrete, forming concentric circles in  $k$ -space. The corresponding momentum space without magnetic field is shown in panel (a) and with magnetic field in panel (b). Without magnetic field, the momentum states are evenly distributed, while within an external field, the states are forced onto concentric circles that correspond to increasing quantum numbers  $N$ .

which means, that the magnetic flux is quantized in units of the flux quantum  $\phi_0 = h/e$ . Now considering the same relation in  $k$ -space and assuming  $B$  to be in  $z$ -direction only, we get

$$\frac{1}{2}e\vec{z} \oint \vec{k} \times d\vec{k} = \frac{B}{\phi_0} \left( N + \frac{1}{2} - \frac{\gamma}{2\pi} \right). \quad (3.10)$$

Further assuming a circular orbit for the integral part, gives the area enclosed in  $k$ -space of  $S(\epsilon) = \pi k^2(\epsilon)$  and using this, we can rewrite Eq. (3.10) as

$$\pi k^2(\epsilon) = \frac{B}{\phi_0} \left( N + \frac{1}{2} - \frac{\gamma}{2\pi} \right). \quad (3.11)$$

We can now use Eq. (3.11) to calculate the LL energy spectrum for any given material by plugging-in its respective bandstructure  $\epsilon(k)$  as well as its Berry phase  $\gamma$ . Together with the band structure of Gr around the K-points  $\epsilon_{Gr}(k) = \hbar v_F k$ , which we derived in Chapter 2, and the Berry phase at the  $K^{(')}$  points of  $\gamma = \frac{(-)}{(+)}\pi$  for electrons and  $\gamma = \frac{(+)}{(-)}\pi$  for holes we get

$$\epsilon_{Gr}(N) = \text{sign}(N) \sqrt{2e\hbar v_F^2 B N} \quad (3.12)$$

for the energy level as function of the LL index  $N$ . For Gr, the sign of  $N$  is included here, since positive and negative energies respective to the Dirac point are possible resembling either electron or hole conduction. For the  $K$  valley,  $N$  goes through the values  $1, \dots, \infty$  for electrons and  $0, \dots, \infty$  for holes, while for the  $K'$  valley, the admissible intervals for electrons and holes are exchanged. For conventional 2DES with a parabolic dispersion (c2DES) like GaAs/Al<sub>x</sub>Ga<sub>1-x</sub>As-heterostructures and

therefore  $\epsilon_{\text{c2DES}}(k) = \frac{\hbar^2 k^2}{2m^*}$ , where  $m^*$  is the effective mass, Eq. (3.11) yields the LL-spectrum

$$\epsilon_{\text{c2DES}}(N) = \frac{\hbar e B}{m^*} \left(N + \frac{1}{2}\right). \quad (3.13)$$

By entering the so-called cyclotron frequency  $\omega_C$  we can simplify Eqs. (3.12) and (3.13) to

$$\epsilon_{\text{Gr}}(N) = \hbar \omega_C \cdot \text{sgn}(N) \sqrt{N} \quad \epsilon_{\text{c2DES}}(N) = \hbar \omega_C \left(N + \frac{1}{2}\right), \quad (3.14)$$

implying  $\omega_{\text{C,Gr}} = \sqrt{2ev_F^2 B/\hbar} = \sqrt{2}v_F/l_B$  and  $\omega_{\text{C,c2DES}} = eB/m^* = \hbar/l_B^2 m^*$ , where  $l_B = \sqrt{\hbar/eB}$  is the magnetic length - the characteristic length scale of interactions of a charge carrier, or its spatial extent as function of  $B$ . Comparing the expressions in Eq. (3.14) highlights the close resemblance of the parabolically dispersing 2DES to the energy spectrum of a harmonic oscillator, while Gr with its unique massless Dirac-fermion system is of an entirely different nature. This semi-classical derivation of the LL spectrum of Gr was chosen for its pragmatic elegance and the possibility to plug in different dispersion relations and Berry phases. The first derivation of Eq. (3.12) was done in the context of the diamagnetism of graphite in 1956 [96]. A quantum mechanical derivation starting from the Dirac Hamiltonian of Gr can be found in [12, 13] and in their referenced literature.

The Landau quantization splits the DOS into a series of degenerate peaks of discrete energy separated by an energy gap  $E_G$ , which is also called the cyclotron gap. The evolution of the LL in Gr as well as for a c2DES as function of energy  $\epsilon$  and magnetic field  $B$  is shown the upper half in Fig. 3.3. The lower panels of the same figure show the DOS of both systems at a constant field of 30 T as function of  $\epsilon$ . For c2DES, the LL are equidistantly spaced in energy and the cyclotron gap is  $E_G = \hbar \omega_{\text{C,c2DES}}$ , while for Gr the spacing shrinks with increasing  $N$  and we can derive the spacing between the  $N$ -th and  $(N+1)$ th LL as

$$E_G = \hbar \omega_{\text{C,Gr}} (\sqrt{N+1} - \sqrt{N}). \quad (3.15)$$

While the quantization in c2DES with massive charge carriers is limited to low cryogenic temperatures, owing to the massless nature of the charge carriers in Gr, the cyclotron gaps are two orders of magnitude bigger and thereby increase the thermal stability of the related physics up to room temperature. This fact also becomes obvious upon comparing the energy scales in Fig. 3.3 and will be of fundamental importance for Chapter 9, in which the quantization abilities of Gr at elevated temperatures and their dependence on the sample disorder level will be investigated.

The total amount of charge carriers inside a 2DES of the area  $A = l \times w$  does not change during the quantization into discrete levels and, therefore, the highly degenerate LL are filled up by the carriers starting from the energetically lowest level until its complete filling and subsequent population of the next highest level. The degen-

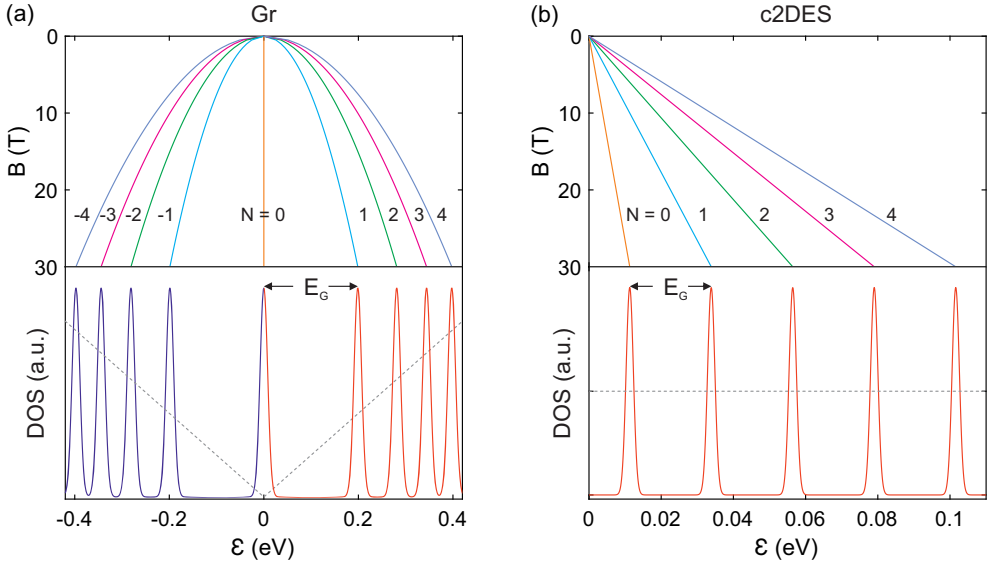


Figure 3.3: **(a)** and **(b)** Landau level (LL) spectra of Gr and a c2DES for different LL indices  $N$ . The upper panels show the evolution of the LL as a function of energy  $\epsilon$  and magnetic field  $B$ , while the lower panels show the corresponding density of states (DOS) at a constant magnetic field of 30 T as a function of  $\epsilon$ . The zero-field DOS of each system is indicated with gray dashed lines. The LL are separated by the cyclotron gap  $E_G$ . Negative  $N$  in Gr are occupied by holes, while positive  $N$  are occupied by electrons, and LL zero (LL<sub>0</sub>) is shared equally between both carrier types. In a c2DES, the doping level and therefore the charge carrier type is fixed.

eracy of each LL or likewise the number of carriers that can populate it  $N_L$ , increases linearly with  $B$ , following

$$N_L = \frac{eBA}{h}. \quad (3.16)$$

With increasing magnetic field, more and more carriers are redistributed towards energetically lower LL until the ground state is reached. A measure of the filling of the LL in a 2DES can be calculated by dividing  $n$  by the density of degenerate states in a LL  $n_L = N_L/A$ , such that

$$\nu = \frac{n}{n_L} = \frac{nh}{eB}. \quad (3.17)$$

This quantity is commonly called the LL filling factor  $\nu$ . The filling factor can analogously be described as the number of electrons within the area  $A$  of a 2DES surface

$N_A = n \times A$  divided by the number of flux quanta  $\phi_0$  within the same area  $N_{\phi_0}$ , such that

$$\nu = \frac{N_A}{N_{\phi_0}} = \frac{N_A}{\phi/\phi_0}. \quad (3.18)$$

In this sense, integer values  $\nu$  for the filling factor mean, that exactly  $\nu$  electrons are present for each flux quantum. In the fractional quantum Hall regime the charge carriers and flux quanta are forming quasi-particles, so called composite fermions, for each of which not one but several flux quanta are attached to single carrier (see section 3.4 below).

Another important distinction between Gr and parabolically dispersing 2DES lies in the different positions of the  $N = 0$  LL in energy. From the Eqs. (3.12) and (3.13) we see that for Gr the ground state is situated at  $\epsilon = 0$ , while for c2DES it is at  $\epsilon = \hbar\omega_C/2$ . This has an important influence on the filling sequence of the LL. While for the latter, a complete filling of  $LL_0$  is reached at  $\nu = 1$ , in Gr  $LL_0$  filled up at  $\nu = 1/2$ . Which can be generalized as  $\nu_{c2DES}(N) = N + 1$  while for Gr it is  $\nu_{Gr}(N) = N + 1/2$ . This little offset motivated researchers to speak of an anomalous or half-integer quantum Hall effect in Gr. Its relativistic Dirac systems and the possibilities to explore the rich physics implied in it contributed hugely to the boom around Gr in the first years after its discovery [97–103]. Taking into account that Gr also has a two-fold spin and valley degeneracy  $g_s$  and  $g_v$  [12], the filling factor at which the  $N$ -th Landau level is fully occupied in Gr becomes

$$\nu_{Gr}(N) = g_s g_v (N + \frac{1}{2}) = 4(N + \frac{1}{2}). \quad (3.19)$$

### 3.3 Degeneracy-Lifting and the Ground-State of Graphene

The above mentioned degeneracy of the LL in Gr can eventually be lifted at larger magnetic fields as it was demonstrated in a series of experiments in the first decade after the discovery of Gr [104–109]. The experiments reveal a subset of new states that emerge at all integer filling factors, adverse from the series expected from Eq. (3.19), implying a splitting of the initial LL spectrum Eq. (3.12) into four spin- and valley-polarized sub-levels, facilitated by different mechanisms that we so far did not include in our considerations. The modifications that the splittings imply for the DOS are indicated in Fig. 3.4. In Fig. 3.4(a), the DOS of the intrinsic, degenerate LL  $N = -1 \dots 1$  is shown for a magnetic field of 30 T while the lower panel shows the DOS for full degeneracy lifting where each LL splits into four sub-levels. Close-ups of the sub-levels splitting for  $N = -1, 0$  are shown as insets. The energy gaps for the splitting of  $\approx 3$  meV are adapted from evaluations of Gr devices presented in Chapter 9 and from [108]. The main contributions to the splitting were identified as the Zeeman splitting  $E_Z$  acting on the spin of the charge carriers [110] and the Coulomb interaction

$E_C$  [111–113] between charge carriers and lattice scale anisotropies  $E_{LS}$  describing electron-electron as well as electron-phonon interactions at lattice scale [114–116]. The different effects scale with the magnetic field as

$$E_Z = g\mu_B B = 1.2[\text{KT}^{-1}] \times B \quad (3.20)$$

$$E_C = \frac{e^2}{4\pi\epsilon_0\epsilon_r l_B} = \frac{643}{\epsilon_r}[\text{KT}^{-1/2}] \times \sqrt{B} \quad (3.21)$$

$$E_{LS} \approx E_C \frac{a}{l_B} \approx \frac{3.5}{\epsilon_r}[\text{KT}^{-1}] \times B, \quad (3.22)$$

with the  $g$ -factor of the electrons, the Bohr magneton  $\mu_B$ , the vacuum permittivity  $\epsilon_0$ , the dielectric constant  $\epsilon_r$  and the lattice vector  $a$ . The energies are given in Kelvin. These effects do not only scale differently with the power of the absolute value of  $B$ , but also differ fundamentally with respect to the magnetic field direction. While  $E_Z$  depends on the total magnetic field  $B_T$ , the interaction-mediated  $E_{C,LS}$  depend only on the perpendicular component of the magnetic field  $B_\perp$ . The energy gap of the symmetry-broken states should hence be constituted as

$$E_G = E_Z(B_T) + E_{C,LS}(B_\perp) - \Gamma. \quad (3.23)$$

One can therefore gain information on the driving mechanisms and state composition by evaluating  $E_G$  for different tilted magnetic fields and from such measurements it could be concluded, that for  $N \neq 0$ , all even-valued  $\nu$  sub-levels are spin polarized while all odd-valued sub-levels are valley-polarized [109, 111].

$LL_0$  is special as unlike the higher  $LL$ , which are exclusively populated by electrons or holes, it is shared equally between both carrier types. It was shown by Giesbers et al., that a single-particle Zeeman gap arises at  $\nu = 0$  in larger magnetic fields, while the splitting at  $\nu = \pm 1$ , which occurs only in low disordered samples, cannot be explained by  $E_Z$  alone, despite the corresponding sub-levels appear to be spin polarized [106, 108, 109].

The microscopic nature of the Gr ground state at  $\nu = 0$  is an ongoing topic of debate. Up to now, four different orderings were proposed for it - namely a charge density wave (CDW), a Kekule distortion (KD), a ferromagnetic ordering (F-phase) and a canted anti-ferromagnetic phase (CAF). In the CDW order, the valley degeneracy is lifted and the electrons reside on one sublattice while having opposing spin [104, 105]. In the KD phase, the valleys hybridize while also allowing opposing spins [54, 107]. As both these orderings facilitate a spin polarization, they could be found at purely perpendicular magnetic fields. In contrast, the F-phase manifests in a spin polarized state, where electrons occupy both valleys. The CAF ordering is similar, only that the spins are non-collinear with identical components along the magnetic field direction and opposing directions perpendicular to it. Schematic illustrations of all the above mentioned ground state orderings are shown in Fig. 3.5(c).



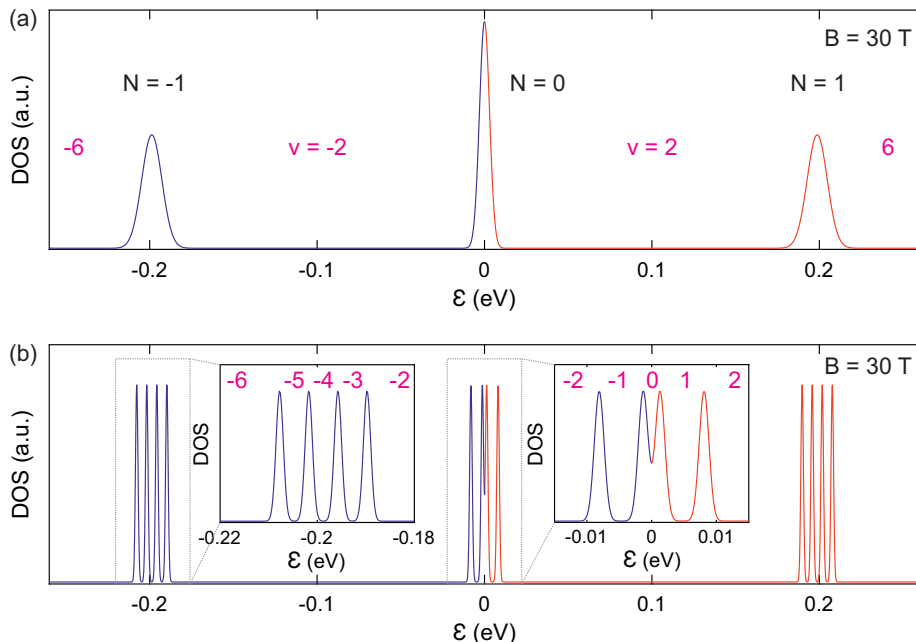


Figure 3.4: **(a)** DOS as function of energy  $\epsilon$  of MLG at a magnetic field of 30 T for the degenerate LLs  $N = -1, 0, 1$ . **(b)** For low temperatures and clean enough systems all degeneracies are eventually lifted and each LL is split into four sub-level. For better visibility, close ups of the sub-level splitting of  $N = -1$  and  $N = 0$  are shown as insets. The pink numbers indicate the filling factor  $\nu$  of the system at the given energy.

Upon application of large in-plane magnetic fields (and hence a boosting of the Zeeman energy while quenching interactions), it was demonstrated that the Gr ground state transitioned from either CDW or KD over CAF to F-phase by Young et al. [54] (see Fig. 3.5(a)). Recently, the F-phase could be realized in Gr as well by employing a high  $\epsilon_r$  dielectric ( $\text{SrTiO}_3$ ), which leads to a screening of the interaction effects in Eq. (3.21) [117]. Still, the exact ordering and its transitions for varying magnetic field strength and direction remains an active topic of research and only a combination of transport measurements probing edge states, capacitive measurements probing the bulk, and, if possible, spatial probing of a channel via scanning probe measurements [118] are needed to provide conclusive evidence. The ongoing interest in this field of research is partially driven by the possibility to realize Majorana bound states at the edges of a superconductor/Gr boundary, where the Gr is in a CAF-phase [119].

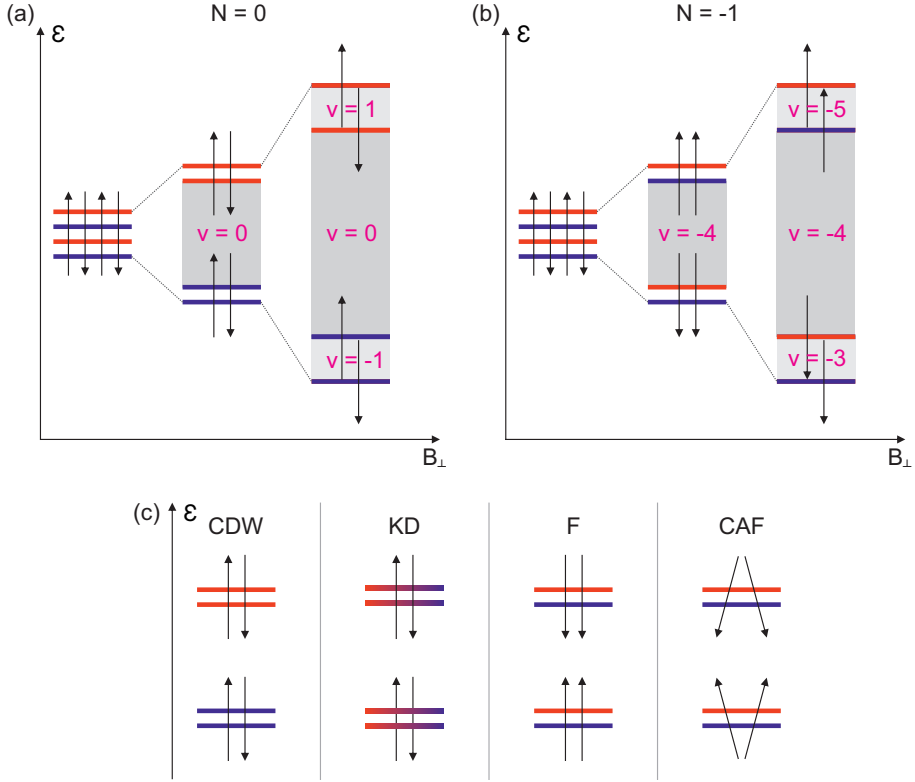


Figure 3.5: Schematic illustration of the spin splitting for the LL  $N = 0$  (a) and  $N = -1$  (b). The spin directions are indicated by arrows, while the different valleys are highlighted by red and blue colors. Energy gaps between states are represented by gray boxes. (c) Illustrations of the possible Gr ground states. In the CDW ground state, each valley is populated by both spin directions, while in the KD state both spin orientations live on linear combinations of the valleys. In the F-state the spins in each valley are fully polarized, while in CAF state, the spins are canted with respect to the external magnetic field direction. Adapted from [109].

### 3.4 Fractional Quantum Hall States

After the discovery of the IQHE (see below), similar measurements were performed in 2DES hosting substantially higher carrier mobilities realized in GaAs/AlGaAs heterostructures. At low temperatures and high magnetic fields, these transport data

revealed signatures<sup>5</sup> of new states, similar to those populating the discrete LL at integer values of filling  $\nu = i$ , but emerging at certain fractional values of  $\nu$  - the first to be reported being  $\nu = 1/3$  in 1982 [120]. Most of these additional states were observed for odd denominator values of  $\nu$  such that

$$\nu = \frac{1}{k+1} \quad \text{and} \quad \nu = 1 - \frac{1}{k+1}, \quad (3.24)$$

with even integer values for  $k$ . Owing to these fractional filling factors, this phenomenon was later called the *fractional quantum Hall effect* (FQHE). The theoretical description of the underlying mechanisms forming the fractional states is rather delicate and not as straight forwards as for the states resulting from the Landau quantization, which can be understood as a single-particle effect. The fractional states appear, when the Fermi energy lies within a highly degenerate LL, implying the existence of many-particle, interaction-driven energy gaps. Correlated motion of many electrons, driven by the reduction of Coulomb interaction between the equally charged carriers is commonly seen as the origin of the FQHE [121].

In the context of multi-particle states, one of the most crucial components is the attachment of magnetic vortices to electrons. When a magnetic field is applied to a 2DES, it can be envisioned as a sum of flux quanta that penetrate through a uniform layer of electrons. At the location of each flux quantum, a small hole is formed, which represents a charge deficit of  $\nu e$  and a zero in the many-electron wave function. These objects are called *vortices*, and they result from the magnetic field imparting a  $2\pi$  phase shift to the wave function at the location of each hole. Vortices can be thought of as tiny coils that pierce through the electron system and generate a single magnetic flux quantum through their cores [121]. Vortices are delocalized in the 2D area, similar to the electrons. However, because of their opposite charges, electrons and vortices attract each other, and bringing them together results in a substantial gain in Coulomb energy. Due to the Pauli exclusion principle, each electron must bind to at least one vortex, and additional vortices may be bound to further minimize their energy. For instance, in the  $\nu = 1/3$  state, three vortices are associated with each electron, and each vortex represents a charge deficit of  $e/3$ .

In 1983, Robert B. Laughlin<sup>6</sup> made the first significant attempt to formalize the considerations surrounding the fractional quantum Hall effect (FQHE). Laughlin proposed trial wave functions to solve a Hamiltonian that described the series of primary fractional states  $1/k$ , where  $k$  is an odd integer value greater than one ( $k = 3, 5, 7, \dots$ ). In these states,  $k$  vortices are attached to each electron, forming quasi-particles [123]. The ground state is composed of a product of Jastrow functions, represented by the following equation:

---

<sup>5</sup>These signatures will be detailed below in section 3.5. For now we are only interested in the corresponding states.

<sup>6</sup>Robert B. Laughlin (\*1950) is an American physicist who, along with Strömer and Tsui, was awarded the Nobel Prize in Physics in 1998 for explaining the fractional quantum Hall effect.

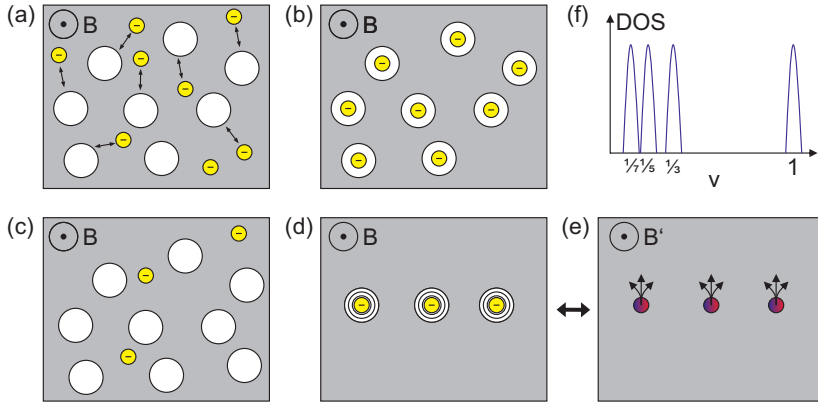


Figure 3.6: Schematic illustration of the attachment of vortices (white circles) to electrons in a 2DES under a perpendicular magnetic field  $B$ . At integer LL filling factor  $\nu = i$ , there is one vortex per electron, and the Pauli exclusion principle forces the vortices to occupy the same quantum state as the electrons. At fractional LL filling factor  $\nu = 1/3$ , three vortices are attached to each electron, which reduces the Coulomb interaction between the electrons. This process can be thought of as the attachment of magnetic flux quanta to the electrons, forming composite quasi-particles with fractional charges in an effective field  $B'$ . The DOS as a function of  $\nu$  shows sub-levels separated by quasi-particle gaps. Adapted from [122].

$$\Psi_{1/k} = \prod_{i < j} (z_i - z_j)^k \cdot \exp \left( - \sum_i \frac{|z_i|^2}{4l_B^2} \right), \quad (3.25)$$

where  $z_i$  and  $z_j$  are the positions of the  $i$ -th and  $j$ -th electrons, respectively, and  $l_B$  is the magnetic length scale [121, 123]. The first term in the equation represents the electron-electron interactions as a product over all complex pair distances between electrons, and the exponent represents the number of attached flux quanta. When  $k = 1$ , Eq. (3.25) yields the wave functions of non-interacting electrons in the integer quantum Hall effect (IQHE). A schematic illustration of this process is shown in Fig. 3.6(a) and (b). Adding additional vortices to the system (e.g., by increasing the magnetic field) at a non-commensurate electron-to-vortex ratio results in a significant

energetic cost, effectively making the fractional states incompressible<sup>7</sup> and attributing to them an energy gap. Laughlin also demonstrated that adding another vortex with one magnetic flux quantum passing through it to a homogeneous<sup>8</sup> 2DES area is equivalent to adding a quasi-particle with an effective fractional charge of  $e^* = e/k$ , as shown in Fig. 3.6(c)-(e) [123].

The description of the FQHE in the electron-vortex quasi particle framework was greatly enhanced by Jain in 1989 by a new concept that also accounted for the higher-order FQHE states with odd-denominators, different from the primary  $1/k$  states [124]. The quasi-particles in this framework are labeled as *composite fermions* (CF) and, accordingly, the concept is called CF-model. As discussed above, at  $\nu = 1/3$  three flux quanta are attached to each electron and consequently, the effective external magnetic field that the quasi-particle feel is reduced to zero  $B^* = B - B_{1/3} = 0$ . Upon increasing  $B$ , additional uncoupled flux quanta enter the system and the CF experience an effective field of  $B^* > 0$ . The charged quasi-particles forming the primary state can then correlate and form a new quantum liquid at neighbouring rational filling factors and this effect can be iterated until all odd-denominator fractions are covered. So to speak, the primary fractional states experience a Landau quantization under the effective magnetic field  $B^*$ . Exploiting the same analogy, similar to electrons that exhibit a Landau gap that scales linear with  $B$  (for parabolic band structures, see above), the FQHE gap energies are expected to open linearly with  $B^*$  as well [125]. However, the CF mass  $m^*$  within the CF cyclotron gaps  $\hbar e B^* / m^*$  is exclusively resulting from interaction and thereby a function of the charge carrier density only. The wave functions proposed for such states are much more complex than the Laughlin wave function Eq. (3.25) and shall not be discussed here. The discussion of even denominator states is also omitted, but a nice overview can be found in [121].

In analogy to Eq. (3.18), the CF system forms fractional quantum Hall states, when

---

<sup>7</sup>Incompressibility in this context means that the electronic system, i.e., the 2DES, is unable to compress and become more dense when the external magnetic field is increased. This is due to the formation of the fractional quantum Hall states, which have a characteristic energy gap and do not allow the electrons to easily move around and occupy lower energy states. The energy cost for compressing the system is so high that it effectively prevents the system from compressing. This property is in contrast to conventional conductors, where the electrons can easily move around and occupy lower energy states when subjected to an external force, resulting in a decrease in resistance. The (in)compressibility of a 2DES will become an important ingredient for the screening-based microscopic picture of the QHE, that will be discussed in Chapter 4.2.

<sup>8</sup>Homogeneity in this context means, that the electron density is constant over the entire area of the 2DES. In other words, the 2DES is uniform without any spatial variations in electron density. The term "homogeneous" is used to describe the system's spatial uniformity. The concept of a homogeneous 2DES is important in the discussion of the fractional quantum Hall effect because it allows for a simpler theoretical treatment of the electronic properties of the system.

the effective filling factor  $\nu^* = N_A/N_{\phi_0}^*$  is integer. The relation of the real filling factor  $\nu$  to the fractional filling factor  $\nu^*$  is given by

$$\nu = \frac{\nu^*}{2p\nu^* \pm 1} \quad \text{and} \quad \nu = 1 - \frac{\nu^*}{2p\nu^* \pm 1} \quad (3.26)$$

for electrons and holes, respectively. The number of flux quanta attached per electron (or its vorticity) is represented by the  $2p$ . A hierarchy diagram of the primary fractional states and their excitations is shown in Fig. 3.7.

As we have seen, the formation of fractional quantum Hall states is a delicate many-body effect, that is only visible at temperature scales below the comparatively small CF energy gaps and thus making it highly sensible to sample disorder, which eventually smears out all signatures of the effect. Hence, the observation of the FQHE is limited to the highest quality devices not governed by disorder effects and as of such, the FQHE can be used as smoking gun evidence of the intrinsic equality of CVD-Gr and Ex-Gr.

## 3.5 Discovery of the Integer Quantum Hall Effect

In the previous sections of this chapter, we established the concept of Landau quantization of a 2DES into discrete energy levels at integer or fractional fillings in the presence of large external magnetic fields. We now aim to investigate the impact of Landau quantization on measurable magneto-transport properties such as the longitudinal resistance  $R_{xx}$  and the Hall resistance  $R_{xy}$ . We also want to examine how these properties would differ from the expectations of the classical Hall effect in low magnetic fields, which we derived earlier (see Eq. (3.6)).

In an ideal homogeneous 2DES under Landau quantization, the Fermi energy as a function of magnetic field ( $B$ ) has a saw-tooth-like shape when following the energy of a partly filled Landau level (LL) until it becomes completely unoccupied. An exemplary occupation diagram of the spin-degenerate LL in Gr for a fixed charge carrier density of  $n = 1.2 \times 10^{12} \text{cm}^{-2}$  as a function of  $B$  is shown in Fig. 3.8(a). The Fermi energy  $E_F$  is represented by a red line and follows the dispersion of the nearest LL until it becomes fully unoccupied. Then, it jumps down vertically to the next lowest LL and continues to deplete it with further increasing  $B$ . All of this is due to the increasing degeneracy of each LL  $n_L$  with rising  $B$ , as stated in Eq. (3.16).

The jumps in the Fermi energy occur precisely at those values of  $B$  at which the filling factor becomes an integer  $\nu = i$ , satisfying Eq. (3.19), and are marked by dark blue circles. The occupied states at these values are separated from the unoccupied states in the next LL by the energy gap  $E_G$ , defined by Eq. (3.15). As long as the gap is much larger than  $k_B T$ , the Pauli principle prohibits any scattering, and the electron system becomes rigid or *incompressible*. In this scenario, combining the equations for the resistances Eq. (3.6) with the filling factor Eq. (3.17) leads to the

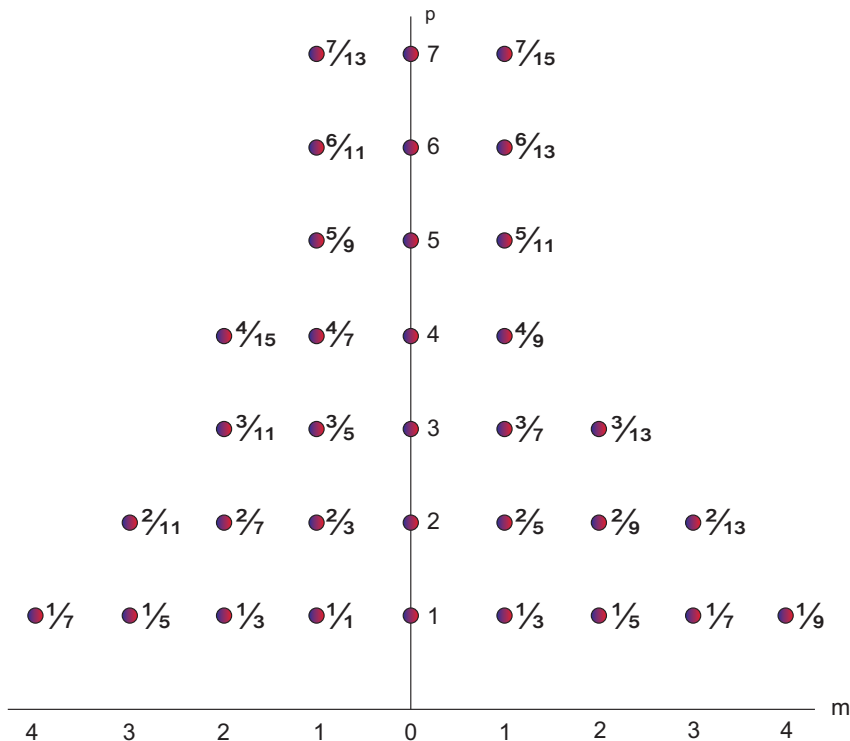


Figure 3.7: Fractional states as combinations of  $m$  and  $p$  following  $p/(2mp + 1)$  and  $p/(2mp - 1)$  on the right and on the left half. All the depicted states were observed experimentally in the years after the discovery of the FQHE [124].

measurable magneto-transport quantities of a Hall bar-shaped 2DES assuming the following values:

$$R_{xx} = 0 \quad \text{and} \quad R_{xy} = \frac{h}{ie^2}, \quad (3.27)$$

and

$$\sigma_{xx} = 0 \quad \text{and} \quad \sigma_{xy} = i \frac{e^2}{h}. \quad (3.28)$$

These results indicate vanishing longitudinal resistance and conductivity (due to absence of scattering) and quantized values for the Hall resistance and Hall conductivity. These quantized values of the conductivity are depicted in Fig. 3.8(b) by blue circles together with the classical Hall curve  $\sigma_{xy} = nh/eB$  as gray dashed line. However, it is important to note that the latter is only a guide to the eye and our

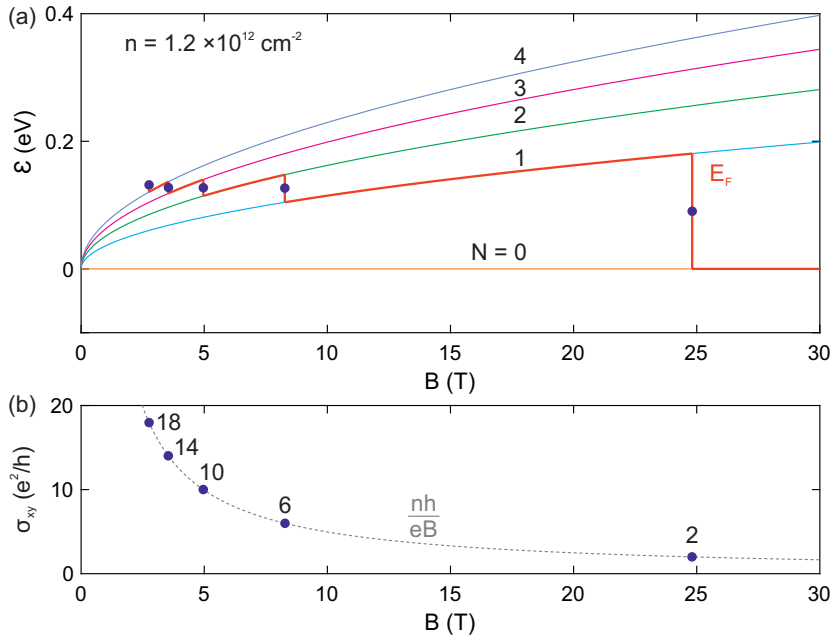


Figure 3.8: **(a)** Energy dispersion of the first five LL in Gr as a function of magnetic field  $B$ . The Fermi energy  $E_F$  for a fixed charge carrier density  $n = 1.2 \times 10^{12} \text{ cm}^{-2}$  is plotted in red as a function of  $B$  over the LL. As the degeneracy of each LL increases with  $B$ ,  $E_F$  jumps to a lower LL at the filling factors determined by Eq. (3.19), which mark the points where the LL are either completely filled or empty (indicated by blue circles). **(b)** Hall conductivity  $\sigma_{xy}$  as a function of magnetic field  $B$ . The classical Hall curve following  $nh/eB$  is indicated as a gray dashed line. The blue circles mark the points of complete filling corresponding to **(a)**, where the conductivity becomes necessarily integer, while it is not defined anywhere else.

considerations so far only yield finite (and in fact quantized) conductivity values at points of complete LL filling, while it remains undefined everywhere else, as the system is gapped out. With rising temperature, the Fermi function develops a finite broadening and, therefore, at one point will allow the occupation of states beyond the energy gap  $E_G$  in the adjacent LL and, hence, imply an Arrhenius-type of activated transport for the longitudinal resistance following

$$R_{xx} = R_0 \exp\left(-\frac{E_G}{2k_B T}\right), \quad (3.29)$$

where  $k_B$  is the Boltzmann constant and  $T$  is the temperature. Yet again, these results are practically not very useful, as they are valid only for singular points of



LL filling at  $\nu = i$  and undefined everywhere else. The Fermi level cannot be shifted continuously between the points of integer filling as no states would be available to be occupied in between. Without making further assumptions, that deviate from an ideal homogeneous 2DES towards a realistic system, nothing more can be said at this point. Therefore, in the following, we will switch to the experimental side of magneto-transport investigations in the last century, which ultimately led to the unexpected discovery of the quantum Hall effect.

The year 1930 marked a significant milestone in the field of quantized magneto-transport. Lev Landau published his initial work on the harmonic oscillator spectrum of free electrons under large magnetic fields [126], while Lev Shubnikov and Wander J. de Haas conducted the first measurements of an oscillating magneto-resistance in Bi wires at low temperatures [127]. Today, this effect, where the longitudinal resistance in a 2DES oscillates with increasing magnetic field, and resistance minima are found at integer filling  $\nu = i$ , is known as the Shubnikov-de Haas (SdH) effect. The investigation of this effect continued over the following decades, particularly after the realization in 1966 that a 2DES could be achieved at the interface between a Si crystal and an oxide layer via electrostatic gating. Scientists heavily investigated the properties of such a system, and the observed magneto-resistance oscillations were related to the formation of LL. Many of the properties of these measurements, such as the magnitude of the oscillation extrema, were approximated by modeling a broadening of the initially discrete LL via different scattering mechanisms. The works of Tsuneya Ando reviewed the experimental and theoretical state of the art at that time [93, 128–131]. In 1975, Ando even predicted the quantization of Hall conductance based on approximate calculations but did not believe it to be correct at the time [132]. Chapter 4 will discuss level broadening mechanisms based on localization assumptions, which are essential for the conventional microscopic picture of the QHE. However, neither theory nor experiment expected anything beyond an oscillating magneto-resistance and an oscillation-modulated Hall resistance.

A major breakthrough in the study of the quantum Hall effect (QHE) occurred in 1980 when Klaus von Klitzing, Gerhard Dorda, and Michael Pepper conducted magneto-transport measurements in a Si-based metal-oxide-semiconductor field-effect-transistor (MOSFET) Hall bar at the high magnetic field laboratory in Grenoble [133]. Initially, the experiment aimed to investigate the dominant scattering mechanisms in the two-dimensional electron system (2DES) by examining the broadening of the Landau levels (LL) that manifest in the Shubnikov-de Haas oscillations, with the hope of identifying ways to enhance the charge carrier mobilities of Si-MOSFETs in the future. To eliminate electron-phonon scattering, the measurements were performed at liquid helium temperatures.

The results were strikingly different from the expected behavior. Rather than oscillations in the magneto-resistance, the Hall resistance  $R_{xy}$  exhibited plateaus at

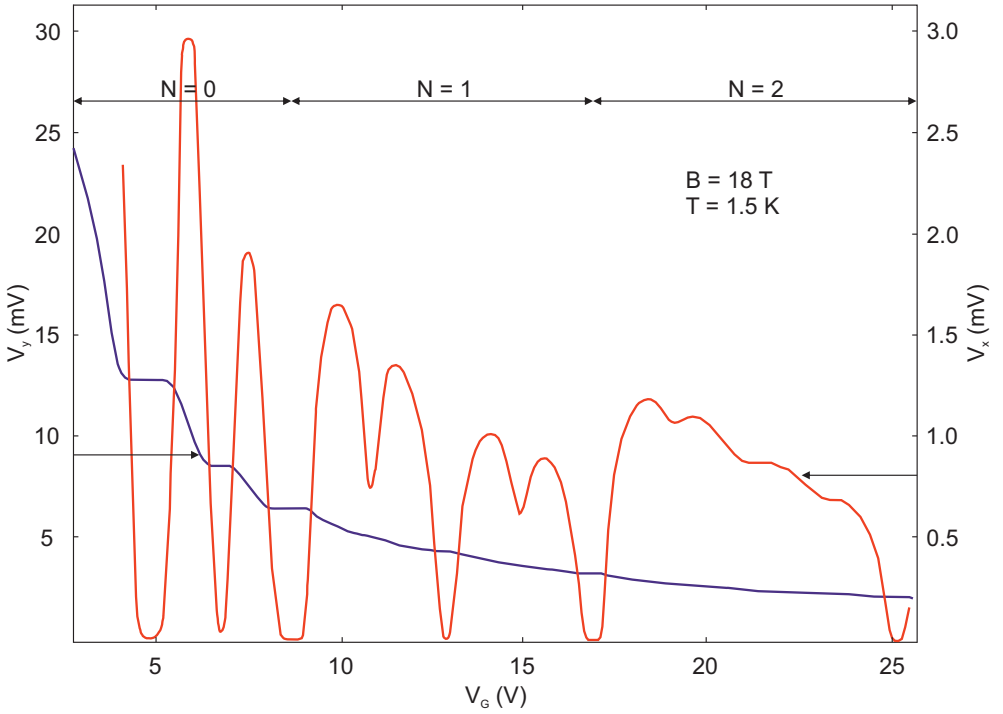


Figure 3.9: Original QHE measurements on a Si MOSFET with channel dimensions of  $130 \times 50 \mu\text{m}$  ( $l \times w$ ) from [133]. Hall voltage  $V_y$  and longitudinal voltage  $V_x$  as a function of the applied gate voltage  $V_G$  at a temperature of 1.5 K, a constant magnetic field of 18 T, and a source-drain current  $I$  of  $1 \mu\text{A}$ . Around integer values of filling factor  $\nu = i$ , the Hall resistance exhibits extended plateaus that precisely match  $i \cdot h/e^2$ , while the longitudinal resistance drops to zero in the plateau regime. The data represents the first observation of the integer quantum Hall effect. Reprinted with permission from [133] ©1980 by the American Physical Society.

integer filling factors  $\nu = i$ , remaining constant over a range of magnetic field  $B$ . At the same time, the longitudinal resistance  $R_{xx}$  approached zero at the minima over the same field range. Moreover, the plateau resistances precisely matched a quantized relation determined by the natural constants  $e$  and  $h$  as  $R_{xy} = h/(ie)$ , in agreement with our expectation in Eq. (3.27). The relation  $U_{xy} = (h/e^2) \cdot I_x$  was confirmed with remarkable accuracy, even accounting for the finite input impedance of  $1 \text{ M}\Omega$  of the  $U_{xy}$  voltmeter. The authors titled their publication "Realization of a Resistance Standard based on Fundamental Constants" to highlight this achievement. Subsequent experiments showed that the relation in Eq. (3.27) held true irrespective

of sample dimensions, measurement configuration, impurity level (up to a limit where the effect vanishes), or the material forming the 2DES and even up to filling factors  $\nu = 42$  [42]. The Hall resistance always approached the value  $h/e = 25812 \, \Omega$  around  $\nu = 1$ , which was named the von-Klitzing constant. The universality of the quantized nature of the effect, irrespective of material properties, led to the term "quantum Hall effect" (QHE), with the case of integer filling factors known as the "integer quantum Hall effect" (IQHE). In recognition of his contributions, Klaus von Klitzing was awarded the Nobel Prize in Physics in 1985.

Since the discovery of the IQHE, extensive efforts have been made to comprehend the quantization phenomenon over broad ranges of carrier density or magnetic field, along with the emergence of new QHE-related phenomena such as the FQHE [134]. These studies have been carried out in 2DES of progressively higher quality. Even today, the field remains active, with researchers exploring new materials such as Gr, which features a unique massless electronic system, enabling the observation of an IQHE up to room temperature [33, 34, 135, 136], as well as various interaction-mediated phenomena like the FQHE [10, 105]. In this work, we present measurements of the FQHE in CVD-Gr, along with fundamental studies of the manifestation and scattering mechanisms in the QHE regime at room temperature, highlighting the continuing relevance of this field.

### 3.6 Summary

In this chapter, we have provided a comprehensive overview of the classical Hall effect, its application to two-dimensional conductive systems in Hall bar structures, and the semi-classical derivation of the quantization of a 2DES into discrete LL at higher magnetic fields. We have also discussed the interaction-mediated degeneracy lifting of the LL, the composition of the ground state of Gr, and the fundamental mechanisms underlying the formation of fractional quantum Hall states. Moreover, we have briefly explored the history of theory and experiments in magneto-resistance measurements, culminating in the discovery of the IQHE. To facilitate understanding, we have explained the mechanisms behind the formation of these effects before delving into their concrete experimental signatures in transport measurements. These signatures include a quantized plateau in  $R_{xy}$  of  $h/(\nu e^2)$ , with  $\nu$  being either integer or fractional, accompanied by a minimum in  $R_{xx}$  exhibiting Arrhenius-like temperature-activated behavior that depends on the energy gap  $E_G$  of the corresponding states, as given by Eq. (3.29). All of these fundamentals are essential to understanding the magneto-transport measurements conducted in this work.

In order to gain a comprehensive understanding of the plateaus formed in various quantum Hall effects, we need to establish a *microscopic* framework of the QHE. So

far, we have omitted this aspect. There are two predominant microscopic pictures that have been developed since the discovery of the QHE. These pictures use considerably different assumptions and result in different conclusions for charge transport in the QHE regime. A detailed understanding of these pictures is key to correctly interpreting the data presented in Chapter 9. Therefore, in Chapter 4, we will review these pictures.



## Chapter 4

# Quantum Hall Effect II: Microscopic Pictures

In the last chapter, we discussed the behavior of a two-dimensional electron system like Gr under the influence of magnetic fields, ranging from the classical Hall effect at lower fields to the onset of the QHE at larger fields. Our discussion focused on idealized, homogeneous 2D electron systems to emphasize the basic mechanisms at play and introduce all relevant quantities that will be used throughout this work. However, when exploring the original discovery of the IQHE by von Klitzing et al., it became apparent that the presented models need further development to explain the formation of quantum Hall plateaus over extended ranges of magnetic field  $B$  or charge carrier density  $n$ . These advanced models introduce additional assumptions within a microscopic framework of the QHE. As one of the goals of this thesis is to understand the role of disorder in the manifestation of the QHE at room temperature in Gr, it is essential to comprehend the microscopic processes involved and review the most common models. Since the discovery of the QHE, numerous microscopic pictures have been proposed and can be grouped into two main branches of thought. The first branch employs localization assumptions within a single-particle model and, due to its historical prominence, is referred to as the *conventional picture* of the QHE. This picture is reviewed in section 4.1. Over the last decades, this picture has been challenged by an alternative approach that uses interaction-mediated screening in a Landau-quantized 2D electron system to derive the formation of Hall plateaus and other experimentally observable characteristics of the QHE. This *screening picture* will be reviewed in section 4.2. Moreover, the roles of disorder and temperature, along with their expected consequences for magneto-transport measurements, will be discussed within each microscopic picture. The choice of microscopic pictures is not arbitrary, as we will see that apart from different starting points, the conventional and screening pictures come to different conclusions about the details of charge transport

in the QHE regime, which will eventually manifest in appropriate measurements. The screening picture is often underrated and omitted in most lectures and textbooks on the QHE. However, it may prove to be crucial for conceiving and interpreting QHE experiments in the present and the future.

## 4.1 The Conventional Picture

The conventional microscopic picture is based on the assumption that the translational invariance of a considered 2DES is broken, resulting in the *localization* of some charge carriers in the system, while others are delocalized and extend throughout the entire system. As will be demonstrated in the following, the formerly discrete LL spectrum transforms into a series of broadened peaks with the *extended states* centered around the undisturbed LL energies, while *localized states* are shifted in energy into the space between two adjacent LLs. A schematic illustration of this process can be found in Fig. 4.1. The current through such a system is carried only by the extended states, while the localized states (at zero temperature) do not contribute to transport. Therefore, once the Fermi level is tuned into the area of the localized states, the current through the system does not change until the extended states in the next LL are reached.

The breaking of translational invariance is typically facilitated by charge disorder, lattice defects, etc., which can be summarized as the sample *disorder level*. Therefore, a remarkable aspect of the conventional picture lies in the fact that it necessarily presupposes the imperfection of the system to result in universal and perfectly quantized transport properties. In the following sections, we will discuss the mechanism of localization using the simplest example of a single impurity, followed by an overview of different types of impurity potentials that all induce a mobility gap. Subsequently, the gauge arguments of Laughlin and Halperin are presented, elegantly showing that extended states in a system carry a quantized current, which does not change upon altering flux. Next, the edge channel picture is discussed, which is most illustrative for understanding the conventional picture in real devices. Finally, the effects of temperature and scattering are highlighted.

### Localization by a Single Impurity Potential

Among the first works on the localizing effects of impurities in the quantum Hall regime were those published by Prange<sup>1</sup> in 1981 [137, 138]. His argumentation will be outlined only briefly, and for a detailed understanding, one should consult the mentioned references. Prange considered a 2DES channel of width  $W$  and length  $L$  with a  $\delta$ -function impurity potential located at a distance  $(x_0, y_0)$ . Further, an electric

---

<sup>1</sup>Richard E. Prange (1932-2008) was an American physicist and among the most active contributors to QHE research in its first decade, culminating in his well-received book on the QHE in 1990 [137].

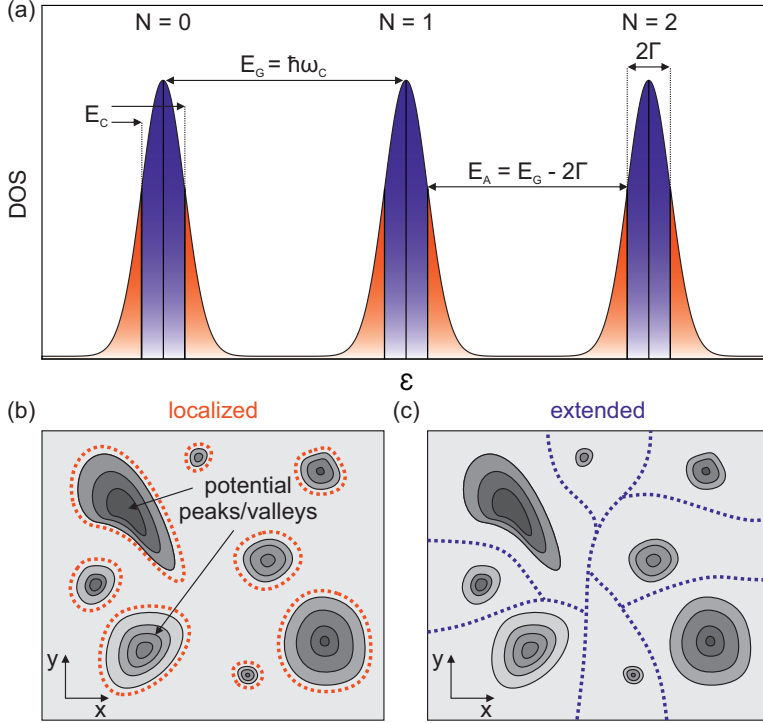


Figure 4.1: **(a)** DOS of a 2DES as a function of energy  $\epsilon$  in a magnetic field  $B$ . In the presence of disorder, charge carriers become localized, leading to broadening of the previously discrete LLs into a series of overlapping peaks. The LL centers are populated by extended states, while the tails contain localized states limited to small areas. The mobility edge  $E_C$  marks the transition from localized to extended states on each side of a LL, and the distance from the LL center to  $E_C$  is called the LL broadening  $\Gamma$ . The intrinsic cyclotron gap  $E_G = \hbar\omega_C$  is reduced to the activation energy between the mobility edges of two adjacent LLs  $E_A = E_G - 2\Gamma$ . **(b)** and **(c)** Schematic illustrations of localized and extended states in the disordered potential landscape of a realistic 2DES. The red dotted lines represent localized states occupied by trapped charge carriers on the equipotential lines of peaks and valleys in the potential landscape, while the blue dotted lines represent extended states that percolate through the entire bulk and can carry a net current across it.



field is assumed in the  $y$ -direction, described by the potential  $eEy$ . Using the drift velocity  $v = cE/B$ , the potential can be written in magnetic units<sup>2</sup> as  $vy$ . Before adding the impurity, the Hamiltonian takes the form  $H_\nu = H_0 + vy$ , the eigenenergies of which are shifted harmonic oscillator states:

$$\psi_{n,k} = L^{-1/2} \exp(ikx) \phi_{n,k}(y + v), \quad (4.1)$$

where  $k = 2\pi p/L$  with  $p$  being an integer and  $\phi_{n,k}$  being the unshifted eigenstates of  $H_0$ . These states are localized in the  $y$ -direction but necessarily extended in the  $x$ -direction as they follow the equipotential lines connected with the introduced electric field. Then, the potential of a single scatterer, characterized by  $V_I = \lambda \delta(x - x_0) \delta(y - y_0)$ , is added. The eigenstates of  $H_\nu + V_I$  can be expanded in terms of the states in Eq. (4.1), and from that, one can obtain a relation which determines the energy level:

$$1 = \lambda \sum_{n,k} \frac{|\psi_{n,k}(x_0, y_0)|^2}{\epsilon - \epsilon_{n,k}}, \quad (4.2)$$

where  $\epsilon_{n,k} = n + vk$  are the eigenenergies corresponding to Eq. (4.1). Every energy  $\epsilon$  that solves Eq. (4.2) must lie between the unperturbed levels  $\epsilon_{n,k}$ . Further, there exists one entirely localized state in each LL, and its energy is shifted considerably ( $\approx \lambda$ ) above or below the original LL position at  $\nu \hbar \omega_C$ , depending on whether  $\lambda$  is repulsive or attractive. The lowest of such states can be approximated as:

$$\psi_{loc} \propto \exp\left(-\frac{x^2 + y^2}{4}\right) \exp\left(\frac{ixy}{2}\right), \quad (4.3)$$

which means that they are centered at the position of the impurity. Since these states are localized, they cannot contribute to the current through the channel, and therefore, the latter also does not change whether a localized state is occupied or not. All other states are extended and located closely around the unperturbed energy levels. The current carried by the states is:

$$I = -\frac{e}{h} \sum_{n,p} (\epsilon_{n,p+1} - \epsilon_{n,p}) = -\frac{e}{h} \sum_n (\epsilon_{n,p_{max}} - \epsilon_{n,p_{min}}), \quad (4.4)$$

where all occupied states are summed up, and  $n, p_{max}$  is the last occupied state at the upper edge, and  $n, p_{min}$  is the first occupied state at the lower edge of the channel. The current is, therefore, proportional to the electrochemical potential difference between the upper and the lower edge but not on the exact number of extended states - as long as all of them are occupied. Prange showed that the extended states

---

<sup>2</sup>The electric field  $E$  is expressed in terms of velocity units, while the magnetic field  $B$  is expressed in terms of energy units. Specifically, in Gaussian units (which are commonly used in magnetostatics), the electric field  $E$  has units of velocity (cm/s), while the magnetic field  $B$  has units of energy per unit area (erg/cm<sup>2</sup>), and the velocity units are given by 1 v.u. =  $(cB)^{-1}$ .

carry an extra Hall current, which exactly compensates for that and is not carried by the localized state, as electrons passing close to the impurity are accelerated.

Generalizing these considerations to  $M$  impurities in a system with  $N$  charge carriers, for  $M < N$ , there will be  $N - M$  extended states unshifted in energy and  $M$  localized states that are shifted away in energy. For  $M > N$  or different kinds of potential, the density of states transforms from singular  $\delta$ -functions to broadened Landau bands of elliptical, Gaussian, or Lorentzian shape with extended states in their centers around the original  $\nu\hbar\omega_C$  and separated by an energy gap that is populated only by localized states (see Fig. 4.1). In this case, it still remains true that only the extended states carry current at zero temperature and that the current remains constant, as long as the occupation of extended states does not change regardless of the occupation of localized states. Similar results were obtained even before the discovery of the IQHE by Ando in renormalized weak-scattering calculations, showing that the presence of an isolated impurity does not affect the Hall current [130]. This aspect is fundamental for the creation of Hall plateaus, as it indicates that once all extended states in a LL are filled and the Fermi level is shifted through the localized states, the Hall current and therefore  $R_{xy}$  and  $\sigma_{xy}$  remain constant as well, while the longitudinal signals  $R_{xx}$  and  $\sigma_{xx}$  drop to zero as no dissipative transport is possible within the localized states. The localized states provide a reservoir that allows the Fermi level to be pinned inside the cyclotron gaps. We can thus resolve the issue we had in Chapter 3.5, where the Eqs. (3.27) and (3.28) were valid only for singular points of filling. However, in order to show that the Hall current not only remains constant within the localized states but is also of the right quantity to result exactly in the before-mentioned equations, we have to recap some famous gauge invariance arguments.

## Gauge Arguments

The idea on which the following arguments are based is that the QHE is essentially a bulk effect, as there is no evidence that changes in size, shape, connectivity, or edge conditions lead to any changes in the fundamental quantum Hall characteristics. Therefore, a favorable geometry can be selected for a theoretical consideration, and general conclusions can be derived from it later on. The first to propose such arguments in order to explain the exact quantization of the Hall plateaus was Laughlin<sup>3</sup> in 1981 [139], whose line of thought will be presented in the following.

We start from a rectangular-shaped channel made of a 2DES (such as Gr) within a homogeneous external out-of-plane magnetic field penetrating it and resulting in a disorder-broadened LL spectrum - similar to the situation in a real device. A

---

<sup>3</sup>See footnote 6 in Chapter 3

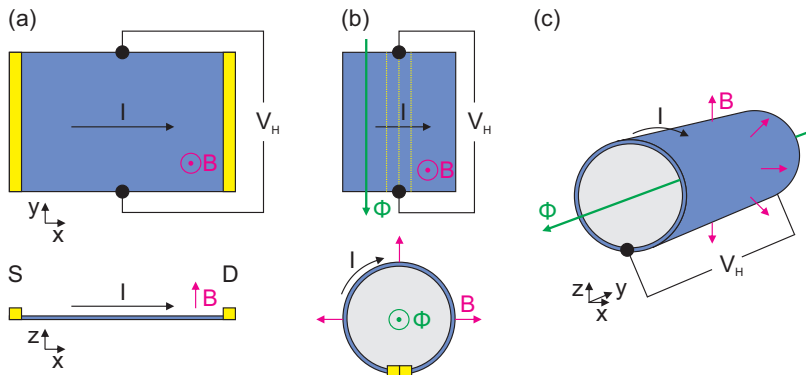


Figure 4.2: Schematic illustration of Laughlin's Gedankenexperiment. **(a)** Initially, a 2DES channel with a source (S) and drain (D) contact transmits a current  $I$ , which, under the influence of a perpendicular magnetic field  $B$ , induces a Hall voltage  $V_H$ . **(b)** The channel is rolled up around the  $y$  axis, resulting in S and D merging and the current encircling the resulting cylinder, while the magnetic field still penetrates the 2DES perpendicularly at each point on the surface. The circular current induces a magnetic flux  $\Phi$  along the  $y$  axis. **(c)** A spherical view of the Laughlin-cylinder.

schematic illustration of this situation is shown in Fig. 4.2(a). Since we can omit edges without losing generality, we virtually roll up the channel such that two of its edges merge and a tube is formed, as shown in Fig. 4.2(b). The magnetic field is transformed along with the tube such that it remains perpendicular to the tube surface at every point. Further, we assume a current  $I$  to flow around the tube. Due to the Lorentz force,  $B$  and  $I$  together will create a Hall voltage drop  $V_H$  between the ends of the tube, while the current generates a flux  $\Phi$  that threads the tube.

We will now investigate how changes in  $\Phi$  affect the other quantities in the system. The current  $I$  equals the adiabatic derivative of the total energy  $U$  of the system concerning the magnetic flux, which can be expressed as the derivative concerning a uniform vector potential  $A$  directed around the tube such that

$$I = c \frac{\partial U}{\partial \Phi} = \frac{c}{L} \frac{\partial U}{\partial A}, \quad (4.5)$$

where  $c$  is the speed of light and  $L$  is the circumference of the tube. This derivative is zero for all localized states, as the only effect of  $A$  on these is an additional factor of  $\exp(ieAx/(\hbar c))$  to their wave functions, where  $x$  is the coordinate around the loop. For the extended states, the gauge transformation in Eq. (4.5) is forbidden unless the vector potential is of the form

$$A = n \frac{\hbar c}{eL} = n \frac{\Phi_0}{L}, \quad (4.6)$$

where  $\Phi_0$  is the magnetic flux quantum and  $n$  an integer. The wave function must be single-valued when a particle is taken around a closed path. When a particle is taken around a loop, its wave function acquires a phase factor  $\exp(ie \oint A \cdot dl/(\hbar c))$ , where  $l$  is the path of the loop. This phase factor must be single-valued, which implies that  $\oint A \cdot dl$  must be an integer multiple of  $2\pi\hbar c/e$ . In the case of the extended states, the wave function is not localized and can be taken around an arbitrarily large loop. This means that  $\oint A \cdot dl$  can take on any value, and the wave function can only be single-valued if  $A$  has the form given in Eq. (4.6), which ensures that  $\oint A \cdot dl$  is always an integer multiple of  $2\pi\hbar c/e$  when the loop encloses an integer number of flux quanta. Therefore, the gauge transformation in Eq. (4.5) is only allowed for vector potentials of the form given in Eq. (4.6) for the extended states.

This gauge invariance implies that the addition of one flux quantum results in the mapping of the system onto itself. Further assuming non-interacting electrons, the phase coherence allows a change in  $A$  to alter the total energy of the system by moving the filled states towards one edge of the tube. Laughlin showed that the energy of a state changes linearly with an increment  $\Delta A$ , and therefore the derivative in Eq. (4.5) can be substituted by  $\Delta U/\Delta\Phi_0$ , where  $\Phi_0$  is a flux quantum [139]. As by the gauge invariance in Eq. (4.6), the energy difference in the system arises from the effective transfer of  $n$  charge carriers from one edge of the tube to the other, and therefore  $\Delta U = neV_H$ . The expression for the current in Eq. (4.5) can then be modified to

$$I = c \frac{\Delta U}{\Delta\Phi_0} = \frac{ne^2 V_H}{h}, \quad (4.7)$$

which then results in a Hall conductivity of

$$\sigma_H = I/V_H = n \cdot \frac{e^2}{h}. \quad (4.8)$$

The original argument by Laughlin was later advanced and further generalized by Halperin in a Corbino geometry [140]. In summary, this line of argumentation shows that the quantized nature of the Hall plateaus is a consequence of gauge invariance and the long-range phase rigidity of the wave functions around the tube, together with the existence of a mobility gap. If the Fermi level lies in such a gap populated by localized states, the longitudinal conductivity vanishes, and the transverse conductivity takes the form of Eq. (4.8).

## Localization, Scaling, and Topology

So far, we have recapped two concepts that allow us to grasp a rough understanding of the manifestation mechanisms behind the QHE when the translational invariance is broken by disorder. However, a realm of rich physics was left to be uncovered in order to understand the localization/delocalization processes in real samples and how different scattering mechanisms impact those. Next, we will outline some of these processes, but leave details to the referenced literature.

In the absence of magnetic fields, a scattering potential is characterized by its resulting mean free path  $l_{\text{mfp}}$  and its strength  $1/(k_F \cdot l_{\text{mfp}})$ . Different potentials equal in these parameters result in roughly the same behavior [137, 141]. In a magnetic field, these quantities are joined by the magnetic length  $l_B$  and the cyclotron energy  $\hbar\omega_C$  in characterizing the system. The QHE now arises if the impurity potential  $V(r)$  can be written as

$$V(r) = V_W + V_{\text{sc}} + V_S. \quad (4.9)$$

The first term is determined by the weakness condition  $\max|V_W(r)| \equiv V^{\text{max}} \ll \hbar\omega_C$  [142]. The second represents a sum of scattering potentials. The requirement for these potentials is that a potential-free region of width  $d \gg l_B$  percolates through the system [141, 143]. The third potential term  $V_S$  is characterized by  $|\nabla V_S| \ll \hbar\omega_C/l_B$ , which is a smoothness condition [143].

The potential Eq. (4.9) creates a LL structure with mobility gaps between the adjacent levels if it locally varies much less than  $\hbar\omega_C$ . In real samples, the weak potential comes from impurities at a distance comparable to  $l_B$  from the charge carriers. The scattering potential arises from charged impurities, and the smooth potential is created by inhomogeneities located at distances greater than  $l_B$  away. The localization properties of electron states in the quantum Hall regime, including descriptions of the Landau model, the random matrix model, the tight-binding-Peierls model, and the network model, are nicely reviewed by Kramer in [144].

Around the same time as the first observation of the IQHE, a significant advancement in the theory of electronic disorder was made by the discovery of weak localization [145]. Abrahams et al. were able to adapt earlier scaling ideas concerning electronic transport to the renormalization group framework. Together with the concept of Anderson localization [146], this led to the formulation of a two-parameter scaling theory by A.M.M. Pruisken, consistent with experimental data [147–152].

Laughlin's argument above already implied that the QHE is of a strong topological nature. The Hall conductivity is usually recognized as a topological quantum number. Assuming periodic boundary conditions, it can be related via the Kubo formalism ([153, 154]) to a topological invariant called the Chern number  $n_{\text{ch}}$ , which is a geometrical feature of the Hilbert space of the wave functions, as  $\sigma_{\text{xy}} = n_{\text{ch}}e^2/h$  (see e.g. Chapter 5.4 in [50] or Ref. [155]). Much of the initial work on the QHE in the context of topology theory was done by Thouless<sup>4</sup>, which laid the groundwork for the discovery, both theoretically and experimentally, of topological insulators, which have an insulating bulk while their surface necessarily remains conductive [156–165]. 2DES in the quantum Hall regime are considered 2+1 dimensional topological insulators in the absence of time-reversal symmetry [166].

---

<sup>4</sup>David J. Thouless (1934-2019) was a British condensed-matter physicist. Together with J. M. Kosterlitz and F. D. M. Haldane, he was awarded the Nobel Prize in Physics in 2016 for theoretical discoveries of topological phase transitions.

## The Edge Channel Picture

A very illustrative picture of the QHE in real devices was developed by Büttiker<sup>5</sup> in the years after the discovery of the effect ([167–171]), finalized in 1988 [172] and further elaborated in great detail in Ref. [173]. He pointed out that the phase rigidity used in the arguments by Laughlin and Halperin is not a fundamental requirement and is limited to situations where the flux circumference is much smaller than the inelastic scattering length. His model explains the QHE for large open channels with contacts, where there is no phase coherence along the entire length of the channel. Instead, the suppression of back-scattering within 1D-edge channels in high magnetic fields drives the manifestation of quantized Hall resistance together with vanishing longitudinal resistances. This absence follows naturally when imagining electrons that semi-classically follow their field-induced cyclotron motion when approaching the edge boundary of a channel. Upon reflection at the boundary or at a scattering center, a charge carrier is forced to move along the channel in a series of semi-circles, while carriers on the opposite edge are effectively moving in the reverse direction. This motion pattern is commonly termed *skipping orbits* and the principle is shown in Fig. 4.3(a). Due to this absence of back-scattering, the transport along the edges is called *quasi-ballistic*. This suppression is valid as long as the scattering potential  $V(r)$  varies smoothly on  $l_B$  scales but rapidly compared to the dimensions of the channel. For strong potentials, it is required that the centers are separated by more than a distance of  $l_B$  [172]. In the following, we will derive the QHE transport landmarks from these initial considerations.

In a real transport channel, the energy of the system  $\epsilon$  consists of the kinetic energy of the Landau levels  $\epsilon_{LL}$  as derived in Eq. (3.12) offset by the potential energy of the disorder potential  $E_D$  as  $\epsilon(N) = \epsilon_{LL}(N) + E_D$ , where  $N$  is the LL index. A schematic example of such a situation can be found in Fig. 4.3(a), where a cross-section of  $\epsilon$  is depicted for various  $N$  in the  $y$ -direction. Due to the confinement,  $\epsilon_N$  must rise to infinity towards the edges of the channel at  $y = \pm W/2$ , while in the bulk, it remains flat and modulated only by the disorder potential. If the Fermi energy is shifted into the proximity of the undisturbed LL  $\epsilon_{LL}(N)$ , it will intersect with  $\epsilon$  at various spots within the bulk due to the disorder potential and necessarily once for every LL at each channel boundary due to the confinement (as highlighted by the circles in Fig. 4.3(a)). It can now be shown that carriers acquire a longitudinal velocity that is proportional to the slope of the bending energy levels  $d\epsilon/dy$  as

$$v(\epsilon) = \frac{1}{\hbar} \frac{d\epsilon}{dy} \frac{dy}{dk}. \quad (4.10)$$

For strong magnetic fields,  $dy/dk$  is negative, resulting in carriers moving in the positive longitudinal direction on the left edge of the channel and in the negative direction on the right side of the right edge of the channel. As only one direction

---

<sup>5</sup>Markus Büttiker (1950–2013) was a Swiss physicist, famous for his works on the Aharonov-Bohm effect, the Landauer-Büttiker transport formalism, and his multi-terminal formulation of the QHE.

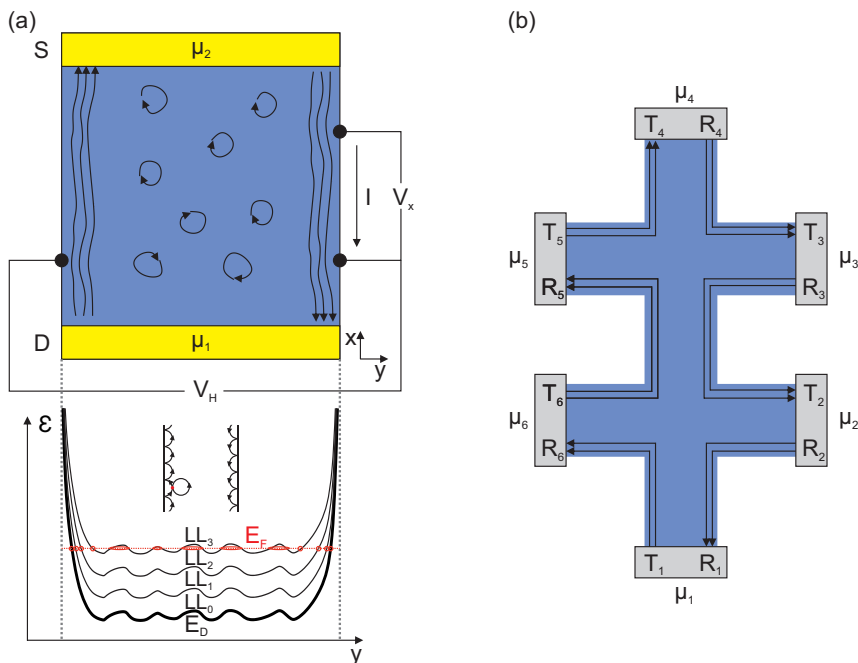


Figure 4.3: Schematic illustration of edge states and the Büttiker model in the quantum Hall regime. **(a)** Edge channels are depicted in a 2DES channel between the source (S) and drain (D) contacts. The longitudinal voltage  $V_x$  and the Hall voltage  $V_H$  are measured. The disorder potential  $E_D$  induces peaks and valleys with steep rises at the sample edges. Under Landau quantization, the LL energies are added to  $E_D$  for each level. The Fermi energy  $E_F$  is within LL3. In the bulk, the double crossings of  $E_F$  with the peaks and valleys of the potential leads to localized states, while at each edge  $E_F$  cuts through each LL only once, creating 1D quasi-ballistic channels along the edge. The quasi-ballistic nature is illustrated in the inset. **(b)** The Büttiker model is applied to a six-port Hall bar device, where every port has a potential  $\mu_i$ , a transmission coefficient  $T_i$ , and a reflection coefficient  $R_i$ . The ports are interconnected by 1D edge channels, and in an ideal QHE device, ports 1-3 have the same potential  $\mu_1$  and ports 4-6 have the same potential  $\mu_2$ , with all contacts having  $R = 0$  and  $T = 1$ .

of motion around the channel per carrier type is allowed, the transport along the edges is of a *chiral* nature, and the carriers are protected from disorder-mediated localization. The same mechanism holds for the potential landscape within the bulk, with the crucial difference that here, it results in carriers enclosing the local peaks and valleys on closed loops and thereby remaining localized. Büttiker showed that contacts along the edge of a channel, as used in a Hall bar geometry, also do not lead to a distortion of the quasi-ballistic motion and the transition probability of a carrier in the edge channels is 1 [172].

If the source and drain electrodes are biased by an external voltage  $V_B$  to the potentials  $\mu_1$  and  $\mu_2$ , respectively, a current  $I$  enters the source and exits the drain through single hot spots. In junctions between materials with a high charge carrier density and Hall angle<sup>6</sup> of nearly zero and a material with low charge carrier density and Hall angle near  $90^\circ$ , there will be a *hot spot* somewhere close to the interface between the materials. The reason for this is that the material with nearly zero Hall angle will have a very small Hall voltage drop along the interface compared to the Hall voltage drop of the material with nearly  $90^\circ$  Hall angle. Since the interface will follow the potential of the high charge carrier density material, the interface will have a nearly constant electrostatic potential. Therefore, the material with nearly  $90^\circ$  Hall angle is unable to drive a current  $j \propto E/B$  through the interface. Thus, the current passes along the contact and focuses into a single spot [174]. The existence of such hot spots could be demonstrated nicely by bringing a layer of superfluid He on top of the transport channel, where little fountains of He emerged at the locations of the greatest electrical energy dissipation [175].

As the carriers from the source are injected into one edge only, and since neither electrodes nor scattering centers can distort their path, the whole edge has the same potential as the source. The whole channel edge on the left side relative to the current direction is therefore on the potential  $\mu_1$  and the whole right edge on  $\mu_2$ . Hence, the measurement of the longitudinal voltage drop  $V_{xx}$  is zero, even if an effective current  $I$  is carried along the edge and we obtain  $R_{xx} = 0$ . Between both edges, there is now a potential difference of  $\mu_2 - \mu_1$  which we can relate to the Hall voltage  $V_H = (\mu_2 - \mu_1)/e$  that is equal to the external voltage  $V_B$  and in order to obtain the corresponding Hall resistance, it remains to further quantify the current  $I$ . Büttiker

---

<sup>6</sup>The Hall angle is a measure of the angle between the direction of an applied magnetic field and the direction of the induced Hall voltage in a material. It is defined as  $\tan^{-1}(A_H/\rho)$ , where  $A_H$  is the Hall coefficient and  $\rho$  is the resistivity of the material. The Hall angle depends on the mobility and density of the charge carriers in the material, as well as the strength of the magnetic field. In general, materials with a high charge carrier density and mobility have a small Hall angle, while materials with a low charge carrier density and mobility have a large Hall angle. The Hall angle is an important parameter in the study of the Hall effect and related phenomena, as it provides insight into the behavior of charge carriers in magnetic fields.



stated that the current flow can be treated similarly to a one-dimensional ballistic conductor channel [50, 172, 173]. Each of those channels carries then a current of

$$I = \int_{\mu_1}^{\mu_2} D(\epsilon) \cdot e \cdot v(\epsilon) d\epsilon = e/h(\mu_2 - \mu_1) = \frac{e^2}{h} V_H, \quad (4.11)$$

where  $D(\epsilon) = (d\epsilon/dk \cdot 2\pi)^{-1}$  is the one-dimensional density of states for spin-polarized electrons,  $v(\epsilon)$  is the longitudinal velocity defined in Eq. (4.10) and the integral goes over all electrons between  $\mu_1$  and  $\mu_2$ . Consequently, every one-dimensional edge channel participates with  $e^2/h$  in the conductivity. As can be seen from Fig. 4.3(a), when the Fermi energy reaches the  $N$ -th LL, it intersects with exactly  $N$  bands at each channel edge, resulting in  $N$  one-dimensional channels and therefore finally  $\sigma_{xy} = N \cdot e^2/h$  and  $R_H = h/(Ne^2)$ .

When the Fermi energy is located within the localized states, the Büttiker-picture concludes that quantized current flows exclusively within 1D-channels along the edge, while the bulk remains insulating and carriers there encircle valleys and peaks of the potential landscape. The longitudinal resistance remains zero and the Hall resistance forms a plateau as long the bulk is gapped out. Around half-filling of a LL, the Fermi energy reaches the extended states at the LL-centers that can carry dissipative current and the bulk becomes conductive—therefore inducing non-zero  $R_{xx}$  and dequantizing  $R_{xy}$ . The quantization within the cyclotron gap holds, as long as no carriers scatter from the upper to the lower edge of a channel. Inelastic scattering enables transitions from one of the circling bulk states to another, but since these states lie at slightly different energies, the hopping from one loop to another has to be activated by temperature. As stated before, the QHE relies on the breaking of the translational invariance and Büttiker demonstrated that this is facilitated by disorder in diffusive devices and by the edge potential in ballistic devices.

The original edge channel picture was further extended for the FQHE [176], foreshadowing the concept of incompressible strips, which we will discuss in section 4.2, as well as for situations in which the gating effect leads to charge accumulation at the edges of a channel in the QH-regime, and, thereby, to a non-monotonic bending of the LL towards the edges. This results in the creation of additional edge channels, that host currents flowing in the opposite direction relative to the regular edge modes (and are therefore called *upstream modes*). Among the first to experimentally reveal this phenomenon were van Wees et al. in 1995, when they attributed longitudinal resistance minima unequal to zero in InAs/AsSb quantum wells to the presence of anomalous counter-flowing edge states [177].

In Gr devices, various researchers found evidence for a charge accumulation at the edges, the origin of which is still under active debate [174, 178, 179]. This charge accumulation induces a non-monotonic LL bending, as described above, and counter-flowing edge states are created. Several experiments have been performed where the upstream modes in Gr were utilized, for example, to explain the electron-hole asymmetry in the QH-regime, to reveal the role of overlapping 1D-contacts for the

precision of QH-measurements in Gr, for the realization of a QH nano-interferometer, and in relation to FQHE edge states [180–183].

## Disorder and Temperature

In the previous sections, we discussed the microscopic basics of the manifestation of the QHE mainly for zero temperature. The effects of finite temperature on the magneto-transport properties within this framework will be examined next, as it is crucial for interpreting the data obtained in Chapter 9. There, the expectations for the role of disorder in the manifestation of the QHE at room temperature are put to the test.

In real devices, the discrete spectrum of LLs is broadened into Landau bands due to disorder-induced localization processes, as discussed earlier. Although the exact shaping of these bands is a subject of intense discussion [93, 137, 184], including ellipsoid, Gaussian, or Lorentzian shapes, the fundamental properties remain the same. The centers of the LL at  $\epsilon(N)$  are populated by extended states until the upper and lower mobility edges at  $\epsilon \pm E_C$  are reached, which mark the transition energy to the realm of localized states that populate the tails of the LLs and, thereby, the cyclotron gaps. When the Fermi level is tuned through such an LL by altering the charge carrier density  $n$  or the magnetic field  $B$ , the Hall plateaus and minima in the longitudinal resistance persist until  $E_C$  is reached, upon which dissipative transport is recovered.

The effects of disorder on the Landau bands are essentially two-fold and mediated by either the *short-range* or the *long-range* parts of the disorder potential. The main effect of the short-range part is the broadening of the LL centers, creating more extended states and, therefore, shifting  $E_C$  further away from the intrinsic LL energy  $E_N$ . This is reflected in a shrinking of the effective energy gap  $E_G$  between adjacent LLs. The intrinsic cyclotron gap  $\hbar\omega_C$  is reduced by the disorder parameter  $\Gamma$ , such that  $E_G = \hbar\omega_C - 2\Gamma$ , where  $\Gamma = |E_C - \epsilon(N)|$ . The effect of the long-range part of the disorder potential lies in the localization of carriers within the cyclotron gap, where more disorder results in a higher density of available localized states. Since both effects are not correlated, i.e., a large number of localized states in the gap is not necessarily accompanied by a large level broadening, the second effect is sometimes referred to as a *background disorder* effect [93, 137, 185].

For Gr, most of the relations elaborated for classical 2DES above remain true. Interestingly, although Gr usually has smaller carrier mobilities than cDES involving GaAs, Martin et al. found in scanning single electron transistor measurements that localization is not dominated by single particle (strong) localization but by Coulomb interaction-driven charge rearrangements [186, 187], and that the single-particle model is valid only in the case of strong disorder. Further differences arise from the non-uniform spacing of the cyclotron gap between individual LLs (see Eq. (3.15)) and the existence of special LLs at zero energy. A large part of the disorder acting in Gr on  $\text{SiO}_2$  can be related to its rippled surface structure, which induces fluctuations of the

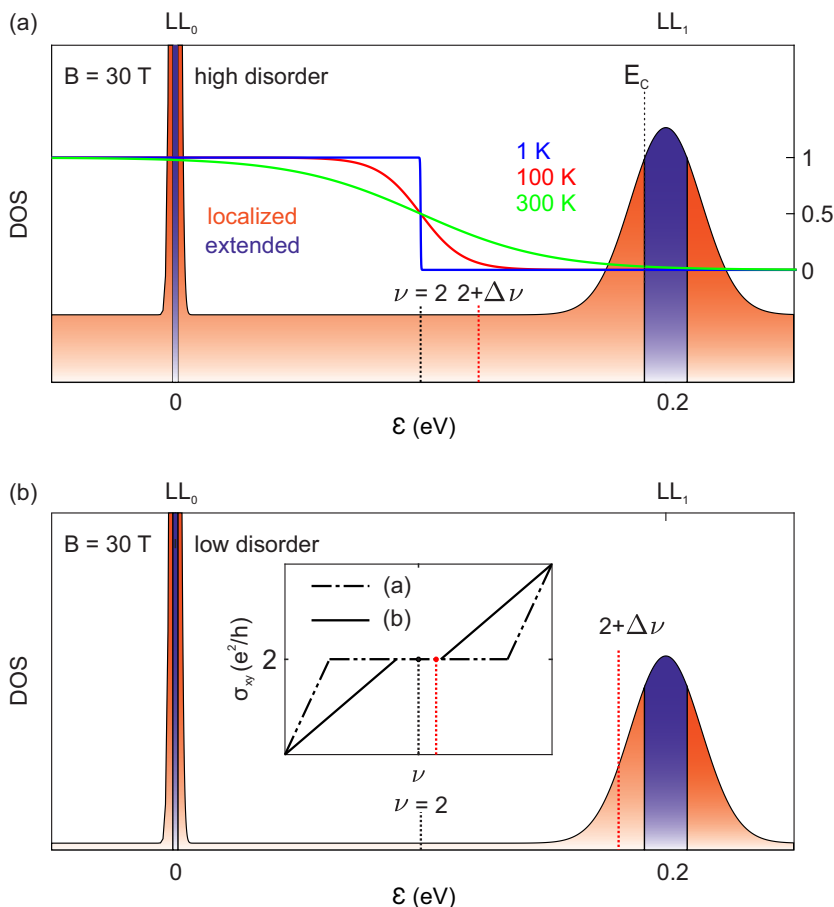


Figure 4.4: Suggested improved caption: **(a)** and **(b)** Density of states of Gr in a 30 T magnetic field for high **(a)** and low **(b)** levels of long-range disorder, while the short-range disorder level is similar in both cases. The Fermi-Dirac distributions for different temperatures are overlaid in **(a)** to highlight the effect of temperature on the level occupation. The red vertical lines indicate the shift in Fermi energy resulting from a fixed increase in filling factor  $\Delta\nu$  away from  $\nu = 2$  for the different disorder levels. The low-disorder case results in a narrower Hall plateau width compared to the highly disordered system due to the mobility edge  $E_C$  being closer to the Fermi energy  $E_F$  with an identical step in filling. The corresponding plateaus are shown in an inset in **(b)**.

locally perceived magnetic field, and fluctuations in the perpendicular field component broaden the Landau bands [185, 188–191].

The zero-LL in Gr is special insofar as it is topologically protected by the Atiyah-Singer index theorem. The number of states inside this level is not determined by the (locally fluctuating) perpendicular component of  $B$ , but only by the total magnetic flux through the surface and, hence,  $LL_0$  is less affected by level broadening [34, 136, 192–194]. The topological protection is a consequence of the fact that the wave function of a Dirac fermion in a magnetic field is described by a two-component spinor, which has a geometric phase factor that depends only on the total magnetic flux through the surface. This phase factor is related to the Berry phase (see Chapter 2), which describes the geometric phase that an electron accumulates as it moves adiabatically around a closed loop in the presence of a magnetic field. In contrast, the higher Landau levels in Gr are not topologically protected, because their wave functions are not described by two-component spinors, but rather by four-component spinors, which do not have a simple geometric phase factor. As a result, the number of states in the higher Landau levels depends on the details of the magnetic field distribution and is not determined solely by the total magnetic flux through the surface. Furthermore, the topological protection of  $LL_0$  in Gr is related to the fact that it is a zero-energy state, which means that the energy of the electrons in this level is exactly at the Dirac point. This is a special feature of the zeroth Landau level, which does not apply to the higher Landau levels, where the energy of the electrons is shifted away from the Dirac point. Therefore, the topological protection of  $LL_0$  in Gr is a unique property that is not shared by the higher Landau levels. The effect gets increasingly dominant at larger magnetic fields when the intrinsic separation of the LL is large, while for lower field, a mixing of LL via inter-level scattering is possible. The first experimental evidence for a narrow  $LL_0$  in Gr was reported by Giesbers et al. [185].

We will now consider a finite temperature within our analysis. If the Fermi level is located in the middle of the cyclotron gap, completely filling a LL, the longitudinal transport is quenched entirely by the localized nature of the carriers. Upon increasing temperature, the step in the Fermi-function determining the system's occupation widens and allows the population of states above the Fermi energy. If this widening becomes significant enough compared to the effective gap  $E_G$ , the mobility edge of an adjacent LL is reached, and the first extended states are occupied. This is followed by a continuous rise in the longitudinal resistance and a shrinking width of the Hall plateaus – the latter resulting from fewer available unoccupied localized states within which the Fermi level can be varied (see Fig. 4.4). The longitudinal resistivity is therefore expected to show activated behavior following an Arrhenius law of the type

$$\rho_{xx}(T) = \rho_0 \exp\left(-\frac{E_G}{2k_B T}\right), \quad (4.12)$$

where  $k_B$  is the Boltzmann constant. In the first decade after the QHE discovery, the temperature dependence of  $\rho_{xx}$  and  $\rho_{xy}$  was studied intensively in various different

2DES. In the activated regime, it was found for some systems that the effective energy gap  $E_G$  was smaller than the intrinsic cyclotron gap  $\hbar\omega_C$ , as expected due to the LL broadening. However, in some cases, the measured gaps exceeded the intrinsic ones by almost 20%, suggesting the presence of additional mechanisms that open an energy gap in the system. One such mechanism is the exchange interaction, which arises due to the Pauli exclusion principle that prohibits two electrons from occupying the same quantum state. This interaction can lead to the formation of a many-body energy gap in the system, which is larger than the intrinsic cyclotron gap. Another possible mechanism is the Coulomb interaction among the electrons, which can also contribute to the opening of an energy gap in the system [195–198]. In some cases, the resistivity at integer filling approached zero well before the Hall plateaus were formed in GaAs devices [120], in InP [199, 200] and in InAs-GaSb [201], indicating that the temperature-dependent mechanisms behind plateau formation and vanishing resistance do not necessarily act on the same temperature scales.

At low temperatures, the Arrhenius activation is frozen out. The electrons may hop from one localized state to another, called the nearest neighbor hopping (NNH), and with increasing temperature, phonon-assisted variable range hopping (VRH) sets in, where the electrons can hop between more distant localized states through the emission and absorption of phonons. At the lowest temperatures, the resistivity scales as

$$\rho_{xx}(T) = \rho_0 \exp\left(-\frac{T_0}{T}\right)^\gamma, \quad (4.13)$$

where  $T_0$  is the Mott-temperature and  $\gamma$  a dimensionless exponent. This exponent was determined in measurements to be  $\gamma = 1/3$  for  $B = 0$  [202] and  $\gamma = 1/2$  for finite magnetic fields [203–205]. Measurements showing  $\gamma = 1/2$  in the presence of magnetic fields were also partially related to soft gaps induced by Coulomb interaction between localized states as proposed by the Efros-Shklovskii (E-S) hopping model [206, 207]. Concerning  $\rho_{xy}$ , a series of evaluations were made extracting the slope of the plateau  $d\rho_{xy}/dn$  as a function of temperature, revealing an exponential behavior  $\propto \exp(-T_0/T)$  when the longitudinal resistivity was not in an activated regime and a linear behavior with  $\rho_{xx}$  when the latter was activated [197].

In the case of Gr, the relatively large LL spacing allows for probing hopping transport in a single LL and localization on a wider energy range before the Arrhenius activation sets in. Temperature-dependent measurements in Ex-Gr [106, 208], epitaxial Gr [209], and CVD-Gr [210, 211] reveal E-S-like VRH with a  $\gamma = 1/2$ . Transitions from E-S to Mott-VRH provide strong evidence for the Polyakov-Shklovskii suggestion that VRH alone describes the transport on the Hall plateaus and at the plateau transition, except for narrow samples [208].

## 4.2 Many-Body Screening Picture

The second major microscopic picture of the QHE is derived from the many-body screening effects under the influence of slowly varying confinement potentials. Its development began with some rather phenomenological works on the effects of screening in the QHE and was soon fueled by experimental results that could not be explained within the framework of the edge channel picture. Here, we will briefly discuss the history of development in this field and its relevance for the QHE in Gr. This is followed by an elaboration of the basic mechanisms of (in)compressible strip formation, current flow, and quantization of the resistances, as well as the common ways to implement simulations of the screening environment in a channel. Afterwards, the effects of temperature and disorder within the screening picture are highlighted.

### Origins, Development and Recent Applications

Around the same time as the development of the single-particle edge channel picture of the QHE, the first works appeared in which the electron-electron interaction and the previously often omitted effect of screening in a 2DES in high magnetic fields were investigated. Among others, Alexei L. Efros<sup>7</sup> made significant contributions with interesting and pioneering works on screening in 2DES [214–219]. These efforts were taken further by Beenakker and Chang in 1990, who, in the quest for advancing the edge-channel picture for the FQHE, first proposed that a 2DES transport channel in the QHE regime under the influence of slowly varying potential splits up into compressible and incompressible carrier liquids, resulting in a series of compressible and incompressible strips running along the longitudinal direction [176, 220]. These rather qualitative works were then further advanced by Chklovskii, Shklovskii, and Glazman (CSG), who, under the assumption of perfect screening, calculated analytically the widths of such incompressible strips [221, 222]. The question of where exactly the current would flow in such a screening-induced landscape was the subject of some debate. Chang argued that current must flow in the incompressible regions, as in the compressible ones, the potential was perfectly flat due to the screening and therefore drift velocities become zero [220]. Otherwise, in a numerical work, it was found that the equilibrium current is distributed over the whole sample [223], while in the edge state model the non-equilibrium current is assumed to flow in the incompressible regions [176]. On the experimental side, the first works calling for an incorporation of many-body effects into model frameworks were reported in 1993, examining current-bias characteristics of edge channels in disagreement with the single-particle theory [224, 225]. These experiments and considerations all fueled the further devel-

---

<sup>7</sup>Alexei L. Efros should not be confused with his brother Alexander L. Efros, who is also a solid-state physicist, or his son, the computer scientist Alexei A. Efros. Sometimes, Alexei is abbreviated as A.L., while Alexander is abbreviated as Al.L. on publications. Works involving B. I. Shklovskii, like the E-S VRH mentioned above, were usually authored by Alexei [212], while Alexander is famous for theorizing the field of quantum dots [213].

opment of the screening approach, which was heavily influenced by Rolf Gerhardt and his co-workers on the theory side. In 1994, Lier and Gerhardt were the first to calculate the distribution and widths of (in)compressible strips (IS/CS) under realistic conditions and finite temperatures [226] and later the local potential and current distribution [227]. Both works use a self-consistent theory of electro-chemical equilibrium to calculate the screening effects instead of the ad-hoc assumption of perfect screening in the CSG model. The next important advancement in this field were the scanning gate measurements on 2DES transport channels in the QHE-regime, first performed by Peter Weitz [228–230] and followed by Erik Ahlswede [231–233]. By directly measuring the spatial Hall potential drop across a channel, the authors could provide proof for the first time that current flow is not limited to 1D channels at the edges (as predicted by the Büttiker picture), but essentially coincides with the spatial positions of the IS as predicted by the CSG model. Furthermore, the current flow shifts from the edges to the bulk, depending on the relative filling of a LL. Similar findings were obtained by Yacobi et al. using a scanning single-electron transistor [234].

The interpretation of the different Hall potential regimes once again inspired the theory side to enhance their modeling for non-equilibrium situations when a current is superimposed on a channel using a (computing time efficient) Thomas-Fermi Poisson-approximation (TFPA) [235]. As the TFPA is applicable only if the potential is sufficiently smooth (see below), it tends to predict IS down to unrealistic widths. To further illuminate plateau formation, Afif Siddiki and Gerhardt in 2004 improved the models by employing Hartree type calculations [236]. An important aspect of their work is the employment of a local transport theory that describes dissipative currents together with a local version of Ohm’s law, instead of the dissipationless currents that were assumed before [227]. The model predicts non-overlapping magnetic field ranges in which IS of integer local filling exist. The imposed dissipative current is confined to these strips, resulting in the global resistances equaling the local (quantized) resistivity within the strips and thereby creating the Hall plateaus.

In the following years, Siddiki and co-workers further investigated the roles of short-range and long-range disorder on the IS and Hall plateaus [237–239] and later focused on interaction mediated effects in high-quality 2DES like plateau asymmetries and situations in which *evanescent* ISs at the edge become leaky and create so-called *overshoots* in the Hall resistance [240–244]. Further works aimed at manipulating the edge or bulk electrostatics by special gate architectures or inner contacts [245, 246]. A notable work was reported by Kendirlik et al., who found in Hall bars with two inner contacts that for certain  $B$ -field ranges *within* a plateau, the bulk becomes compressible (i.e., metallic), which strongly challenges the so far assumed topological nature of the QHE within the single-particle picture [155, 247].

Reviews of several aspects of the screening picture can be found in [237, 248, 249], but, unfortunately, no recent or more general reviews exist. This chapter aims to fill this gap in order to help future students and researchers understand the screen-

ing picture without having to browse all the primary literature. The relevance of the screening picture is high, whenever narrow channels of high carrier mobility are considered, which is the case for the Gr devices measured within this work.

The role of IS for the QHE in Gr has been omitted for quite a while, and many review articles on the electronic properties explain the plateau formation within the conventional localization picture and speak of incompressible electron liquids only in the context of the FQHE [12, 13]. However, due to the highly interacting nature of the carrier system in state-of-the-art heterostructures, the screening picture becomes more and more important, and we will quickly mention the most important works and fields of interest. On the front of spatially measuring (in)compressible landscapes in Gr, a lot of pioneering work was done by Panos [174], revealing the expected structure and dynamics of IS in Gr on a bare SiO<sub>2</sub> substrate via scanning probe measurements. His work further evidenced an accumulation of negative charges at the Gr edges, the origin of which is still under debate. Spatial imaging of the IS within LL<sub>0</sub> of Gr was recently shown in sophisticated Kelvin probe measurements [250]. Furthermore, CS and IS in Gr were used to measure magnetic monopole-responses [251].

## Edge Reconstruction, Current Flow, and Resistance Quantization

Free electrons will always rearrange themselves to screen and minimize potential fluctuations, creating a rearranged electrostatic potential landscape. In transport devices, these potential fluctuations can be caused by charged impurities and charges on the substrate, by local gates, and, for the most part, by the outer boundaries of the channel. Classical 2DES host a depletion zone at the sample edge, where  $n$  gradually decreases to zero. Gr can either be physically confined into a channel, creating a hard wall potential at the edges, or it can be soft confined by gating [39]. The strong electrostatic potential rearrangement at the edges is usually denoted as *edge reconstruction* [252].

The situation becomes interesting when the 2DES undergoes Landau quantization in a large magnetic field. In this case, the classical picture predicts that the LL bend up continually towards the edges, while the carrier density  $n$  exhibits sudden step-like changes until it reaches zero. This scenario is depicted in the left panel row of Fig. 4.5. The Fermi level cuts through each energy level exactly once and thereby creates 1D transport channels along the edge. This setting changes fundamentally once screening is included. Instead of the usual local chemical potential  $\mu_{\text{ch}}(r)$ , the local electrostatic single-electron energy  $-e \cdot \phi(r)$  is also considered in the electrochemical potential  $\mu_{\text{elch}} = \mu_{\text{ch}} - e \cdot \phi(r)$ . The CSG model shows that alternating CS and IS along the edge are energetically favorable [221]. When  $n$  increases from the edge towards the bulk, the first LL is gradually filled. Upon complete local filling, a considerable amount of energy is required to occupy the second LL, and it is more favorable to keep  $n$  constant over a finite width  $a_\nu$ . Within this region of constant carrier density,



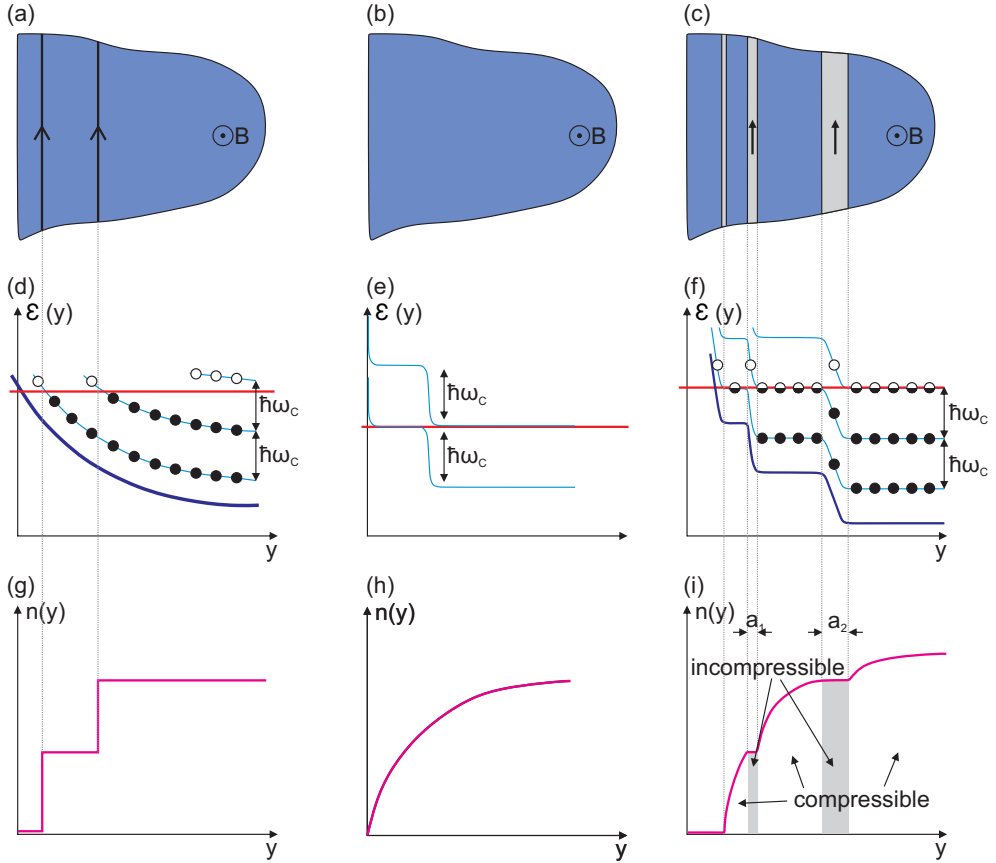


Figure 4.5: Schematic illustration of different scenarios at the edge of a 2DES channel, including the LL structure and charge carrier density. **(a)**, **(d)**, and **(g)** depict Büttiker-like band bending and edge states due to the neglect of electrostatic energy. **(b)**, **(e)**, and **(h)** show unperturbed depletion towards the edge, due to neglect of the chemical potential. **(c)**, **(f)**, and **(i)** display screening-mediated edge reconstruction, taking into account both the electrostatic energy and the chemical potential. Sections of increasing and constant  $n$  alternate, resulting in compressible and incompressible strips along the edge, which become wider towards the center of the channel. Partially adapted from [174, 221].

the LL energies bend downwards towards the bulk (see the right-hand row of panels in Fig. 4.5), until it is more favorable to fill the second LL instead of keeping  $n$  constant. The alternating sequence of regions with constant  $n$  and constant  $\mu_{\text{elch}}$  continues until the bulk filling level is reached. This scenario is depicted in the right row of panels in Fig. 4.5. The compressibility  $\kappa$  of the electron system can be expressed in terms of the derivative of the electrochemical potential with respect to the carrier density as

$$\frac{1}{\kappa} = n_{2D}^2 \frac{\partial \mu_{\text{elch}}}{\partial n}. \quad (4.14)$$

In the regions with constant  $n$ , the so-defined compressibility falls to zero, while it is finite elsewhere. Therefore, these regions are called *incompressible* and the regions of constant  $\mu_{\text{elch}}$  *compressible*. Along a transport channel, these regions result in (in)compressible strips running parallel to the channel edge. In the incompressible regions, the Fermi energy lies between the completely filled LLs underneath it and the empty LLs above it, implying that the local filling there is integer valued. The incompressibility further implies that due to the lack of available free states for the carriers, they cannot rearrange themselves to screen off potential gradients, giving them an insulator-like nature. In the compressible regions, however, rearrangement and screening remain possible.

The groundbreaking aspect of the work of Chklovskii et al. [221] was their analytic calculation of the positions  $y_\nu$  and widths  $a_\nu$  of the IS under the assumption of perfect screening for a semi-infinite channel, given by

$$y_\nu = \frac{d_0}{1 - \left(\frac{\text{int}(\nu)}{\nu}\right)^2} \quad a_\nu = \frac{4y_\nu}{\nu} \sqrt{\frac{\text{int}(\nu)a_B^*}{\pi d_0}}, \quad (4.15)$$

with the effective Bohr radius  $a_B^*$  of the material with dielectric constant  $\epsilon$  and the screening length  $d_0$ , which are defined as

$$a_B^* = \frac{4\pi\epsilon_0\epsilon\hbar^2}{e^2m^*} \quad \text{and} \quad d_0 = \frac{4\epsilon_0\epsilon|V_{\text{BG}}|}{\pi en}. \quad (4.16)$$

In the case of Gr, the effective mass  $m^*$  is not constant as in other 2DES (see Eqs. (2.18) and (2.19)), but depends on the Fermi-wavevector  $k_F = \sqrt{\pi n}$ , such that  $m^* = \hbar k_F/v_F$  and therefore  $a_{B,\text{Gr}}^* = 4\pi\epsilon_0\epsilon\hbar v_F/(e^2\sqrt{\pi n})$ . The IS can only exist as long as their width is greater than the magnetic length ( $a_B^* > l_B$ ) as otherwise, they become transparent for electrons in the compressible regions. For the usual screening lengths obtained in 2DES or in etched Gr on a Si substrate, this means that only the innermost IS is wide enough to manifest. Comparing the relation for  $d_0$  with the definition of the lever arm  $\alpha_{BG} = \epsilon_0\epsilon/(ed)$ , where  $d$  is the gate spacer layer thickness, one finds  $4/\pi d = d_0$ , or that the screening length should be roughly 30 % greater than the gate spacer.

The qualitative evolution of the width and position of the strips with magnetic field is similar for every integer filling factor. With rising field, narrow IS form at the edges of a channel and subsequently move inside towards the bulk while becoming wider until they merge to a wide stripe in the center close to integer filling. Right around integer filling, the IS vanish, leaving the whole bulk compressible. In the following, the current distribution within an (in)compressible landscape and how it leads to the quantization of the global resistances will be discussed.

Following the description in Ref. [237], the model system considered here is a channel  $|y| \leq d$  in the  $xy$ -plane, with translation invariance in the  $x$  direction. A fixed current is imposed along the channel  $I_0 = \int_{-d}^d dy j_x(x, y)$ , where the current density follows Ohm's law with a local resistivity tensor  $\bar{\rho}$  and a driving electric field  $\vec{E}$ , which is defined as the gradient of the electrochemical potential  $\mu_{\text{elch}}$  such that

$$\bar{\rho}(\vec{r})\vec{j}(\vec{r}) = \vec{E}(\vec{r}) \equiv \nabla\mu_{\text{elch}}(\vec{r})/e, \quad \bar{\rho}(\vec{r}) = [\bar{\sigma}(\vec{n})]^{-1}, \quad (4.17)$$

where the resistivity- and conductivity tensors depend only on the charge carrier density  $n(y)$  and we write for the components  $\rho_{yy} = \rho_{xx} = \rho_L$  and  $\rho_{xy} = -\rho_{yx} = \rho_H$ . In case of a thermodynamic equilibrium, where  $\mu_{\text{elch}}$  is constant over the whole channel, the current density vanishes. For a stationary current density, one obtains  $\nabla\vec{j}(\vec{r}) = 0$  and  $\nabla \times \vec{E}(\vec{r}) = 0$ , and further with  $\partial_x j_x = 0$  and  $\partial_x E_y = 0$  follows  $\partial_y j_y = 0$  and  $\partial_y E_x = 0$ , and therefore  $j_y(x) \equiv 0$  and  $E_x(y) = E_x^0$ . Now using Eq. (4.17), we can write

$$E_y(y) = \frac{\rho_H(y)}{\rho_L(y)} E_x^0 \quad E_x(y) \equiv E_x^0 \quad j_x(y) = \frac{1}{\rho_L(y)} E_x^0, \quad (4.18)$$

and for the electro-chemical potential and the whole imposed current, we get

$$\mu_{\text{elch}}(x, y) = \mu_0 + eE_x^0 \left( x + \int_0^y dy' \frac{\rho_H(y')}{\rho_L(y')} \right) \quad I_0 = \int_{-d}^d dy \frac{E_x^0}{\rho_L(y)}. \quad (4.19)$$

Using Eqs. (4.18) and (4.19), the current distribution and electro-chemical potential can be calculated for any given resistivity/conductivity model, such as for the Drude case (see Chapter 3.1)  $\rho_L(y) = m^*/(e^2\tau n(y))$  and  $\rho_H(y) = \omega_C\tau\rho_L(y)$ , which yields a  $j_x(y)$  that is proportional to  $n(y)$  and a constant Hall field  $E_y(y)$  created by a linearly varying potential.

This theoretical framework allows for the investigation of current distribution and electro-chemical potential in various material systems, such as 2DES or Gr on a Si substrate. The interplay between the resistivity and conductivity tensors, as well as the charge carrier density, results in a rich landscape of current and potential distributions that ultimately lead to the quantization of global resistances observed in experiments.

Understanding these processes and the intricate behavior of the current distribution within an (in)compressible landscape is essential for the development of novel electronic devices that take advantage of these unique transport properties. The

work of Chklovskii et al. and subsequent research efforts have provided valuable insights into the complex nature of quantum Hall systems and opened new avenues for exploration and application of these phenomena in modern electronics.

In a system that undergoes Landau quantization, the presence of the cyclotron gap suppresses any elastic scattering for zero temperature, and at integer filling of the LLs, one obtains  $\rho_L(\nu = i) = 0$  and  $\rho_H(\nu = i) = h/ie^2$  (see Chapter 3.5). The local model assumes that these relations hold for IS of sufficient width with integer local filling factor. When we now evaluate Eqs. (4.18) and (4.18) under these conditions, we first note that the integral over  $1/\rho_L(y) \rightarrow \infty$  and since  $I_0$  remains finite, this implies  $E_x^0 \rightarrow 0$  and consequently the current density  $j_x(y) \rightarrow 0$  and the Hall field  $E_y(y) \rightarrow 0$  outside the IS. The Hall potential therefore drops only over the IS in the channel, and every strip carries a fraction of the total imposed current  $\Delta I_x$  proportional to the Hall potential drop  $\Delta\Phi_y$  across its width  $w = y_2 - y_1$  such that  $\Delta I_x = \nu \frac{e^2}{h} \int_{y_1}^{y_2} dy E_y(y) = \nu \frac{e^2}{h} \Delta\Phi_y$ , independent of the details of the potential drop. When the channel hosts only IS with the same integer local filling factor  $\nu = i$ , the whole imposed current  $I_0$  consequently becomes proportional to the accumulated Hall potential drop across the channel, which is exactly the Hall voltage  $V_H$ , implying  $I_0 = \nu \frac{e^2}{h} \int_{-d}^d dy E_y(y) = i \frac{e^2}{h} V_H$  and leads to global resistances

$$R_L \propto E_x^0 \rightarrow 0 \quad \text{and} \quad R_H \rightarrow \frac{h}{ie^2}, \quad (4.20)$$

and thus the well-known quantized relation. The current  $I_0$  flows without dissipation inside the strips, as the drift velocity of the carriers is a property of the eigenfunctions solving the respective Hamiltonian [249]. From the arguments presented above, we can postulate that as long as well-defined IS are inside a channel, the resistance quantization should hold, resulting in extended Hall plateaus. The quantization neither depends on localization assumptions nor on a concrete conductivity model to be plugged into Eq. (4.19). The latter only determines the transport behavior *between* the plateaus.

Having now established an understanding of the IS formation and their dynamics upon changing global filling via  $B$  or  $n$ , as well as the mechanisms of the current flow within the resulting (in)compressible landscapes, we can now microscopically describe the dynamics of a channel as probed via transport measurements together with scanning probe mapping of the Hall potential across the channel in four regimes (i)-(iv):

(i) Around integer filling and in the absence of an external bias, the screening-induced (in)compressible landscape is roughly symmetric on both edges of the channel, and the current integral in Eq. (4.19) becomes zero. Similar to the conventional edge channel picture, in this equilibrium case, a persistent current encircles the channel as

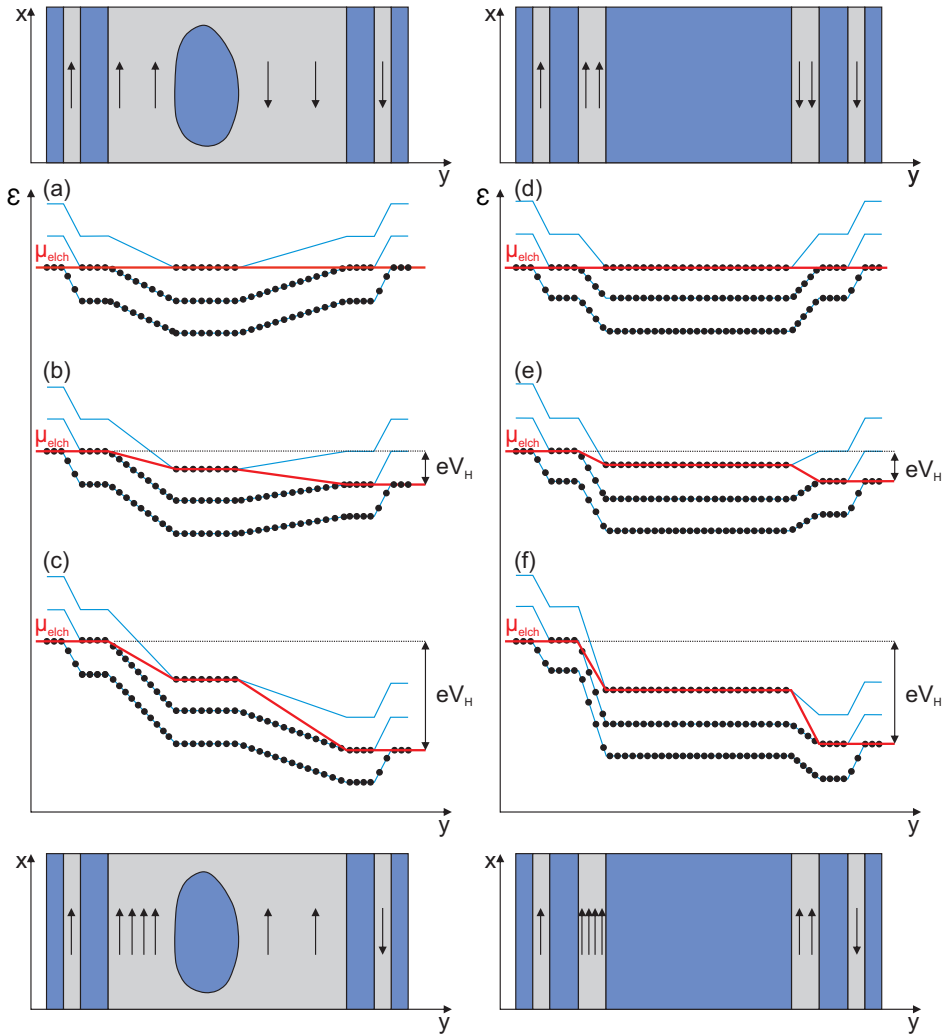


Figure 4.6: Schematics of LL bending in the transverse ( $y$ ) direction of a transport channel in the regime of an incompressible (a)-(c) and a compressible (d)-(f) bulk, and the corresponding electro-chemical potential  $\mu_{\text{elch}}$  as a red line. The first row ((a)+(d)) shows the equilibrium situation without an externally imposed current. The second row ((b)+(e)) shows the bending for a small Hall voltage drop  $V_H$  across the channel, driving an external net current in the  $x$  direction. The third row ((c)+(f)) represents a scenario where  $e \cdot V_H$  exceeds the LL spacing. The illustrations above and below the energy diagrams show the corresponding equilibrium and non-equilibrium situations in the bulk, with the arrows indicating the current flow. A net current is generated by gradients of  $\mu_{\text{elch}}$  and flows on both sides of the channel in the same direction. Adapted from [249].

well as islands in the potential landscape in the bulk. This situation is depicted in panels (a) and (d) of Fig. 4.6.

(ii) In the non-equilibrium case, around integer filling  $\nu = i$ , the Hall potential drops over most parts of the bulk corresponding to a wide incompressible inner region of local filling  $n$  limited by small CS at the channel edges, distributing  $V_H$ . The global resistances are quantized following Eq. (4.20). The LL bending in this situation is shown in Fig. 4.6(b).

(iii) Increasing the bulk filling  $\nu > n$  (e.g. by decreasing  $B$ ) creates a compressible region at the center of the channel, resulting in two separated IS with local filling  $n$  around it, which move towards the edges upon further bulk filling. This case is illustrated in Fig. 4.6(e). Although further IS are theoretically possible from Eq. (4.15), their widths are small compared to  $l_B$  and hence are equilibrated by the CS around. The current flow is limited exclusively to the innermost IS. The Hall voltage  $V_H$  causes an enhancement of the drop in  $\mu_{\text{elch}}$  by a coefficient  $\alpha \approx 0.5$  on one side of the channel and a reduction of the drop by  $(1 - \alpha)$  on the other side [249]. The local dissipation-less current inside one IS is then enhanced to  $\Delta I_x = n \frac{e^2}{h} \alpha V_H$  and decreased to  $\Delta I_x = n \frac{e^2}{h} (1 - \alpha) V_H$  in the other. Integration over the whole channel then leads again to a dissipation-less net current in the  $x$ -direction, and the global resistances remain quantized following Eq. (4.20). At high bias voltages, exceeding the cyclotron gap several times ( $e \cdot V_H > \hbar\omega$ ), the bending of the LLs on the right channel side (relative to the net current flow direction) is reversed, and the whole current density in both the right and left IS are oriented in the same direction.

(iv) Further increasing the bulk filling moves the narrowing IS close to the edges. At some point, scattering across the IS into the central compressible region and subsequently to the opposing edge becomes possible. The voltage drop across the IS decreases, and therefore the induced current also decreases. A gradient in  $\mu_{\text{elch}}$  is created in the  $x$ -direction, resulting in a drift of the electrons in the compressible regions, accompanied by a Hall potential drop in the CS. Scattering between the edges and the bulk de-quantizes  $R_H$ , and the longitudinal potential gradient results in  $R_L > 0$ . Eventually, the IS lose all insulating abilities, and the channel behaves like a classical (compressible) Hall system. Further increasing the bulk filling will bring us back to (i) with  $\nu = n + 1$ .

It is crucial to note that as a consequence of Eq. (4.17), all net currents in the IS are imposed via gradients in the electro-chemical potential  $\mu_{\text{elch}}$ , and that the current direction depends on the sign of the derivative. Hence, we can see from Fig. 4.6(c) and (f) that in the non-equilibrium situations, the net current flows in the  $x$ -direction on *both* sides of a channel. This is in contrast to the strictly counter-propagating edge currents implied in the Büttiker picture.

Another important aspect is the role of contacts usually present at a Hall bar used as electrodes to measure the voltages. In the Büttiker picture, the edge channels are directly connected to the contacts and the fundamental requirement for a measurement of the QHE is that an equal amount of carriers enters and leaves a contact,

or likewise, that the transition rate  $T = 1$ . Scanning gate measurement in the contact regions of a c2DES revealed fundamentally different results [249, 253, 254]. The c2DES is depleted in front of the contacts, leading to a formation of (in)compressible strips similar to those at the channel edges. However, in devices which show a QHE, the IS do not extend into the contacts, implying the externally biased current does not pass through the contacts. The contacts then only probe  $\mu_{\text{elch}}$  in the outermost compressible region. The authors in Refs. [249, 254] discuss in detail how special contact geometries can be used to optimize the screening landscape and therefore the measured precision of the Hall plateaus. It is to be expected that similar mechanisms influence the measurement of the QHE in Gr devices - especially those employing 1D side contacts with slightly overlapping metal on top [182].

Since in the equilibrium situation, the persistent current encircles a channel and is carried by the IS, which themselves at no point connect to the contacts, the question arises how and where the externally biased current in the non-equilibrium situation is imposed onto the IS. This last ingredient is missing for a complete microscopic picture of the QHE in the screening framework and lies in the hot spots in front of the externally biased contacts, which we briefly mentioned before in the description of the single-particle picture [175]. The carriers enter the channel at the left-hand side of the source contact (relative to the transport direction) in the compressible region and are then transferred into the IS through the local hot spot. The potential of the source is distributed by the outermost compressible region along the left-handed channel edge to the drain contact and even along it until it reaches the second hot spot at its right-hand side. There, the carriers exit the IS and are transferred into the drain contact. An illustration of the hot spots in a transport channel is shown in Fig. 4.7(b). The presence of the hot spots was shown in experiments [175, 254, 255], as well as in modeling of the current distribution [256].

We now have all the ingredients of the microscopic picture of the QHE in the screening theory together. J. Weis and K. von Klitzing nicely summarize the microscopic requirements for the QHE formation in the screening picture in contrast to the conventional model in [249]:

The quantum Hall effect does not necessarily require disorder to be present. The depletion at the 2DES edges and in front of the alloyed contacts might be enough.

The CSG expressions for the positions and widths of IS are a good approximation for  $T = 0$  K and without further disorder assumptions. However, since we are interested in real samples at finite temperatures up to room temperature and with varying degrees and types of disorder, we need to involve modeling and self-consistent calculations to obtain the (in)compressible landscapes. In the following sections, an overview of the common ways to implement such calculations is presented, followed by a review of the influences of temperature, short- and long-range disorder on the dynamics of IS, obtained from such calculations. However, note that all the above-

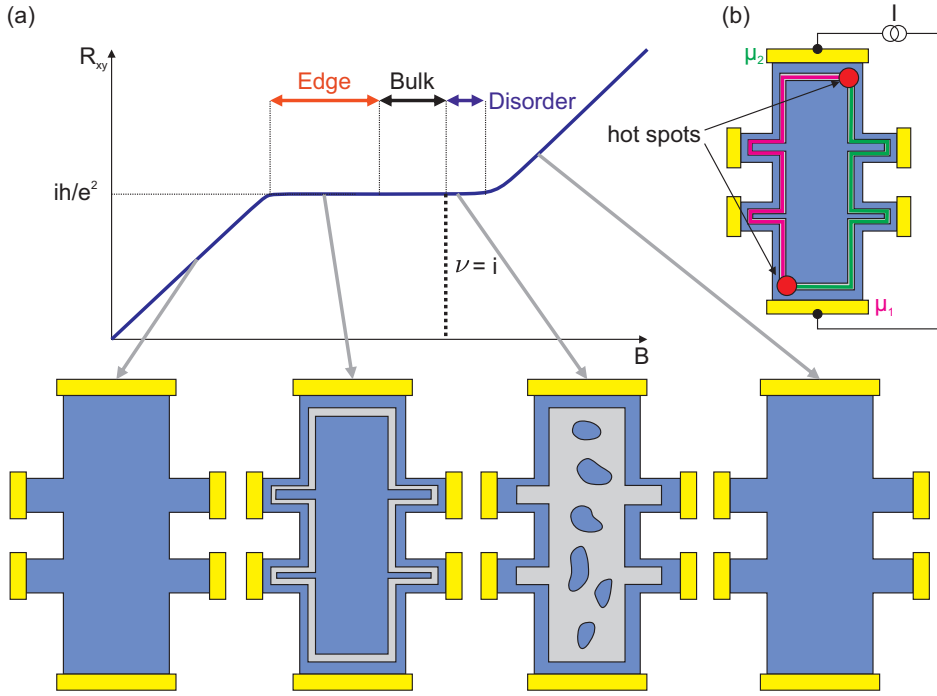


Figure 4.7: **(a)** Schematic illustration of the evolution of the (in)compressible landscapes as the magnetic field  $B$  is increased. Starting from an entirely compressible bulk, the Hall resistance begins to develop a plateau once the first narrow incompressible strip (IS) is stabilized at the edges of the channel, resulting in an *edge-dominated* plateau. As the IS broadens, moves towards the channel center, and merges with increasing  $B$ , a mainly incompressible channel bulk is formed, with compressible droplets inside, leading to a *bulk* or *disorder-dominated* plateau as long-range disorder causes an elongation of the plateau across the point of integer filling  $\nu = i$ . Eventually, all incompressible regions disappear, and the whole channel becomes compressible again. **(b)** Illustration of hot spots forming at the current-inducing contacts, which allow carriers from the leads to enter the IS. Adapted from [249].

discussed mechanisms and dynamics remain valid, as long as incompressible regions exist in 2DES.

## Theoretical Modeling of (In)compressible Landscapes

After Chklovskii et al. set out with an analytical approach assuming perfect screening to calculate the positions and widths of IS, Lier et al. were the first to model the



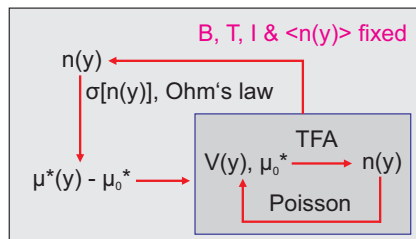


Figure 4.8: Schematic illustration of the self-consistent calculation loops used in the study. The magnetic field  $B$ , temperature  $T$ , imposed current  $I$ , and average charge carrier density  $\langle n \rangle$  are fixed parameters. The inner loop calculates the potential  $V(y)$ , effective chemical potential  $\mu_0^*$ , and carrier density  $n(y)$  using a suitable approximation (e.g., the Thomas-Fermi approximation), for a given electro-chemical potential  $\mu_{\text{elch}}$ . The carrier density is then used in the outer loop to calculate the conductivities via Ohm's law and the electro-chemical potential via integration. The loop is repeated until convergence is achieved. Adapted from [248].

screening in a self-consistent way, which also allowed investigating the role of temperature [221, 226]. They considered an equilibrium of the electro-chemical potential  $\mu_{\text{elch}} = \mu_{\text{ch}}(n) - e\phi(y)$  and used an iterative loop to first calculate the charge carrier density  $n$  from  $\mu_{\text{ch}}(y)$  and  $\phi(y)$ , followed by a recalculation of  $\phi(y)$  via the Poisson equation and  $\mu_{\text{ch}}(y)$  from the filling of the DOS. This process is usually repeated until the solutions converge. In a second loop, a local version of Ohm's law can be included, allowing the modeling of non-equilibrium situations with an imposed current. An illustration of the nested self-consistent calculation loops can be found in Fig. 4.8.

Among the easiest ways (in terms of computation time) to calculate  $n(y)$  is by using the Thomas-Fermi approximation (TFA)

$$n(y) = \int_{-\infty}^{\infty} d\epsilon D(\epsilon) f(\epsilon + e\phi(y) - \mu_{\text{ch}}(y)), \quad (4.21)$$

where  $f(E) = (1 + \exp(\epsilon/k_B T))^{-1}$  is the Fermi function, and  $D(\epsilon)$  is the density of states. In the simplest case, the DOS can be approximated as a series of delta functions at the LL energies  $E_n$  and thus omitting any collision broadening assumptions as

$$D(\epsilon) = \frac{g_s}{2\pi l_B^2} \sum_n \delta(\epsilon - \epsilon_n), \quad (4.22)$$

where  $g_s$  is the spin degeneracy. The TFA yields good results as long as the potential varies slowly on the scale of  $l_B$ , or likewise, as long as no relevant length scales are comparable to the spatial extent of the wavefunctions. As a consequence, one has to keep in mind that the TFA will predict strips with unrealistically small widths.

In a situation where the potential varies significantly on the scale of  $l_B$ , a more complex calculation of  $n(y)$  must be employed using a Hartree approximation, where the electrostatic potential is inserted into Schrödinger's equation

$$\left[ \frac{1}{2m} \left( \vec{p} + \frac{e}{c} \vec{A} \right) + \phi(y) \right] \Phi_\lambda(\vec{r}) = E_\lambda \Phi_\lambda(\vec{r}), \quad (4.23)$$

where  $\vec{A}$  is the vector potential describing the magnetic field. Using the Landau gauge  $\vec{A} = (0, Bx, 0)$  and a substitution for the center coordinate  $Y = -l_B^2 k$ , the electron density becomes [236]

$$n(y) = \frac{g_s}{2\pi l_B^2} \sum_n \int dY f(E_n(Y) - \mu_{\text{ch}}(n) + e\phi_{n,Y}(y)) |\phi_{n,Y}(y)|^2. \quad (4.24)$$

The self-consistent nested loops for a non-equilibrium situation are arranged as follows [248]: The magnetic field  $B$ , the temperature  $T$ , the external current  $I$ , and the average carrier density  $\langle n(y) \rangle$  are fixed. Initially,  $\mu_{\text{ch}}(y)$ ,  $\phi(y)$ , and  $n(y)$  are calculated, e.g., using the TFA in the inner loop. In the outer loop, the carrier density is then plugged into the local version of Ohm's law  $\bar{\sigma}(n(y))$  (see Eq. (4.17) and Eq. (4.19)) giving the conductivities and by integration over the current inducing field  $\mu_{\text{ch}}$ , which is then entered into the inner loop.

Using such calculations, a lot of the dynamics in the evolution of (in)compressible landscapes could be derived, finally shedding light on so far unresolved features in experiments, such as plateau dips or overshoots [240–244, 257]. Furthermore, fundamental insights into the role of short- and long-range disorder potentials for Hall plateau width dynamics as a function of temperature could be made. The main findings will be presented in the next section.

## Temperature and Disorder

The screening-mediated formation of IS, wide enough to allow a quantized Hall measurement, emerges even for vanishing levels of sample disorder at low enough temperatures. However, it is of great importance for metrological measurements of the plateau quantization as well as for the investigation of the role of disorder for the manifestation of the QHE at room temperature in the scope of this thesis to understand the interplay of different types of potential variations (i.e., types of disorder) in the evolution of IS-widths and, consequently, plateau widths, with temperature.

The temperature is straightforwardly included into the model via the Fermi function  $f(\epsilon)$  as used in Eq. (4.21). Lier and Gerhardtts were the first to model the temperature dependence of a 2DES in a screening environment [226]. They found that with increasing temperature, the IS shrink in width until the whole channel becomes compressible. The slope of the electrochemical potential in the compressible region increases proportional to temperature because screening by electrons becomes

less effective, while the width of the incompressible regions decreases linearly with increasing temperature. This shrinking can be expressed relative to the cyclotron gap  $\hbar\omega_C$ . The IS were nicely pronounced up until around  $0.06 \cdot \hbar\omega_C$  and fully vanished at  $T > 0.1 \hbar\omega_C$ . Since the quantized nature of the global resistances crucially depends on the existence of well-insulating IS, the Hall plateaus are expected to follow a similar trend respective to the gap with temperature. These results can be referenced as a lower boundary for the critical temperature of the QHE, valid for systems dominated by screening effects instead of localization.

The disorder potential can be included into the calculations either via the DOS Eq. (4.22) or by direct integration into Schrödinger's equation Eq. (4.23). For the DOS, both Gaussian approximations [235] for collision-broadened LL, as well as the self-consistent Born approximation (SCBA), have been employed [93, 128, 236]. Compelling reviews on the matter can be found in [237, 248]. The results can be summarized as follows:

(i) Short-range disorder, like that caused by charged impurities with Gaussian potentials, leads to a shrinking of the IS widths, similar to an increase in temperature as discussed above. This corresponds to the case of strong LL-broadening in the conventional picture, which shrinks the effective cyclotron gap down and thereby leads to an occupation of the first extended states in an adjacent LL at lower temperatures compared with the unbroadened case.

(ii) The long-range part of a disorder potential, on the other hand, leads to a stabilization and extension of the Hall plateaus. It creates regions of the bulk with slightly varying local doping, which in the QHE case leads to these regions becoming incompressible at higher magnetic fields (or lower filling likewise) compared with a homogeneous bulk. As long as sufficiently large parts of the bulk are incompressible and allow a drop of the Hall potential across them, the Hall resistance remains constant, and, therefore, the plateaus are enhanced towards the high field side. This case corresponds to the background density of localized states in the conventional picture.

An example of the separation of a given potential into long- and short-range components can be found in Fig. 4.2. The initial potential in (a) as created by randomly distributed donor impurities can be split up into a short-range part approximated by Gaussians in (b) and a long-range part approximated by a Fourier analysis in (c), where the summation of both parts in (d) closely resembles the original potential in (a).

We can, therefore, expect that in a device with vanishing long- and short-range disorder, the QHE will be facilitated mainly by the edge IS, and the plateau widths would approach an intrinsic lower limit  $\Delta\sigma_{xy,0}$  at a given base temperature, as well as a lower limit for their critical temperature  $T_{C,0}$ . With increasing long-range disorder, the plateaus are then extended towards the high field side such that  $\Delta\sigma_{xy} > \Delta\sigma_{xy,0}$  and consequently, the critical temperature of the plateaus would rise  $T_C > T_{C,0}$ .

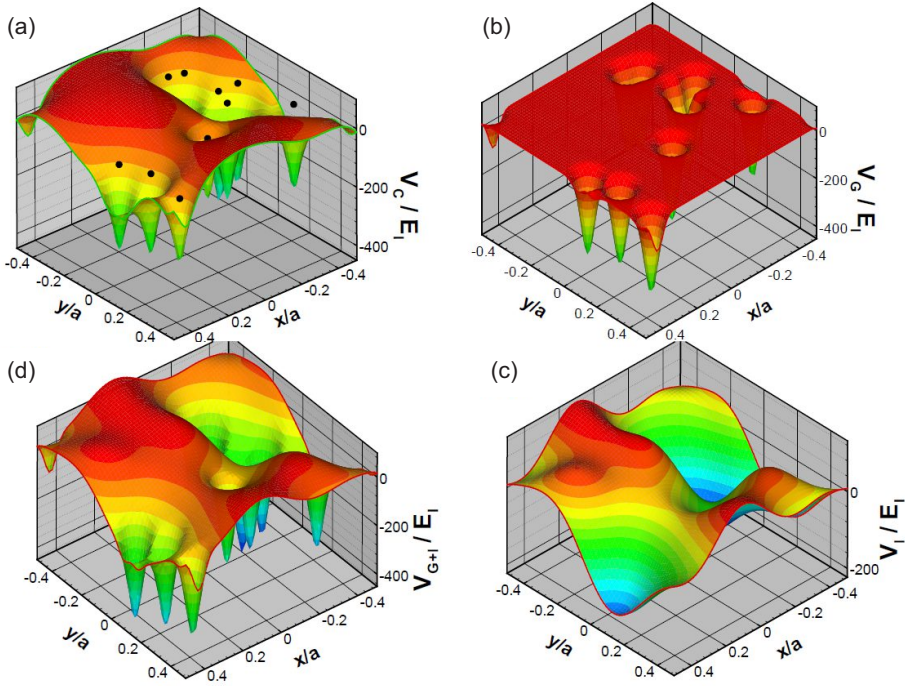


Figure 4.9: **(a)** Schematic illustration of an external potential generated 90 nm below a plane containing ten Coulombic donors. **(b)** Same situation but with Gaussian donors. The range of the Gaussian potential is determined by the spacer thickness. **(c)** The low-rank Padé (LRP) of the Coulomb potential profile, where only the lowest two Fourier components are back-transformed to configuration space. **(d)** Gaussian potential profile plus the LRP of the Coulomb potential used for comparison of the potential landscape. Reprinted with permission from [237], ©World Scientific Publishing Company.

### 4.3 Summary

In this chapter, we reviewed in detail the common microscopic pictures developed over the decades after the discovery of the IQHE and their assumptions and characteristic properties. The conventional model can be split into a bulk picture, which assumes disorder-broadened LL hosting extended states in their centers that have finite amplitudes at every point in the infinite 2DES and localized states in the LL tails that have finite amplitudes only in narrow regions with closed trajectories on equipotential lines of the disorder potential. Hall plateaus appear as the localized states are gradually filled up, while the extended states and therefore the conductivity remain unchanged.

The quantization of it can be derived from the arguments by Laughlin and Halperin as long as we can assume periodic boundary conditions.

For real samples with boundaries, the conventional picture was extended by Büttiker's edge states. He adapted the Landauer approach, in which conduction is interpreted in terms of the transmission and reflection of charge carriers and extended it to open systems by including contact terminals. In the QHE-regime, the LL bend up at edges due to the confinement and are crossed by the Fermi level, creating one-dimensional quasi-ballistic channels at the edges connecting the sample terminals with a transmission rate of 1, while the bulk remains gapped out. The Hall plateaus again arise from the gapped natures of the sample bulk, while the quantization of the Hall signal directly follows from the assumption of integer-numbered ballistic 1D channels. The effect of temperature in the conventional framework lies in the broadening of the Fermi function within the cyclotron gap, resulting in activated transport. The sample disorder level increases the reservoir of localized states that can be gradually filled until the extended states are reached, thereby *ceteris paribus* increasing the disorder level results in a widening of the Hall plateaus.

Both the bulk and the edge state picture within the conventional framework are single-particle pictures, neglecting any electron-electron interaction effects like screening. As the screening length is usually a few times smaller than  $\lambda_F$ , it was assumed that screening plays no role. Upon realizing that a pool of charge carriers, in fact, produce a long-range Coulomb interaction, the first screening models predicting IS and CS were developed by Chklovskii et al. to describe the FQHE as well as the IQHE. Later on, the purely analytical and simplified model by CSG was enhanced by self-consistent calculations of the (in)compressible landscapes as a function of temperature by Gerhards and coworkers, who deduced that the currents are confined to the IS regions. This was followed by the works of Siddiki and coworkers, who included the finite extent of the wavefunctions into the self-consistent models, leading to effects like evanescent IS and overshoots in plateaus. In the screening picture, the plateaus arise from the existence of IS that isolate the opposing compressible sample edges, while the quantization follows from the constant inter-valued filling factor in the IS regions that carry the current. With increasing temperature, the IS shrink in width and thereby allow activated transport across them. Increasing the long-range part of the disorder potential leads to an enhanced filling range in which IS are present in the device and hence *ceteris paribus* widen and stabilize the plateaus on the bulk side.

The predictions of the screening picture for the locations and widths of IS are in precise agreement with scanning probe experiments, contradicting the conventional edge channel picture. Furthermore, it explains several phenomena like the plateau overshoot and dip effect, the finite impedance within a transport channel bulk probed by inner contacts. The latter strongly challenges the interpretation of a QHE system as a topological insulator. It resolves many shortcomings of the single-particle picture, like its limitation to systems with periodic boundary conditions. It should be taken into account for any QHE measurement in interacting electron systems in order not to

overlook important effects at play, and there is much room for comparing experiments to calculations or, in short, it is of great relevance for the future of any QHE-related research.

With the knowledge we reviewed here, we are now well-equipped to interpret the magneto-transport measurements presented in Chapter 8 and 9.



## Chapter 5

# Chemical Vapor Deposition

The fundamental exploration and industrial application of the many fascinating properties of Gr necessitate reliable production processes and techniques. While the mechanical exfoliation of natural graphite (also called *scotch tape* method) has been the workhorse for fabricating the highest quality Gr devices for fundamental research, this technique is far from being reliable or scalable. It involves considerable amounts of expensive human labor and produces a lot of waste, as most exfoliated flakes are not monolayer and hence discarded. Several top-down approaches based, for example, on the liquid phase exfoliation of bulk graphite, yielding Gr-based powders or solutions, were developed and have already found their way to applications as chemical additives or conductive inks [258]. However, the resulting material has a different morphology, hosting at best multilayered flakes with varying thickness and diameter, which share almost none of the outstanding electrical, mechanical, or optical properties of ideal MLG sheets. Therefore, the demand for a process that yields exfoliation-grade Gr in a scalable and reliable manner is enormous. Two such techniques emerged after the discovery of Gr, one of which is the *epitaxial growth* on single-crystalline SiC<sup>1</sup> and the other is the *chemical vapor deposition* (CVD)<sup>2</sup> on metal substrates from carbon precursors [265]. The chemical interplay between carbon and metal surfaces has been studied for more than 40 years on metals such as Ni, Cu, Co, Ru, Pt, Rh, Pd, Ir, etc. [266], although the research was predominantly aimed at understanding surface effects, rather than at growing singular basal layers of graphite. After the first demonstration of large-area growth of MLG with decent quality on Cu foils in 2009 by the

---

<sup>1</sup>See, for example, Refs. [259–261] for the pioneering works in this field, as well as the recent publications by Walt A. de Heer’s group for the contemporary state, e.g. Refs. [262–264].

<sup>2</sup>The term CVD was introduced in 1960 by John M. Blochner to contrast the process from physical vapor deposition (PVD) methods that involve chemical reactions. CVD, in general, has become an important process for the deposition of high-quality, high-performance thin solid films in the semiconductor industry for applications like light-emitting diodes or power electronics.



Ruoff group<sup>3</sup> [7], the research interest in CVD-Gr greatly increased and eventually left other competing technologies behind. The reasons for this boom lie partially in the comparatively simple means required to achieve CVD-growth of Gr on metals like Cu or Ni, such that even high school grade chemistry equipment was demonstrated to suffice for this purpose [268]. For this reason, many research groups working with Gr set out to build their own CVD systems, either to investigate the CVD process itself or the resulting Gr and its applicability for their regular Gr research. Seeking to attain a similar end, we once set out to build a CVD system for our institute and later on eventually invented our own dry transfer process [8], which in the end played a crucial role both in the fabrication of the Gr devices presented in this work and no less in proving the equality of the intrinsic capabilities of CVD-Gr and Ex-Gr (see Chapter 8). To fully grasp the extent of the relevance of these findings, it is mandatory to review in detail the basic growth mechanisms and kinetics of the CVD process, together with a summary of the most recent advancements in overcoming adverse growth effects degrading the quality of CVD-Gr, as well as an overview of the most common transfer methods. The focus will lie on the CVD growth of Gr on metal foils, as, for now, this branch of research is the closest to achieving the much sought-after industry-readiness<sup>4</sup>. Most of the knowledge depicted here will be applied when we discuss the actual CVD growth and transfer carried out for this thesis in Chapter 6 and upon judging the perspectives of CVD-Gr in general and of our dry-transfer process at the end of this chapter and in Chapter 10.2.

## 5.1 Typical Gr-CVD Setups and Processes

A typical CVD setup for the growth of Gr consists of the following functional parts: The *reaction chamber* hosting the *substrate* on which the growth is facilitated and which is heated via a *heating system*, while the atmosphere inside it is controlled via a *gas mixing station* on one side, allowing the injection of various *process gases*. The other side of the reaction chamber is usually connected to a pump rack, which is used to control the total *pressure* within the system. The reaction chambers often consist of quartz tubes of varying diameter, and the heating is facilitated by resistive heating elements outside the tube (hot wall reactors). Alternative approaches can be realized by directly and exclusively heating the metal substrate, e.g. via inductive heating (cold wall reactors). As we will see below, the latter yield more homogeneous

---

<sup>3</sup>Rodney S. Ruoff (\*1957) is an American physical chemist currently based in Korea with an astonishing h-index (exceeding 170). Most of the major breakthroughs in the CVD-Gr research field have been achieved by his group, and to get an overview of the state of the art in this field, it is usually a good starting point to read his most recent publications. His personal perspectives on Gr [267] as well as his talks on CVD-Gr (e.g. <https://www.youtube.com/watch?v=F63vXCV7q4I>) are very worthwhile.

<sup>4</sup>Interested readers can find more information and references on the fascinating branches of CVD-Gr research in recent reviews on growth of single-crystal Gr, on CVD-Gr growth on thin metal films, on Gr/metal interfaces, and on CVD-Gr transfers in [258, 269–272].

growth results but are also more complex to build (and hence more expensive) than the former. Over time, Cu has emerged as the go-to substrate for Gr growth, due to its comparatively low carbon solubility (e.g. Ni has a carbon solubility of 0.9 % at 900 °C, while Cu has only 0.00074 % at 1020 °C) and the ease of transfer of the deposited Gr, especially on foils, which can be scaled up even to a roll-to-roll process [273]. The process gases in most Gr-CVD systems already contain the *carbon precursor* in the form of CH<sub>4</sub> (methane), but, in principle, various carbon-containing precursors from gases over liquids to solids can be made to work<sup>5</sup>. Using CH<sub>4</sub> gas as a carbon precursor has the advantage of good thermal stability, preventing pyrolysis (thermal decomposition) at high temperatures, which turned out to be a prerequisite for high-quality Gr deposition<sup>6</sup>. The other process gases either act as active agents (like H<sub>2</sub>) or achieve specific *partial* and *total* pressures in the system, while they themselves are inert (like Ar). The partial and total pressures also determine the output ranges required of the mass flow controllers (MFC) in the gas mixing station, as well as the pumps setup in the pump rack. The growth can be realized either by a low-pressure CVD (LPCVD) process with total pressures in the mTorr range (which usually requires an additional turbo molecular pump) or at higher pressures in the 10-100 Torr range up to atmospheric pressure (APCVD).

A typical CVD process starts with the mounting of the growth substrate within the reaction chamber, followed by the sealing of the system and the creation of a defined atmosphere by starting the flow of some process gases together with the pump(s). The substrate is then heated up to a desired growth temperature under the permanent flow of gases and annealed either passively (only by temperature) or actively (e.g. by H<sub>2</sub>, which removes most of the oxygen from it) for time spans between minutes and days. This is followed by the actual growth stage, where the precursor is injected into the system, which decomposes and facilitates the formation of Gr crystals on top of the substrate surface (see below for details on the growth mechanisms and kinetics). Afterwards, the system is cooled down, the pumps are stopped, and the reactor is filled with an inert gas, such that the substrate can be dismantled safely. As the Gr is of little use while being on top of the growth substrate, it is usually detached from it and placed on an arbitrary substrate using a *transfer process* (see below).

## 5.2 Growth Mechanisms and Kinetics

Two predominant growth mechanisms have been identified for Gr growth on catalyzing metal substrates: the surface segregation/precipitation process of carbon, resulting in the growth of multilayered Gr, and the surface adsorption process, yielding MLG [266, 275]. While the first process governs growth on metals with finite carbon

---

<sup>5</sup>A collection of exotic carbon precursors, including various foods, insects, and waste, that were all successful in the growth of Gr can be found in [274].

<sup>6</sup>As we will discuss below, pyrolysis leads to the unwanted formation of amorphous carbon in the reaction chamber and on the growth substrate.

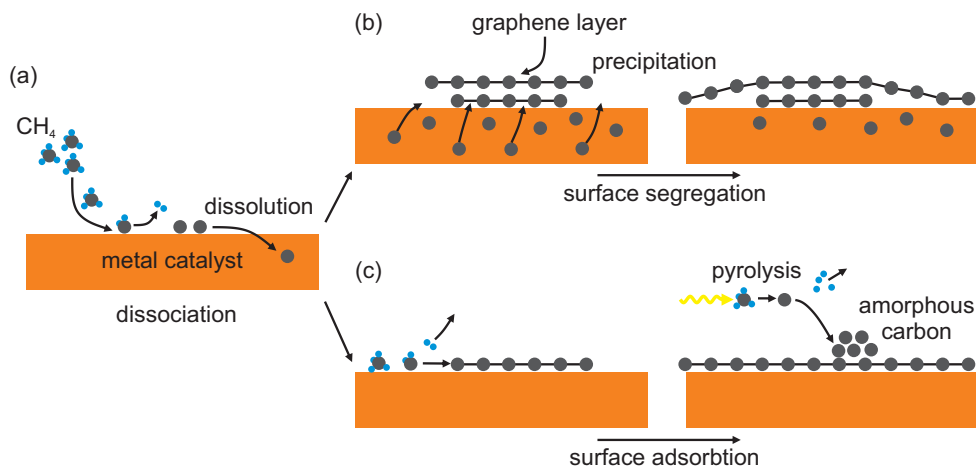


Figure 5.1: Schematic illustration of the two predominant growth mechanisms of Gr. **(a)** At high enough temperatures, carbon-containing precursor molecules (e.g.  $\text{CH}_4$ ) dissociate on the surface of a metal catalyst material. The resulting carbon atoms are partially dissolved in metals with finite carbon solubility (e.g. Ni). **(b)** In such a case, upon lowering the temperature the carbon solubility is reduced and the excess carbon species precipitate at the surface, forming Gr multilayers. Even when the whole area is covered, adlayers can continue to grow underneath the initial layer, as long as carbon species are expelled from the metal bulk. **(c)** On metals with a low carbon solubility (e.g. Cu), the growth is dominated by a surface adsorption process, where the dissociated carbon species traverse the metal surface until they are attached to monolayer graphene crystals at a nucleation site. Once the catalyzing metal surface is covered, the growth is terminated and no adlayers can appear. During both growth mechanisms, the temperature-induced pyrolysis of carbon precursors can lead to contamination of Gr with amorphous carbon.

solubility like Ni, the latter determines Gr growth on Cu surfaces. The catalyzing effect of the metal surface breaks up the  $\text{CH}_4$  molecules, and the resulting C atoms are absorbed by the metal surface until the carbon solubility for a given temperature is reached. Afterwards, a closed monolayer of Gr forms on top of the metal surface, starting from so-called *nucleation sites*. When cooling down the reaction chamber, the carbon solubility of the substrate is reduced and, consequently, carbon atoms are expelled from the metal bulk, forming additional Gr layers underneath the initial ones. In the case of Cu substrates, almost no carbon is absorbed into the metal surface and the growth is governed by a self-limiting surface adsorption process. The self-limiting character is enhanced by using a low methane partial pressure, which allows molecular decomposition only at the metal surface. The surface adsorption process is always

present on metal substrates, while the segregation/precipitation process is limited to metals with high enough carbon solubility. In an atmosphere with higher amounts of methane, or when using precursors less stable at high temperatures, finite pyrolysis can create enough C species to form small adlayers or amorphous carbon on top of the first monolayer, as found in hot wall APCVD processes. The predominance of either of the two growth mechanisms can be revealed by alternating injection of  $^{12}\text{CH}_4$  and  $^{13}\text{CH}_4$  gas during the growth stage and subsequent mapping of the Raman G-peak of the obtained Gr crystals, the position  $\omega_G$  of which is sensitive to different masses of carbon isotopes. The segregation-mediated growth of multilayered Gr results in a mix of the isotopes in the final crystal, while the surface adsorption mechanism leads to alternating annuli of isotopically pure areas [7, 266].

The surface adsorption growth also allows the formation of adlayers underneath the initial layer if gas molecules or decomposed intermediate species diffuse into the interface between the as-grown layer(s) and the Cu surface. This *higher-order* growth process is quenched once all neighboring initial Gr domains merge, and the C diffusion stops. Another higher-order adlayer growth mechanism was first described by Hao et al., taking into account the finite remaining solubility of C in Cu, which, especially in Cu enclosures (see below), results in C diffusing from one surface of the Cu to the other and to the Cu/Gr interface, forming Bernal-stacked adlayers underneath the initial Gr layer [276]. As the  $\text{CH}_4$  molecules need to completely decompose before the C can enter the Cu bulk, oxygen impurities on the surface further play a key role in the growth of bilayer Gr (BLG).

The growth always starts from nucleation sites, and the number of such nuclei per surface area is called the *nucleation density*. Such sites can be formed by the reduction of hydrocarbon particles, at metal grain boundaries or nanoparticles, or from amorphous carbon formed by the pyrolysis of the precursor. On polycrystalline foils, one usually aims at reducing the nucleation density as far as possible to achieve large Gr grain sizes, and, to this extent, substrate surface pre-treatments, as well as a low  $\text{CH}_4$  partial pressure and higher temperatures, are favorable.

To summarize, the growth of Gr on metal surfaces consists of the following stages: (i) gas phase reactions, (ii) adsorption and dehydrogenation of C-containing species, (iii) diffusion on metal surfaces and/or dissolution in the bulk, (iv) aggregation of C-containing species to nucleate Gr at nucleation sites, and (v) 2D Gr growth. All stages mentioned above are impacted by the growth temperature, the reaction chamber pressure, the gas composition and their partial pressures, the time for each stage, and conditions of the substrate like purity, roughness, crystalline orientation, and chemical condition. Changes in these parameters result in different nucleation densities, domain sizes, domain morphologies, growth rates, layer numbers, stacking orders, and physical and electrical quality of the Gr sheets.

Increasing the temperature and decreasing the methane partial pressure decreases the nucleation density, allowing for larger individual crystals. Pre-oxidation treatments can further reduce nucleation by passivating existing nucleation sites and at

the same time increase the growth speed as oxygen vacancies help to fully decompose the  $\text{CH}_4$  [266, 277]. Cu foil enclosures further reduce the methane partial pressure and prevent net Cu evaporation, resulting in a smoother surface and hence less nucleation. The growing domain morphologies depend on the growth mechanisms. Compact hexagonal shapes result from an edge-attachment limited growth, while dendritic domains grow by a diffusion-limited process. H attached to the graphene edge increases the energetic barrier for further C ad-atoms, and hence the  $\text{H}_2$  to  $\text{CH}_4$  ratio is crucial for achieving optimal growth conditions. Air leaks into the system and gas desorption from the chamber walls can also have a significant impact on the Gr growth [266].

### 5.3 Growth Reactors

The growth reactors used in CVD processes are an often neglected part in the puzzle that needs to be solved in order to obtain pleasing Gr growth results<sup>7</sup>. It is a well-known phenomenon in the CVD-Gr community that the *external* and *global* growth parameters, like the reactor temperature, total pressure, and relative gas flow rates/composition, cannot be adapted one by one between different CVD systems, even when the setup consists of similar functional parts. Time-consuming process optimization steps have to be carried out to adapt a given process from published literature. The researchers operating hot wall CVD systems, like quartz tubes within furnaces, usually have only poor knowledge of the *internal* and *local* distribution of temperature, pressure, and gas flow, as these parameters are complicated to measure in a meaningful way. The lack of adaptability, therefore, implies that the sometimes stated assumption of a laminar gas flow and a homogeneous temperature distribution (at least over the extent of the substrate metal foil) due to the predominantly radiative heating are invalid. Only recently, a work was published which simulated for the first time the reactor conditions during Gr growth, using a computational fluid dynamics toolbox [278]. Carried out for outer parameters that result in the growth of adlayer-free single crystal MLG films on Cu(111) foils (see Ref. [279]), the authors found that the reactor flow is in a turbulent regime and that the temperature profile of the Cu foil exhibits large gradients that depend on the total pressure, the total mass flow rate, and the composition of the process gases, as well as on the interfacing area where the foil touches the reactor chamber and the relative position of the foil inside the tube. Growth reactors under ideal and real conditions are illustrated schematically in Fig. 5.2. These results imply that cold-wall reactors should be favored over hot-wall systems for reproducible and scalable growth processes. As cold-wall systems

---

<sup>7</sup>In fact, this problem is more severe in small, lab-sized CVD setups used for graphene research. On the other hand, the major selling points of commercial systems for industry-scale CVD of semiconductors are their advanced technological solutions. These solutions ensure highly precise and homogeneous temperature profiles and gas flows, and are achieved through showerhead or planetary reactor designs.

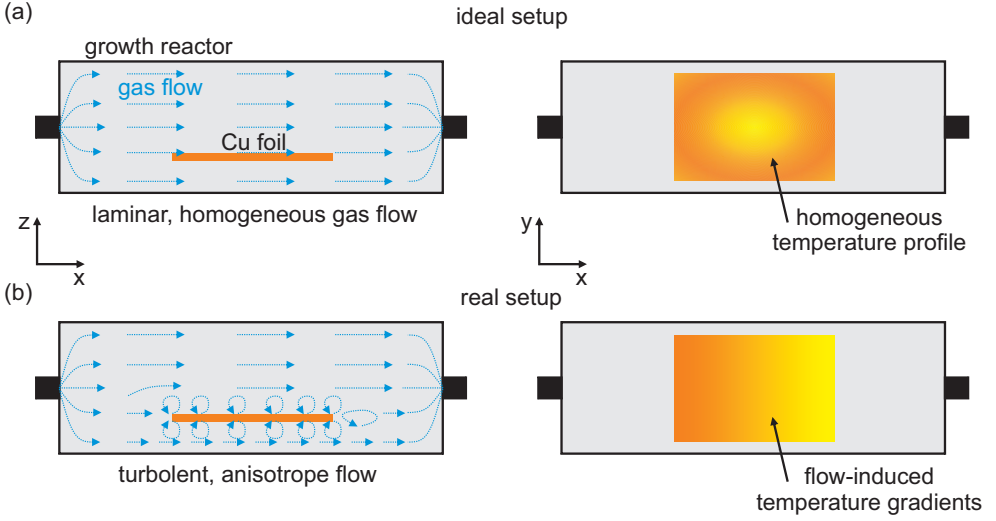


Figure 5.2: **(a)** Schematic illustration of an ideal growth reactor. The gas flow is laminar and homogeneous everywhere inside the growth reactor, and the catalyst metal foil exhibits a homogeneous temperature profile at the growth temperature. **(b)** In a realistic growth reactor, the gas flow is partially turbulent, and the flow profile depends crucially on the position and shape of the catalyst foil inside the chamber, which then results in a temperature gradient in the gas flow direction on the foil.

tend to be more expensive, a cold-wall-like behavior could be implemented in hot-wall systems by optimizing the Ar gas flow during growth.

## 5.4 Catalyst Metal Foils

Over the years, a number of growth substrate-related phenomena were reported, each of which has unwanted effects on the resulting Gr crystals. It was shown that folds and wrinkles in the Gr, together with grain boundaries as well as additional layers on top of the initial monolayer, all tend to significantly decrease the charge carrier mobilities achievable at room temperature [279, 280]. Therefore, it is worthwhile to discuss the state-of-the-art understanding of these phenomena and how they can be avoided.

## Surface Smoothness

Obtaining a smooth Cu surface is key to achieving large single crystal (SC) Gr areas. As Gr preferably nucleates at small dents in the metal surface or its grain boundaries, making the surface smoother and overall more homogeneous reduces the nucleation density. Grooves on a rough Cu substrate trap more carbon residuals than a flat landscape, thereby causing the formation of amorphous carbon Gr fragments. Ultra-smooth surfaces, on the other hand, can prevent or reduce the incidence of cracks and wrinkles during subsequent Gr transfer stages [281, 282]. The purity of a metal foil was also shown to impact growth results, as on 99.999 % Cu foil an identical growth process yields MLG while on 99.8 % Cu foil, only BLG was grown [271]. Methods to clean and polish the substrates include baths in organic solvents, chemical etchants, electropolishing and electroplating, mechanical polishing, metal evaporation, and pre-oxidation, which also speeds up the growth [266, 277].

A very handy workaround to achieve the growth of millimeter-sized SC Gr flakes in most hot wall reactors without dramatically reducing the  $\text{CH}_4$  flow<sup>8</sup> lies in the fabrication of Cu foil envelopes (so-called *enclosures*) [283]. The space inside the enclosures is sealed off from the reactor chamber by crimping the edges, and gases can enter it only by diffusion through the folds and the Cu bulk, resulting in a very low  $\text{CH}_4$  partial pressure. Furthermore, due to the equilibrium of Cu evaporation and re-adsorption, the surface is smoothened, and the Cu sub-grains become very large. As a consequence, the nucleation density is very low, allowing the growth of large SCs of Gr.

## Obtaining Single Crystal Foils

The commercially available metal foils for Gr growth are usually polycrystalline with Cu grain sizes in the range of microns. After the CVD growth process, the small grains are usually found to have merged into bigger ones, resulting in a patchwork of grains with diameters of tens of microns to millimeters. As the Gr lattice orientation follows the crystal orientation of the underlying metal surface during growth, the grain boundaries in the foil will be reproduced in the Gr lattice, decreasing its electrical and mechanical qualities. The only way to overcome these grain boundaries lies in the employment of SC metal growth substrates. The (111) planes of many metals have very small lattice mismatches to Gr (3-4 % for Cu(111), 1 % for Ni(111)), allowing heteroepitaxial growth. As single crystal metals are usually obtained either by crystal growth (like the Czochralski method) or by deposition of thin metal films on oriented inorganic substrates, they are very expensive and of limited size - and thereby not suited for industry-scale production of Gr and even beyond the budgets of many research groups. Hence, the growth on such surfaces was not investigated exhaustively for years. This changed drastically when Jin et al. in 2018 introduced a

---

<sup>8</sup>To reduce the  $\text{CH}_4$  partial pressure, while at the same time keeping a constant  $\text{H}_2/\text{CH}_4$  ratio, one either has to use very precise MFCs or work with a mixture of  $\text{Ar}/\text{CH}_4$  as a precursor.

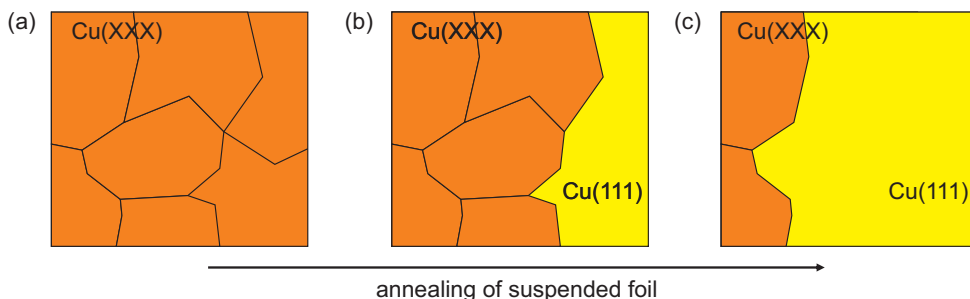


Figure 5.3: **(a)** Schematic illustration of a commercially available polycrystalline Cu(XXX) foil surface as received. **(b) + (c)** Suspending the foils in a long-term annealing process induces the formation of a Cu(111) nucleus on one side of the foil, and the size of this grain gradually extends until the whole foil is turned into SC Cu(111).

colossal grain growth method that can be used to transform standard commercial foils like Cu, Ni, Pt, Pd, as well as alloy foils like Cu-Ni, into SC foils with a homogeneous (111) direction [284]. The polycrystalline foils are suspended in a quartz tube and consequently annealed under  $H_2$  gas flow close to their individual melting points. A schematic illustration of this process is shown in Fig. 5.3. The authors argue that the driving mechanism behind the SC formation is most likely the minimization of the surface energy of the foils, which results from the elimination of stacking folds during the rotation of the pre-existing grains (The (111) plane has the lowest surface energy in an *fcc*-lattice). During normal CVD growth, which is performed also close to the melting point of, e.g. Cu, the surface energy minimization is not the only relevant mechanism at work, but rivaled by the thermal stress building up from the contact points of the foil with the quartz tube - explaining why the formation of a colossal SC surface is not observed there. The suspended mounting of the foils in the reaction chamber, therefore, is the key ingredient, as most of the thermal stress is released. The work of Jin et al. enabled the industry-scale production of (111)-oriented metal foils<sup>9</sup> and likewise enabled the CVD community (or at least the Ruoff group and their collaborators) to further investigate the CVD growth of Gr on SC substrates. Many of the other breakthroughs summarized in this chapter were achieved on such foils, like the ultra-fast growth of meter-sized SC graphene [287] on Cu(111) foil or on Cu-Ni(111) alloy foils [288], and the growth kinetics on oriented substrates were investigated in detail [289].



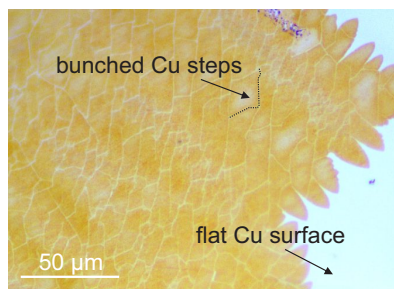


Figure 5.4: Microscope image of a Cu foil partially covered by an MLG crystal grown by CVD. The Gr-covered areas show a network of bright lines corresponding to steps in the Cu surface. No such steps are visible on the bare Cu surface.

## Step Bunching

Despite various extensive pre-treatments of the catalyst foils and the annealing process of the foils near the melting point of Cu, a rough Cu surface is typically found underneath the Gr after growth, while uncovered Cu areas remain almost atomically smooth [291–296]. Upon closer inspection, this roughness mainly consists of steep steps in the Cu surface that, depending on the Cu surface facet, growth parameters, and the number of Gr layers on top, range from 3 to 50 nm. Considering that a single atomic step in Cu(111) has a height of around 0.21 nm, this implies that these macro steps are 15 to 250 times higher. This phenomenon is called *step bunching* (SB). An optical image of a step bunching network is shown in Fig. 5.5. These steps were originally attributed to the large mismatch between the thermal expansion coefficients of Cu ( $\alpha_{\text{Cu}} \approx 2 \cdot 10^{-5} \text{K}^{-1}$ ) and the negligible, and even negative, one of Gr [297], which, upon cooldown from the growth temperature to ambient conditions, would induce a compressive strain of  $\approx 2\%$  in the Gr. However, a comprehensive investigation by Yi et al. provided evidence that compressive strain is not the driving mechanism behind SB, as the strain of Gr crystals manually transferred onto Cu foils, followed by subsequent heating cycles, did not change, although SB took place underneath the Gr [290]. Instead, the step bunching of singular or smaller steps into macro steps in the Cu surface is proposed to be based on two ingredients: temperature-activated fast diffusion of Cu ad-atoms beneath the Gr and a driving force that makes the agglomeration in a single macro step energetically more favorable. This driving force lies in the bending of the Gr sheets at the steps. For multiple singular steps, the Gr sheet has to bend more often than for one big step in the Cu surface. Furthermore, with an increasing number of Gr layers, the corresponding energy gain in the reduction of steps increases, such that the average bunched step height should also increase, which is in agreement with evaluations of CVD-grown bilayer and trilayer Gr on Cu

<sup>9</sup>Which also resulted in valuable patents claimed by Jin and Ruoff [285, 286].

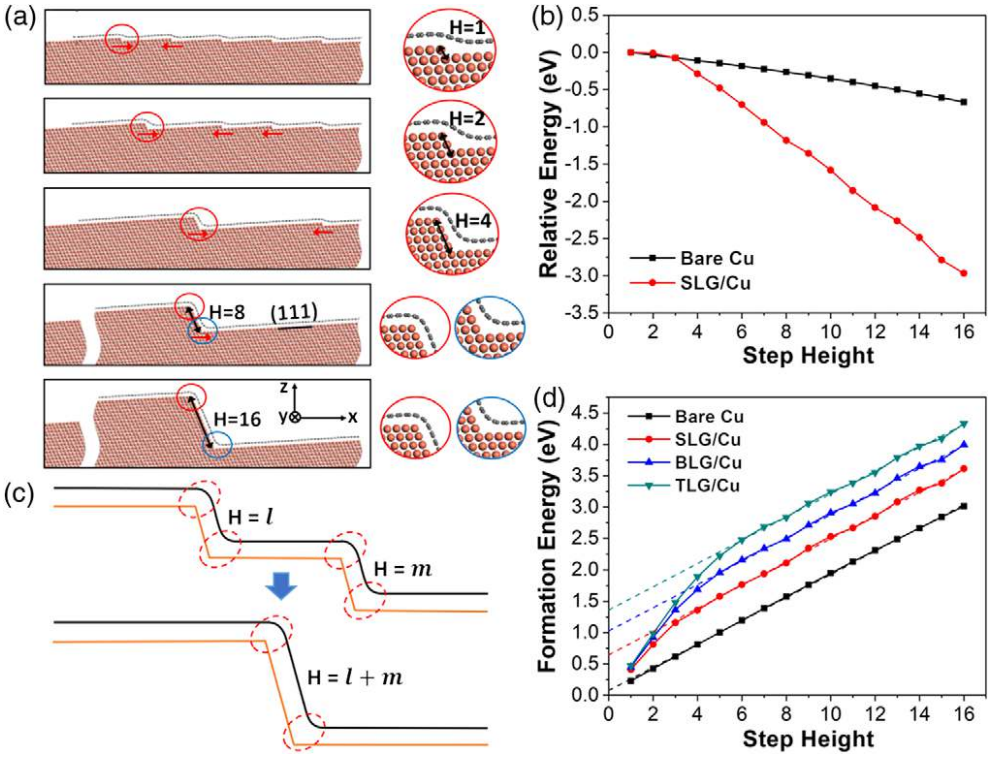


Figure 5.5: **(a)** The process of the Cu(111) surface SB beneath a Gr layer. A series of schematic images from top to bottom showing the increase in height of the highest step in each configuration, marked by black arrows with  $H = 1, 2, 4, 8$ , and  $16$ . **(b)** The relative energy variation of bare Cu (black line) during the SB process. **(c)** Schematic illustrations showing the different ways of bending the Gr overlayer during the SB process. **(d)** Formation energies of bare Cu (black line), Cu covered by single-layer Gr (SLG, red line), bilayer Gr (BLG, black line), and trilayer Gr (TLG, green line) as a function of step height. Reprinted with permission from [290] ©2018 by the American Physical Society.

foils [290]. A schematic illustration of the SB process together with calculations of the relative energy and a formation energy as a function of step height are shown in Fig. 5.5. While in the standard polycrystalline Cu foil, the SB manifests in a network of randomly connected steps, the CVD growth on large Cu(111) surfaces leads to centimeter-long, parallel steps that are distanced up to  $50 \mu\text{m}$  [279]. Furthermore, the phenomenon of SB is not limited to Gr, but should be a general side effect of 2D material growth on metal foils. The only ways to avoid SB lie in avoiding any

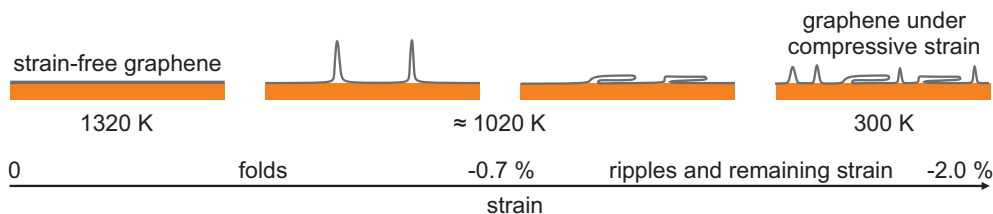


Figure 5.6: Schematic illustration of a possible folding mechanism of the Gr during the CVD process. After the growth stage, the Gr is strain- and fold-free. Upon lowering the temperature, the induced compressive strain increases until at  $\approx 0.7\%$  the so-created wrinkles in the Gr sheet fall over, resulting in folds. At room temperature, these folds remain present together with further wrinkles. Adapted from [298].

initial steps on the Cu surface, as well as in reducing the growth temperature, as the diffusion of ad-atoms is then exponentially reduced.

## Folds and Wrinkles

The aforementioned SB leads to the formation of wrinkles and folds in the overlying Gr sheet. The underlying mechanisms could be nicely studied for the highly ordered fold formation during the epitaxial growth on Cu(111) [299]. Upon cooldown, the mismatch in the expansion coefficients leads to the formation of tall wrinkles on top of the bunched Cu(111) surface steps, which fall over, partially fracture, and bind to the Gr surface. A schematic illustration of the fold formation upon decreasing temperature or likewise increasing compressive strain on the Gr sheet is shown in Fig. 5.6. The experimental findings are supported by molecular dynamics simulations of the induced von Mises<sup>10</sup> stress as a function of the compressive strain, which yield a fracture strength of  $\approx 70$  GPa for MLG, while folds in BLG might twist or doubly fold, but never show fractures in their structures. Although the authors mention several worthwhile transport experiments that could be performed with the highly ordered folds of MLG on Cu(111) [300–302], the folds in general remain an obstacle to be overcome for the scalable production of MLG.

A breakthrough in that field was recently reported by Wang et al. in Ref. [298], where they showed the growth of SC, large-area, fold-free MLG on Cu-Ni(111) alloy foils (with 20.0 at.% Ni). Using an alloy instead of pure Cu(111), as well as employing ethylene instead of methane as a carbon precursor, allowed them to grow Gr at temperatures below the onset threshold of excessive step bunching, which for their

<sup>10</sup>Named after the Austrian mathematician Richard von Mises (1883–1953), who should not be confused with his brother, the famous economist and sociologist Ludwig von Mises, whose works were touched upon in Chapter 1.

system was at  $\approx 757^\circ\text{C}$  (1030 K). Alloys might therefore be a deciding factor in the future success of large-scale synthesis of high-quality Gr.

In summary, step bunching and the formation of folds and wrinkles are challenges that need to be addressed for the scalable production of high-quality graphene. Understanding the underlying mechanisms, as well as exploring alternative growth methods and materials, such as alloys, can help in overcoming these obstacles and pave the way for the large-scale synthesis of graphene and other 2D materials.

## Adlayers

Another bothersome side effect, which can be traced back to the catalyzing metal foil, is the growth of additional layers (*adlayers*) on otherwise MLG crystals. The presence of such adlayers is mentioned in the great majority of CVD-Gr related publications and, thereby, poses an important challenge that needs to be overcome on the road to industry-ready growth processes. To decrease the number of adlayers, the influences of surface roughness and cleanliness, the crystal orientation of the growth substrate, and the growth parameters (like methane to hydrogen ratios) have been investigated. Electro-polishing Cu foils before growth removed up to 95 % of adlayers [303], while similar effects could be obtained by oxidizing the Cu foils in air prior to growth, as adlayer feedstocks created by organic contaminants can be removed this way [304]. Moreover, growth on Cu(111) facets generally shows less adlayer growth [305]. The fundamental mechanism behind the formation of additional layers, as well as recipes to prevent it entirely, were discovered only recently [279]. The nucleation of adlayers is facilitated exclusively by carbon atoms that are dissolved in the Cu *bulk* even prior to growth, rather than by surface carbon which enters the foil due to the decomposition of the methane precursor gas which feeds the actual growth of both the initial monolayer and the adlayer. The bulk carbon is present in most commercially available Cu foils and is introduced most likely from oils used on rollers during the manufacture, explaining why this phenomenon is observed so widely across the CVD community. By removing bulk carbon from the as-received Cu foils through long annealing in  $\text{H}_2$  and Ar, or by using foils transformed into large single-crystal Cu(111) prior to growth (see above), the authors were able to decrease the adlayer content to zero.

## Growth Within Sapphire/Cu(111) Interfaces

In the introduction to this chapter, it was already mentioned that direct growth on insulating substrates is far behind the growth on foils in most commonly accepted measures of quality [306]. For example, in Ref. [307], an oriented sapphire substrate was annealed under high temperatures.  $\text{H}_2$  flow was acting as an etchant to reconstruct the surface into Al-rich terraces that could then catalyze methane decomposition and subsequent Gr growth. Wafer-scale growth of poly-crystalline Gr was achieved this way with mediocre carrier mobilities. However, very recently, a process was developed that allows the direct growth on sapphire substrates, combining many of the discussed

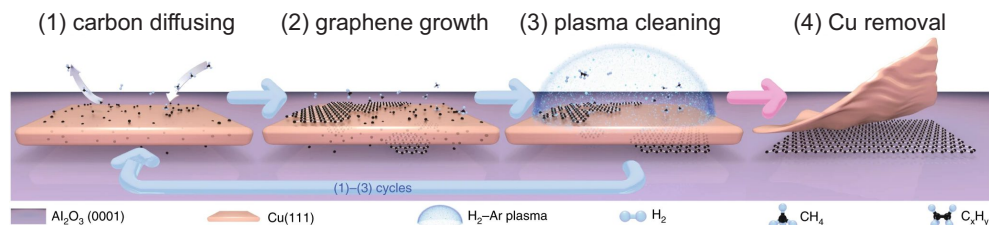


Figure 5.7: Schematic illustration of Gr growth during plasma-enhanced CVD on sapphire/Cu(111) interfaces. A Cu foil is bonded onto a sapphire surface and annealed into a Cu(111) single crystal.  $\text{CH}_4$  dissociates at the upper Cu surface, partially diffuses into the Cu foil, and forms MLG on both Cu surfaces. In a plasma cleaning step, the MLG on the upper surface is removed to allow further carbon diffusion to the sapphire/Cu(111) interface. Finally, the Cu foil is removed by a dip in liquid  $\text{N}_2$ , followed by rapid heating. Reprinted with permission from [280] ©2022 Springer Nature Limited.

techniques and resulting in wafer-scale SC ultra-flat MLG [280]. A schematic illustration of this growth process is shown in Fig. 5.7. A poly-crystalline  $25\ \mu\text{m}$  Cu foil is electro-polished and subsequently fused onto an  $\text{Al}_2\text{O}_3(0001)$ -substrate. Next, the Cu foil is long-time annealed under  $\text{H}_2$  flow into a Cu(111) SC. While the upper Cu-side shows the usual surface steps (that eventually bunch after Gr growth), the Cu(111) at the interface to the sapphire substrate is atomically smooth. During the following growth step, carbon atoms from the decomposed precursor gas enter the Cu layer and partially diffuse through it to the sapphire/Cu(111) interface, initiating Gr growth both within the interface and on the top side of the Cu. As the growth on the top side is much faster than within the interface, a closed layer of Gr eventually seals off the Cu from absorbing more carbon species that could facilitate interface growth. Therefore, the growth process is paused several times, and an  $\text{O}_2$ -plasma is ignited, which removes the top side Gr entirely. After a couple of such cycles, the whole interface area of a  $2''$ - $\text{Al}_2\text{O}_3(0001)$  wafer is covered by monolayer Gr. In contrast to the top side, the Gr does not grow epitaxially with the Cu(111) surface but aligned with the super-lattice potential that results from the  $\text{Al}_2\text{O}_3(0001)$  and the Cu(111). The Gr is adlayer- and fold-free and grows into an SC. The second major breakthrough of this work lies in their ingenious method of removing the Cu(111) foil: The as-grown substrate is immersed in liquid nitrogen for several minutes and subsequently transferred within seconds to a chamber heated to  $500\ ^\circ\text{C}$ . Afterwards, the Cu foil looks crumbled and can be removed by tweezers, leaving the MLG on the  $\text{Al}_2\text{O}_3(0001)$  substrate<sup>11</sup>. The authors argue that small amounts of liquid nitrogen

<sup>11</sup>It is very worthwhile to watch the schematic videos showing the plasma-enhanced growth and liquid nitrogen-induced separation of the Cu foil in the supplementary materials of <https://www.nature.com/articles/s41563-021-01174-1>

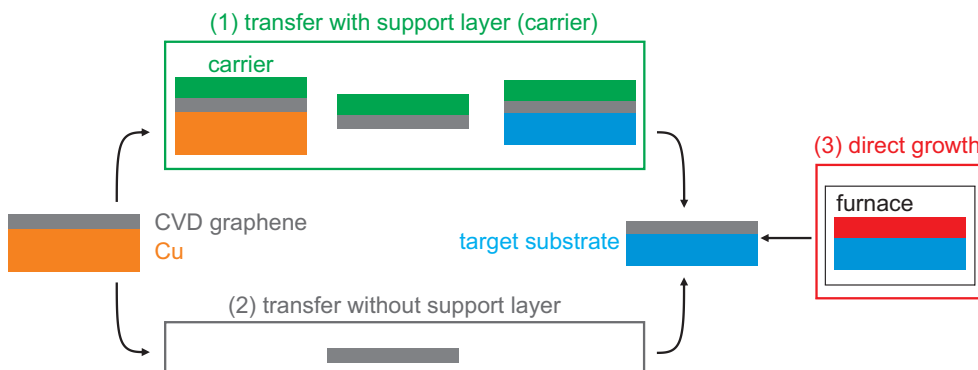


Figure 5.8: Schematic illustration of the three possible transfer strategies possible for CVD-Gr. (1) is the transfer using a support (carrier) layer like the commonly wet transfer employing PMMA membranes or the dry transfer method. (2) summarizes transfer processes without a carrier and (3) all methods, which grow Gr directly on the target substrate from a precursor (indicated in red).

enter the Gr/Cu(111) interface and expand upon heating, which then decouples the foil. The Gr shows homogeneous carrier mobilities of around  $10^4 \text{ cm}^2/(\text{Vs})$  at room temperature, which is very good for Gr on a bare substrate. The authors further state that this process can be adapted to grow BLG, hBN, or to subsequently grow hBN and other 2D materials on top of the initially grown Gr layer. The relevance and potential of these findings cannot be underestimated.

## 5.5 Transfer Methods

As the ultimate goal of all production processes of Gr is to obtain the material on an insulating substrate, a transfer process after the growth stage is required. The three possible transfer strategies are illustrated in Fig. 5.8. The first strategy is the transfer using a support layer (or carrier), the second is the transfer without a carrier, and the third is the direct growth on the target substrate. The fundamental requirements for an ideal transfer process are that it separates Gr from the growth substrate and subsequently moves it onto a target substrate, both without decreasing the intrinsic structural and electronic quality of the material. These processes usually make use of a support layer and can be furthermore grouped into *wet*, *semi-dry*, and *dry* transfers depending on which chemicals are involved.

The role of the support layer is to ensure the structural integrity of the Gr once it is separated from the growth substrate, as metal-etching agents might otherwise crack the vulnerable sheets due to their strong surface tension. An ideal support layer does not by itself degrade the quality of Gr, is flexible enough to allow lamination, and

can easily be removed without residues after the transfer is finished. Among the most widely used support layers are polymers like poly-methyl-methacrylate (PMMA), but there were also several reports of organic or metallic support layers that were successfully employed to transfer CVD-Gr [272, 308]. The adhesion between Gr and a carrier polymer is proportional to the surface energy as described by the modified Hertz theory [309]. The surface energy of the polymer furthermore plays a crucial role in the amount of residues, cracks, and folds that are created in Gr. A lower surface energy results in a weaker binding force and subsequently easier detachment of Gr with fewer residues. However, a finite amount is still required to allow conformal contact of Gr, resulting in fewer cracks and folds after transfer. A typical PMMA transfer is illustrated in Fig. 5.9(a) and consists of the following stages: (i) spin-coating and baking of PMMA on top of the metal/Gr, (ii) floating of the metal/Gr/PMMA on top of an etching agent until the metal is fully removed, (iii) "fishing" of the floating Gr/PMMA membrane with the target substrate and subsequent lamination to its surface, e.g. by heating, and finally (iv) the removal of the PMMA by solvents like acetone and isopropyl alcohol (IPA). The stages of this transfer could be similar for any kind of substrate metal and support layer with modifications only in the involved chemicals. Although this method is scalable and shows good reproducibility, it is very cost-intensive as the growth substrate is completely dissolved<sup>12</sup>. Moreover, the quality of the derived Gr is impacted, as the different thermal expansion coefficients of Gr and polymers tend to introduce cracks and folds and as the PMMA tends to leave small residues that are hard to remove. Spin-coated PMMA on Gr can be divided into three categories, namely (i) thick PMMA layers with disordered structures facing the air, (ii) PMMA with almost 2D characteristics in direct contact with Gr, and (iii) thin PMMA layers between (i) and (ii) - of which only (i) is fully dissolved by an acetone treatment [281]. Different polymers or substances have been tested to overcome these shortcomings of PMMA, the most recent of which is the use of paraffin wax at temperatures not exceeding 40 °C [310]. Alternatives to the etching of the metal substrate lie in the so-called bubble transfer, where either O<sub>2</sub> bubbles are transferred into the Gr/metal interface [311] or H<sub>2</sub> bubbles are created right at the interface electrochemically [312]. In both cases, this results in the detachment of the Gr/support membrane from the metal surface. Most crucially, the growth substrates can be recovered and used for re-growth, which dramatically decreases the production costs. As liquid chemicals get into direct contact with the Gr during both the removal of the metal substrate and the support layer in the processes described above, they are classified as a *wet* transfer processes. Alternative support layers like thermal release tape allow their detachment from the Gr on the target substrate only by increasing the temperature and without involving any further chemicals [294]. This is very relevant for scalable manufacturing, like the already demonstrated roll-to-roll process in [294], as well as for any target substrate, that is sensitive to water or any

---

<sup>12</sup>In order to produce 1 g of Gr, one would need around 300 kg of the commonly used 25  $\mu\text{m}$  thick Cu foil [296].

other chemical involved in removing the support layer. Such transfers can be called *semi-dry*<sup>13</sup>.

The first fully *dry* transfer, where the transferred Gr does not get into direct contact with any solvents was reported by Banszerus et al. in 2015 [8] and is illustrated in Fig. 5.9(b). The authors used exfoliated hBN crystals on top of a polymer stamp to directly pick the Gr up from the growth substrate (Cu foils). This process only relies on the van-der-Waals forces between Grand the hBN being greater than the binding energy of the Cu/Gr interface. The resulting hBN/Gr heterostructure can be laminated onto arbitrary substrates (e.g. another hBN crystal on SiO<sub>2</sub>). The details of this process as applied within this work can be found in Chapter 6. This process combines several advantages, like the re-usability of the growth substrate together with the contamination-free nature of the dry pick-up and the quality-enhancing properties arising from the use of hBN crystals, which manifest in the outstanding electronic properties reported in [? ]. A crucial success factor of the dry-transfer lies in the weakening of the Cu/Gr interface. It can be attained by the oxidation of the Cu in the interface, as naturally occurring on the Cu foils after several days post-growth in ambient conditions. As this process is crucial for the success of the dry transfer and as ambient conditions sometimes do not suffice (see Chapter 6), we will briefly recap what is known about the interface oxidation on Cu so far.

## 5.6 Copper Oxidation

A variety of compounds can be formed by different pathways from Cu and O, including CuO, Cu<sub>2</sub>O, CuO<sub>2</sub>, and Cu<sub>2</sub>O<sub>3</sub>. The predominance of each of these compounds depends on the temperature, atmosphere, and potential reaction agents present at the Cu surface - such as Gr. When a clean Cu surface is heated within an atmosphere of pure O<sub>2</sub>, layers of Cu<sub>2</sub>O start to form from  $\approx 150$  °C on, while above 320 °C mainly CuO is formed [313]. The oxidation process can be monitored optically by the gradual color change from bright orange to darker orange. When repeating a similar heating process with partially Gr-covered Cu foil, we notice immediately that the Cu areas underneath the Gr remain bright and shiny. The Gr acts as a barrier for the O<sub>2</sub> molecules and therefore protects the surface underneath it from direct thermal oxidation. Oxygen species can enter the interface only via the Gr edges or partially through nucleation sites [314].

The situation changes considerably when the atmosphere hosts a finite humidity. As mentioned before, Cu foils with isolated Gr flakes on their surface under ambient conditions show only a very slow oxidation of the bare Cu surface with time, while the Cu underneath the Gr is gradually oxidized, starting from the edges and continuing towards the flake center until the whole Gr-covered area is oxidized. Optically,

<sup>13</sup>In reviews like [272, 308] such processes are classified as *dry*, which is very misleading, considering the existence of truly dry transfers like the one applied within this work.



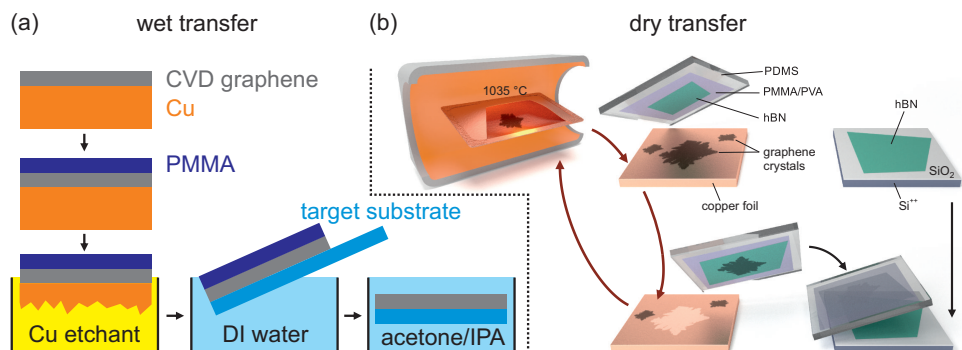


Figure 5.9: Schematic illustrations of support layer based transfer processes. **(a)** Commonly used wet transfer process. The Cu foil with the as-grown Gr on top is spin-coated with a PMMA layer and subsequently the Cu is dissolved in a suitable etchant. Afterwards, the Gr/PMMA stack is fished with the target substrate and finally, the carrier is removed in acetone and IPA leaving the Gr on the target substrate. **(b)** Dry van-der-Waals pick-up process, that uses hBN crystals on top of a PVA/PMMA membrane to directly peel the Gr sheet from the Cu surface. The hBN/Gr half-sandwich can subsequently be placed on arbitrary substrates like another hBN crystal avoiding the direct contact of the Gr with any chemicals. Reprinted with permission from [8] ©2015 American Association for the Advancement of Science.

the contrast manifests in the opposite way as before - the Gr-covered areas appear dark on the bright bare Cu surface. The underlying mechanisms of this adverse oxidation were investigated in detail for the first time in [296]. Using isotopically labeled H<sub>2</sub>O and O<sub>2</sub>, followed by Raman spectroscopy and time-of-flight secondary ion mass spectroscopy measurements, the authors proved that the oxide underneath the Gr was formed exclusively from water vapor in the atmosphere. The respective Raman measurements are shown in Fig. 5.10, where panel (a) shows the Raman spectra recorded on the bare Cu surfaces of three different Cu foils, while panel (b) shows the corresponding spectra recorded on Gr crystals grown on the foils. The foils were treated either with regular water and air (black lines), <sup>18</sup>O-labeled water and normal air (red), or <sup>18</sup>O-labeled air and normal water. As the positions of the appearing Raman peaks of the oxides are sensitive to the atomic mass of the oxygen, the incorporation of <sup>18</sup>O leads to shifts away from the reference positions for normal air and water. As can be seen from Fig. 5.10, only the red curves show significant shifts of the oxide peaks. From this, the authors concluded that the oxidation of the Cu/Gr interface is mediated predominantly by water or water vapor. They further showed by XPS measurements that the oxidation occurs in steps, where it starts with Cu<sub>2</sub>O, followed by a metastable layer of Cu(OH)<sub>2</sub> on top of the Cu<sub>2</sub>O, and

finally ends with a transition of the  $\text{Cu}(\text{OH})_2$  to a more stable  $\text{CuO}$  layer [296, 315]. In this, the Gr plays the role of a chemical reaction agent. It dissociates the  $\text{H}_2\text{O}$  molecules at the crystal edge, and the oxygen species can subsequently enter the interface and gradually contribute to its oxidation. During this process, the Gr edge gets functionalized, which can be visualized by the sudden appearance of a Raman D-peak in the edge region. The crystal orientation of the Cu surface plays an important role in the speed of the oxidation process, as the oxygen species can only penetrate interfaces that are not too strongly coupled. This can be nicely visualized by the adverse oxidation contrast on Cu sub-grains [316], and the oxidation capabilities together with interface strength were investigated as a function of the Cu surface orientation [317, 318]. Quite recently, the water-mediated oxidation of SC Gr/Cu(111) was investigated [315], where the authors found that such strong interfaces can only be penetrated by oxygen species via the bunched Cu steps (see above). When these steps are avoided, and the Cu surface is ultra-flat, the oxidation is completely quenched.

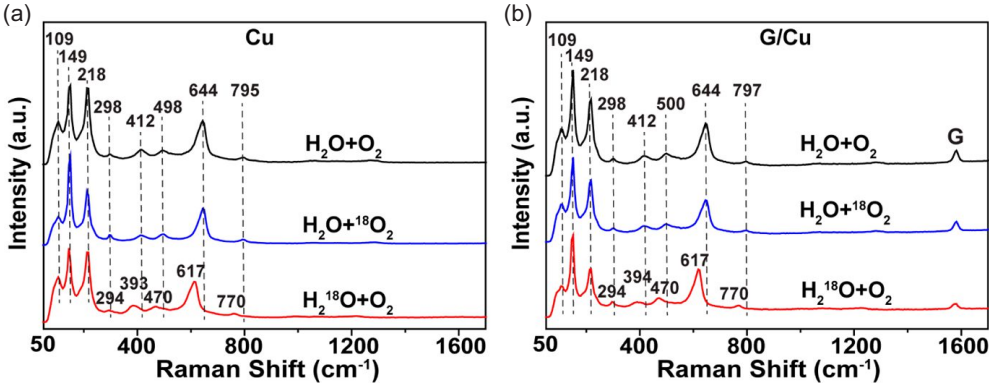


Figure 5.10: (a) Raman spectra of bare Cu foils post growth. (b) Similar spectra on an MLG sheet grown on the respective foils. The foils were treated with  $^{18}\text{O}$ -labeled water and  $^{18}\text{O}$ -labeled oxygen gas. Reprinted with permission from [296] ©2017 American Chemical Society.

## 5.7 CVD Growth of hBN and Bilayer Graphene

For the sake of completeness, we will briefly review the state-of-the-art in the CVD growth of hBN and bilayer graphene (BLG), although neither of them are used within this thesis.

As hBN is used as an insulating substrate material, growing only one layer of polycrystalline material is usually not desirable for applications. For many years, however, hBN growth was limited to small-grain-sized monolayers or rough multilayers with varying numbers of layers, which were not feasible for the production of high-quality heterostructures. The advent of large-scale single-crystal (SC) substrates (see above) at least led to the growth of SC monolayer hBN on Au(111), Cu(111), and Cu(110) [319–321]. A major breakthrough was reported very recently in [322]. The authors demonstrated the uniform SC growth of trilayer hBN on single-crystal Ni(111) for the first time. The growth mechanism on Ni works by the dissociation of borazine gas, followed by the B species dissolving into the Ni surface. hBN islands subsequently nucleate and grow epitaxially on the Ni(111) surface. The growth was shown to be surface-mediated rather than precipitation-mediated. Excess B species in the Ni bulk fall out as a  $\text{Ni}_{23}\text{B}_6$  layer underneath the as-grown hBN. The authors mentioned that, depending on the parameter windows, up to 5 layers could be grown as a single crystal. Combined with a reasonable transfer process, a couple of these crystals stacked on top of each other could already suffice for high-quality heterostructure production. Further breakthroughs in the near future are highly likely.

Meanwhile, the growth of BLG as adlayers on initial monolayers has been observed since the beginnings of the CVD-Gr research, and their favorable growth conditions and mechanisms have been investigated [276, 323–325]. While on the scales of tens of microns, these CVD BLG crystals were shown to achieve similar qualities as their top-notch exfoliated counterparts [326], on larger scales, the formation of AB/BA stacking domain walls precluded the large-scale exploitation of the tunable bandgap, which can be induced in BLG via dual-sided gating. Therefore, a challenge for the CVD growth of BLG remains in achieving single-crystal material with homogeneous stacking throughout. Quite recently, some promising advances were made by the growth of large-area SC AB-bilayer and ABA-trilayer Gr in [327], where the authors used Cu/Ni(111) alloy substrates that, depending on the Ni content, favored the growth of two or three layers of Gr. For the growing field of twistronics, it is worthwhile to mention the works in [328, 329], which achieved the growth of twisted BLG with varying twist angles either by hetero-site nucleation as well as by folding Cu(111) foils.

## 5.8 Summary

Over the past decade and a half, there has been a tremendous amount of research done on CVD growth of graphene on copper foils. With new publications being submitted every day, it can be a challenge to review this field in a comprehensive way. In this chapter, we have covered the fundamental growth mechanisms and the main challenges in producing scalable high-quality material.

The most notable advancements in CVD graphene growth include the development of technology to obtain single-crystal substrates from polycrystalline foils and the use of Cu/Ni alloys instead of mono-metallic substrates for fold-free, adlayer-free growth of single-crystal monolayer and multilayer graphene, as well as for growing high-quality hBN. Additionally, significant improvements have been made in the transfer of as-grown materials to target substrates, and wafer-scale production of high-quality graphene heterostructures is now within reach. This marks the maturing of graphene to a stage where its unique properties can be exploited in commercial applications.

Despite the fact that decent carrier mobilities can already be achieved in CVD graphene, a significant fraction of the research community remains in doubt about whether the intrinsic quality of CVD graphene can truly equal that of the highest-quality exfoliated reference material. Contamination and disorder, introduced either by the remaining growth substrate atoms or during the transfer process, might lead to a cut-off in the high-end capabilities of the resulting graphene crystals, which are not reflected in Raman measurements or carrier mobility extractions. Therefore, the only pragmatic way to prove the equivalence of intrinsic qualities lies in demonstrating that the same high-end phenomena known from exfoliated graphene are also achievable in CVD graphene. Hence, one of the main goals of this thesis is to demonstrate the FQHE in dry-transferred CVD graphene heterostructures. Having covered all the details of CVD growth and transfer of graphene in general, we can move on to the actual fabrication processes and improvements made to them, necessary to obtain hBN/CVD-Gr/hBN heterostructure devices of the highest possible quality.



## Chapter 6

# Fabrication of High Quality CVD Graphene Devices

This chapter has been published in parts in:

**Fractional quantum Hall effect in CVD-grown graphene**

**M. Schmitz**, T. Ouaj, Z. Winter, K. Rubi, T. Taniguchi, K. Watanabe, U. Zeitler, B. Beschoten and C. Stampfer

2D Mater. **7**, 041007 (2020) (or: arXiv: 2005.08938)

©2020 IOP Publishing Ltd

**Individual contributions:**

C.S., M.S. and U.Z. conceived the experiment. M.S. fabricated the sample with the help of Z.W. and T.O.. M.S. performed the experiments with the help of T.O. and analyzed the data. K.W. and T.T. synthesized the hBN crystals. All authors provided input to data analysis, discussed the results and assisted in manuscript preparation.

### 6.1 Introduction

In this chapter, we describe the techniques and processes used to fabricate high-quality hBN/CVD-Gr/hBN heterostructures. These heterostructures consist of a monolayer Gr crystal sandwiched between two hBN crystals, referred to as the bottom and top hBN, respectively, and are placed on a Si/SiO<sub>2</sub> chip. We begin with a description of the exfoliation method used to obtain hBN crystals, followed by the growth of MLG flakes using our CVD system. We then describe the Raman-monitored oxidation of the Cu/Gr interface, as well as the dry van-der-Waals (vdW) pick-up of the Gr from

the Cu foils and subsequent stacking and cleaning in our transfer system. The resulting hBN/CVD-Gr/hBN heterostructures are characterized using Raman mapping, and structurally sound areas are selected for device patterning. We also include a critical analysis of the changes in CVD growth process parameters, followed by a brief summary.

## 6.2 Exfoliation of 2D Materials

The mechanical exfoliation of 2D materials, also known as the *scotch tape* method, was first introduced by Novoselov et al. in 2004 to obtain MLG [4]. Since then, it has become the standard method for producing high-quality crystals of various 2D materials, including Gr and its multilayers, hBN, and transition-metal dichalcogenides (TMDs).

The method involves placing a bulk crystal of the 2D material onto an adhesive tape, which is then folded and unfolded onto itself. With each fold, the material is distributed further across the tape and thinned out due to the cleaving effect. After a given number of foldings  $n_{\text{folds}}$ , the tape is pressed onto a target substrate for time  $t_{\text{sub}}$  and finally peeled off, leaving a number of individual crystals (or *flakes*) on the substrate surface with wide distributions of diameters and thicknesses. The substrates are then investigated with optical microscopy to find suitable flakes for further device fabrication. The diameter and thickness distributions, which can be interpreted as the *yield* of an exfoliation, depend on many factors, including the morphology of the initial bulk crystal,  $n_{\text{folds}}$ ,  $t_{\text{sub}}$ , the angles and speed of the tape peel-off, and the temperature. Some systematic studies of these influences have been reported [330], but they are always of qualitative character, and universal parameters for desired quantitative exfoliation yields cannot be given. This explains the highly artistic and imprecise nature of the process, as well as the demand for controlled scalable production methods such as CVD (see Chapter 5).

The exfoliation substrates for the top hBN flakes for the dry pick-up of CVD-Gr consist of a glass slide covered by tape and several polymers, which are described below. The standard substrates used for exfoliation of bottom hBN and graphite flakes within this thesis are Si wafers with 90 nm thermally grown SiO<sub>2</sub> layers. This thickness is chosen so that the 2D materials, around their desired respective thicknesses, create favorable color and contrast in the visible optical range. The 4-inch wafers are cut down into several slides in the centimeter range to allow for efficient exfoliation.

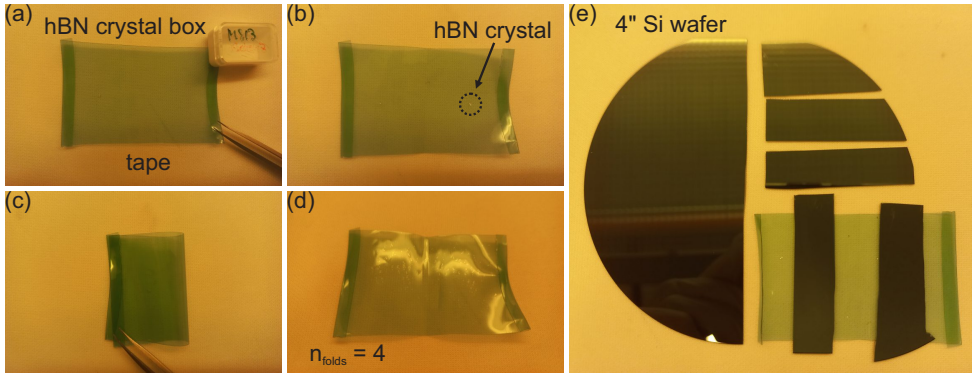


Figure 6.1: (a) Optical image of a typical thermal release tape prepared for the exfoliation of hBN. The tiny bulk hBN crystals are stored in the boxes on the upper right corner of the foil. (b) A single bulk hBN crystal is placed in the middle of one side of the tape (highlighted by dashed circle). (c) The tape is folded over several times, each time exfoliating hBN crystals onto different parts of the foil. (d) Homogeneously covered tape after  $n_{\text{folds}} = 4$  foldings ready for the exfoliation onto a substrate. (e) partially cut-down 4-inch Si wafer. The slides on the right side are pressed onto an exfoliation tape and after subsequent peel-off act as initial substrate for the exfoliated 2D materials.

For all the heterostructures fabricated in this work, the hBN was exfoliated from bulk material produced by a high-pressure, high-temperature process in Japan<sup>1</sup> [53]. A typical exfoliation process is illustrated in Fig. 6.1. A single millimeter-sized bulk crystal is placed on thermal release tape (Nitto BT-150P-LC) and homogeneously distributed on the tape surface with an initial set of 4 – 6 foldings, while avoiding overfolding of crystals onto each other as much as possible. This is followed by  $n_{\text{folds}} = 3 - 5$  additional foldings for out-thinning the crystals. Afterwards, the tape is laminated to Si wafer-slides or dry-pick up substrates for  $t_{\text{sub}} = 10$  min, followed by a slow peel-off under a small angle. Such an exfoliation can yield up to  $10^1$  usable hBN crystals per Si wafer slide. Usability in this context means that a given crystal is of a homogeneous thickness of around 10 – 40 nm, has a diameter in the range of 10 – 100  $\mu\text{m}$  (special requirements for flake geometry might apply), shows neither cracks, folds, nor excessive contamination, and is isolated from neighboring flakes. The flake thickness and their optical blue-channel contrast have an almost linear relationship for the substrates used here. Hence, atomic force micros-

<sup>1</sup>This process was developed by Kenji Watanabe (\*1962) and Takashi Taniguchi (\*1959). For over a decade, they intensely researched Gr, 2D materials, and heterostructures, and were the only suppliers of high-quality hBN bulk crystals. Agreements assuring them co-authorships on any publication using their materials helped them become some of the most cited researchers ever [331].



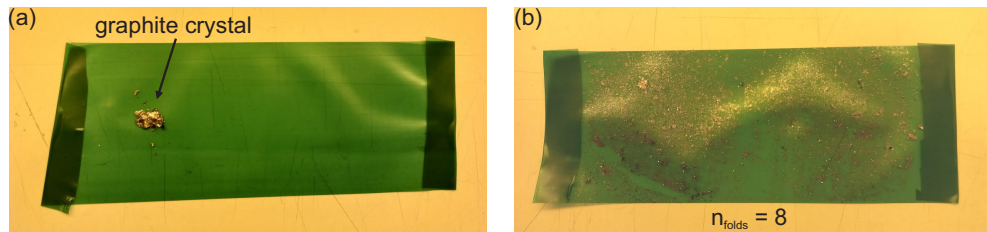


Figure 6.2: (a) Optical image of a thermal release tape prepared for the exfoliation of graphite and Gr crystals. A graphite crystal of several millimeters in diameter is placed in the center of one side of the tape. (b) The same tape after  $n_{\text{folds}} = 8$  foldings, ready for the exfoliation onto substrates.

copy (AFM) measurements of the actual thicknesses of flakes can be used to create a contrast-to-thickness reference table, which can be consulted for judging individual flake thicknesses during microscopic investigation of the substrates.

For the exfoliation of graphite or Gr flakes, bulk crystals of natural graphite (Graphenium Flakes by NGS Naturgraphit) with diameters up to centimeters are placed on thermal release tape (Ultron Systems article No. 1008R) and distributed similarly to the hBN process, followed by  $n_{\text{folds}} = 6 - 10$  and  $t_{\text{sub}} = 5$  min. Optical images of a thermal release tape before and after the preparation for graphite/Gr exfoliation are shown in Fig. 6.2. Optical microscope images of typical hBN, graphite, and Gr exfoliation onto Si/SiO<sub>2</sub> substrates are shown in Fig. 6.3. While hBN crystals below 100 nm appear in shades of blue, graphite flakes appear dark purple with decreasing contrast for decreasing number of layers. On our substrates, a Gr monolayer has a green channel contrast  $\alpha_{\text{Gr}} = 6 - 8$  %, and we found that for small integer numbers of Gr layers  $n_l$ ,  $\alpha_{n_l} = n_l \cdot \alpha_{\text{Gr}}$ , allowing for quick determination of layer number via contrast measurement rather than the more time-consuming Raman measurement (see Chapter 2).

In this work, we focused on thicker graphite flakes of at least 10 nm, which can be utilized as gate electrodes. If such graphite gates are too thin, they might undergo a Landau quantization of their charge carrier system under high magnetic fields, which precludes their gating abilities. Despite that, the requirements for graphite flakes are quite similar to those for hBN flakes as stated above.

### 6.3 CVD Growth of Monolayer Graphene Crystals

The CVD setup used in this work consists of a tube furnace (PI-KEM OTF-1200X-III-C) with three separately controllable heating zones with resistive heating elements, qualifying it as a *hot wall* reactor, with a maximum applicable temperature of 1200 °C. Images of the CVD setup and a close-up of the central heating zone are shown in

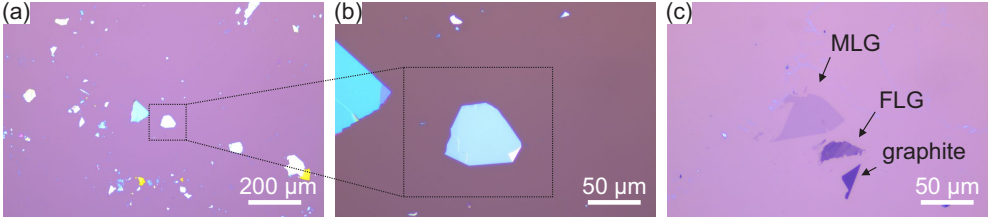


Figure 6.3: Optical microscope images of typical exfoliation results on Si/SiO<sub>2</sub> substrates. **(a)** Overview of an hBN exfoliation. Multiple crystals of various thicknesses (encoded by color and contrast) and dimensions are obtained. Suitable crystals for Gr encapsulation range between 15 nm and 50 nm in thickness. **(b)** Close-up of a suitable hBN crystal from **(a)**. **(c)** MLG, few-layer graphene (FLG), and graphite appear as different shades of gray, eventually turning into purple and dark blue with increasing layer number.

Fig. 6.4. The furnace can be opened via hinges to remove the reaction chamber or to facilitate rapid cooldown. The reaction chamber is a quartz tube 100 cm in length and has an inner diameter of 8 cm. On the upstream side, the quartz tube is connected to a gas mixing station that hosts MFCs for the process gases Ar, H<sub>2</sub>, and CH<sub>4</sub>, while the downstream side is connected to a turbomolecular pump followed by a rotary vane pump. The Cu growth substrates are positioned in the center of the reactor chamber via a small quartz boat that can be moved by a steel rod. The chamber also hosts two heat shields made of Cu, situated at the outer ends of the left and right heating zones, to reduce radiative heat losses.

As a growth substrate enclosures are folded from 25  $\mu\text{m}$  thick poly-crystalline Cu foil (Alfa Aesar 46365, 99.8 %). Therefore, a  $7.6 \times 12$  cm long piece of foil is cut and subsequently cleaned and pre-etched in acetone, IPA, FeCl<sub>3</sub> (Sigma-Aldrich 31233) solution (7 g per 200 ml DI water) and DI water for 2 min each, followed by dry blowing with a nitrogen gun. The foil is then folded in half and the edges are crimped by folding them over two times over a width of 7 mm with a glass slide, yielding an enclosure of  $\approx 4 \times 6$  cm. Optical images of the different stages of the folding process are shown in Fig. 6.5.

The Gr in this work was grown using an LPCVD process with a pre-growth annealing step, as discussed in the following. A process diagram of the reactor temperature as a function of growth time is shown in Fig. 6.6. Two enclosures were loaded into the reaction chamber at once. The quartz tube was closed, and the pumps were started. During the initial evacuation, the enclosures expanded due to the remaining air inside them greatly expanding due to the under-pressure in the chamber. Once the turbo pump ran at full speed, a flow of 15 sccm of H<sub>2</sub> was introduced, and the heating elements were ramped up to 1035 °C over a period of 45 min. The system remained

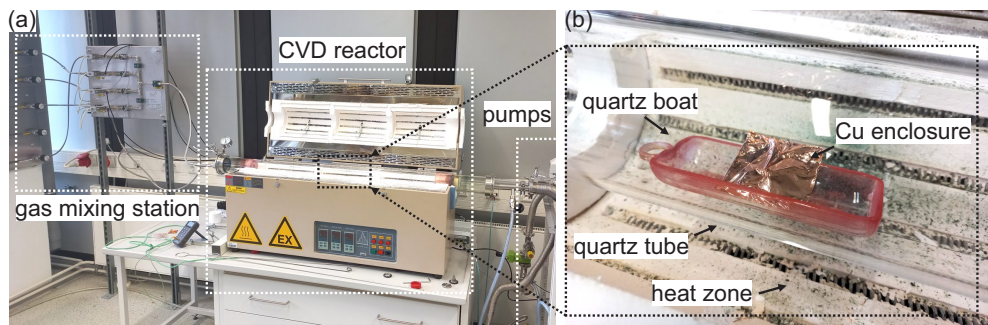


Figure 6.4: **(a)** Overview picture of the CVD setup used in this work. A gas mixing station with MFC units for each process gas is connected to the left flange of the quartz tube in the CVD reactor. The tube sits in a three-zone furnace that can be opened via a hinge mechanism. The right-hand (downstream) side of the quartz tube is connected to a pump rack that consists of a rotary vane pump and a turbo molecular pump. At both sides of the tube, close to the flanges, movable heat shields made of Cu plates limit radiative heat losses to the outside and the flanges. **(b)** Close up of the quartz tube in the central heating zone of the furnace. For a growth process, one or two Cu enclosures are loaded into a quartz boat and moved to the center of the heating zone.

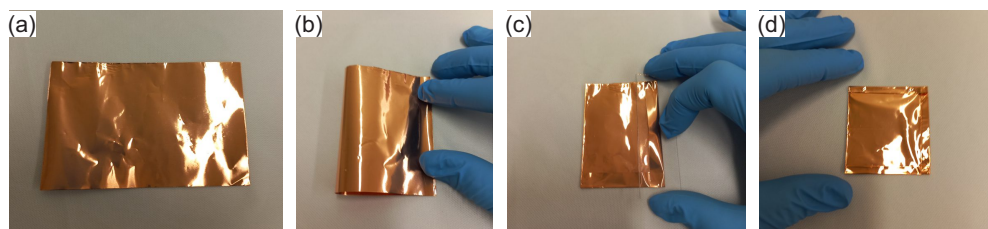


Figure 6.5: Optical images of the enclosure folding process. **(a)** A rectangular piece of Cu foil is cut and subsequently cleaned and pre-treated with different chemicals. **(b)** The foil is folded along the short side. **(c)** the edges are folded over twice using a microscope slide. **(d)** Final enclosure ready for CVD growth of Gr crystals on the inside.

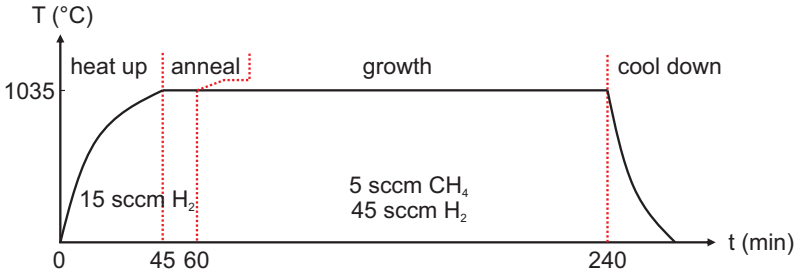


Figure 6.6: Reactor temperature  $T$  as function of process time  $t$  for a typical LPCVD process used in this work. The first four consists of a heating up and annealing the Cu enclosures under  $H_2$  flow, followed by a 3 h growth stage and subsequent cool down under combined  $H_2/CH_4$  flow.

at the target temperature with an unchanged gas flow for 15 min as an annealing step prior to growth, to reduce contamination and Cu bulk carbon content and to increase the Cu grain size. For the growth stage, a mixed flow of  $CH_4$  and  $H_2$  (5 sccm and 45 sccm, respectively) was injected over a growth period of three hours. Afterwards, the system was rapidly cooled down under an unchanged gas flow by switching off the heating elements and subsequently opening the lid of the furnace. Once the temperature was under  $100^\circ C$ , the process gasses and the turbo pump were switched off, and the chamber was slowly flushed with Ar gas. Upon flushing, the enclosures deflated again as the under-pressure vanished.

## 6.4 Forced Interface Oxidation

After growth, the enclosures are removed from the reactor chamber, cut open along the crimped edges, and unfolded. Using dark-field optical microscopy [293], the individual Gr crystals on the foils can be investigated. Fig. 6.7 shows a bright field and a dark field microscope image of a Cu foil after a 24 h growth process. While the contrast of the Gr flakes is hardly visible in the bright field image, they become easily recognizable in the dark field image, even revealing several aligned adlayers underneath the initial monolayer crystal. The outside of the enclosure is fully covered with a closed layer of MLG and multiple adlayers, while on the inside, due to the reduced  $CH_4$  partial pressure, both the nucleation density and the growth speed are low enough to produce isolated MLG crystals with sizes around  $200\ \mu m$ .

During the development of our dry-transfer process, in which parts of our CVD system were installed in a provisional way<sup>2</sup>, storing the unfolded enclosures under ambient conditions for at least one full day was usually enough to induce Gr-mediated

<sup>2</sup>The process gas bottles were stored inside the lab and connected via hoses to the gas mixing station.

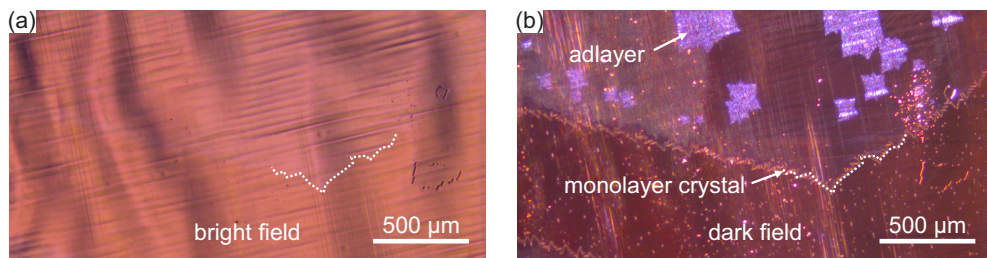


Figure 6.7: **(a)** Bright field microscope image of a Cu foil after growth. **(b)** Dark field microscope image of the same foil revealing a huge MLG crystal with several aligned adlayers underneath it. Parts of the monolayer crystal contour are highlighted by a dotted line in both images.

oxidation - i.e., rapid oxidation of the Cu/Gr interface, while the uncovered areas of the Cu foils remained unchanged (see Chapter 5.6). However, after upgrading our CVD lab<sup>3</sup>, we noticed two changes in the process: (i) to achieve similarly sized MLG crystals as before inside the enclosures, the gas flow had to be increased from 1.3/45 sccm  $\text{CH}_4/\text{H}_2$  to the above stated 5/45 sccm. (ii) even after weeks stored under ambient conditions, the Cu/Gr interfaces did not show complete oxidation. While (i) could be overcome by adjusting the gas flows, (ii) became a severe problem, as the success of our dry-transfer depends crucially on the weakening of the Cu/Gr interface by its oxidation.

The oxidation problem could finally be resolved by building a Cu foil storage chamber (which we called the *humidifier*) with controllable atmosphere. To this end, a desiccator with a water reservoir at the ground and a stage for the Cu foils was mounted on top of a hot plate. The temperature and humidity inside the chamber could be monitored via respective sensors. After at least 48 h at > 99 % relative humidity and temperatures around 30 °C, most of the Gr crystals showed oxidized interfaces underneath them again<sup>4</sup>. Optical images of Gr flakes on Cu foil with partial and fully oxidized Cu/Gr interfaces, as well as of the humidifier setup, are shown in Fig. 6.8.

To further monitor and study the progression of the oxidation, a blue (457 nm) laser was added to our confocal room-temperature micro-Raman system. A standard Raman laser excitation wavelength of 532 nm (green) cannot be used to characterize Gr on copper as it creates a broad photoluminescence (PL) emission peak from the underlying Cu, which dominates the emission spectrum [332]. When using the shorter

<sup>3</sup>The gas bottles were moved to a cabinet outside the building and all hoses were replaced by metal capillaries.

<sup>4</sup>A discussion of the reasons behind occurrence and resolving the issues will be given in Chapter 6.9



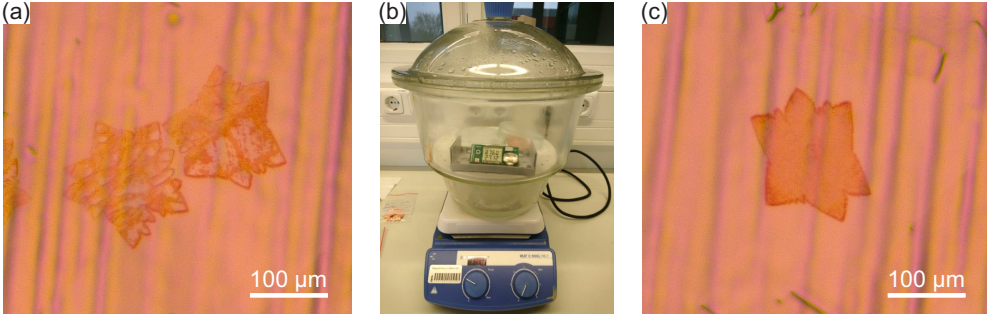


Figure 6.8: **(a)** Optical image of Gr crystals on a Cu foil with partially oxidized Cu/Gr interfaces. **(b)** Humidifier setup that was developed to store the Cu enclosures in a heated high humidity atmosphere after growth. It consists of desiccator partially filled with water, that is placed on a hot plate. The foils are stored on a stage and covered by a glass dish to avoid precipitation of water. **(c)** After sufficient time in the humidifier, the interfaces of most flakes could be oxidized homogeneously.

excitation wavelength, the PL emission from the Cu is shifted to larger wavenumbers, thereby allowing to analyze all relevant Raman peaks up to  $3000\text{ cm}^{-1}$ . The water intercalation and oxidation process can thus be monitored as shown in Fig. 6.9(c). Raman spectra recorded at the oxidized and non-oxidized areas (black and red spectra in Fig. 6.9(c), highlighted by color matching circles in Fig. 6.9(a)) show both the characteristic Gr Raman G and 2D peaks at  $\omega_G = 1582\text{ cm}^{-1}$  and  $\omega_{2D} = 2720\text{ cm}^{-1}$  [66]. The absence of the defect-related D-peak around  $1340\text{ cm}^{-1}$  in the spectra indicates that the Gr is grown defect-free [82] and remains virtually undamaged by the oxidation process. In further comparison of the two spectra, we denote the emergence of a variety of intense peaks visible in the left part of the black spectrum. These peaks can be attributed to Raman-active modes of various Cu oxides formed at the Cu/Gr interface [296, 333], where the three most prominent peaks are due to cupric oxide CuO ( $500\text{ cm}^{-1}$ ), cuprous oxide Cu<sub>2</sub>O ( $640\text{ cm}^{-1}$ ) and copper hydroxide Cu(OH)<sub>2</sub> ( $800\text{ cm}^{-1}$ ) and the less prominent peaks ( $422\text{ cm}^{-1}$ ,  $1284\text{ cm}^{-1}$ ) are overtones of the Cu<sub>2</sub>O mode (see also Chapter 5.6). All these peaks are absent in the red spectrum, which has been taken at a spot where the Cu surface is not yet oxidized.

As the oxidation process proceeds with time and the oxide layer underneath the Gr grows in thickness, the intensity of these peaks relative to the Gr modes rises. The oxidation process in water-saturated air essentially works by the functionalization of the Gr edge by water molecules forming oxygen-containing groups like hydroxyl, which in recombination allow the formation of Cu<sub>2</sub>O [296]. This mechanism allows an advanced quantification of the oxidation status of the Cu/Gr interface in addition to microscope imaging, as the relative intensity of the Cu<sub>2</sub>O peaks rise with ongoing

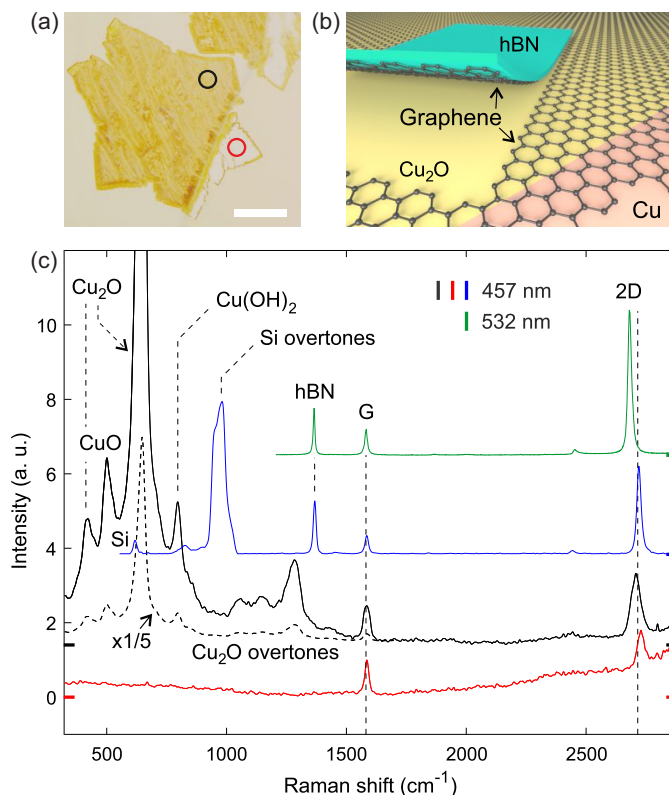


Figure 6.9: **(a)** Optical image of CVD-Gr crystals on a Cu foil after a partially oxidized Cu/Gr interface. Scale bar is 25  $\mu\text{m}$ . **(b)** Schematic illustration of the mechanical delamination process. **(c)** Raman spectra recorded with two different laser excitation wavelengths (457 nm and 532 nm, see color legend) at the locations highlighted by color matching circles (red and black) on the partially oxidized/non-oxidized Cu/Gr areas shown in panel (a) and on a final hBN/CVD-Gr/hBN heterostructure in (blue and green Raman spectra were measured at the circle in Fig. 6.14(a)). The spectra are shifted by constant offsets in intensity for comparability (see colored ticks on the right axis) and the black dashed spectrum is a scaled-down version of the black spectrum.

oxidation. As illustrated in Fig. 6.9(b), the Gr crystal can only be delaminated from the Cu surface oxide by means of a dry transfer technique using a soft stamp based on hBN [8] or other 2D materials [334].

## 6.5 Dry-Transfer of CVD Graphene

Once the Cu/Gr interface is sufficiently weakened, the dry-transfer can be initiated. The principle behind it is similar to the dry stacking of Ex-Gr flakes into heterostructures, where a transparent polymer stamp is used both as a supportive and adhesive substrate for 2D crystals, which subsequently are used to pick up Gr from exfoliation substrates only by van der Waals interaction [51, 57].

The transfer slides for the CVD dry-transfer are fabricated by cutting microscope glass slides (ROTH 0656,  $76 \times 26 \times 1$  mm) in half, cleaning them in acetone and IPA, and subsequently laminating a layer of tape onto their surface (Pritt Klebefilm). In the next step, a solution of poly-(vinyl alcohol) (PVA) (Sigma-Aldrich 363065) in water is drop-coated onto the slides and left to dry out. Afterwards, the slides are spin-coated with 50 K PMMA (AR-P 639.04) and baked out on a hot plate at  $145^\circ\text{C}$ .

The slides are then used as a substrate for hBN-exfoliation. A schematic illustration of the CVD dry-transfer process, as well as several images of the setup and the transfer materials during the different process stages, are shown in Fig. 6.10. The hBN crystals appear in different shades of gray depending on their thickness, which is in contrast to our usual  $\text{SiO}_2$  substrates as shown above. Once a suitable hBN crystal is identified via microscopy, a box section around it is cut with a knife into the polymer stack. The PVA/PMMA-box (the so-called transfer *stamp* or *membrane*) with the hBN crystal on its top surface can then be peeled off from the glass slide using tweezers. Special attention needs to be paid in order not to twist or fold it.

For the actual transfer, an old optical lithography machine is used to align and subsequently bring into contact the transfer stamp with a desired Gr crystal on a copper foil. The transfer stamp rests on the upper part of the mask aligner chamber on top of a polydimethylsiloxane (PDMS) (Gel-Pak 4) cushion, providing adhesion as well as the necessary flexibility, while still being transparent. The Cu foil is marked near the desired Gr flake and cut into a roughly  $5 \times 5$  mm wide piece and placed on the movable lower stage of the mask aligner.

The Cu foil is moved upwards in close proximity to the transfer stamp, while the target hBN-crystal and the Gr flake are inspected by the on-light microscope of the lithography system. The flakes are aligned by moving the Cu foil micro-mechanically until the hBN crystal is situated directly above a promising section of the Gr flake. The Cu foil is then moved upwards again until an interference pattern indicates close proximity to the transfer stamp. The Cu is heated to  $125^\circ\text{C}$  and brought into contact under pressure, and kept in contact for at least 2 min. Afterwards, the heating is switched off, and the stamp/Cu stack is removed from the lithography machine. The hBN crystal on top of the Cu foil can be investigated by optical microscopy again,



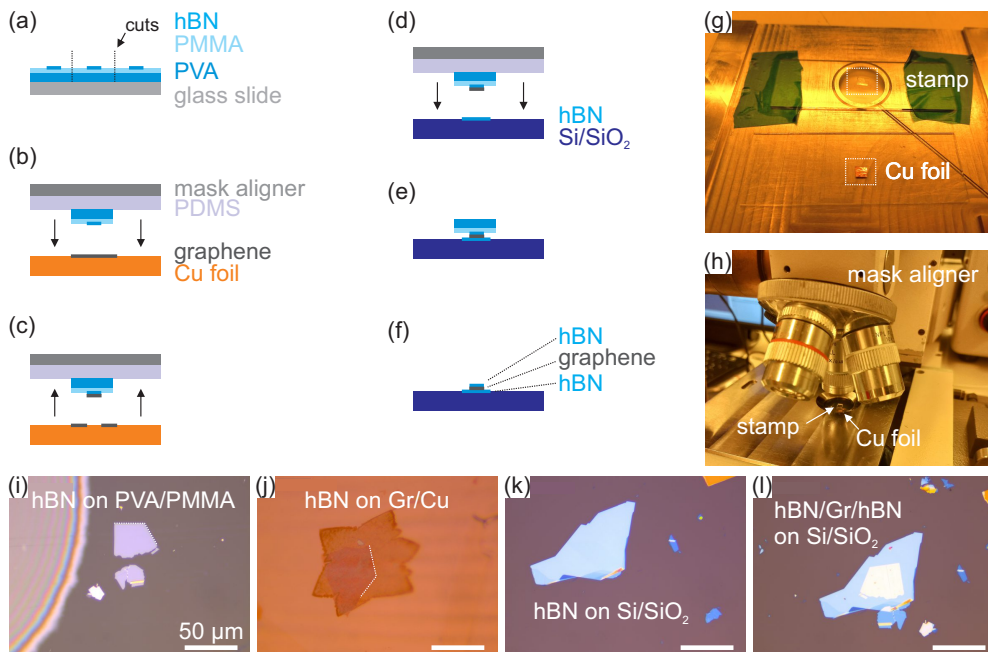


Figure 6.10: **(a)-(f)** Schematic illustration of a typical CVD dry-transfer process. **(a)** hBN crystals are exfoliated onto a PVA/PMMA covered glass slide. Suitable crystals are identified, and a stamp is cut around. **(b)** Such a stamp is then mounted in the mask aligner on a PDMS support layer, aligned, and brought into contact with a Gr crystal on Cu foil. **(c)** Upon detachment, the fraction of the Gr that is in contact with the hBN is peeled off the Cu foil. **(d)** The hBN/Gr half sandwich is aligned and finally brought into contact with another hBN crystal, previously exfoliated onto a Si/SiO<sub>2</sub> substrate and baked. **(e)** Afterwards, the PDMS is removed, and **(f)** the PVA and PMMA polymers are dissolved in hot water and acetone, leaving an hBN/CVD-Gr/hBN heterostructure on the Si/SiO<sub>2</sub> substrate. **(g), (h)** Optical images of an isolated PVA/PMMA stamp on top of a PDMS cushion and a Cu foil, as well as both mounted and aligned within the mask aligner system. **(i)-(l)** Optical microscope images of the transfer materials in the different stages. **(i)** Top hBN crystal on top of a PVA/PMMA stamp. **(j)** The same hBN crystal stamped onto a Gr crystal on a Cu foil (see dotted outline of the hBN). **(k)** Bottom hBN crystal on a Si/SiO<sub>2</sub> substrate. **(l)** Final hBN/Gr/hBN heterostructure on the Si/SiO<sub>2</sub> substrate. All scale bars represent 50  $\mu\text{m}$ .

before the Cu foil is peeled off from the transfer stamp. The stamp then hosts an hBN/Gr half-sandwich. This half sandwich can be investigated on the stamp by Raman spectroscopy and AFM to quickly check if the transfer was successful. The criteria for the latter are: (i) there is MLG on the hBN, that is (ii) a closed layer and of (iii) good structural quality (low 2D-peak width). When the oxidation of the Cu/Gr is incomplete, Raman mapping often shows patchy Gr of poor quality on the hBN after transfer, highlighting once again the great importance of this aspect for the success of the dry transfer. The half sandwich structure obtained from the CVD-dry pick up can be placed on a multitude of substrates. In former works, the mask aligner of the optical lithography machine was used by replacing the Cu foil piece with e.g. a Si/SiO<sub>2</sub> wafer slide with exfoliated hBN crystals. The hBN/Gr half sandwich can be aligned with the bottom hBN on the slide and subsequently be brought into contact, followed by a heat-induced lamination of the stamp onto the chip at 150 °C for 2 min. After dissolving the PVA/PMMA stamp in DI water and acetone, this yields an hBN/CVD-Gr/hBN heterostructure.

## 6.6 Stack Refining by PC Stacking

A crucial aspect of the hBN/Gr interfaces is that during the stacking process, contamination like hydrocarbons [335], water [336, 337], or air [338] can become trapped between the materials and, due to the self-cleaning interface forces [339, 340], agglomerate into so-called *bubbles* that reach diameters up to micrometers [338, 339]. As the bubble-free areas in between are of superior structural and electronic quality, it usually suffices to pattern electronic transport devices there and discard the rest of the stacks. However, when considering a scalable CVD dry-stacking process, it is mandatory to either avoid the formation of such bubbles or develop strategies for their removal. The only way to completely avoid hydrocarbons, air, and water would be to facilitate the transfer/stacking process under ultra-high vacuum (UHV) conditions, probably involving an annealing step and heating to remove any contamination from the 2D-material surfaces. Such a UHV bonder could be realized for wafer scale processing, once the growth and transfer process and especially the oxidation of the Cu/Gr interface is fully understood and controllable. However, at this point, such a machine is far beyond the scope of this work. Therefore, the focus in this thesis was laid on cleaning Gr/hBN interfaces for enhanced device performance over larger areas than previously achievable.

In order to increase handling capabilities, our highly-precise micro-mechanical transfer system was adapted for the stacking of the hBN/Gr half-sandwich onto the bottom hBN and all further stacking steps, instead of the mask aligner of the optical lithography machine. Furthermore, a process for the mechanical removal of bubbles, as first described by Purdie et al., was adapted [341].

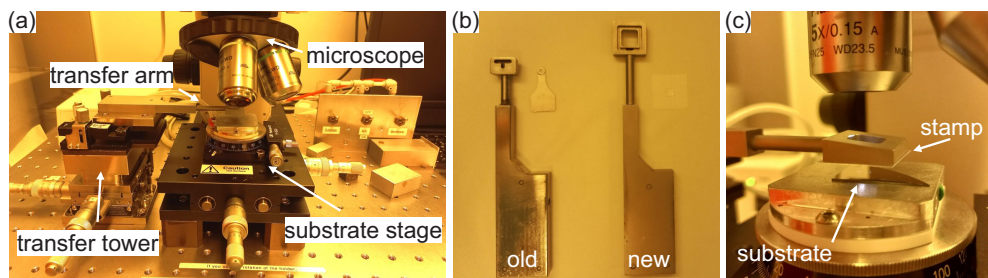


Figure 6.11: **(a)** Optical image of the micro-mechanical transfer system. It consists of a substrate stage with an on-light microscope mounted above and a transfer arm, that can be moved as well as tilted. **(b)** The old transfer arm that was used for PVA/PMMA membrane transfer processes was replaced by a specially designed new transfer arm, allowing transfer with PC membranes on top of glass slides. **(c)** Side view of a transfer process. The transfer arm holding a stamp is positioned above a substrate hosting 2D materials on the substrate stage and carefully lowered towards it until the stamp gets into contact.

The transfer system was specially designed for the dry stacking of exfoliated 2D materials into heterostructures with micro-mechanical control over the alignment, as well as the contact angle. Optical images of the transfer system are shown in Fig. 6.11. It consists of a substrate stage, a transfer arm, an optical on-light microscope, and several secondary units, like a heating mechanism, a vacuum pump, and computer software. The substrate stage holds a bottom substrate via vacuum suction and can be moved in the laboratory table plane (i.e.,  $X$ - and  $Y$ -direction) via micro-manipulators. It can also be rotated either micro- or macroscopically and features a resistive heating unit together with a temperature sensor, allowing for desired temperatures between room temperature and  $200\text{ }^{\circ}\text{C}$  to be set via a LabView program. Using this machine, flakes can be aligned and stacked with a precision down to  $\approx 1\text{ }\mu\text{m}$  (depending on the skill level of the operator). Furthermore, the adjustment of the transfer arm tilt and the precise temperature setting allows a high degree of control over the contact angle and speed during the lamination, which is not possible in the mask aligner. The transfer arm is mounted via vacuum suction on a mounting tower, allowing it to move in all directions, as well as to set a tilting angle in  $X - Z$ - and  $Y - Z$ -directions separately.

At the beginning of this work, the standard method for transferring involved the fishing of PMMA membranes with specially designed metal-fishing tools attached to the transfer arm via vacuum suction. A detailed description of this process can be found in [31]. However, these fishing tools were incapable of holding the comparatively larger CVD transfer stamps, and hence a novel transfer arm was developed

that can accommodate larger membranes. A side-to-side comparison of the old and the new transfer arm with the corresponding membrane fishing tool, as well as a transfer slide with a stamp mounted on it, is shown in Fig. 6.11(b). The new transfer arm consists of a metal arm similar to the old one but with a square-shaped and cut-out head section, using vacuum suction along all four sides to hold a 0.13 mm thin  $2 \times 2$  cm cover glass. The transfer membrane can then be mounted on the lower side of the cover glass, e.g., via an adhesive PDMS cushion layer. The cut-out in the head of the transfer arm allows viewing flakes on the bottom substrate and on the transfer membrane simultaneously just by varying the focus point. The new transfer arm enables the exploration of a multitude of alternative polymers for transferring that cannot be used by a fishing tool, is much easier to operate, and also increases reproducibility.

The bubbles within the interfaces are not fixed but can be moved around along the interface by mechanical forces easily with increasing temperature. This happens naturally while stacking heterostructures, as the lamination process on a heated substrate applies respective mechanical forces on the interface and also drives the agglomeration of smaller contamination into larger bubbles [338, 339, 341]. Purdie et al. even demonstrated that at high enough temperatures, bubbles could be removed entirely from heterostructures by picking up a stack and subsequently laminating it very slowly onto the substrate, again at high temperatures [341]. By laminating the hBN/Gr slowly and controlled onto the bottom hBN, the amount of contamination could be reduced, along with cracks and folds that, in some cases, appeared randomly when using the mask aligner. However, as the initial dry pick-up from the Cu foil could not be adapted to work in the transfer system<sup>5</sup>, the contamination within the upper hBN/Gr interface cannot be affected in this way, and we found that the temperatures suitable for PVA/PMMA membranes were not high enough to move bubbles within the stacks.

A rough orientation for the temperature range in which a polymer is operable is the glass-transition temperature  $T_g$ , which marks the transition from a hard and brittle "glassy" state to a viscous, more liquid-like state with increasing temperature. The glass transition temperatures of PVA and PMMA are  $T_{g,PVA} = 85$  °C and  $T_{g,PMMA} = 105$  °C, from which we see that our lamination temperature of 125 °C is already well into the viscous regime of the polymer stack, and increasing temperatures even further will result in a breakdown of their structural integrity. Therefore, to increase the applicable temperature window, the employment of a novel membrane polymer with a higher glass-transition temperature is required. One of the major fabrication-related advancements of this work lies in the adaption of poly(bisphenol A carbonate) (PC) membranes, as used by Purdie in [341], for our transfer system, to improve the

---

<sup>5</sup>Probably the transfer system cannot apply enough pressure to push the rigid PVA/PMMA stamps into good contact with the Cu foil. Attempts with these membranes, as well as with PC membranes (see below), either showed no Gr transferred at all or small patches only.

quality and ease of use, not only for CVD-related structures but for most 2D-material stacking processes done within our group. This replaces the PVA/PMMA membranes as go-to materials for dry-assembly.

PC has a high glass-transition temperature of  $T_{g,PC} = 147\text{ }^{\circ}\text{C}$  allowing functional operation up to  $185\text{ }^{\circ}\text{C}$  within our set-up. Furthermore, it can be removed without residues in  $\text{CHCl}_3$  (chloroform). For the membrane creation, a PC solution is produced by mixing 7 g of PC-granulate (Sigma Aldrich 428132) with 93 g of chloroform, followed by inductive stirring for 24 h. This 7 %wt solution is spin-coated onto pre-cleaned glass slides at 500 rpm without pre-acceleration and subsequently soft-baked at  $50\text{ }^{\circ}\text{C}$  for 5 min. Although PC could withstand much higher baking temperatures, it was found that above  $60\text{ }^{\circ}\text{C}$ , the adhesion to the glass substrate became so strong that the polymer could not be detached from it again without ripping or exhaustively straining it. The soft bake is followed by another 10 min resting in air and the cutting of the PC layer into a grid of roughly  $5 \times 5\text{ mm}$  membranes using a scalpel. These membranes can then be carefully peeled off by tweezers. When stored under clean room conditions, such a PC-membrane grid can be consumed over period of several months without noticeable quality degradation.

## PC Pick-Up Process

A PC membrane pick up as developed for our transfer system is described in the following: A  $5 \times 5 \times 2\text{ mm}^3$  piece of PDMS (Gel Pak 4) is placed in the center of a cover glass. A PC membrane is peeled from the carrier glass slide by tweezers and rested on top of the PDMS. The cover glass is then placed on a hot plate at  $120\text{ }^{\circ}\text{C}$  for 10 s which helps to laminate the PC membrane homogeneously onto the PDMS and flattens upstanding edges. Before mounting the cover glass with membrane stack underneath the new transfer arm, the head section of the transfer arm is calibrated to be plan parallel with the substrate stage using the tilting screws. A defined tilting angle is set in the  $YZ$ -direction, such that when the transfer arm is lowered, the transfer membrane goes into contact with the substrate at its lower end (relative to the system operator), along a straight line (the so-called *contact front*) in the  $X$ -direction. Upon further lowering down, the contact front will move upwards in the  $Y$ -direction, allowing precise control over the lamination direction and its speed. A schematic illustration of the following transfer steps is shown in Fig. 6.12. A substrate is fixed on the substrate stage such that the desired flake or heterostructure on its top surface is located roughly in the center of the microscope image. Then, the transfer arm is positioned over the substrate, such that flake or heterostructure is centered in the lower third of the PC membrane. The temperature regulation of the substrate stage is set to  $110\text{ }^{\circ}\text{C}$ <sup>6</sup> and the PC membrane is lowered gradually until it

---

<sup>6</sup>Note, that in literature reports, PC membranes can successfully pick up MLG and hBN crystals even at temperatures as low as  $50\text{ }^{\circ}\text{C}$  [341] but for our system and substrates the pick-up success rate was found to be much higher when using increased pick-up temperatures.

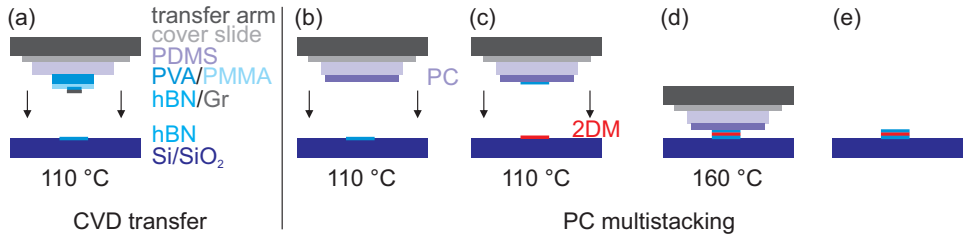


Figure 6.12: Schematic illustration of the different transfer processes possible in the transfer system. **(a)** Instead of using the mask aligner for the final lamination, the PVA/PMMA stamp with hBN/Gr underneath (see Fig. 6.10(d)) is mounted underneath the transfer arm on a PDMS cushion attached to a cover glass slide, resulting in a much higher alignment precision. **(b)-(e)** Typical (multi-)stacking process using a PC stamp on top of PDMS cushion. The stamp is laminated onto the desired 2D material (2DM) at temperatures of around 110 °C and subsequently lifted up, detaching the 2DM from the substrate. **(c)** Another substrate with a 2DM is mounted on the substrate stage and the stamp with the first 2DM is aligned and subsequently laminated followed by a lift up. This step can be repeated indefinite times. **(d)** Once the heterostructure is stacked completely, it is laminated onto the target substrate at temperatures above 160 °C, baking the PC stamp onto the substrate and thus allowing to remove the transfer arm and PDMS. **(e)** After dissolving the PC stamp in chloroform, the final heterostructure resides on the target substrate.

gets into contact with the substrate at its lower edge. From this point on, the further lamination can be controlled either via the *Z*-micro-manipulator screw of the transfer tower or by further increasing the temperature, where the latter method allows finer control but requires more time. Once the contact front has moved across the flake or heterostructure, the temperature can be decreased or the transfer arm can be moved upwards to reverse the lamination into a delamination of the PC membrane. Eventually, the flake or heterostructure is detached from the substrate and rests on the PC. In case the pick up is repeatedly unsuccessful or if already assembled heterostructures shall be picked up, a slightly different procedure can be applied. Therefore, once the membrane is in contact with the substrate, the temperature is gradually increased to 145 °C and kept there for 2 min, afterwards it is lowered to 110 °C again. Bringing the PC membrane so close to its glass-temperature increases its adhesive forces, as well its capability to cover the whole flake or heterostructure smoothly by the reduced rigidity of the membrane. Upon the subsequent temperature decrease the membrane becomes more rigid again and detaches the flake or heterostructure from the substrate. Caution has to be paid, as at temperatures above 145 °C, the PC membrane adheres so strongly to the substrate, that upon cooldown and lifting of

the transfer arm, it detaches from the PDMS and is laminated to the substrate.

## PC Multi-Stacking

Once the transfer arm is lifted up far enough, the PC membrane detaches completely from the substrate and the substrate can be exchanged for another one, that either hosts another 2D material flake for subsequent hetero-stacking or acts as the final substrate (e.g. marked chips). In the former case, the next material to be picked up, is positioned underneath the first material on the PC membrane and rotated if necessary. Using a software tool, the outlines of both the upper and the lower flakes can be traced digitally at their individual focus points, allowing a micrometer-precise pre-alignment. Subsequently, the transfer arm is lowered again, and the above described pick-up process is repeated. This time, the 2D-materials are slowly laminated on top of each other and subsequently detached from the bottom substrate. During the pick-up, the alignment of the flakes needs to be permanently monitored, as both the mechanical lowering and the heating leads to shifts of both the transfer head and the substrate in the  $XY$ -plane on the range of micrometers. Such aligned and controlled stacking of 2D materials on top of each other can be repeated for an indefinite amount times with the new transfer arm and the PC membranes, such that complex heterostructures can be built with relative ease, benefiting the whole research group<sup>7</sup>.

## Final Lamination and Bubble Removal

When a flake or heterostructure is laminated onto its final substrate, the process is slightly different to lamination during the pick-up. In case of this thesis, the final substrate is always a  $7 \times 7 \text{ mm}^2$  Si/SiO<sub>2</sub> chip with a 285 nm thick oxide-layer and a pre-patterned grid of Cr/Au electron-beam-lithography (EBL) markers. For this work, the chips also host pre-patterned macroscopic bond pads and attached leads connecting them to a  $200 \times 200 \text{ }\mu\text{m}^2$  region in the center of the chip reducing the number of EBL and metalization steps required later on (see below). A schematic illustration of the bubble removal process, together with several microscope images taken at various process steps is shown in Fig. 6.13. The heterostructure on the PC membrane is located above the center of the chip and gradually lowered. Once the membrane gets into contact with the chip, the temperature is increased to 185 °C, which in our transfer system takes at least 10 min. During the heating, the contact front advances in  $Y$ -direction until the whole membrane is laminated onto the substrate. Upon lifting the transfer arm up, the PDMS detaches from the PC on the substrate and the substrate with the flake or heterostructure on top can be removed

---

<sup>7</sup>It has to be noted here, that the success of the stacking by and large depends on the skill level and experience of the operator and many factors play into it that cannot be described verbally, rendering the whole process a form of art that every user performs slightly different.

from the transfer system.

For the cleaning of the interfaces of the heterostructure, the advancement of the contact front across the heterostructure and therefore its lamination onto the chip is upon increasing temperature is prohibited by carefully lifting the transfer arm upwards, such that the contact fronts always remains in front of the heterostructure until the substrate has reached the target temperature. Then, the transfer arm is lowered carefully, such that the contact front approaches and subsequently traverses the heterostructure as slowly as possible. The bubbles in the interface are then moved by the contact front until they are eventually pushed out at the edges of the structure, leaving clean interfaces behind. Once the contact front has traversed the whole heterostructure, the PC membrane can entirely be laminated onto the chip.

The bubble removal was found to work reliably if performed as described above, however, sometimes the operator loses control over the contact front at too low temperatures or laminates the heterostructure too quickly, which can result in incomplete cleaning or even the destruction of the heterostructure. Furthermore, it was found, that when the constituting 2D materials have defects in their surface (like larger holes in the Gr), the bubbles tend to get trapped in these and cannot be moved any more. Likewise, observing, that a bubble does not move at all upon lamination usually is a strong indication, that the Gr has structural defects at the location of the bubble.

After lamination and subsequent detachment of the PDMS layer, the chips can be removed from the transfer system. The PC membrane is dissolved in a chloroform bath for 5 min, followed by further cleaning steps in acetone and IPA for 2 min each and subsequent blow dry with a nitrogen gun. Afterwards, the heterostructures on the chips are ready for further characterization via Raman mapping and device patterning. For this work, the hBN/CVD-Gr/hBN heterostructures, that were initially assembled using PVA/PMMA stamps, were picked up entirely from the exfoliation substrates by PC membranes and laminated onto chips removing all bubbles not trapped in holes. The usable Gr areas of high quality within the heterostructures could therefore be expanded.

## 6.7 Device Patterning

In order to transfer a heterostructure consisting of multiple 2D-material crystals into a device, that can be measured in a low temperature transport setup, several patterning steps have to be performed, including the identification of suitable areas within the heterostructure, the etching of the heterostructure into a device and finally the electrical contacting via metal evaporation. These steps will be described in the following.



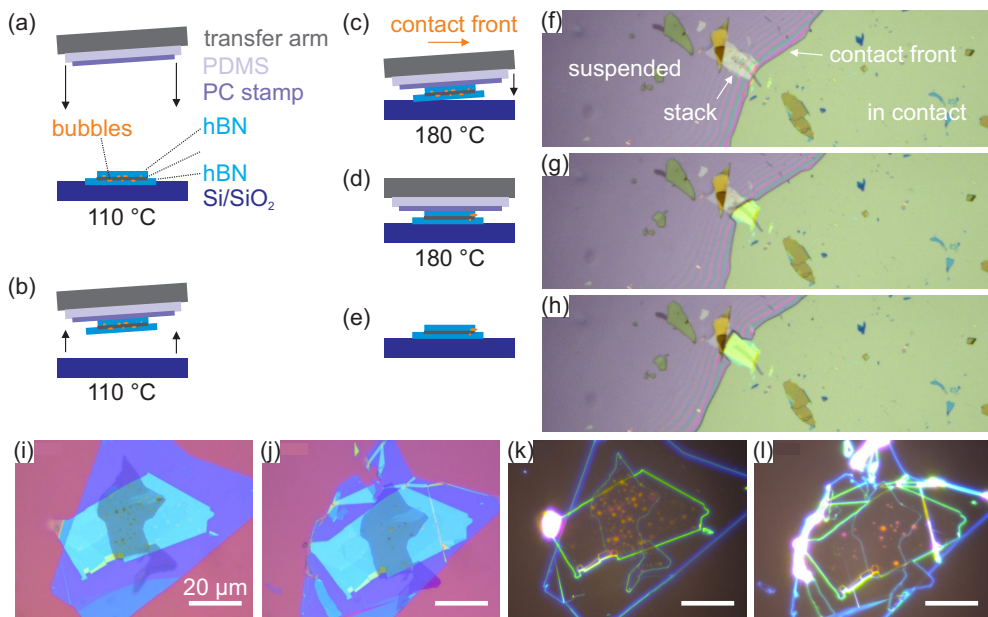


Figure 6.13: **(a)-(e)** Schematic illustration of a typical bubble removal process. **(a)** An already assembled hBN/Gr/hBN heterostructure with bubbles inside the 2D interfaces is aligned with a PC stamp on a PDMS cushion under the transfer arm and brought into contact at temperatures inside the usual transfer window. **(b)** The whole heterostructure is picked up from the substrate. **(c)** The temperature is increased to at least 180 °C while the stamp is lowered down slowly again. Eventually it goes into contact along the contact front. The contact front moves further and further along the stamp until the stack is slowly laminated onto the substrate at high temperature, upon which the bubbles are pushed out of the interfaces. **(d)** In the end, the whole stamp is in contact with the substrate and backed to it. **(e)** Subsequently, the transfer arm can be raised, the PDMS detaches and the PC stamp can be dissolved in chloroform, leaving the cleaned stack behind. **(f)-(h)** Optical microscope images of the bubbles removal process in progress. In **(f)** the contact front has just reached the stack in the center. The areas where the PC is in full contact appear in light green, while the areas, where the stamp is still suspended above the substrate appear in gray. **(g)** The contact front moved half the way across the stack, taking most of the bubbles along with it. **(h)** Full stack laminated into contact. **(i)-(l)** Optical bright- and dark field microscope images of a stack before and after a bubble removal process. All scale bars represent 20  $\mu\text{m}$ .

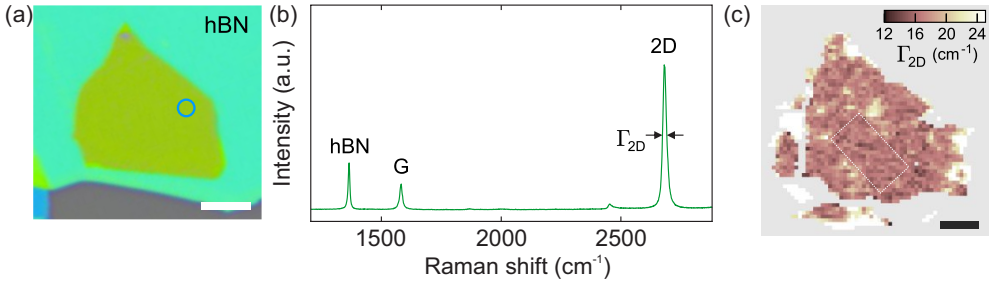


Figure 6.14: **(a)** Optical microscope image of a finished hBN/CVD-Gr/hBN heterostructure (scale bar is 5  $\mu\text{m}$ ). **(b)** Raman spectrum recorded at the location marked by the circle in **(a)** with a 532 nm laser. **(c)** Raman map showing the 2D line width  $\Gamma_{2D}$  of the Gr layer encapsulated in the heterostructure shown in **(a)** (scale bar is 5  $\mu\text{m}$ ).

## Raman Mapping

The first step on the way to a high quality device is recording of a high resolution Raman spectroscopy map of the heterostructure. A grid of Raman spectra (see Chapter 2.5) is recorded across the area of the heterostructure, where a measurement is performed every 500 nm. The characteristics of the spectra like the peak positions  $\omega$  and their FWHM  $\Gamma$  can be plotted as a color-coded map. The analysis workflow usually involves mapping of  $\Gamma_{2D}$  in the range of 15 to 25  $\text{cm}^{-1}$  and the identification of homogeneous areas of below 20  $\text{cm}^{-1}$ . Considering maps of e.g.  $\Gamma_G$ , the previously identified areas are then checked for holes or cracks.

Fig. 6.14(b) shows a representative Raman spectrum of the sandwich shown in Fig. 6.14(a) recorded with a laser wavelength of  $\lambda = 532 \text{ nm}$ . The spectra exhibit the characteristic Raman hBN peak at  $\omega_{\text{hBN}} = 1366 \text{ cm}^{-1}$  as well as the Raman G and 2D peaks of graphene that were discussed in Chapter 2.5 [66, 67, 82, 86]. The low frequency copper-oxide peaks present in Fig. 6.9(c) have disappeared entirely and the D-peak remains absent within the entire heterostructure. This highlights the contamination-free and non-invasive nature of our dry transfer process. A difference of around 20  $\text{cm}^{-1}$  in the 2D peak position  $\omega_{2D}$  recorded with the blue and green laser, respectively, can be explained by the energy-dispersive nature of the 2D peak [342].

Since the overall Raman intensity yield from the green laser excitation is much higher than the intensity obtained from the blue laser and to allow a comparison with previous works, we discuss further examinations with the green laser only. The 2D-peak exhibits a narrow FWHM of 17  $\text{cm}^{-1}$ . This value is comparable to other reported

high mobility samples obtained from both exfoliated and CVD-Gr [8, 9, 57]. The positions of the Raman G and 2D peaks around  $\omega_G = 1582 \text{ cm}^{-1}$  and  $\omega_{2D} = 2680 \text{ cm}^{-1}$  point to an overall low doping concentration of the Gr [73]. Fig. 6.14(c) shows a spatial map of  $\Gamma_{2D}$  recorded on the hBN/CVD-Gr/hBN heterostructure shown in Fig. 6.14(a).  $\Gamma_{2D}$  is lowest at regions where the Gr is fully encapsulated in hBN with values around  $17 \text{ cm}^{-1}$  indicating very small nanometer-scale strain variations over the entire Gr layer [29, 38]. Areas with the lowest mean Raman 2D line width values are considered for devices and such an area is indicated by the white dotted line in Fig. 6.14(c).

## Device Design, EBL, RIE and Metal Evaporation

The relevant maps together with optical microscope images of the heterostructures are then imported into a EBL mask editing software and aligned with the grid of EBL markers, that were pre-patterned on the chips. Subsequently, the final device geometry and the leads connecting it with the bond pads are designed in different layers. The process of device patterning and contacting involves standard electron beam lithography (EBL) with reactive ion etching (RIE) and metal evaporation. Schematic illustration of the device patterning and contacting process steps together with optical microscope images of a heterostructure in certain of these steps are shown in Fig. 6.15. PMMA is spin-coated onto the samples followed by an EBL step and development (see Appendix A for details). After development, the areas exposed to the electron beam are not covered by PMMA anymore. For the device shaping, a Hall bar shaped pattern is written on pre-identified areas of high quality in the heterostructures and after the development a 25 nm thick layer of Al is evaporated onto sample, followed by a lift off step. The remaining Hall bar shaped Al on top of the heterostructure then acts as an etching hard mask in an Ar/SF<sub>6</sub> RIE step. Afterwards the Al hard mask is stripped (AR 300-47), leaving just the patterned heterostructure on the chip.

In order to contact the heterostructures, PMMA is again spin-coated followed by an EBL step defining small contact leads connecting the pre-structured leads around the device with the contacts ports at the device itself. After development, these samples are metalized with 5/95 nm Cr/Au followed by a lift of step. Some of the devices, fabricated for this work were covered after the initial RIE patterning with an additional hBN crystal, that was transferred on top using a PC membrane. The additional layer is used to seal-off and protect the fragile Gr edges at the boundaries of the heterostructure from contamination present in atmosphere as well as in one of the measurement systems. In order to contact the device, the contact leads are written and developed by EBL as described above. Prior to metalization, an additional RIE step with Ar/CF<sub>4</sub> gas is carried out that etches through the protective hBN and the heterostructure allowing to contact the Gr. All contacts to the Gr inside the heterostructures are 1D side contacts as first reported by Wang et al. with contact resistances in the few k $\Omega$  regime [57]. After successfully contacting the devices, the

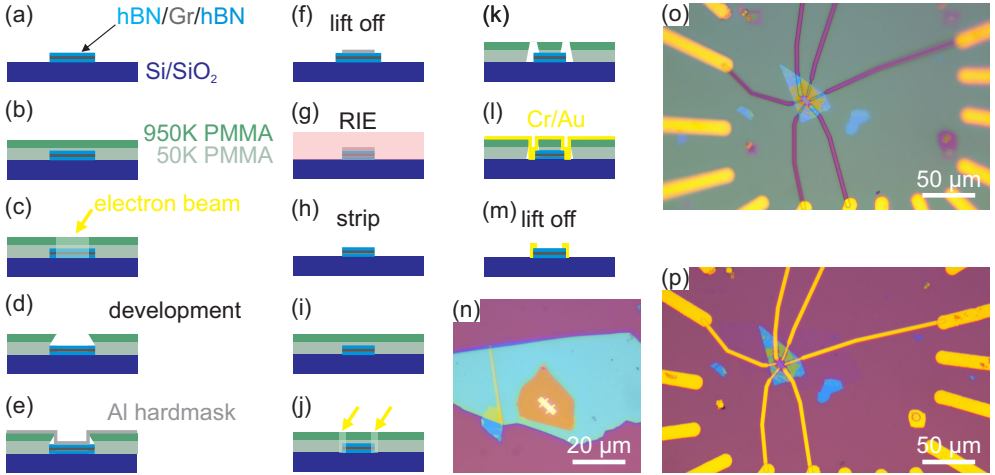


Figure 6.15: Schematic illustration of the different fabrication process steps required to pattern and contact Gr heterostructures. **(a)** Initial hBN/Gr/hBN heterostructure on the Si/SiO<sub>2</sub> substrate. **(b)** Two PMMA resists with different chain lengths are spin coated onto the substrate. **(c)** A mask is written via electron beam lithography. **(d)** The resist are developed. Afterwards, the written areas are removed and the trenches feature undercuts. **(e)** An Al hardmask is metalized onto the substrate. **(f)** In a lift off process, the Al is removed everywhere except for the written areas. **(g)** Reactive ion etching (RIE) etches the heterostructure down, where it is not covered by the hard mask. **(h)** The remaining Al on top of the heterostructure is removed with a stripping agent. The patterning of the device is completed. **(i)** For the contacting of the device, another resist stack is spin coated onto the substrate, **(j)** a mask written via EBL in the edge region of the device, **(k)** the mask is developed and **(l)** Cr/Au is metalized onto the substrate. **(m)** After a final lift off step, the patterned device features one dimensional side contacts, leading to macroscopic bond pads. **(n)-(p)** Optical microscope images of a heterostructure in various stages of device fabrication. **(n)** Heterostructure with Al hard mask on top after lift off (corresponding to **(f)**). **(o)** Patterned device with with contact lithography after development (corresponding to **(k)**). **(p)** Final device with contacts after lift-off (corresponding to **(m)**).

chips can be glued into standard chip carriers using silver lacquer and wire-bonded using a wedge bonder.

## 6.8 Graphite-Gated CVD-Graphene Devices

During the time of this thesis major breakthroughs in the performance of mono- and bilayer Gr devices could be achieved by using closely spaced graphite crystals underneath the bottom hBN as back gate electrodes [39, 40]. On the quest for achieving the highest possible quality devices, adapting such graphitic bottom gates for CVD-Gr devices was therefore very appealing. The most simple way to realize such a device would be to exfoliate a suitable<sup>8</sup> graphite flake and pick it up in the last step of a PC-dry stacking process as described above. However, specially for the CVD-Gr, this methodology has several short comings. As mentioned before, the CVD-Gr heterostructures obtained by our dry transfer are not of a homogeneous quality but sometimes host holes, folds or regions bad quality in between the good ones. All these adverse areas are usually excluded via Raman mapping and the devices are fabricated only in the good areas. On a graphite bottom gate, the Raman signal of the Gr is overlaid by the response of the graphite making it difficult to obtain the same precision of information on the structural quality. One can only hope that high quality areas of Gr by chance are located on top of the bottom graphite. Even if that by chance is the case, it can still happen that the Gr leads connecting the active channel area to metal contacts are of adverse quality. For this work a series of graphite gated CVD-Gr heterostructures were fabricated. However, all of them showed adverse transport behaviour, when subjected to a magnetic field, that indicates the presence of structural defects and therefore they are not further discussed here.

## 6.9 Changes in our CVD System

After refurbishing and permanently installing our CVD set-up in the labs, two adverse changes in the derived Gr crystals on the Cu foils became apparent:

- (i) The obtained crystals were very small in diameter, requiring a substantial increase in the  $\text{CH}_4$  flux from 1.3 sccm to 5 sccm for identical growth times to yield the same diameters as before.
- (ii) The Cu/Gr interfaces of the crystals rarely oxidized by themselves under ambient conditions anymore. In many cases, even after weeks of storing in air, there was no sufficient oxidation underneath the Gr to allow successful dry-transfer.

When attempting to identify the causes of such changes, it is important to distinguish between statistical and systematic variations in the process. In each CVD process, there are statistically varying parameters that we can neither control nor

---

<sup>8</sup>Such a graphite flake should be of an homogeneous thickness without folds or cracks and furthermore should be of an roughly rectangular shape with the shorter side being smaller than the width of the heterostructure, such that contacts can be fabricated to the Gr without short-cutting the graphite gate, and the longer side exceeding the length of heterostructure, such that the graphite itself can be contacted.

measure, such as the tightness of the Cu enclosures, the distribution of Cu grains in the foil, and the position of the foil within the reactor along with the heat shields. These factors can significantly impact the gas flow patterns and local temperatures of the Cu enclosure (see Chapter 5.3). Since the aforementioned changes manifested quite suddenly and persisted over many growth cycles, it is unlikely that any of the statistically varying parameters can be attributed to them, and we must consider systematic influences.

One possible factor might be the reconstruction of the gas lines from Teflon hoses connecting the gas bottles inside the lab to the CVD system, to standard metal capillaries and moving the gas bottles into a cabinet outside the building. The old hoses might not have been perfectly tight, allowing a finite inflow and mixing of air with the process gases. As discussed in Chapter 5.2, the presence of oxygen species leads to an increased decomposition rate of the  $\text{CH}_4$  molecules, thereby considerably increasing the growth speed. The reconstruction of the gas lines might have stopped any air leaks present and thus explain the substantial reduction of the obtained Gr crystals.

Regarding point (ii), our knowledge from Chapter 5.6 suggests that water-mediated oxidation of the Cu/Gr interface necessarily requires bunched steps in the Cu surface with folds in the Gr sheet along them, allowing oxygen species to percolate into the interface. The absence of interface oxidation, therefore, implies that step bunching is either reduced, or that the Cu surface facets, and hence the Cu/Gr interface, exhibit an increased homogeneity, allowing only partial oxidation along isolated steps/wrinkles. In that sense, it might be that by increasing the homogeneity of the whole process through reconstructing the setup, we actually lowered the output rate of transferable Gr. However, the fact that with our humidifier, we can forcefully oxidize most interfaces implies that there is likely a bottleneck limiting the  $\text{O}_2$  transport into the interfaces under ambient conditions, while we are still far from achieving the large area single-crystal Gr flakes produced on single-crystal Cu(111) foils that show no oxidation at all when bunched steps are avoided (see Chapter 5.4).

## 6.10 Summary

In this chapter, all the required techniques and processes needed to fabricate CVD-Gr into state-of-the-art heterostructures were presented, including conventional exfoliation of 2D materials, the CVD growth and transfer, as well as stacking and device patterning. Besides well-established and proven processes, several advancements and adaptations were developed within this work, such as the acquisition of a blue Raman laser to study and control the oxidation of the Cu/Gr interface, the adaptation of our transfer system for the stacking of hBN/CVD-Gr half sandwiches that involved the design of a new transfer arm, and most importantly, the adaptation of a PC membrane-based stacking process for all kinds of 2D materials. This process is much easier to conduct and even allows the mechanical lamination-induced cleaning of material

interfaces at high temperatures. Using these means, a series of hBN/CVD-Gr/hBN devices of the highest structural quality were fabricated on silicon chips, ready to be further characterized in low-temperature magneto-transport measurements. These measurements will be described in the subsequent chapters.

## Chapter 7

# Measurement Systems

The electrical magneto-transport measurements that form the main core of this work were performed in sophisticated cryostat systems in our labs in Aachen as well as in the facilities of the High Field Magnetic Lab (HFML-EMFL) in Nijmegen. In this section, the individual systems and measurement devices will be described briefly.

### 7.1 VTI System

All pre-characterizations on the CVD-Gr devices were performed in a *variable-temperature-insert* (VTI) system within our laboratories in Aachen. A schematic drawing of the VTI system is shown in Fig. 7.1(a). The VTI consists of an insert stick, holding the sample and the cryostat around it. The insert is a long metal rod with a chip socket at its tip, an array of DC measurement lines leading to connector boxes at the upper end of the stick, and metal heat shieldings. The cryostat itself consists of multiple concentric chambers and a superconducting magnet coil. The chambers include a sealing vacuum shield on the outside, a liquid N<sub>2</sub> shield reservoir, a liquid <sup>4</sup>He bath reservoir, and the inner chamber. The inner chamber is connected to a pumping system and a He recovery line. In use, both the N<sub>2</sub> and the He reservoirs have to be refilled regularly. A sample in its chip carrier is pushed into the chip socket of the insert, which is subsequently slid into the inner chamber of the cryostat and sealed off. The inner chamber is pumped down, and via a needle valve connecting the <sup>4</sup>He bath to it, a small flow of He can be set, which, due to the pumping, evaporates near the sample. Base temperatures of down to 1.6 K can be stabilized at 7 mbar of chamber pressure. Higher temperatures can be achieved either by increasing the chamber pressure or via a resistive heater at the bottom of the chamber. In this way, temperatures up to room temperature can be stabilized with relative ease in the system. The magnet allows applying perpendicular magnetic fields of up to 9 T, as long as the magnet rests in the liquid He bath and hence remains superconductive.



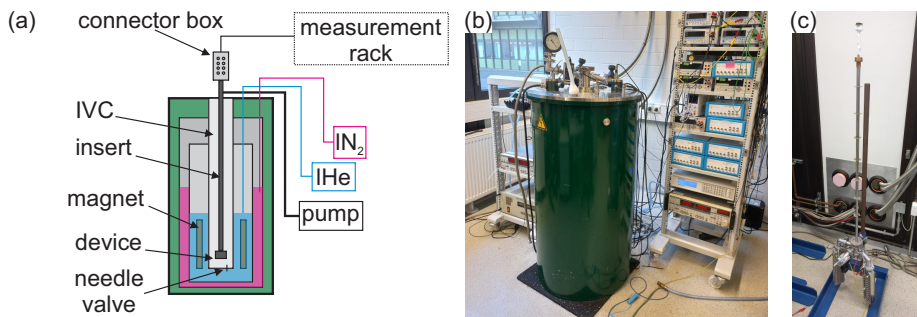


Figure 7.1: **(a)** Schematic drawing of the VTI system. The device chip carrier is placed on the tip of an insert that is mounted inside the inner vacuum chamber (IVC). The IVC is connected to a liquid He bath via a needle valve and is constantly pumped on from the top. By adjusting He flow into the IVC and the IVC pressure, together with a resistive heater, temperatures between 1.6 K and room temperature can be realized. Thermal insulation is provided by a liquid N<sub>2</sub> shield and an isolation vacuum at the outer shell of the cryostat. A superconducting magnet coil sits inside the He bath that can apply perpendicular magnetic fields up to 9 T. **(b)** Overview picture of the VTI setup without an insert mounted inside the cryostat. **(c)** One of the inserts used in the VTI system, with two connector boxes attached to it at the bottom and the fragile chip socket on its head.

## 7.2 HFML Systems

After having worked for years with lab-sized cryostats and measurement systems like the VTI, it was a thrilling experience to measure transport devices twice within the facilities of the HFML in Nijmegen. It is one of the few places on earth, where high static<sup>1</sup> magnetic fields above 30 T can be created and employed for various disciplines of fundamental research.

The facility hosts several resistive Bitter electromagnets, which can create fields of up to 38 T and is currently developing a hybrid magnet system that can reach up to 45 T. Electromagnets are temporary magnets that are magnetized by the magnetic field produced by an electric current  $I$  through a conductor like a wire. They obtain their magnetic properties only while the current is flowing, and the strength of the generated field depends on the current, with its direction determined by the right-hand rule. When a current-carrying conductor is wound  $n$  times around a bore, a magnetic field of  $B = \mu n I$  is created perpendicular to the bore area, where  $\mu$  is the permeability of the bore material. This principle is applied for coils in consumer

<sup>1</sup>Pulsed magnetic fields can be created, that over pulse lengths of 10 ms exceed 300 T in single turn (the magnet is destroyed during the pulse) systems and 100 T in multi-shot systems.

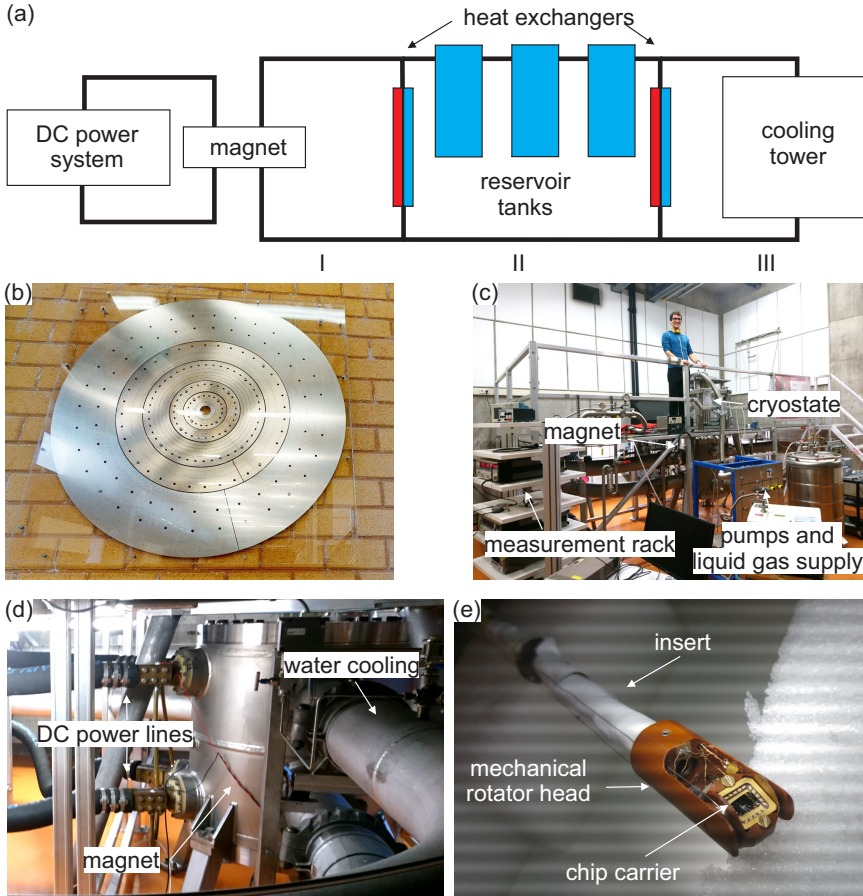


Figure 7.2: **(a)** Schematic of the high magnetic field installation at the HFML. The magnet is powered by enormous DC currents of up to 40 kA. The Joule heat created thereby is dissipated via three (I-III) thermo-coupled water circuits to the outside atmosphere. Cycle I takes the heat away from the magnets and transfers it to cycle II, where big reservoirs of cold water are used to store it. The heat from the reservoirs is transferred to cycle III which finally dissipates it to the outside via a large cooling tower. **(b)** Optical image of one of the Bitter coil discs used in the electro-magnets. **(c)** Overview picture of one of the measurement Cell, consisting of the magnet standing on the floor, with a big stage round it and a cryostat on top of it, as well as a pumping rack, liquid gas vessels and the measurement rack. **(d)** Side view of the electro-magnet under the stage. The DC power lines are connected from behind, while huge pipes connect to the sides for the water cooling the magnet. **(e)** Close up of the head of the insert used for the measurements performed within this work. It hosts a mechanical rotator and a chip socket connected with 20 DC lines, in which a chip carrier can be mounted.

electronics as well as for the sophisticated electromagnets used in research, where the conductive material is either superconducting wire (like in our VTI system) or a Cu-alloy. Superconducting wires have the advantage that the huge currents necessary to create fields in the  $10^1$  T range can be passed without dissipation through them, and hence can be integrated into lab-scale cryostats. However, due to the critical fields of the superconducting materials, they are limited in the maximum applicable fields to around 30 T in state-of-the-art systems. Resistive magnets are limited only by the Joule-heating power  $P = I^2 R$ , which is dissipated within them. The Bitter magnets, as adapted for the HFML systems, consist of Cu-alloy sheets stacked up in a helix with insulating plates in between and a central bore with a diameter of 32 mm. Aligned holes run through both metal and insulator sheets from the bottom to the top of the helix and are used to pass large amounts of cooling water through the magnet. An image of such a coil sheet is shown in Fig. 7.2(b). Besides the electromagnets themselves, the remainder of the HFML technical facility consists of the huge installation that generates the direct current (up to 40 kA at a voltage of 550 V for up to 22 MW of power) for the magnets from the Dutch power grid and, at the same time, pumps up to 170 l/s of deionized cooling water under a pressure difference of 30 bar through the coils and into big reservoirs, finally dissipating the absorbed heat from the reservoirs through large cooling towers to the air outside [343]. A schematic of the installation around the electromagnets is shown in Fig. 7.2(a).

The operation time of the magnets is limited only by the available amount of cold cooling water in the reservoirs, which usually suffices to run one of the magnets at maximum field for roughly three hours. The HFML hosts half a dozen electromagnets with a stage and small laboratory space around them (called Cells), all connected to the installation, allowing multiple groups to set up (and perform without field) measurements in parallel, while only one magnet is actively used at a time. The usage is regulated between the groups in morning, evening, and night shifts of 6.5 h of magnet time each and a maintenance slot around lunchtime. The measurement shifts, together with the limited amount of cooling water per session, force the users to optimize all measurements for maximum efficiency.

The HFML has a wide variety of measurement systems readily available that can be plugged onto any of their magnets and probe either optical, mechanical, magnetic, or electro-transport properties of various samples. In the following, the cryostats used for this work are briefly described.

### 7.3 Single Shot $^3\text{He}$ Cryostat

For the measurements in Chapter 8 in Cell 2 with the 38 T magnet, where a low base temperature of 300 mK and no more than 30 K for temperature-activated transport were required, we chose to use a single-shot  $^3\text{He}$  cryostat. The sample is mounted in a leadless chip carrier on the tip of an almost two-meter-long probe stick that hosts 20 DC lines, several heat shields, and a mechanical rotation mechanism. An optical

image of the probe head can be found in Fig. 7.2(e). After a sample is installed, the probe is slipped into the cryostat, which is mounted on top of the magnet but decoupled from it to reduce vibrations at the sample. The cryostat hosts a vacuum and liquid N<sub>2</sub> thermal shield, a liquid He bath, as well as connections to introduce liquid He into the inner space to adjust the sample temperature. The probe inside the cryostat reaches down the bore such that the sample is located at the center of the magnet, where the magnetic field is the strongest and homogeneous. The measurement rack is connected via a long multi-pole cable and a connector box, and a pumping system is connected to respective ports at the cryostat. Both liquid He and N<sub>2</sub> have to be refilled regularly once the system is cooled down. In use with regular <sup>4</sup>He, the system temperature can be lowered to around 1.2 K, similar to the VTI system, by pumping on the injected <sup>4</sup>He gas. If one wants to go below these temperatures, the <sup>4</sup>He is pumped out completely from the inner chamber, and a single shot of <sup>3</sup>He is injected and subsequently pumped, allowing to establish temperatures of down to 300 mK. The <sup>3</sup>He and <sup>4</sup>He spaces are separated by a vacuum and thermally connected via a copper cone. For temperatures above 4.2 K, where the <sup>4</sup>He is liquid, a resistive heater is installed on the probe, allowing the system to stabilize up to 30 K. The temperature can be read out via a thermal resistor at low fields or via the system pressure at larger magnetic fields, as the finite magneto resistance of the thermal resistors leads to significant errors in the readout then.

## 7.4 Flow Cryostat

For the measurements presented in Chapter 9 performed in Cell 4, we chose to use the flow cryostat system. The probe used to mount the sample was identical to the one used in the single-shot system. While this cryostat also hosts vacuum and liquid N<sub>2</sub> thermal shields, the way it uses Helium to cool the sample is different. Liquid <sup>4</sup>He is pumped via a needle valve and a capillarity through a Cu-sinter on the bottom of the insert, which acts as an evaporator. The temperature of the <sup>4</sup>He gas passing along the sample is stabilized by the gas flow rate and the power dissipated in the evaporator and the heating works in different ranges. The range from 2 - 4.2 K can be reached by pumping on the liquid <sup>4</sup>He alone, while in the range of 4.2 - 160 K, the temperature is stabilized by the flow rate of He gas from the bath at liquid He base temperature. The range between 160 - 320 K can be accessed by flowing He gas along the sample, where the reservoir is at liquid N<sub>2</sub> temperature. Especially in the transition regimes between the ranges, it can be quite challenging to stabilize a desired temperature.

## 7.5 Measurement Set-Ups

All measurements were performed using a similar set of voltage sources and lock-in amplifiers, controlled via a measurement software from a computer. As voltage sources for gating, we used Yokogawa DS200 units, while for applying bias voltages and measurement of the respective currents and voltage drops across the samples, a set of Stanford Research 830 lock-in amplifier units were used. In order not to disturb the fragile effects at low temperatures, a constant bias measurement scheme was employed in all measurements. Therefore, the output signal of one of the lock-in amplifiers is transmitted into a home-built IV-converter, which applies the bias symmetrically with a gain of  $1/10000$  across the source and drain ports of a device and at the same time translates the current flowing into the source and out of the drain port into voltage signals (amplified by an adjustable gain), that can be probed again by a lock-in. This way, knowing the bias voltage  $V_{\text{bias}}$  and drain-source current  $I$ , the 2-terminal resistance and conductance can be calculated as  $R_{2T} = V_{\text{bias}}/I$  and  $G_{2T} = 1/R_{2T}$ . The  $V_{xx}$  and  $V_{xy}$  signals are measured directly by additional lock-ins, and can be calculated into further quantities by the expressions mentioned in Chapter 3.1. The lock-in frequency is chosen with respect to the capabilities of the individual measurement system. In the VTI, with its short cable lengths and absence of mechanical noise, a higher frequency of 213 Hz was applied, as it allowed faster gate sweeping and therefore a higher data acquisition rate. However, in the HFML systems, with the considerably longer cable lengths and the overall increased noise level due to the mechanical oscillations coming from the magnets, the lock-in frequency had to be reduced to 17 Hz and the gates were swept slower as well. The thermal resistors, as well as the heaters, were read-out and controlled by Lakeshore temperature controllers. To test the contacts of a sample in the chip socket of the VTI insert or an HFML probe, a Keithley 2401 source meter was employed. To control, program, and catalog the measurements, the Labber Software environment was used throughout.

## Chapter 8

# Fractional Quantum Hall Effect in CVD-grown Graphene

This chapter has been published in parts in:

**Fractional quantum Hall effect in CVD-grown graphene**

**M. Schmitz**, T. Ouaj, Z. Winter, K. Rubi, T. Taniguchi, K. Watanabe, U. Zeitler, B. Beschoten and C. Stampfer

2D Mater. **7**, 041007 (2020) (or: arXiv: 2005.08938)

©2020 IOP Publishing Ltd

### Individual contributions:

C.S., M.S. and U.Z. conceived the experiment. M.S. fabricated the sample with the help of Z.W. and T.O.. M.S. performed the experiments with the help of T.O. and analyzed the data. K.W. and T.T. synthesized the hBN crystals. All authors provided input to data analysis, discussed the results and assisted in manuscript preparation.

## 8.1 Introduction

We have seen in Chapter 5 that the branch of research dealing with the scalable production of high-quality MLG for industrial purposes has matured considerably over the years since the first demonstration of CVD growth of Gr on Cu foils. However, from the early days of the Gr synthetization on, it was doubted whether the

so-derived material could match the high-standard of Ex-Gr. The growth process at high temperatures accompanied by the step-bunching of the Cu and the formation of wrinkles and folds might have detrimental influence on the intrinsic quality of the resulting crystal lattice. Moreover, in the subsequent transfer of the Gr onto arbitrary substrates, there might be contamination and residues stemming from the metal growth substrate, the transfer carrier material or the etchants and chemicals involved in the process, all of which might decrease capabilities of the produced graphene.

Using our dry-transfer process, we could already demonstrate that CVD-Gr is able to compete with the transport properties of highest-quality exfoliated devices with average carrier mobilities exceeding  $100,000 \text{ cm}^2/(\text{Vs})$ , mean free paths of up to  $28 \text{ }\mu\text{m}$  and well-developed integer quantum Hall states at moderate magnetic fields [8, 9, 326, 344]. These works essentially proved, that the transfer process indeed has a tremendous effect on the resulting material quality and that by employing only van-der-Waals forces to facilitate the pick-up a high initial quality is maintained.

Still, the fascinating variety of delicate, interaction-driven phenomena like the observation of an increasing number of CF states (see Chapter 3.4) [10, 11, 345–347], achieved by the progress in the device fabrication of Ex-Gr heterostructures, has so far not been reported in CVD-Gr. The absence of CF-states in the so far measured LL-spectra might indicate a cut-off in the upper end of achievable intrinsic quality or of CVD-Gr or of the dry-transfer technique. It is therefore of great importance to establish whether the already high carrier mobilities observed in CVD-Gr [8, 9, 348] also translate into sufficiently low residual charge carrier fluctuations, high enough homogenities and quantum mobilities allowing for the clear emergence of correlation-induced states.

In this chapter, measurements on dry-transferred CVD-Gr heterostructures are presented, that show fractional quantum Hall states comparable to Ex-Gr devices. The activation gaps extracted from these experiments are in good agreement with reported values for silicon-gate based samples and promise even richer CF-state spectra when using latest generation of graphitic gating technologies as well as macroscopic devices promised by a CVD-Gr based technology [39]. We have therefore provided evidence that CVD-Gr intrinsically equals the quality of its exfoliated counterpart and that potential quality degradation can mainly attributed to transfer techniques.

## 8.2 Low-Temperature Magneto-Transport Measurements

Transport measurements were performed partially in the VTI system in our labs in Aachen as well as in the single-shot  $^3\text{He}$  cryostat system at the HFML in Nijmegen (see Chapter 7 for details on the systems and the measurement techniques). When cooled down to 4.2 K the device showed a low overall doping ( $n = 5 \times 10^9 \text{ cm}^{-2}$ , with the CNP situated close to zero gate voltage,  $V_{\text{CNP}} = -0.8 \text{ V}$ ) and low residual charge carrier inhomogeneities of  $n^* = 5 \times 10^9 \text{ cm}^{-2}$ , see Figs. 8.1(a) and (b). These findings are in good agreement with spatially-resolved confocal Raman measurements on the heterostructure as well as with earlier works on dry-transferred CVD-Gr [8, 9].

Fig. 8.1(c) shows the charge carrier mobility  $\mu$  as function of charge carrier density  $n$  for two different temperatures extracted using the Drude formula  $\sigma = ne\mu$ , where  $\sigma$  is the electrical conductivity. Close to the CNP, the mobility at 4.2 K increases to values around  $350,000 \text{ cm}^2/(\text{Vs})$  and around  $250,000 \text{ cm}^2/(\text{Vs})$  at 220 K. In agreement with earlier work [39], we observe a slight discrepancy in quality for the two carrier types and will therefore only focus on the electron governed regime for the remainder of this work.

After demonstrating the high electronic quality of the device, we next discuss magnetotransport measurements with the magnetic field applied perpendicular to the Gr device. Fig. 8.1(d) shows the Hall conductivity  $\sigma_{\text{xy}}$  as function of back gate voltage  $V_{\text{BG}}$  at a fixed magnetic field of 2.5 T. Even at this low magnetic field, the onset of degeneracy lifting into integer quantum-Hall states is well visible. This lifting becomes clearer at higher magnetic fields as shown by the Landau fan diagram in Fig. 8.1(e), which shows a false-color plot of the differential Hall conductivity  $d\sigma_{\text{xy}}/d\nu$  as function of the filling factor  $\nu$  and the magnetic field  $B$ . The former is given by  $\nu = (V_{\text{BG}} - V_{\text{CNP}})\alpha h/(eB)$  with  $V_{\text{BG}}$  being the back gate voltage and  $h$  the Planck constant. The lever arm of the back gate  $\alpha = 6.34 \times 10^{10} \text{ cm}^{-2}\text{V}^{-1}$  was extracted from quantum Hall measurements and is in good agreement with the value obtained from the parallel plate capacitor model ( $C_{\text{BG}}/A$ ; see above). The Hall conductivity displays well-developed integer quantum Hall plateaus arising from spin- and valley splitting (see Chapter 3.3) and furthermore reveals clear indications of states at fractional filling factors  $p/3$  even below 8 T, as highlighted by the dashed lines.

## 8.3 High Field Measurements

FQHE-states can be attributed with a CF filling factor  $\nu^*$  that can be related to the integer quantum Hall filling factor  $\nu$  by Eq. (3.26). In order to study these fractional states in more detail, the device was further characterized at magnetic fields up to 35 T. It should be mentioned at this point that the sample changed slightly after the first cool-down around the CNP. In particular, in contrast to Fig. 8.1(e), the 1st



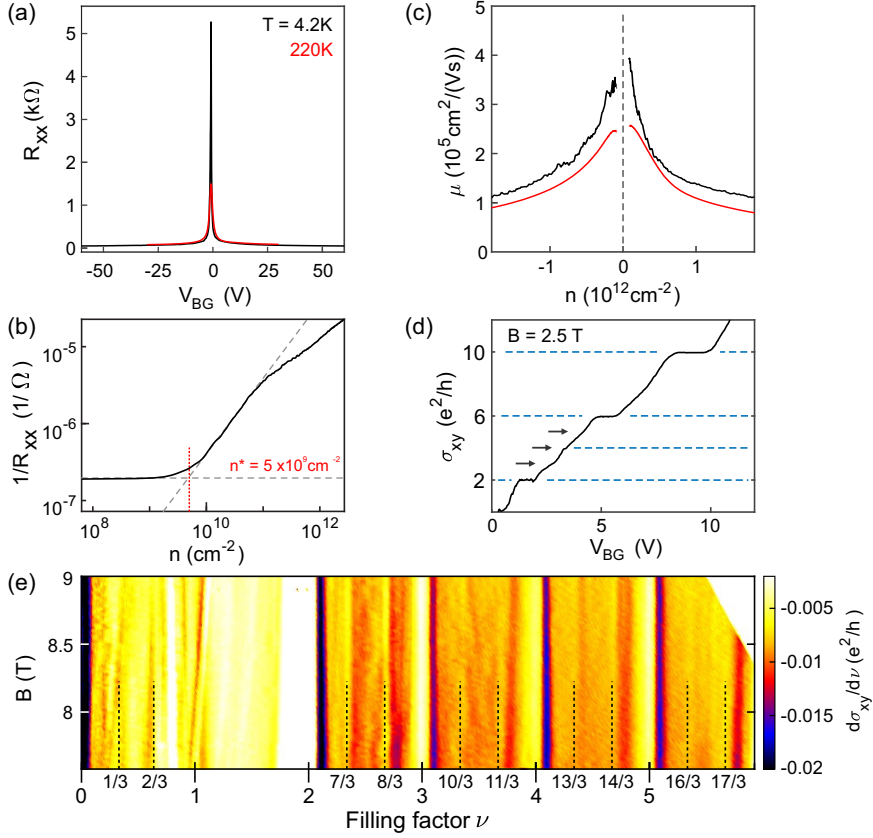


Figure 8.1: **(a)** Four terminal resistance  $R_{xx}$  as function of back gate voltage  $V_{BG}$  at a temperature of 220 K (red) and 4.2 K (black). **(b)** The inverse four terminal resistance  $1/R_{xx}$  as function of the charge carrier density  $n$ . The intercept of two lines following the regimes of constant slope provides an estimate of the residual charge carrier fluctuations  $n^* = 5 \times 10^9$  cm $^{-2}$ . **(c)** Carrier mobility  $\mu$  as function of charge carrier density  $n$  for  $|n| > 5 \times 10^{10}$  cm $^{-2}$ . **(d)** Hall conductivity  $\sigma_{xy}$  as function of back gate voltage  $V_{BG}$  at a perpendicular magnetic field of  $B = 2.5$  T ( $T = 1.8$  K). The black arrows highlight the integer conductance plateaus due to the lifting of the fourfold Landau level degeneracy. **(e)** Landau fan diagram. Differential Hall conductivity  $d\sigma_{xy}/d\nu$  as function of filling factor  $\nu$  and magnetic field  $B$  recorded at  $T = 1.8$  K.

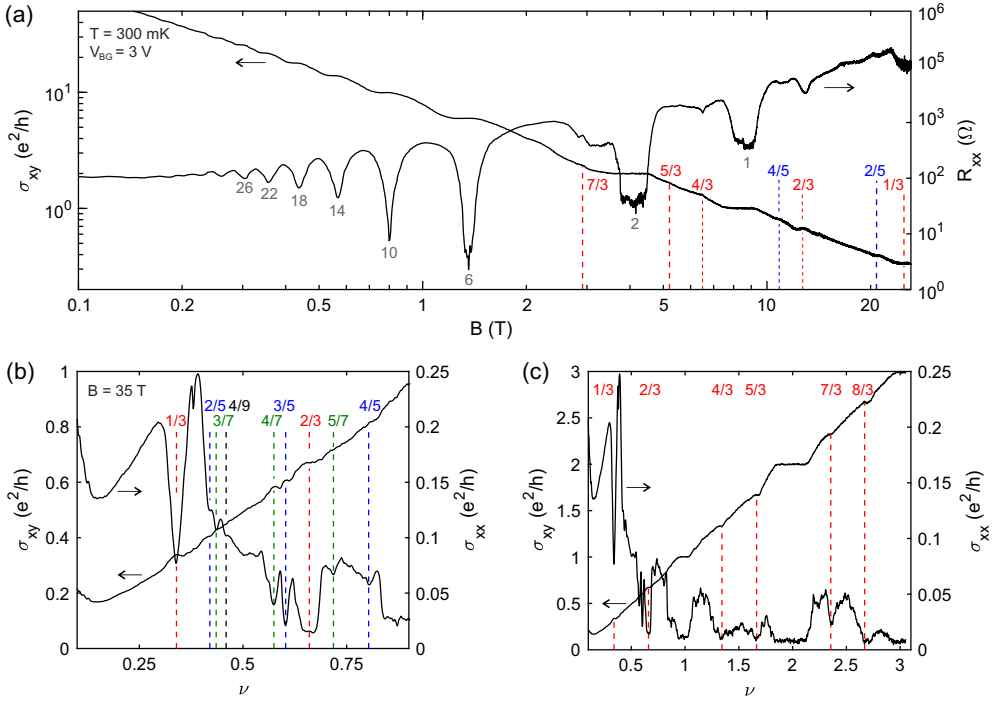


Figure 8.2: **(a)** Hall conductivity  $\sigma_{xy}$  and resistance  $R_{xx}$  as function of magnetic field  $B$ . **(b),(c)** Hall conductivity  $\sigma_{xy}$  and longitudinal conductivity  $\sigma_{xx}$  as function of filling factor  $\nu$  at a fixed magnetic field of  $B = 35$  T. States with filling factors being integer multiples of  $\frac{1}{3}, \frac{1}{5}$  and  $\frac{1}{7}$  are highlighted in red, blue and green for better visibility.

LL now also becomes clearly visible (see below). Fig. 8.2(a) shows the four terminal resistance  $R_{xx}$  as well as the Hall conductivity  $\sigma_{xy}$  as a function of  $B$  (logarithmic scale) at a fixed back gate voltage of  $V_{BG} = 3$  V and a temperature of 300 mK. First signatures of the  $7/3$  state already appear below 3 T and more clearly pronounced FQHE states start to develop at higher magnetic fields.

Figs. 8.2(b) and 3(c) show the Hall conductivity  $\sigma_{xy}$  and the corresponding longitudinal conductivity  $\sigma_{xx}$  as a function of filling factor  $\nu$  at  $B = 35$  T. Well developed plateaus at all  $\nu = p/3$  fractional filling factors are visible. Moreover, we can identify all 2-flux CF-states ( $2p = 2$ ) up to  $\nu^* = 4$  ordered symmetrically around half filling in  $\sigma_{xy}$  as well as in  $\sigma_{xx}$ . Even more, we denote plateaus at  $\nu = 5/7$  and  $4/5$  which can be identified as 4-flux CF hole states ( $2p = 4$ ) with  $\nu^* = 1, 2$  centered around  $\nu = 3/4$ . We emphasize, that it is certainly interesting to investigate the 4-flux CF

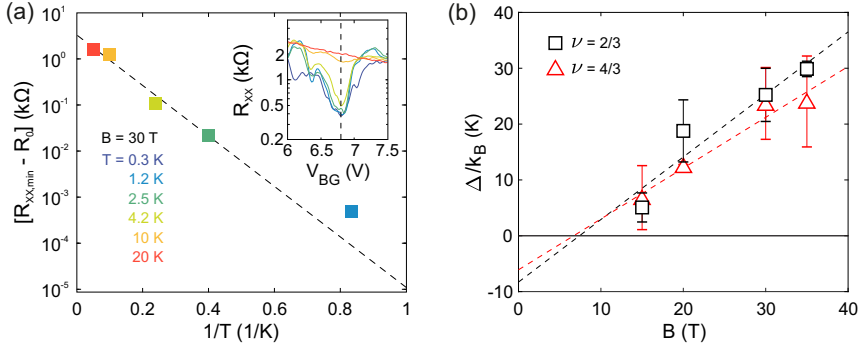


Figure 8.3: **(a)** Bulk resistance  $R_{xx,min}$  of the  $4/3$  state corrected by an offset  $R_0 = 390 \Omega$  (see text) as function of inverse temperature  $1/T$  at a constant magnetic field of  $30$  T. The dashed line shows a fit of the temperature activated model  $R_{xx,min} - R_0 = R \exp(-\Delta_\nu/2k_B T)$ . The inset illustrates the vanishing bulk resistance dips when increasing  $T$  from  $300$  mK to  $20$  K. **(b)** Extracted activation gaps  $\Delta$  as function of magnetic field for the  $2/3$  and  $4/3$  fractional quantum Hall states. Dashed lines represent linear fits.

states [347, 349] in more detail and to compare them to other semiconductor FQHE systems [350–355]. Indeed, the perspective to grow macroscopic Gr samples using CVD does open this avenue.

These results indicate an outstanding material quality considering the fact that a rather simple  $\text{Si}^{++}/\text{SiO}_2$  gate/gate oxide was used instead of the state-of-the-art graphitic gating approaches, which allow for precise tuning of the sample edge [40, 43, 356, 357] or omit the edge completely when using Corbino geometries or electrostatically defined channels [358–360].

## 8.4 Activation Gap Measurements

In order to further quantify the robustness of the observed FQH states, we performed temperature dependent activation gap measurements for the most pronounced fractional filling factors  $\nu = 2/3$  and  $\nu = 4/3$ . A set of back-gate traces was recorded at constant magnetic fields for a range of temperature steps. An Arrhenius-like temperature activated model is used to fit the data where the minimum of  $R_{xx}$  at a given filling factor  $\nu$  is assumed to follow  $R_{xx,min}^\nu = R \exp(-\Delta_\nu/2k_B T) + R_0$ , where  $k_B$  is the Boltzmann constant,  $\Delta_\nu$  is the activation gap and  $R_0$  is a resistance offset. Fig. 8.3(a) shows a fit of the  $R_{xx}$  minimum minus the offset  $R_0$  at  $4/3$  filling as a function of

temperature between 300 mK and 20 K at  $B = 30$  T; the corresponding resistance traces are shown in the inset. The extracted results for  $\Delta_{2/3}/k_B$  and  $\Delta_{4/3}/k_B$  as function of the magnetic field are shown in Fig. 8.3(b). The activation gaps increase roughly linearly with magnetic field reaching a value of 29 K and 24 K, respectively, at  $B = 35$  T. This behaviour is in good quantitative agreement with other studies on FQHE states in Gr, where values in the range of 30 to 60 K were reported for  $\Delta_{2/3}/k_B$  [39, 359] and 16 K for  $\Delta_{4/3}/k_B$  [11]. Assuming the  $B$ -field dependence being purely given by the CF-Zeeman energy (reduced by LL broadening) following  $\Delta_\nu = \frac{1}{2}\mu_B g B + \Gamma_\nu$ , where  $\mu_B$  is the Bohr magneton and  $g$  is the Landé  $g$  factor, we can interpret the intercepts  $\Gamma_\nu$  as a measure of the disorder-induced LL broadening. In our device we extract  $\Gamma$  values between 6 and 8 K, which is in agreement with values of around 10 K on Ex-Gr reported in other studies [11, 39, 359]. The extracted values of the  $g$  factor, ranging between 2.7 and 3.4 are roughly a factor 2 smaller compared to values reported in Refs. [39, 359]. Since the  $g$  factor is known to strongly depend on the electron-electron interaction renormalization [361] this value may crucially depend on the electrostatic environment substantially influenced by the different gating technologies.

## 8.5 Summary

In summary, we have demonstrated the presence of fractional quantum Hall states in CVD-Gr underlining the high electronic quality of this material when assembled into heterostructures by a dry transfer process. Neither CVD growth on Cu substrates nor the oxidation of the Cu surface via water intercalation nor the dry transfer process induce enough disorder to quench the interaction-driven formation of CFs. Even though using a conventional silicon gate to tune the carrier density, CF states emerge even at moderate magnetic fields below 3 T. The full spectrum of 2-flux states up to  $\nu^* = 4$  could be identified at  $B = 35$  T as well as several 4-flux states. The results are unambiguously proving that the high quality of CVD-Gr equals that of mechanically exfoliated graphene flakes. Therefore, a new generation of large-area ultra high quality devices might be achieved using scalably grown 2D materials to dry-transfer CVD-Gr and open the door to a deeper understanding of the interaction effects driving the emergence of CF states in Gr.



## Chapter 9

# Room Temperature Quantum Hall Effect in Graphene

This chapter has been published in parts in:

**The role of disorder in the temperature-induced breakdown of the quantum Hall effect**

**M. Schmitz**, ..., T. Ouaj, K. Rubi, T. Taniguchi, K. Watanabe, S. Pezzini, ..., U. Zeitler, B. Beschoten, M. Morgenstern and C. Stampfer

*In preparation*

**Individual contributions:**

U.Z., M.S. and S.P. conceived the experiment and coordinated the collaboration. M.S., D.V. and V.C. fabricated the Gr devices and performed the transport measurements. C.S.A.M. and K.R. provided technical assistance during the high-field experiments. K.W. and T.T. provided single crystals of hBN. B.B. and C.S. supervised the experimental work. M.S. performed the data analysis. M.S. wrote the manuscript with input from all the co-authors.

**Phonon-mediated room-temperature quantum Hall transport in graphene**

D. Vaquero, V. Clerico, **M. Schmitz**, J.A. Delgado-Notario, A. Martin-Ramos, J. Salvador-Sanchez, C.S.A. Müller, K. Rubi, K. Watanabe, T. Taniguchi, B. Beschoten, C. Stampfer, E. Diez, M.I. Katsnelson, U. Zeitler, S. Wiedmann and S. Pezzini

Nat. Commun. **14**, 318 (2023)

©The author(s) 2023

**Individual contributions:**

U.Z., S.W. and S.P. conceived the experiment and coordinated the collaboration.

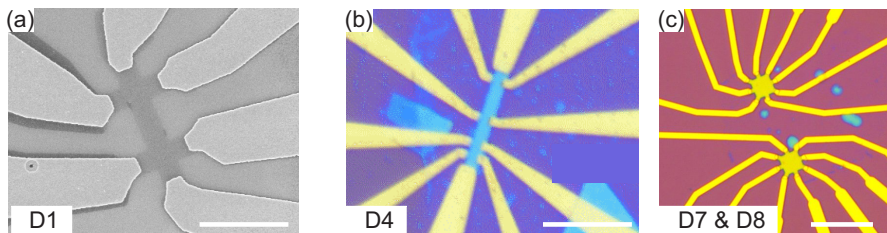


Figure 9.1: Representative images of the different device geometries used for this work. **(a)** SEM image of Ex-Gr device D1 on bare  $\text{SiO}_2$  [185]. **(b)** Optical image of the hBN/Ex-Gr/hBN heterostructure Hall bar D4. **(c)** Optical image of the hBN/CVD-Gr/hBN heterostructures D7 and D8. The scale bars represent  $5\ \mu\text{m}$ ,  $10\ \mu\text{m}$  and  $10\ \mu\text{m}$ .

D.V., V.C. and M.S. fabricated the Gr devices and performed the transport measurements. J.A.D.-N., A.M.-R. and J.S.-S. provided technical assistance in the cleanroom processing. C.S.A.M. and K.R. provided technical assistance during the high-field experiments. K.W. and T.T. provided single crystals of hBN. B.B., C.S. and E.D. supervised the experimental work. D.V., V.C., M.S., and S.P. performed the data analysis. M.I.K. provided theoretical input for the interpretation of the results. S.P. wrote the manuscript with input from all the co-authors.

## 9.1 Introduction

In Chapter 8 we could finally prove that the quality of CVD-Gr matches that of the exfoliated reference material in all relevant transport properties. This legitimizes the use of CVD-Gr devices together with others obtained from exfoliation for the systematic evaluation of specific transport phenomena in a meta analysis without having to fear systematic errors arising from the production method of the Gr. Two such meta-analysis will be presented in this chapter, where high-field magneto-transport measurements at temperatures ranging from 4 K to 300 K are evaluated for a set of Gr devices with varying degrees of sample disorder. The aim of the first study is to investigate the role of disorder in the manifestation and the temperature-induced breakdown of the QHE at room temperature (RT) and to test the validity of the microscopic models concerning the temperature dependence that we discussed in Chapter 4, while the second work investigates the predominant scattering mechanisms in the RTQHE regime.

## 9.2. The Role of Disorder in the Temperature-Induced Breakdown of the QHE

Name	Stacking order	$l \times w$ [ $\mu\text{m}^2$ ]	$\mu_{\text{cold}}$ [ $\frac{\text{cm}^2}{\text{Vs}}$ ]	$\mu_{\text{warm}}$ [ $\frac{\text{cm}^2}{\text{Vs}}$ ]	$n^*_{\text{cold}}$ [ $\frac{1}{\text{cm}^2}$ ]	$n^*_{\text{warm}}$ [ $\frac{1}{\text{cm}^2}$ ]
D1	Gr	$1.5 \times 0.5$	15'000 (4 K)	10'000 (220 K)	$1.60 \times 10^{11}$	$2.00 \times 10^{11}$
D2	Gr	$1.5 \times 0.5$	10'000 (4 K)	10'000 (297 K)	$1.00 \times 10^{11}$	$1.20 \times 10^{11}$
D3	hBN/Gr/hBN	$3 \times 1.5$	64'000 (4 K)	60'000 (220 K)	$4.20 \times 10^{10}$	$6.96 \times 10^{10}$
D4	hBN/Gr/hBN	$4.5 \times 1.5$	65'000 (25 K)	65'000 (220 K)	$2.37 \times 10^{10}$	$5.21 \times 10^{10}$
D5	hBN/Gr/hBN	$3 \times 1.5$	-	161'000 (220 K)	-	$3.70 \times 10^{10}$
D6	hBN/CVD-Gr/hBN	$4 \times 2.3$	350'000 (4 K)	240'000 (220 K)	$5.00 \times 10^9$	$3.17 \times 10^{10}$
D7	hBN/CVD-Gr/hBN	$5 \times 5$	>800'000 (4 K)	250'000 (220 K)	$2.50 \times 10^9$	$4.00 \times 10^{10}$
D8	hBN/CVD-Gr/hBN	$5 \times 5$	>800'000 (4 K)	100'000 (220 K)	-	-

Table 9.1: Overview of the devices considered for this work including the stacking order, channel length and width ( $l$ ,  $w$ ), charge carrier mobilities  $\mu$ , and residual charge carrier fluctuations  $n^*$  at low as well as at high temperatures for electrons.

### Device Fabrication

We examine an ensemble of electronic transport devices created using various fabrication processes (see Table 9.1 for details). Two Hall bar-shaped devices (D1 and D2) were assembled by exfoliating monolayer Gr onto bare Si/SiO<sub>2</sub> substrates [185, 362]. Three additional Hall bar-shaped devices (D3 to D5) were constructed using dry transfer techniques to encapsulate exfoliated Gr between two hBN crystals on Si/SiO<sub>2</sub> substrates [51, 363]. Lastly, one Hall bar-shaped device and two square-shaped devices (D6 to D8) were assembled using dry-transferred CVD-Gr, encapsulated in hBN crystals on Si/SiO<sub>2</sub> with an extra step to remove contamination from the hBN/Gr interfaces as described in Chapter 6. All samples were patterned into devices and contacted using electron beam lithography, reactive ion etching, metal evaporation, and lift-off processes. For the hBN encapsulated devices, we employed one-dimensional contacts following [57]. The devices have SiO<sub>2</sub> gate oxide thicknesses of 300 nm, ensuring a similar screening and gating environment with screening lengths around 250-300 nm [364] and gate lever arms of approximately  $\alpha_{\text{BG}} = 7 \times 10^{10} \text{ cm}^2\text{V}^{-1}$ . Micro-Raman spectroscopy was utilized in D6-D8 as a non-invasive method to spatially map the structural properties of the heterostructures, enabling the selection of areas with the highest quality for devices [38, 66]. D7 and D8 were shaped into squares ( $5 \times 5 \mu\text{m}$ , see inset in Fig. 9.3(a)) with eight contact leads to allow for a larger channel width compared to a Hall bar in a roughly quadratic area of high structural quality.

## 9.2 The Role of Disorder in the Temperature-Induced Breakdown of the QHE

In Chapter 4, we provided a detailed recap of the two primary microscopic models that have been developed since the discovery of the IQHE. The first model is based on disorder-induced localization of charge carriers, enabling the pinning of  $E_{\text{F}}$  between collision-broadened bands and the formation of quasi-ballistic one-dimensional chan-



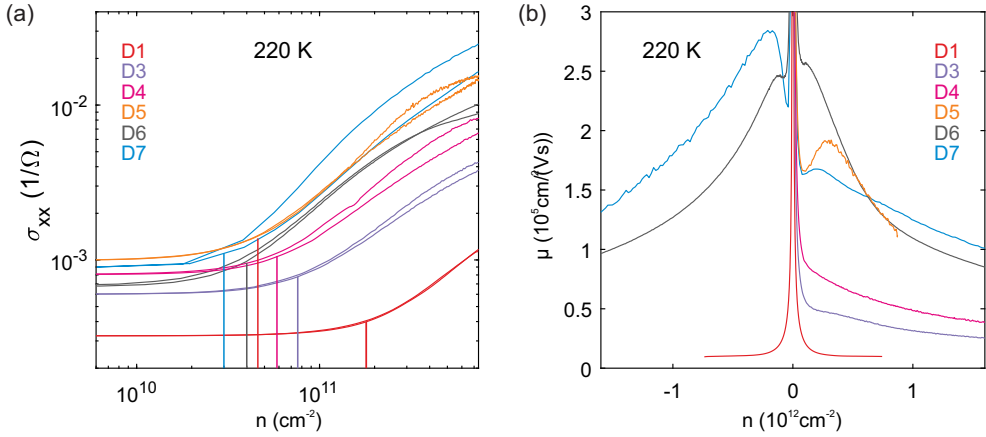


Figure 9.2: **(a)** Longitudinal conductivity  $\sigma_{xx}$  as function of charge carrier density  $n$  for multiple devices of the ensemble at a temperature of 220 K on a double-logarithmic scale. Intersection points of the linear subsections of the curves (horizontal for low densities and positive sloping for higher densities) yield the amount of residual charge carrier fluctuation  $n^*$  (marked by vertical lines). **(b)** Drude mobility  $\mu$  as function of charge carrier density  $n$  for the same devices as in **(a)**.

nels where  $E_F$  intersects the up-bend LL at the channel edge [137, 172]. The second model considers the screening effects between charge carriers, resulting in landscapes of compressible and incompressible regions within a channel, the topography of which depends on the filling factor [248, 249]. Although the conventional view that disorder is a necessary prerequisite for the QHE has been challenged at low temperatures by integer valued Hall plateaus (HPs) still emerging in the highest quality 2DES where disorder vanishes [365], the role of disorder in the manifestation of the QHE at high  $k_B T$  up to room temperature (RT) has yet to be investigated.

From Chapter 2 and 3 we have learned that Gr serves as an ideal candidate for studying the QHE at elevated temperatures due to its massless carrier system providing large intrinsic cyclotron gaps of  $\hbar\omega_C \approx 2300$  K at 30 T, along with high and relatively temperature-independent carrier mobilities up to  $10^6 \text{ cm}^2/(\text{Vs})$  [57, 185]. The DOS of Gr from  $\text{LL}_{-2}$  to  $\text{LL}_2$  ( $\text{LL}_N$  denotes the  $N$ -th LL) at a magnetic field of 10 T is shown in Fig. 9.3(a). Since its discovery in 2004, the QHE has been demonstrated in Gr at both cryogenic temperatures and RT (RT) [33, 105, 135, 136], and advanced fabrication techniques have substantially improved the structural quality and disorder level of Gr devices, enabling the investigation of intricate interaction-driven phenomena like the FQHE as demonstrated in Chapter 8. Fig. 9.3(b) highlights the measurable differences in Gr devices with varying disorder levels by showing  $R_{xx}$  and  $\sigma_{xy}$  for device D2 (high disorder) and D7 (low disorder), at a constant magnetic

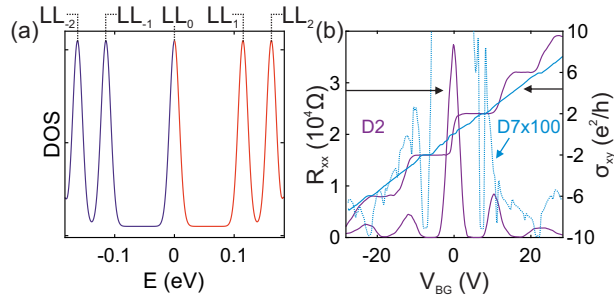


Figure 9.3: **(a)** Density of states LL spectrum of Gr for a perpendicular magnetic field of 10 T. LL0 is shared equally between holes (purple) and electrons (orange), while all higher LL are populated by one carrier type only. **(b)** Longitudinal resistance  $R_{xx}$  and transversal conductivity  $\sigma_{xy}$  as function of applied back gate voltage  $V_{BG}$  for D2 (purple) and D7 (orange) at 4 K.

field and energy intervals identical to Fig. 9.3(a) (controlled by the back gate voltage  $V_{BG}$ ). D2 exhibits overall broader HPs, while D7 reveals additional HPs at all integer values of  $e^2/h$ , indicative of an interaction-driven degeneracy lifting [105]. The ability of various fabrication techniques to significantly alter the disorder level in Gr, coupled with its intrinsic LL spectrum, establishes it as an ideal vehicle for exploring the role of disorder in the temperature induced breakdown of the QHE up to RT.

In this study, we present the first coherent experimental investigation of the QHE at elevated temperatures in relation to sample disorder. Specifically, we showcase magneto-transport measurements for a set of Gr devices fabricated using different techniques, resulting in varying degrees of disorder while maintaining similar device dimensions and screening lengths. We compare the extracted activation energies with the temperature dependence of the HP widths, serving as separate indicators of LL broadening and the number of localized states present in the devices.

Our observations reveal a distinct trend of overall wider HPs and increasing breakdown temperatures with increasing disorder levels. Meanwhile, the activation gaps across all devices remain of a comparable magnitude. Notably, a RTQHE is exclusively observed in the most disordered devices. We discuss our findings within the frameworks of both the conventional single-particle picture and the screening-mediated picture. Consequently, we provide the first experimental verification of the previously unproven assumption that a finite amount of disorder is necessary for the manifestation of the QHE at RT.

## Results

All devices were characterized using low-temperature magneto-transport systems, enabling temperature settings between 4 K and 300 K while applying perpendicular

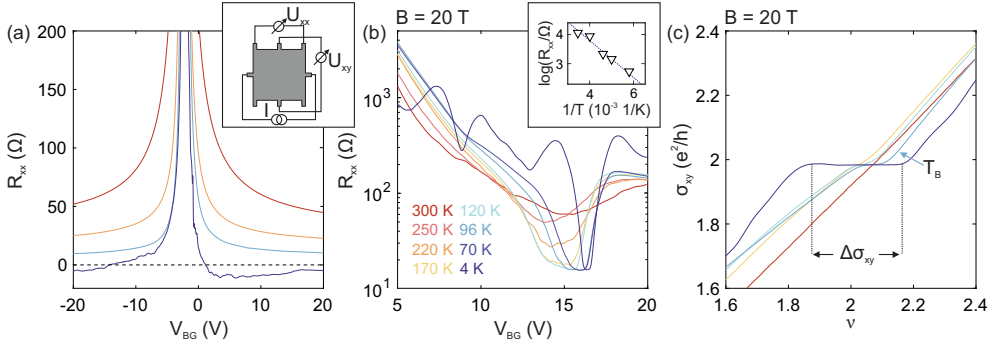


Figure 9.4: **(a)** Longitudinal resistance  $R_{xx}$  as a function of back gate voltage  $V_{BG}$  for different temperatures in device D7. Inset: Schematic of the square-shaped device as well as the measuring scheme. **(b)** Longitudinal resistance  $R_{xx}$  as a function of back gate voltage  $V_{BG}$  for different temperatures at a fixed magnetic field of  $B = 20$  T. The inset shows the extracted minimum resistance  $R_{xx,min}$  at filling factor  $\nu = 2$  as a function of inverse temperature  $T^{-1}$ . The blue line shows the result of a temperature-activated fit to these data, yielding an activation energy  $E_A = 1270$  K. **(c)** Hall conductivity  $\sigma_{xy}$  as a function of back gate voltage  $V_{BG}$  for different temperatures  $T$  at a magnetic field of  $B = 20$  T. The horizontal extent of the HPs is denoted as  $\Delta\sigma_{xy}$ . The highest measured temperature at which a HP shows a horizontal extent is defined as the breakdown temperature  $T_B$ . All panels use the color coding of the temperatures shown in **(b)**.

magnetic fields of up to 30 T. Preliminary characterizations at zero and low magnetic fields were conducted to examine the basic electronic properties of the devices. The individual groups contributing to this study used different numbers of temperature steps between 4 K and RT, which is why some of the relevant quantities cannot be extracted at the same temperatures for all devices.

Fig. 9.4(a) shows the longitudinal resistance  $R_{xx}$  as a function of applied back-gate voltage  $V_{BG}$  for the highest quality device (D7) at different temperatures between 4 K and RT. We observe a sharp peak in resistance at the charge neutrality point (CNP) around a back-gate voltage  $V_{CNP} = 2$  V, revealing a low overall residual doping of the device. The back-gate voltage can be converted into the charge carrier density  $n$  using  $n = (V_{BG} - V_{CNP}) \times \alpha_{BG}$ , where  $\alpha_{BG}$  is the gate lever arm. Very low residual charge carrier fluctuations  $n^*$  ( $5 \times 10^9$  cm $^{-2}$  at 4 K to  $3 \times 10^{10}$  cm $^{-2}$  at RT) indicate a high overall homogeneity of the sample and a low level of disorder [8, 9]. At 4 K, we note that the measured four-terminal voltage switches sign at finite carrier densities and becomes negative, indicating ballistic transport present in the sample. The carrier density at the zero crossings, together with the diagonal length of the square ( $5.6 \mu\text{m}$ ), provides us with a lower limit for the carrier mobilities of 800,000 cm $^2$ /Vs using

$l_{\text{mfp}} = (h/2e)\mu\sqrt{n/\pi}$  as the elastic mean free path;  $h$  is Planck's constant and  $e$  is the electron charge [9]. The negative four-terminal voltages remain up until around 100 K, indicating ballistic transport up until that temperature and a transition to a diffusive transport regime above it. Even at 220 K, the mobility remains remarkably high ( $250,000 \text{ cm}^2/\text{Vs}$ , as deduced from a van-der-Pauw measuring scheme), underlining the extraordinary high quality of the device [366]. The low- and high-temperature carrier mobilities for all other Hall bar shaped devices were extracted using the Drude formula  $\sigma = ne\mu$  and are summarized, along with the corresponding residual charge carrier fluctuations  $n^*$ , in Table 9.1. The devices D1 and D2 exhibit the lowest carrier mobilities and largest residual carrier fluctuations, while D3-D6 range in the intermediate regime and D6-D8 host cutting-edge mobilities and low  $n^*$ . As shown in Fig. 9.4(b)+(c), when subjected to a perpendicular magnetic field, the sample displays quantization into LLs, visualized by distinctive minima in  $R_{\text{xx}}$  in Fig. 9.4(b) and lateral HPs in the Hall conductivity  $\sigma_{\text{xy}}$  at integer filling factors in Fig. 9.4(c) [105]. Similar measurements were performed on all considered devices (see Table 9.1 for an overview).

As the temperature increases, the  $R_{\text{xx}}$  minima at integer filling factors  $\nu$  begin to rise, and the HPs in  $\sigma_{\text{xy}}$  shrink in width. The temperature dependence of the minima is well described by an Arrhenius-type activation mechanism  $R_{\text{xx,min}} = R_0 \exp(E_A/2k_B T)$ , where  $E_A$  is the activation energy to the extended states of the adjacent LLs and  $k_B$  is the Boltzmann constant, as seen in the inset of Fig. 9.3(b), in agreement with earlier works [185]. Fig. 9.4(c) shows how the HPs shrink in their horizontal extend  $\Delta\sigma_{\text{xy}}$  with increasing temperature. In the phase transition from quantum Hall to conventional Hall transport, the critical temperature  $T_C$  is used to characterize the point at which the transition occurs [184]. However, due to the limited number of temperature points in our experiments, we often find one trace above and one below  $T_C$ . Consequently, we denote the highest temperature below  $T_C$  as breakdown temperature  $T_B$ , for our analysis (e.g. 96 K in Fig. 9.4(c)). Above  $T_B$  only a slight change in slope of  $\sigma_{\text{xy}}$  remains in D7 (e.g. at 120 K), or the classical Hall curve is recovered entirely, in contrast to previous reports of a RTQHE in Gr [136].

In order to better understand the role of disorder level in the formation of RTQHE, we compare the magneto-transport properties of various devices at large magnetic fields, as a function of temperature. The results are summarized in Fig. 9.5(a), where we present the extracted activation energies  $E_A$  as a function of magnetic field  $B$ . We also include the expected cyclotron gaps for massless Dirac fermions  $E_G(B) = v_F \sqrt{2\hbar e |BN|}$ , where  $v_F$  is the Fermi velocity as a dashed line. The extracted activation energies, within their error bars, are consistent with one another and closely match the expected energies, particularly at large  $B$ . Fig. 9.5(b) displays the  $\nu = 2$  HP widths  $\Delta\sigma_{\text{xy}}$  at 4 K as a function of  $B$  for different devices. While  $\Delta\sigma_{\text{xy}}$  remains roughly constant with  $B$  for a specific device, we note substantially lower overall widths in devices with lower disorder levels. Fig. 9.5(c) showcases  $T_B$  as a function of  $B$  for various devices. Unfilled symbols indicate that no breakdown

temperature was found in within the measured temperature range ( $T_B \notin T_{\text{meas}}$ ), either because the HPs did not vanish at the highest measured temperatures (D1+D2) or since the HPs already vanished at the lowest measured temperature (D3+D4). The most disordered devices exhibit RTQHE, while the HPs in high-quality devices disappear completely well below 200K. Fig. 9.5(d) further highlights this contrast by comparing the Hall conductivities  $\sigma_{xy}$  at the highest measured temperatures at 30 T for different devices. In D1 and D2, the HP is still clearly pronounced around RT, while in D3, D4, and D6, there remains only a slight change of slope in the signal around  $\nu = 2$  and a straight line for the devices D7 and D8. Fig. 9.5(e) and (f) display scatter plots for various devices at  $B = 20$  T, with Fig. 9.5(e) depicting  $\Delta\sigma_{xy}$  at 4 K against the corresponding low-temperature values of  $n^*$ , and Fig. 9.5(f) illustrating  $T_B$  against the corresponding high-temperature values of  $n^*$ .

## Discussion

Different fabrication techniques and device designs enable the creation of transport devices with various levels of disorder within the same active material. Although the dimensions of these devices vary, all fall within the micrometer range, classifying them as narrow transport channels. With identical 300 nm gate oxide thicknesses leading to similar screening lengths, disorder remains the sole crucial parameter that varies between the samples. An investigation of the scattering mechanisms for different disorder levels at elevated temperatures is discussed in a separate work [363]. Investigating the influence of modified screening environments, such as advanced close graphite gates, gate-defined channels, or substrates with distinct dielectric constants, is beyond the scope of this work and further experiments are necessary to explore these aspects [39, 117]. The disorder within the devices arises from various factors, including substrate-induced electron-hole puddles, wrinkles, fixed contamination at the interface, and disturbances from the sample edge. Encapsulation in hBN crystals by employing dry transfer techniques alters the electrostatic environment, flattens the Gr, relieves strain, and localizes contamination within bubbles [51, 57, 367]. Bubbles can be either expelled from a heterostructure [341] or circumvented when shaping devices in conjunction with areas of low structural quality, identified through methods like micro Raman spectroscopy [38, 82].

When ranked by carrier mobilities, D1 and D2 (Gr on bare  $\text{SiO}_2$ ) demonstrate the lowest quality, followed by D3-D5 (hBN/Gr/hBN heterostructures) in the intermediate range, and D6-D8 (hBN/CVD-Gr/hBN) representing the highest quality devices. The key findings from the temperature-dependent magneto-transport measurements are as follows: Although the activation energies were comparable within their errors across all devices and approached the expected cyclotron gaps at the highest magnetic fields, the HP breakdown temperature decreases with diminishing disorder levels. Notably, extended HPs at RT were exclusively found in the lowest quality devices (D1+D2). It is important to note that disorder remains the only crucial parameter exhibiting significant variation between the devices, as dimensions, substrate,

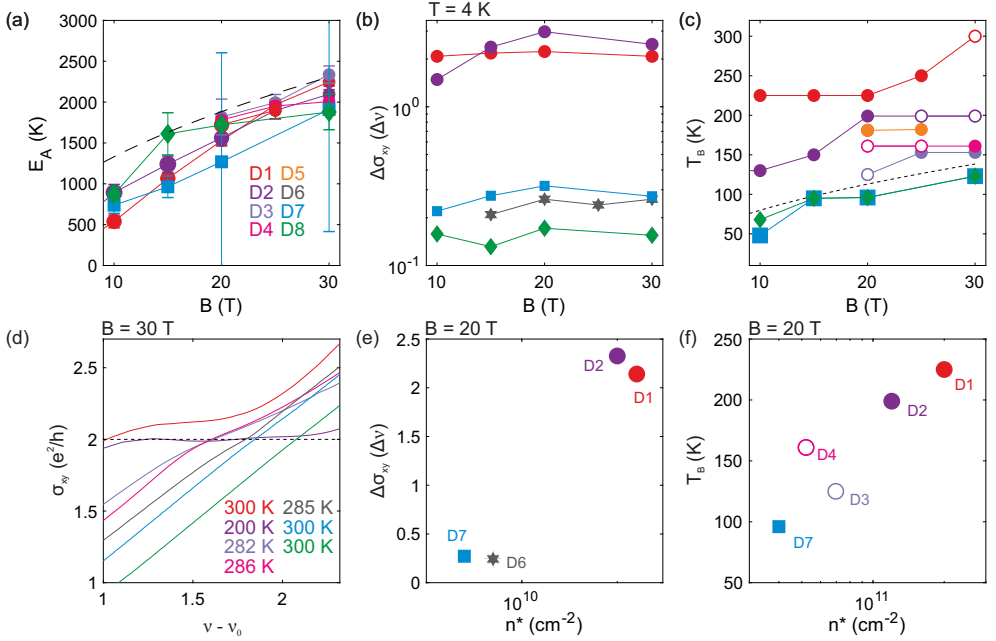


Figure 9.5: **(a)** Activation energy  $E_A$  as a function of magnetic field  $B$  for the different devices considered in this work, together with the expected intrinsic energy gap for massless Dirac fermions  $E_G(B) = v_F \sqrt{2\hbar e |BN|}$  as a gray dashed line. The color coding of the devices is applied in all figures. **(b)** Width of the  $\nu = 2$  HP  $\Delta\sigma_{xy}$  as a function of  $B$  at  $T = 4$  K for different devices. **(c)** Breakdown temperature  $T_B$  as a function of  $B$  for different devices. Unfilled symbols indicate that, in the measured temperature interval, no HP matches the definition of  $T_B$ . The gray dashed line indicates  $0.06 \cdot E_G(B)$ . **(d)**  $\sigma_{xy}$  as a function of filling factor  $\nu$  at the highest measured temperatures and  $B = 30$  T for different devices. The traces are offset horizontally for clarity. **(e)**  $\Delta\sigma_{xy}$  versus the corresponding residual charge carrier fluctuation level  $n^*$  at 4 K and  $B = 20$  T for different devices. **(f)**  $T_B$  as a function of  $n^*$  extracted close to RT at  $B = 20$  T.

and screening lengths are comparable. Consequently, we can rule out influences such as charge transfer, observed in epitaxial Gr, which leads to exceptionally broadened HPs [368].

Next, we will interpret our results within the framework of the two primary microscopic models discussed in Chapter 4 to explain the manifestation of the QHE. In the conventional single-particle framework, these findings can be attributed to varying levels of bulk disorder between LLs with similar broadening. Fig. 9.6(a)+(b) display the DOS for the Gr system, ranging from  $LL_0$  across  $\nu = 2$  to  $LL_1$  in a constant

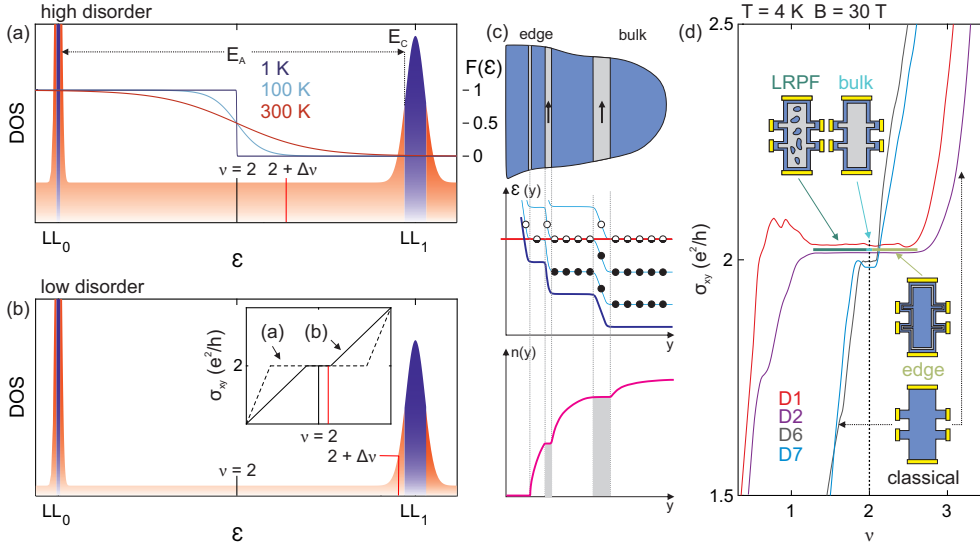


Figure 9.6: **(a) + (b)** Density of states of Gr in a perpendicular magnetic field of 30 T for high **((a))** and low **((b))** disorder levels. Extended states (drawn in dark blue) populate the LL centers until the upper and lower mobility edges  $E_C$ . All states outside  $E_C$  are localized (drawn in red). To highlight the effect of different temperatures, corresponding Fermi-Dirac distributions are shown in **(a)** as an overlay. Due to the different magnitudes of the localized state background, a fixed step in filling  $\Delta\nu$  away from  $\nu = 2$  results in different shifts in the Fermi energy, as indicated by the red vertical lines. For low disorder, an identical step in filling already moves the Fermi energy close to  $E_C$ , and subsequently the resulting HPs are much narrower in width compared to the high disorder case. The corresponding HPs are shown as an inset in **(b)**. **(c)** Schematic of the edge reconstruction resulting in alternating compressible (blue) and incompressible (gray) strips in the screening-mediated picture of the QHE, together with the corresponding energy and charge carrier density cross-sections  $\epsilon(y)$  and  $n(y)$ . **(d)** HPs as a function of  $\nu$  at 4 K and  $B = 30$  T for a set of devices, together with schematic illustrations of the classical, edge, bulk, and LRPF-stabilized regimes.

magnetic field of 30 T. We assume a Gaussian shape for the LLs and account for differences in disorder by a varying magnitude of the localized state background (large in (a) and small in (b)), independent of the LL broadening. The LL centers are occupied by extended states, which are limited in energy by the mobility edge  $E_C$  on both sides of the peak (dark blue color). Outside of  $E_C$ , localized states (red color) populate the region.  $LL_0$  exhibits minimal broadening, as it is protected against disorder by the Atiyah-Singer index theorem, first demonstrated in Gr by Giesbers

et al. [185]. This is consistent with our data, as the extracted activation energies  $E_A$  across all devices in Fig. 9.4(a) are similar within the error margins and independent of their respective bulk disorder levels due to the negligible broadening (for  $LL_1$ , we plot a broadening of  $\Gamma = 400$  K, in line with [185]). In a system with a high density of available disorder-induced localized states, a fixed change in the filling  $\nu = 2 + \Delta\nu$  (e.g., by a constant fixed amount of back gate voltage) leads to only a small shift of the Fermi energy  $E_F$  (as highlighted by the vertical black and red dashed lines in Fig. 9.6(a)). Several such steps can be made before  $E_F$  reaches  $E_C$  of the adjacent LL, which causes the breakdown of the Hall conductivity quantization (see inset in Fig. 9.6(b)). On the other hand, in a low-disorder device, the same change in filling  $\Delta\nu$  shifts  $E_F$  considerably closer to  $E_C$ , reaching it within another step as shown in Fig. 9.6(b). As a result, this leads to a much narrower HP compared to the high-disorder case. This model effectively explains the individual low-temperature HP widths depicted in Fig. 9.4(b) and (e).

As the system temperature increases, the occupation function  $F(E)$  broadens around the Fermi energy  $E_F$ , as depicted for three different temperatures in Fig. 9.6(a). The Hall conductivity quantization at elevated temperatures can persist only if the occupation does not reach the mobility edge  $E_C$ , and a finite HP width will be maintained if a sufficient number of unoccupied localized states remain between  $E_F$  and the adjacent LL's mobility edge. Within this framework, we deduce that with decreasing bulk disorder levels, we can expect a lower breakdown temperature  $T_B$  for the HPs, which is well-represented in the data shown in Fig. 9.4(c) and (f). Furthermore, we conclude that the higher-quality devices in our study lack an adequate number of available localized states within the cyclotron gap to enable the formation of a HP at RT, while the highly disordered devices D1 and D2 still exhibit the effect, as illustrated in Fig. 9.4(d).

The other microscopic picture of the QHE focuses on screening and interactions, where the key factor is the gradual change in carrier density towards the sample edges in narrow channels, rather than disorder-induced localization. The screening concept in the context of Gr has been explored in various studies, including scanning probe measurements on Gr/SiO<sub>2</sub> [174], research on Gr edge reconstruction [252], charge accumulation at the edges [178], edge-to-bulk correspondence [364], and more recently in relation to non-topological currents and interaction mechanisms in the ground state of LL<sub>0</sub> [250, 251]. It is important to interpret our findings within this framework as well.

In the screening model, the LLs don't merely bend upwards near the boundary edge to form quasi-ballistic channels at each LL's intersection with  $E_F$ . Instead, interactions and screening reconstruct the edge potential into a series of plateaus, producing a pattern akin to a wedding cake, as depicted in Fig. 9.6(c) [249]. Upon partial filling of a LL, a conductive compressible strip (CS) of constant energy



forms, bordered by insulating incompressible strips (IS) of constant charge carrier density, which bend up in energy towards the channel edges. The presence of IS enables the Hall potential to drop across a transport channel by effectively isolating the opposing compressible edges from the bulk and driving a Hall current within the IS, which results in the measurable QHE transport characteristics. The QHE dynamics are then dictated by the positions,  $y$ , and the widths,  $w$ , of the ISs, which can be calculated either analytically for simple geometries or by sophisticated self-consistent models, which also take the effects of temperature and disorder into account [221, 237, 248]. A key conclusion from both computations and experiments is that the screening-induced (in)compressible landscape is dynamic as the system is tuned through a HP, undergoing dynamic transitions between various regimes, as shown in Fig. 9.6(d) [237, 242, 249]. When approaching a HP from the high filling factor side, narrow IS form at the channel edges, while the bulk remains compressible. As  $\nu$  reduces further, the IS at the edges widen and migrate closer to the channel center until they merge, creating a wide incompressible region in the bulk center around integer global filling. Further reduction in  $\nu$  below inter filling ultimately disrupts the QHE, turning the channel fully compressible and resulting in classical Hall transport behavior [249]. When the width of an incompressible strip falls below the spatial extent of the electron wave functions and the average distance between carriers (given by the magnetic length  $l_B$  and the Fermi wave vector  $\lambda_F$ ), electrons can tunnel through the incompressible strip. This results in the current diffusing across the entire Hall bar, thus restoring the classical Hall effect [248]. The effect of increasing temperature on the formation of (in)compressible regions manifests in a shrinking of the IS-widths and thereby resulting in decreasing HP widths until both IS and HPs vanish entirely [226]. The disorder potential plays an ambivalent role in the dynamics of HPs as it can be split into short-range potential fluctuations (SRPFs) and long-range potential fluctuations (LRPFs) [237]. While SRPFs tend to induce a reduction in the HP width due to collision-broadening the LLs, LRPFs serve to stabilize and extend their widths to filling factors lower than integer values. This extension due to the LRPFs is realized as different regions of a transport channel reach local integer filling only when the global filling is already below integer value, and thus prolonging the duration of quantized transport [237].

Upon revisiting our devices, we note that the similar activation energies portrayed in Fig. 9.5(a) imply a uniform presence of SRPFs across all devices. As a result, any variations detected in the magneto-transport dynamics can be ascribed to differing magnitudes of LRPFs and we further note, that  $n^*$  should function as a valuable gauge of LRPFs [38]. Hence, we can interpret Fig. 9.5(b) and (e) as testament to the HP width-extending effect of LRPFs on the bulk-regime side, a phenomenon further underlined by the finite extend beneath integer filling of the HPs shown in Fig. 9.6(d). Devices with stronger LRPFs are predicted to host both wider IS and HPs at reduced temperatures, but also to sustain these up comparatively higher temperatures. This

prediction is in good agreement with our extractions of  $T_B$  in Fig. 9.5(c) and (f) and underlined further by solely devices D1 and D2 exhibiting a RTQHE in Fig. 9.5(d).

A key distinction between the conventional and the screening picture of the QHE is that the latter permits the formation of narrow HPs even in the complete absence of disorder [249]. Therefore, we deem it worthwhile to explore whether in our highest-performing devices, the QHE is driven by disorder at all. As evident from Fig. 9.6(d), the HP of our highest-quality device, D7, is significantly narrower compared to D1 and D2. Moreover, the authors in Ref. [226] calculate that in a disorder-free system, the IS at the channel edge reach a critical temperature of  $\approx 0.06 \cdot E_G$ , beyond which they lose their insulating properties, resulting in a HP breakdown. This temperature is illustrated as a gray dashed line in Fig. 9.5(c), and we can observe that  $T_B$  of D7 aligns well with this threshold. On the other hand, Fig. 9.6(d) reveals that all HPs extend below integer filling, indicating stabilization by LRPF. Additionally, we performed self-consistent calculations for disorder-free Gr resulting in  $\Delta\sigma_{xy} = 0.011$  which is approximately an order of magnitude smaller than those of D7. Therefore, we conclude that at least within our device ensemble, the QHE is driven by localization or, likewise, LRPFs.

## Conclusion

In conclusion, we present temperature-dependent magneto-transport measurements for an ensemble of Gr devices, each fabricated using different techniques resulting in varying levels of disorder. In the absence of a magnetic field, these variations manifest as different carrier mobilities and residual charge carrier fluctuations. At high magnetic fields, we observe a clear correlation between increased HP widths and their temperature-induced breakdown, and higher levels of disorder. Notably, the RTQHE is only observed in the most disordered devices. Our results can be interpreted by both the conventional single-particle framework, which assumes backgrounds of disorder-induced localized states of varying magnitudes, as well as by the screening model, which explains our findings by varying levels of LRPFs. Finally, we can confirm the hitherto unproven assumption that disorder is a necessary component for the manifestation of the QHE at elevated temperatures up to RT.

## 9.3 Role of Electron-Phonon Mediated Scattering in the QHE at RT

In Gr, the large LL separation allows at RT the coexistence of the QHE together with a non-negligible population of acoustic phonons with a wave-vector commensurate to  $1/l_B$ . In the following, we will demonstrate that Gr encapsulated in hBN realizes a novel transport regime, where dissipation in the QH phase is governed predominantly

by electron-phonon scattering. After investigating the HP dynamics in the previous section, we will now focus on the thermally activated transport at filling  $\nu = 2$  up to RT of the same device ensemble, showing that the high magnetic field behaviour correlates with the zero field charge carrier mobility. By these means, we extend the well-accepted notion of phonon-limited resistivity in ultra-clean Gr to a hitherto unexplored high-field realm.

## Introduction

The use of hBN as atomically-flat encapsulating dielectric, as we already saw above, permits a drastic reduction of extrinsic disorder in Gr devices [367], leading to zero-field transport regimes dominated by either electron-electron [369], electron-hole [370] or electron-phonon (e-ph) interaction [57], which manifest over different carrier density and temperature ranges. Towards RT the scattering of electrons with acoustic phonons was theoretically identified as the main intrinsic contribution to the electrical resistivity in Gr [371–373], implying a charge carrier mobility exceeding  $10^5 \text{ cm}^2/(\text{Vs})$  at low charge carrier concentration ( $n < 10^{12} \text{ cm}^{-2}$ ). While such figures could already be inferred from early data on disordered Gr on bare  $\text{SiO}_2$  surfaces ( $\mu \approx 10^5 \text{ cm}^2/(\text{Vs})$ ) [374, 375], at present, the reach of the zero-field acoustic-phonon limit is firmly established as a generic property of high-quality Gr devices [57], also when encapsulated in hBN crystals from different sources [60] or engineered to high doping levels ( $n > 10^{13} \text{ cm}^{-2}$ ) [376]. Notable exceptions to the cleanness-implies-high-RT-mobility scenario are suspended Gr samples, where flexural phonons dramatically contribute to carrier scattering leading to a  $T^2$  behaviour of the resistivity [377], and rotationally faulted Gr bilayers close to magic-angle, showing strong phonon-driven  $T$ -linear resistivity [378]. The difference between freely suspended Gr and Gr encapsulated in hBN is due to the fact that in the latter case van-der-Waals interaction between Gr and substrate makes flexural phonons harder, suppressing an intrinsic ripping stability [12]. This work addresses the fundamental question whether the e-ph mechanism in clean Gr could also govern the electrical transport in the QH regime CITE at temperatures close to RT. Previous literature on RTQHE in Gr on exclusively  $\text{SiO}_2$ -supported devices precluded such investigations [105, 136, 185].

## Results

The interplay of the LL spacing  $E_G$  and the thermal energy  $k_B T$  governs the basic phenomenology of the electrical transport in the QHE regime. When  $k_B T \ll E_G$  the localized bulk together with the quasi-ballistic edge channels, or likewise the incompressible strips isolating the compressible edge region (see Chapter 4) lead to zero longitudinal resistivity  $\rho_{xx}$  (see Fig. 9.7(a), upper panel). As the temperature increases and  $k_B T \approx E_G$ , thermal excitation of extended bulk states or likewise of carriers across incompressible strips exponentially restores bulk conduction and carrier scattering (Fig. 9.7(a), lower panel), resulting in a finite value of the longitudinal

resistivity minimum at integer filling according to  $\rho_{xx} = \rho_0 \exp(\frac{-E_G}{2k_B T})$  (or Eq. (4.12) for  $R$ ). The pre-factor to the the exponential term  $\rho_0$ , which is often not considered explicitly, determines the magnitude of the temperature activated resistivity (shaded yellow area Fig. 9.7, lower) and contains information regarding the disorder potential [379, 380]. In perpendicular magnetic fields, e-ph scattering requires lattice vibrations with a wave-vector in the order of the inverse magnetic length [381], which defines a third energy scale relevant to our problem  $E_{ph} = \hbar v_s / l_B$ , where  $v_s$  is the sound velocity in the material. In conventional 2DES, the small  $E_G$  leads to a complete suppression of the QHE within a few K [137], where the  $E_{ph}$ -controlled phonon population can be considered negligible. The necessary condition  $k_B T \gg E_{ph}$ , as sketched in Fig. 9.7(b), is instead fulfilled by Gr in RTQHE regime. Under this circumstance, the temperature activated resistivity (shaded dark cyan area in Fig. 9.7) should directly relate to e-ph scattering [381]. Fig. 9.7(c) shows a representative measurement of the RTQHE, acquired at  $B = 30$  T in an hBN/Gr/hBN back-gated Hall bar (D4). The Hall conductivity presents weak slope changes around filling factors  $\nu = \pm 2$ , while the shelves-like features at low charge carrier concentration originate from the onset of electron-hole in  $LL_0$  [382]. The resistivity exhibits two sizeable minima in addition to the pronounced maximum at the CNP (Fig. 9.7, inset), indicative of temperature activated QH states. In the following, we will focus on the magnitude of  $\rho_{xx}$  in RTQHE regime and identify the underlying mechanism.

Fig. 9.8 shows the main transport characteristics of the devices measured at zero magnetic field and at elevated temperatures. Fig. 9.8(a) shows the RT charge carrier mobility of three encapsulated devices, calculated using Eq. (2.25), as function of  $n$ . All the mobility curves are well above the typical values for Gr devices on bare  $\text{SiO}_2$  substrates (gray shaded area) over the whole  $n$  range. Importantly, sample D5 shows a  $\mu(n)$  dependence comparable to the data of [57] (dash-dotted line), demonstrating the standard fingerprint of phonon-limited RT mobility in zero magnetic field [60, 376]. Note that, although Wang et al. employed a  $15 \mu\text{m}$ -wide van-der-Pauw device, e-ph scattering imposes a  $\approx 1 \mu\text{m}$  upper bound to the electronic mean free path at  $B = 0$  and RT [57]. Therefore, the zero-field e-ph limit can also be realized using narrow Hall bars, provided that their channel widths exceed one micron (this condition is fulfilled in all devices considered here, see Table 9.1). The overall high quality of the samples is also supported by the observation of the FQHE at low temperatures (see e.g. Chapter 8 for D6). In Fig. 9.8(b) we explore the correlation between the carrier mobility  $\mu$  and the residual charge carrier fluctuations  $n^*$ . We consider data  $T = 220$  K, where clear thermal activation is observed in the RTQHE regime. The residual disorder, which is indicated by  $n^*$ , which, in our devices remains well below the typical observations for Gr on  $\text{SiO}_2$ . In addition, as for Refs. [29, 383], the linear  $1/\mu(n^*)$  dependence (see shaded area in Fig. 9.8(b)) indicates scattering from long-range potentials, attributed to random strain variations generic to Gr on substrates [38]. We can therefore conclude, that our device ensemble (i) spans a

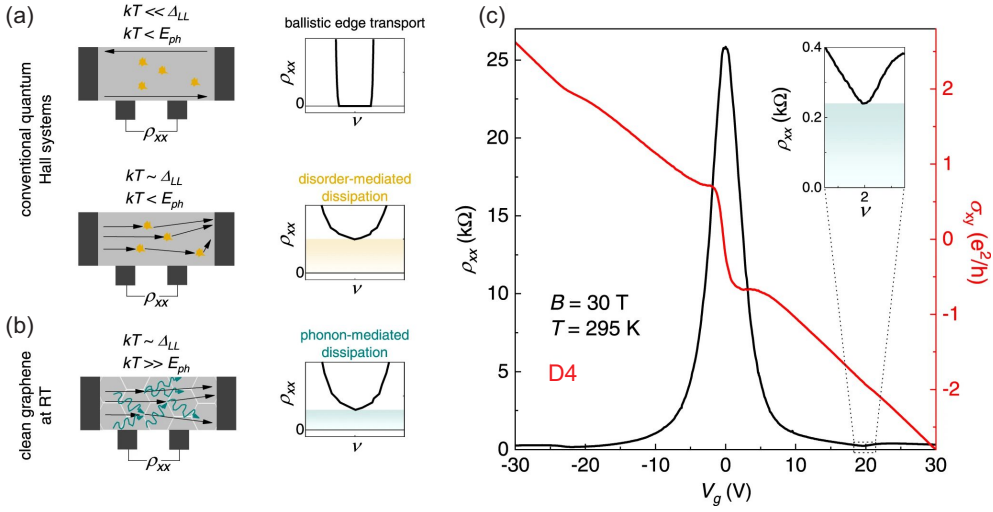


Figure 9.7: **(a)** Schematics of temperature-dependent transport in conventional quantum Hall systems, such as 2DESs in semiconductors. At low  $T$  (relative to the LL separation, upper part), the electrical current is carried by chiral edge states, leading to zero longitudinal resistance. At higher  $T$  (lower part), thermally-excited bulk states give a finite resistivity due to disorder scattering (yellow shading), with negligible contribution from lattice vibrations. **(b)** At RT, Gr supports both the QHE (due to large inter-LL spacing) and predominant e-ph scattering in high-mobility samples, enabling the realization of a different transport regime, with phonon-mediated dissipation at high magnetic fields (dark cyan shading). **(c)**  $\rho_{xx}$  (black) and  $\sigma_{xy}$  (red) as a function of the back-gate voltage (corrected by a 5.2 V offset from the CNP), measured in hBN-encapsulated sample D4 at  $B = 30$  T and  $T = 295$  K. Inset: zoom-in of  $\rho_{xx}$  in the vicinity of filling factor  $\nu = 2$  (the dark cyan shading indicates the finite value of the resistivity minimum).

low-disorder range unexplored in previous RTQHE experiments, and (ii) present a well-defined disorder type, with increasing impact along the D6 to D3 sequence.

Next, the sample temperature is used as an experimental knob to control the excitation of both phonons and bulk-extended electronic states (or likewise states in IS) in strong magnetic fields. In Fig. 9.9(a) we sketch the effect of increasing  $T$  on the DOS in Gr at  $B = 30$  T. Towards RT, the broadening of the Fermi-Dirac distribution around the Fermi energy  $E_F$  ensures excited charge carriers from both  $LL_0$  and  $LL_1$  across  $E_G$  (or likewise the shrinking in width of the IS). Accordingly, the local resistivity minimum at  $\nu = 2$  leaves zero and increases continually, as shown in Fig. 9.9(b). Fig. 9.9(c) shows a complete picture of the temperature dependence

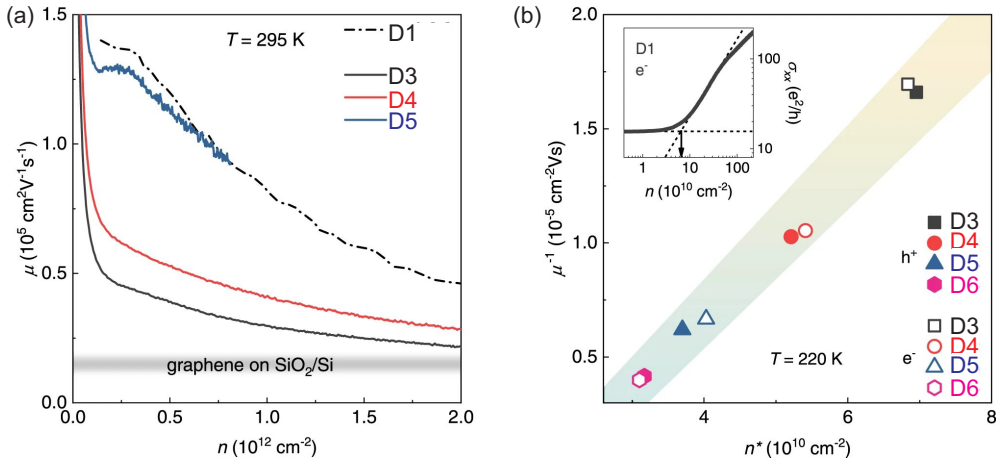


Figure 9.8: **(a)** RT carrier mobility (calculated according to the Drude model) as a function of the carrier concentration, for three hBN-encapsulated devices. The reference dash-dotted line are data from Ref. [57], indicating a carrier mobility limited by electron-acoustic phonon scattering. The grey-shaded area shows the typical mobility for  $\text{SiO}_2$ -supported Gr devices,  $1 - 2 \times 10^4 \text{ cm}^2/(\text{Vs})$ . **(b)** Inverse of the high-temperature (220 K) field-effect mobility as a function of charge inhomogeneity  $n^*$ , for hBN/Gr/hBN devices D3-6. The shaded area covers a linear fit to the data, as in Ref. [29],  $\pm$  one standard error on the best-fit intercept and slope. Inset: Log-Log plot of the longitudinal conductivity of sample D3 as a function of the carrier density, exemplifying the extraction of  $n^*$  (black arrow).

of  $\rho_{xx}$  for the devices D3-D5, at selected magnetic fields. In addition to our data, we show reference points from D1 (black diamonds, Gr on  $\text{SiO}_2$ ), and two theoretical calculations defining different dissipation limits (continuous lines). In both cases we take an activation energy equal to  $E_G/2$ , as this was shown to be accurate for high magnetic fields (see Fig. 9.9 and [185]) and should hold true for clean Gr with reduced LL-broadening. The upper line (yellow) assumes the universal conductivity pre-factor due to long-range disorder ( $2e^2/h$ ) [380], multiplied by a factor 4 taking the LL degeneracy of Gr into account (see Chapter 3.3). The lower line (dark cyan) is based on the work by Alexeev et al. [381], who calculated the conductivity mediated by two-phonon scattering for Gr in the RTQHE regime. The relevant e-ph process conserves the LL number, but modifies the in-plane electronic momentum. We note that this phenomenology is fundamentally different from that of magneto-phonon oscillations, recently discovered in extra-wide Gr devices [384], which rely on resonant inter-LL scattering at  $T < 200 \text{ K}$ . Here, two-phonon scattering within each LL contributes with a conductivity pre-factor  $\sigma_0 = \sigma_N(T/300 \text{ K})(B/10 \text{ T})^{1/2}$ , which depends both

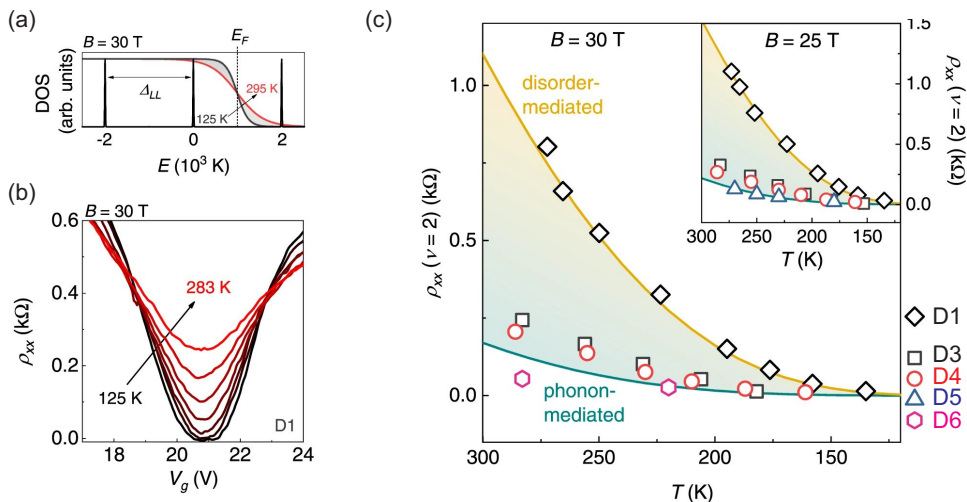


Figure 9.9: **(a)** DOS of Gr as a function of energy, at  $B = 30$  T (with a realistic value of LL broadening of 15 K). On top of the DOS we show the Fermi-Dirac distribution, with  $E_F$  positioned in the middle of  $LL_0$  and  $LL_1$ , at two different temperatures, representative of the experimental range considered. **(b)** Temperature-activated longitudinal resistivity in the vicinity of  $\nu = 2$ , measured in sample D3. **(c)** Minimum of  $\rho_{xx}$  at  $\nu = 2$  as a function of temperature, for the hBN-encapsulated devices. The yellow and dark cyan continuous line are theoretical calculations based on Ref. [380] and Ref. [381], respectively (the shading covers resistivity values within the two theoretical calculations). The magnetic field is 30 T (25 T) in the main panel (inset).

on temperature and magnetic field (in contrast to the constant pre-factor commonly assumed in QHE studies). In the  $\nu = 2$  state, the predominant contribution to the  $\sigma_N$  terms comes from the  $LL_0$  ( $0.65 e^2/h$ , one order of magnitude larger with respect to  $N = 1$ ,  $0.06 e^2/h$ ) [381]. Strikingly, the resulting activated behaviour, not including any free parameter, is well approximated by our devices, while the reference data from Gr on bare  $\text{SiO}_2$  follow the long-range disorder limit. The qualitative agreement between theoretical calculations and experimental data, together with the contrasting behavior with respect to previous reports [185], indicate that Gr/hBN heterostructures support an e-ph-dominated transport in the RTQHE regime. Arrhenius-type fits to the conductivity [385], confirm the contrasting magnitude of the pre-factor for the two generations of the Gr devices, as well as the correctness of the assumed gaps (see Fig. 9.9).

Despite the presence of long-range potentials (Fig. 9.9(b)), our data clearly indicate that the e-ph pre-factor does not simply add up to the standard long-range

disorder term. To elucidate this point, we quantitatively analyze the deviation from the phonon-mediated limit in the different devices. We proceed by fitting the data from D3-D5 (only two high  $T$  curves are acquired for D6 due to experimental limitations) with a generalized relation (Fig. 9.10, inset), which adds to the theoretical e-ph dependence from Ref. [381] an activation part with a constant pre-factor ( $\rho_D$ ). This term is intended to account for the effect of residual disorder, and it is the only free parameter in the fits. In Fig. 9.10 we plot the extracted  $\rho_D$  for the three samples at different magnetic fields, as function of the  $n^*$  parameter (averaged between the electron and hole side). The linear  $\rho_D(n^*)$  behaviour observed here (shaded area in Fig. 9.10) indicates that the random strain variations inducing the CNP broadening are also responsible for  $\rho_{xx}$  exceeding the e-ph limit in the RTQHE. Notably, the only device to display an exact e-ph-type dependence (D5,  $\rho_D \approx 0$ ), is also the one to show a Drude mobility comparable to the zero-field e-ph limit [57]. Taking into account the sample-dependent correction due to residual disorder, we proceed with a quantitative investigation of the field and temperature dependence of the conductivity pre-factor in the samples, revealing the expected  $B1/2$  behaviour of the e-ph term (see the SI of [363]). However, we note that the simplified pre-factor proposed in Ref. [381] is the result of several approximations and, more importantly, it neglects the effect of disorder. To better understand the interplay between the different scattering mechanisms underlying the activated resistivity, in the SI of [363], we also discuss additional data at lower temperature (down to 50 K) and magnetic field (down to 1 T). We find that  $\rho_D$  drastically increases toward low  $T$ , with the activated resistivity exceeding the e-ph limit by more than one order of magnitude in a clean sample. However, as the temperature and magnetic field are increased,  $\rho_D$  progressively drops (i.e., the activated resistivity tends toward the e-ph limit), suggesting a temperature-driven crossover between regimes dominated by either disorder or e-ph interaction (the latter being realized only close to RT). While it is not surprising that the e-ph limit works as a lower bound to the activated resistivity of real samples, the non-universality (i.e. the sample and temperature dependence) of the disorder contribution deserves particular attention in future theoretical treatments of the RTQHE in Gr.

The physics of Gr is essentially determined by its deviations from flatness (ripples), due to either thermal fluctuations associated to flexural phonons for freely suspended samples or to roughness of substrate like for Gr on  $\text{SiO}_2$  [12]. In both cases, ripples induce inhomogeneity of the electron density creating electron and hole puddles in the vicinity of the CNP [386, 387]. In particular, for the case of Gr on  $\text{SiO}_2$  the amplitude of induced inhomogeneity of the charge carrier density is estimated as  $3 \times 10^{11} \text{ cm}^{-2}$  [387], in agreement with the above cited experimental values for  $n^*$ . This makes the system strongly disordered, and any intrinsic scattering mechanisms become irrelevant. Oppositely, the hBN substrate is atomically flat and at the same time suppresses intrinsic ripples which increase the RT carrier mobility by an order of magnitude and makes intrinsic scattering mechanisms dominant [12]. Indeed, exper-



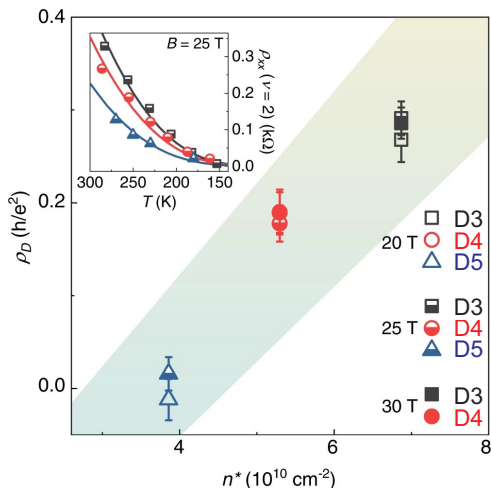


Figure 9.10: Correlation between the temperature independent pre-factor to the activated resistivity and  $n^*$  (220 K) for devices D3-5. The shaded area is defined as in Fig. 9.8(b). The error bars correspond to  $\pm$  one standard error from the fits shown in the inset. Inset: fit to the minimum resistivity as a function of temperature (continuous lines), using the generalized formula including both e-ph and disorder contributions, at  $B = 25 \text{ T}$ .

imentally measured  $n^*$  for our samples is an order of magnitude smaller than what is supposed to be induced by ripples at RT. This results in an essentially different picture of QHE physics at high enough temperatures.

## Conclusion

In conclusion, we presented experimental evidence of predominant e-ph scattering in the QH regime. This is realized by uniquely combining strong magnetic fields, high temperatures and hBN-encapsulation of Gr. Although the RTQHE in Gr has long been known, we showed that mitigation of disorder via van-der-Waals engineering provides novel insights on the transport mechanisms in this phenomenon.

## 9.4 Summary

In this chapter, our encapsulated CVD-Gr devices were used as top-notch references in an ensemble of transport devices fabricated by different techniques resulting in varying degrees of disorder. Measuring the device ensemble at varying temperatures in high magnetic fields up to 30 T allowed us to investigate in two different works

the manifestation and temperature-induced breakdown of the RTQHE as well the predominant scattering mechanisms in this regime. The interpretation of the findings of these studies allowed us to apply all the insights into the microscopic pictures of the QHE gained in Chapter 4. The long-range part of the disorder potential proved to be an essential ingredient in both topics. We provided conclusive experimental evidence for the first time, that LRPFs facilitate the stabilization of the HP resulting in the perseverance of the QHE up until RT in the most disordered devices on bare  $\text{SiO}_2$ , while the effect vanished already at few percent of the cyclotron gap in high-quality encapsulated heterostructures. Furthermore, we could show, that decreasing the LRPF level shifts the predominant scattering mechanism in the RTQHE regime from extrinsic (disorder mediated) to intrinsic (electron-phonon mediated). Future studies analogue to the ones presented in this chapter, but with devices employing different screening lengths, might provide extremely interesting further insights for the conditions and influences of the Gr edge on the manifestation and temperature-induced breakdown of the QHE and moreover take the devices closer to the disorder-free limit. These experimental efforts should go hand in hand with detailed self-consistent modelings of the investigated systems.



# Chapter 10

## Summary and Outlook

### 10.1 Summary

In 2009, CVD-Gr emerged as the most promising candidate for scalable industrial applications of the material. However, due to the wet transfer methods commonly employed to prepare CVD-Gr on arbitrary substrates after growth, the quality of Gr decreases, leading to devices with much poorer electrical performance in transport measurements. Lacking non-invasive transfer methods for comparison, researchers were led to believe that the intrinsic quality of CVD-Gr was inferior to Ex-Gr.

In 2015, we demonstrated that the intrinsic quality of CVD-Gr must be considerably higher than expected when a dry transfer method, relying only on van der Waals forces, is used to directly fabricate the as-grown material into hBN/Gr/hBN heterostructures. Dry-transferred CVD-Gr devices were shown to achieve on average very high carrier mobilities, well comparable to state-of-the-art exfoliated reference devices. However, the question remained whether this comparability of basic transport properties also implied that the intrinsic qualities were truly equal.

These considerations mark the starting point of this thesis, which aimed primarily to provide evidence for the equality of CVD-Gr and Ex-Gr. To this end, the LPCVD process as well as the dry-transfer and the 2D fabrication process were optimized to obtain heterostructures of the highest structural quality. Methods were introduced to monitor and forcibly control the oxidation of the Cu/Gr interface for reliable dry pickup, including blue Raman spectroscopy on the Cu foil using a blue laser and a humidifier setup. To allow a deeper understanding of our CVD process, the dry transfer, and their perspectives for the future, a detailed review of the state of the art of the CVD-Gr research field was presented in a separate chapter of this thesis. Several adaptations and enhancements were made to our 2D material transfer system to enable highly precise heterostructure assembly and removal of contamination-containing bubbles from the heterostructure interfaces afterward. As a result, a new

transfer arm was designed, allowing the transfer system to be used for sandwiching CVD-Gr half-stacks and introducing PC membranes to stack heterostructures from scratch or pick up already assembled ones to remove bubbles from their interfaces. As a result of these enhancements, several hBN/CVD-Gr/hBN heterostructures of the highest structural quality were built on top of SiO<sub>2</sub> substrates and processed into transport devices. After pre-characterizations in our facilities, these devices were measured in a high magnetic field laboratory, where signatures of the FQHE were visible at magnetic fields below 3 T, and at 35 T, fractional states with an effective CF filling factor  $\nu^* = 4$  could be clearly resolved along with higher-order (4-flux) states. Activation gap measurements revealed that the  $p/3$  states had gaps of up to 30 K, comparable to those in the best Ex-Gr heterostructure devices on SiO<sub>2</sub> substrates. We thus provided evidence for the first time that the quantum mobility in our CVD-Gr samples matches that of exfoliated material and, therefore, that the intrinsic quality of both is equal.

Achieving this fundamental goal enables us to use our CVD-Gr devices in an ensemble of other Gr devices based on Ex-Gr, fabricated by different techniques and device geometries that result in varying degrees of sample disorder level. Temperature-dependent high magnetic field measurements were carried out on all these devices, allowing us to compare the dynamics of several interesting Gr transport properties in the QHE regime with respect to the disorder level. In the first study, the manifestation dynamics of the RTQHE in relation to the disorder level was investigated by evaluating the Hall plateau widths at filling factor  $\nu = 2$  as a function of temperature. Although the extracted activation gaps were comparable in all devices at various magnetic fields, the plateaus at base temperature shrank in width with increasing device mobility, as did the breakdown temperature at which the plateaus vanished. A pronounced RTQHE was only observed in the lowest quality devices fabricated on bare SiO<sub>2</sub> surfaces, while the plateaus disappeared well below 150 K in the highest quality devices at 30 T. The observed dynamics confirm for the first time that the long-range part of the disorder potential (which is strongest in our lowest mobility devices) leads to a stabilization of the Hall plateaus at room temperature, which can be understood as an increased density of localized states in the conventional microscopic picture of the QHE or as an extension of incompressible regions above integer filling located in the channel bulk in the screening picture frame of the effect. To elucidate the often-neglected role of the microscopic pictures of the QHE, the most important aspects of the conventional single-particle picture and the interaction and screening-mediated picture are reviewed in detail in Chapter 4 of this thesis.

In a second study, the predominant scattering mechanism in Gr channels in the RTQHE regime in relation to the disorder level was investigated for the first time. Evaluating the resistivity minima at filling factor  $\nu = 2$  and introducing a non-constant pre-factor in the Arrhenius formula allowed us to locate the devices between

a purely disorder-mediated and an intrinsic, electron-phonon scattering-mediated regime. The strongly disordered devices on bare  $\text{SiO}_2$  matched the expected dynamics for disorder-mediated scattering, while with increasing device mobility, we observed a continuous shift towards a purely electron-phonon-mediated scattering regime, where our CVD-Gr devices were most closely fitting the intrinsic scattering model.

This thesis, therefore, presents significant advancements and comprehensive reviews in the fields of CVD process engineering and 2D material fabrication, as well as in the realm of high magnetic field transport physics in Gr and the quantum Hall effect in general. It paves the way for future research and technological developments.

## 10.2 Outlook

The findings of this work, along with the reviewed research and models on the QHE and CVD, enable us to outline open questions, possible future experiments, and perspectives on the future potential of technologies like our dry transfer. Some of these thoughts will be discussed in the following.

### Quantum Hall Effect in Graphene

The unique electronic properties of Gr lead to fascinating consequences, such as a QHE observable at RT and a wide array of intricate many-body phenomena at low temperatures. The interaction-driven nature of these effects necessitates the adoption of suitable microscopic models to fully understand their consequences and conceive new experiments. Therefore, the relevance of the screening picture of the QHE for future research cannot be emphasized enough, and efforts should be made to understand the formation of (in)compressible landscapes and their dynamics at various fillings in Gr systems. Many open questions remain concerning the microscopic conditions at the Gr channel edges, usually obtained by etching, as various works imply an edge-agglomeration of electrons leading to the well-known electron-hole asymmetries in transport measurements. The conclusive explanations for the charge accumulation are missing so far, and thus, the Gr edges cannot be modeled without remaining doubts in self-consistent calculations. Experimental investigations of the IS formation at the edges in the QHE regime could be one way to gain information on the edge potentials and might be realized in combined transport and scanning probe or STM measurements on exposed Gr sheets. Another aspect to explore would be the screening length, which is predominantly determined by the gate dielectrics and thickness. Performing similar measurements like the ones shown in Chapter 9 of this work in devices with close graphitic gates, or even in gate-defined channels would provide valuable insights. Lastly, it is, of course, possible to tune the interaction strength in the Gr itself by employing materials with high dielectric constants like  $\text{SrTiO}_3$

( $\epsilon \approx 30000$  at 1.6 K) and investigate how the QHE manifestation is altered microscopically in the ground state as well as for higher LL. Effects of evanescent IS could also provide valuable insights, and all the mentioned experiments should be supported by self-consistent calculations.

## Perspectives of the Dry Transfer of CVD Graphene

As of now, chemical vapor deposition remains the most promising candidate for achieving scalable growth of high-quality Gr for high-tech applications. Our work on the dry transfer process is of significant pioneering character, first by providing a proof-of-work along with a demonstration of the greatly increased device performance of so-transferred mono- and bilayer Gr [8, 9, 326]. In this thesis, several process optimizations were carried out to gain control over the water-mediated oxidation of the Cu/Gr interfaces and improve the transfer mechanics, which ultimately allowed proving the intrinsic equality of CVD-Gr and exfoliation-derived material [388]. This allows us to envision the remarkable properties of Gr being exploited to an even greater extent in the future. However, it is crucial to evaluate whether our dry transfer has the potential to be adapted on scales much larger than the tens of micrometers scale given by the size of the exfoliated hBN crystals used for pick-up.

To achieve the final goal of high-quality Gr heterostructures on wafer-scale, an ideal dry-transfer process must fulfill three requirements:

- (a) Wafer-scale single-crystal adlayer- and fold-free monolayer Gr on top of a smooth metal surface.
- (b) Wafer-scale single-crystal 2D materials like hBN with sufficient thickness on a carrier substrate.
- (c) A strategy to weaken the metal/Gr interface homogeneously over the entire covered area.

From the extensive review of the state-of-the-art in CVD growth in Chapter 5, we can conclude that requirements (a) and (b) have been fulfilled in recent years. However, our detailed understanding of the water-mediated oxidation process of Cu(111)/Gr surfaces implies that for a perfectly smooth Cu surface without step-bunching-induced wrinkles in the Gr sheet, the reactive oxygen species from dissociated water molecules cannot percolate into the interface and drive its oxidation (i.e. (a) precludes (c)). This issue can only be resolved either by modifying (a) or (c) again. One could, for example, explore the wide range of Cu surface orientations and try to find others than (111) that match the properties of (a) (as was done, e.g. in [318]), or investigate techniques for weakening the interface that do not rely on water-mediated oxidation. In this regard, the growth of Gr in the interface between a sapphire substrate and Cu(111) with a liquid N<sub>2</sub> mediated detachment of the Cu [280] could turn out to be a significant breakthrough, as the Gr might already be picked up and encapsulated by

wafer-scale 2D materials in a controlled environment. One can imagine adapting the concept of wafer bonding machines for this purpose, realized in ultra-high vacuum conditions to reduce the contamination with hydro-carbon species and water usually present in the air. However, it is evident that with our current LPCVD setup and growth process on the inside of Cu enclosures, we can hardly participate in the quest for a perfect dry-transfer, as we cannot match the state-of-the-art technology and processes for either requirement (a) or (b). In order to increase the outcome and quality of our CVD process, it would be desirable to adapt, if possible, some of the knowledge presented above. The annealing process used to transform polycrystalline Cu foil into single-crystal Cu(111) foil could be adapted for our system to step up from the foil used at the moment. Furthermore, it might be worthwhile to abandon the enclosure growth approach, as several relevant growth parameters like the partial pressures inside the enclosures can neither be monitored nor controlled. For maximized reproducibility as well as Gr orientation homogeneity, adapting a growth process on pre-annealed plain Cu(111) foils would be optimal. Therefore, higher total pressures together with much lower  $\text{CH}_4$  partial pressures should be established to obtain a low nucleation density. Switching to MFCs with lower minimum flows and/or gas mixtures (e.g.  $\text{H}_2$  with 5 %  $\text{CH}_4$ ) would be required. To avoid contamination with amorphous carbon, mimicking the conditions in cold-wall reactors would be beneficial, i.e., by implementing inductive heating of the metal substrate. This might also help to establish a more homogeneous temperature across the metal foil.

By addressing these challenges and optimizing the CVD and dry transfer processes, we can move closer to realizing the full potential of Gr for various applications. The advancements made in this thesis set the stage for future research and development in the fields of CVD process engineering, 2D material fabrication, and high magnetic field transport physics in Gr and the quantum Hall effect in general. With continued improvements and innovations, we can expect to see even greater progress in the production and application of Gr, paving the way for new technologies and applications in electronics, photonics, and other emerging fields.





# Appendices

## A Fabrication Details

Process	Description of process steps
<b>CVD growth of monolayer graphene</b>	<ol style="list-style-type: none"> <li>1. Cu foil preparation               <ol style="list-style-type: none"> <li>(a) Cut the foil into <math>7.6 \times 12</math> cm pieces</li> <li>(b) Process the foil in ammonium persulfate solution (3-7 g/200 ml), 2 subsequent DI water baths, acetone, and IPA for 2 minutes each. Blow dry afterward.</li> <li>(c) Bring the short edges of the foil together and start folding the edges over with a 7 mm width, then crease with a glass slide. Afterward, refold all three edges again and crease with a glass slide.</li> </ol> </li> <li>2. CVD growth               <ol style="list-style-type: none"> <li>(a) Place 2 Cu enclosures on the glass boat and move it to the center of the reactor tube. Mount the Cu heat shield on the left side of the reactor and connect the flange.</li> <li>(b) Start the rotary vane pump and evacuate the system. The enclosures should inflate. Open the Ar, H<sub>2</sub>, and CH<sub>4</sub> MFCs and valves to clear potential gas contaminants. Afterward, close them off again and start up the turbo pump.</li> <li>(c) Set a flow of 15 sccm H<sub>2</sub> and start the oven heating system, ramping the reactor temperature up to 1035 °C in 45 minutes, and close the lid of the oven.</li> <li>(d) After reaching growth temperature, anneal the enclosures at a constant flow for another 15 minutes to reduce and remove contamination.</li> <li>(e) Initiate graphene growth by setting a flow of 5/45 sccm CH<sub>4</sub>/H<sub>2</sub> for 3 hours.</li> <li>(f) Stop the heating system and carefully open the lid of the oven for rapid cool down. Once at room temperature, switch off the process gases, stop the pumps, and flood the reactor chamber with Ar gas until ambient pressure is reached. Remove the flange and take out the enclosures.</li> </ol> </li> <li>3. Interface oxidation               <ol style="list-style-type: none"> <li>(a) Cut open the enclosures along the over-folded edges and inspect the growth result using dark field microscopy. If needed, flatten them off using a microscope slide.</li> <li>(b) Place the opened enclosures on the stage of the humidifier and cover them with a Petri dish to avoid direct precipitation of water drops onto it.</li> <li>(c) Close the desiccator and start the hot plate underneath. Store the enclosures in the humidifier for 48h at 30 °C and 99</li> <li>(d) Monitor the Cu/Gr interface oxidation via optical microscope and Raman spectroscopy with the 457 nm laser.</li> </ol> </li> </ol>

Process	Description of process steps
<b>Dry pick-up of CVD-Gr</b>	<p>1. Prepare transfer slides</p> <ul style="list-style-type: none"> <li>(a) Break a glass slide in half with a diamond razer and cover the upper side with Pritt tape. Smooth the tape using Kim wipes</li> <li>(b) Drop coat PVA solution (13 %) onto the slides with a pipette and smear it until the whole surface is covered with a thick homogeneous layer</li> <li>(c) Set slides on hot plate first at 98 °C to dry the PVA out, afterwards bake for 10 minutes at 110 °C</li> <li>(d) Spin coat PMMA (50K) onto the slides with 3000 rpm for 60 s</li> <li>(e) Bake on hot plate for 10 minutes at 110 °C</li> <li>(f) Prepare an hBN tape and exfoliate hBN crystals onto the PMMA surface of the slides</li> <li>(g) Identify suitable hBN flakes with an optical microscope, take meaningful pictures and cut a square shaped box (4 mm) around them using a sharp knife</li> </ul> <p>1. Dry pick up in the mask aligner system</p> <ul style="list-style-type: none"> <li>(a) Identify a suitable graphene crystal with fully oxidized Cu/Gr interface on the Cu foil in the microscope, acquire meaningful images and mark the flake region by making scratch</li> <li>(b) Cut the foil down to a small square around the scratch and flatten it using a microscope slide. Mount the foil on the lower stage of the mask aligner</li> <li>(c) Fix a microscope slide across the cut out section of the upper stage of the mask aligner using tape and place a PDMS cushion in its center</li> <li>(d) Carefully detach the PVA/PMMA stamp with the marked hBN crystal on it from its slide using tweezers and place it on top of the PDMS cushion</li> <li>(e) Mount the upper stage inside the mask aligner such that the PVA/PMMA stamp is facing downwards</li> <li>(f) Locate the hBN crystal and the graphene on the Cu foil and align them using the micro manipulators of the lower stage</li> <li>(g) Use the z-screw to bring the Cu in close proximity of the hBN stamp</li> <li>(h) Set the stage heater to 120 °C and bring the foil into contact with the stamp, such that the hBN sits on the graphene. Leave in contact at this temperature for 2 minutes</li> <li>(i) Switch-off the heating system and, once the temperature is below 80 °C, move the lower stage down</li> <li>(j) Remove the Cu/stamp from the mask alinger, acquire microscope images if necessary and carefully detach the stamp from the Cu foil using tweezers</li> </ul>
<b>Sandwich completion using the transfer system</b>	<p>1. Prepare bottom hBN crystal</p> <ul style="list-style-type: none"> <li>(a) Cut a 4 inch Si/SiO<sub>2</sub> wafer down into slides suitable for exfoliation using a diamond scratcher</li> <li>(b) Prepare an hBN tape press the wafer slides onto it.</li> <li>(c) After peeling the tape off after 10 minutes, inspect the slide surface with a microscope and identify suitable hBN crystals. Acquire meaningful images and mark the hBN flake region with a marker pen</li> </ul>

Process	Description of process steps	
	<p>2. Stacking in the transfer system</p> <p>(a) Mount the slide with the bottom hBN on the substrate stage of the transfer system and move the desired hBN crystal into the center using the stage mechanics</p> <p>(b) Mount a PDMS cushion on top of a cover glass and place the PVA/PMMA stamp with the hBN/CVD-Gr on its surface on it</p> <p>(c) Vacuum mount the cover glass with the PVA/PMMA stamp facing downwards under the new transfer arm, such that the stamp is in its center</p> <p>(d) Identify the hBN/CVD-Gr on the stamp and pre-align it with the bottom hBN on the substrate stage using the transfer tower mechanics.</p> <p>(e) Bring the transfer stamp and the bottom hBN in close proximity using the z-screw of the transfer tower. Carefully adjust the alignment.</p> <p>(f) Heat the transfer stage to 120 °C and slowly bring the stamp into contact with the substrate, laminating the hBN/CVD-Gr onto the bottom hBN.</p> <p>(g) While still in contact, rise the temperature to 140 °C and bake the stack for 5 minutes.</p> <p>(h) Lift the transfer arm up, detaching the stamp/substrate from the PDMS cushion.</p> <p>2. Removing the stamp</p> <p>(a) Dissolve the PVA in hot DI water (90 °C) for 10 minutes</p> <p>(b) Dissolve the PMMA in acetone and subsequently clean in IPA for 5 minutes each, followed by blow dry with a nitrogen gun</p>	
<b>Bubble removal</b>	<p>1. Preparing PC stamps</p> <p>(a) Drop coat PC solution (7 %wt. in chloroform) onto glass slides cut in half and spin coat for 1 minute at 500 rpm without pre acceleration</p> <p>(b) Slowly dry the slides on a hot plate at 50 °C for 10 minutes and leave them in air for at least 1 hour afterwards.</p> <p>(c) Cut square shaped stamps into the PC layer with sharp knife</p> <p>2. Stack pickup/Bubble removal</p> <p>(a) Mount a substrate with the to be cleaned heterostructure on top on the substrate stage of the transfer system</p> <p>(b) Detach a PC stamp from its slide using tweezers and place it on a PDMS cushion mounted in the center of a cover slide</p> <p>(c) Mount the transfer stamp on the bottom side of the new transfer arm with stamp facing downwards in its center</p> <p>(d) Align the stamp over the heterostructure, such that it will sit in the center of the lower third of the stamp</p> <p>(e) Preheat the substrate stage to 110 °C, and bring the stamp into contact with the heterostructure. While in contact, raise the temperature to 145 °C and decrease it to 110 °C again</p> <p>(f) Carefully rise the transfer arm, detaching the stamp with the heterostructure from the substrate. At this point, the substrate can be exchanged, e.g. for a marked chip</p> <p>(g) Move the transfer arm down again until the lower end of the stamp gets into contact with the substrate. Then set the heating system to 185 °C and during heating stop the contact front of the stamp from advancing by carefully moving up the transfer arm.</p> <p>(h) Once the temperature is above 180 °C use the z-screw to move the contact front across the heterostructure slowly laminating it onto the substrate. Movable bubbles will follow the contact front. The stamp will go into full contact with the substrate.</p> <p>(i) After baking for 5 minutes at maximum temperature, deactivate the heating system and rise the transfer arm, such that the stamp/substrate detach from the PDMS.</p> <p>2. Removing the PC stamp</p> <p>(a) Dissolve the PC stamp in chloroform for 5 minutes, followed by cleaning in acetone and IPA for 2 minutes each and blow dry with nitrogen gun afterwards.</p>	

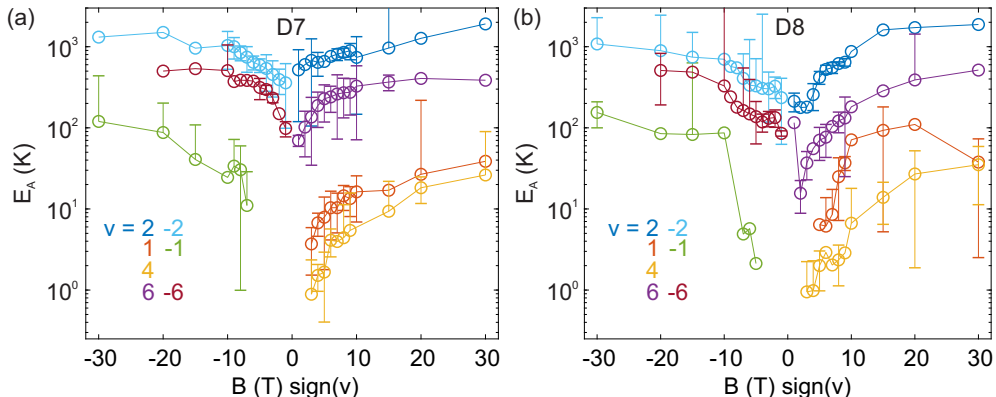


Figure B.1: (a) and (b) Extracted activation energies  $E_A$  for different integer filling factors  $\nu$  as function of the magnetic field times the sign of filling  $B \text{ sign}(\nu)$  for D7 and D8.

## B Supplementary Material RTQHE

### Breakdown Temperature

#### B.1 Activation of the Interaction-Mediated Landau Levels

The measurements on D7 and D8 performed in the HFML as presented in Chapter 9 were complemented by respective transport studies in our VTI system covering the phase window between 1.6 K and 300 K in temperature and 0 to 9 T in magnetic field. From the longitudinal resistance data, the activation energies  $E_A$  were extracted using (4.12) for different integer filling factors and the results are shown in Fig. B.1. The considerable error bars on some of the values resulting from fitting indicate, that the applied method might have to be reevaluated. Since we found evidence in Chapter 9, that our HQ CVD-Gr devices well approach the limit of intrinsic electron-phonon scattering at higher temperatures, these effects should be included in the model. However, due to the square shaped geometry of D7 and D8, the required resistivity cannot be calculated right away and van-der-Pauw evaluations following Eq. (2.23) yielded no constant calibration curves. Owing to these difficulties, a deeper analysis of these data cannot be presented within this work but might be investigated in future measurements, that could also compare them with activation energies from similar devices using a gate defined channel geometry like [39].

## B.2 Plateau Overshoots on the Bulk Side

Upon closer inspection of the Hall conductivities of D7 in Chapter 9 a buckle-like feature appears on the lower filling/charge carrier density side, that gets more pronounced (the height of the buckle increases) with increasing magnetic field. Fig. B.2 shows the evolution of the Hall plateaus of D7 with temperature for fixed magnetic fields from 10 T to 30 T. At 10 T, no adverse behavior is noted. At 20 T the lowest temperature curves slightly detach upwards from the otherwise linear slope in between the plateaus at the higher temperatures. At 20 T and 30 T the a pronounced buckle is visible, with an amplitude increasing with decreasing temperature.

The origins of this buckle could not be clarified in the frame of this work, however, they resemble the overshoot features recognized as an effect of evanescent IS as described in Chapter 4.2. While in the works of Siddiki et al., the overshoots were predominantly visible on the *edge-dominated*, low magnetic field side of the Hall plateaus in conventional 2DES transport channels, in our CVD-Gr, the feature manifests on the *bulk-dominated* side of the plateaus as a *dip* in the resistivity. Although a similar mechanism basing on the interplay of *leaky* IS of different filling factor that coexists at the same magnetic fields, a quantitative elaboration to which these data could be compared is so far missing from the theory side and offers future potential.

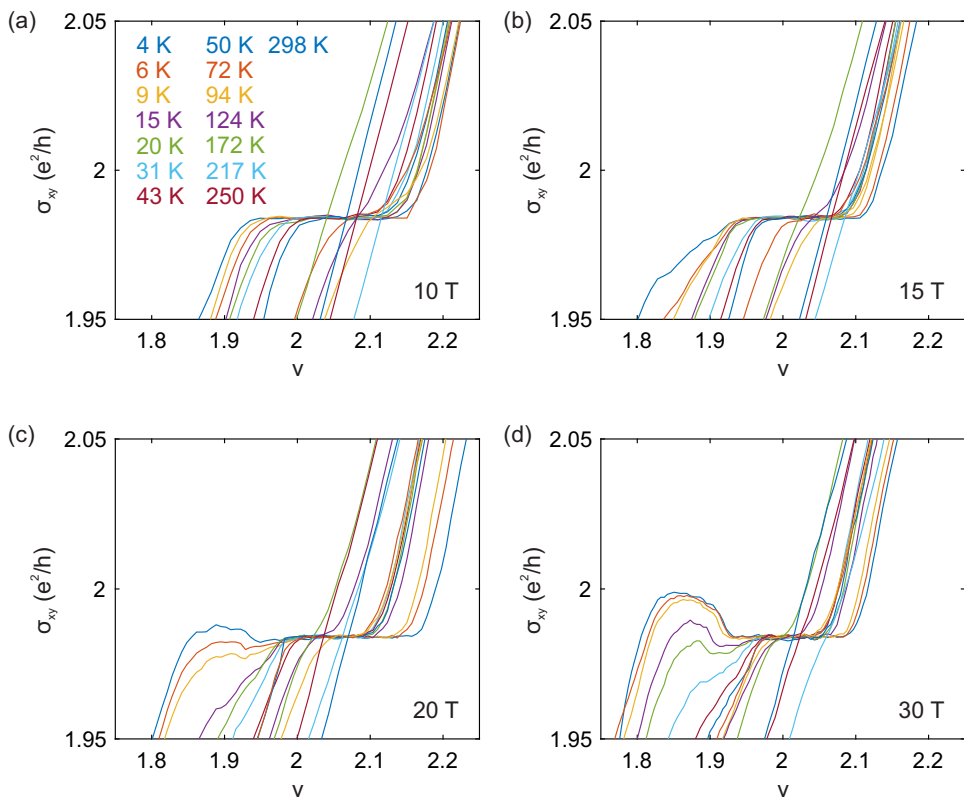
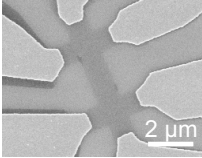
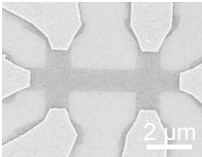
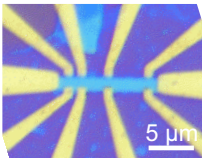
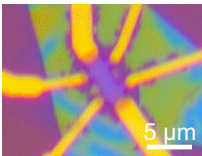
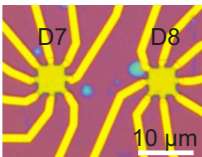


Figure B.2: **(a) - (d)** Hall conductivity  $\sigma_{xy}$  as function of filling factor  $\nu$  for different temperatures and fixed magnetic fields for D7. In **(c)** and **(d)**, the plateaus exhibit a pronounced overshoot on the low filling side.

## C List of samples

name	picture	device info	measurements
D1		<ul style="list-style-type: none"> <li>• 1 Channel, <math>1.5 \times 0.5 \mu\text{m}</math></li> <li>• Gr</li> </ul>	<ul style="list-style-type: none"> <li>• Chapter 9</li> </ul>
D2		<ul style="list-style-type: none"> <li>• 1 Channel, <math>1.5 \times 0.5 \mu\text{m}</math></li> <li>• Gr</li> </ul>	<ul style="list-style-type: none"> <li>• Chapter 9</li> </ul>
D3-D5		<ul style="list-style-type: none"> <li>• 3 Channels, <math>3 \times 1.5 \mu\text{m}</math>, <math>4.5 \times 1.5 \mu\text{m}</math>, <math>3 \times 1.5 \mu\text{m}</math>,</li> <li>• hBN/Gr/hBN</li> </ul>	<ul style="list-style-type: none"> <li>• Chapter 9</li> </ul>
D6		<ul style="list-style-type: none"> <li>• 1 Channel, <math>4 \times 2.3 \mu\text{m}</math></li> <li>• hBN/CVD-Gr/hBN</li> </ul>	<ul style="list-style-type: none"> <li>• Chapter 8</li> <li>• Chapter 9</li> </ul>
D7-D8		<ul style="list-style-type: none"> <li>• 2 Channels, <math>5 \times 5 \mu\text{m}</math></li> <li>• hBN/CVD-Gr/hBN</li> </ul>	<ul style="list-style-type: none"> <li>• Chapter 9</li> </ul>



# Publications

Authors marked with \* contributed equally.

## Phonon-mediated room-temperature quantum Hall transport in graphene

*D. Vaquero, V. Clerico, M. Schmitz, J.A. Delgado-Notario, A. Martin-Ramos, J. Salvador-Sanchez, C.S.A. Müller, K. Rubi, K. Watanabe, T. Taniguchi, B. Beschoten, C. Stampfer, E. Diez, M.I. Katsnelson, U. Zeitler, S. Wiedmann and S. Pezzini*  
Nat. Commun. **14**, 318 (2023)

## Fractional quantum Hall effect in CVD-grown graphene

*M. Schmitz, T. Ouaj, Z. Winter, K. Rubi, T. Taniguchi, K. Watanabe, U. Zeitler, B. Beschoten and C. Stampfer*  
2D Mater. **7**, 041007 (2020) (or: arXiv: 2005.08938).

## High mobility dry-transferred CVD bilayer graphene

*M. Schmitz, S. Engels, L. Banszerus, K. Watanabe, T. Taniguchi, C. Stampfer and B. Beschoten*  
APL **110**, 263110 (2018) (or: arXiv: 1704.04352).

## Ballistic Transport Exceeding 28 $\mu\text{m}$ in CVD Grown Graphene

*L. Banszerus\*, M. Schmitz\*, S. Engels\*, J. Dauber, M.Oellers, F. Haupt, K. Watanabe, T. Taniguchi, B. Beschoten and C. Stampfer*  
Nano Lett. **16**, 1387 (2016) (or: arXiv: 1511.08601).

## Line shape of the Raman 2D peak of graphene in van der Waals heterostructures

*C. Neumann, L. Banszerus, M. Schmitz, S. Reichardt, J. Sonntag, K. Watanabe, T. Taniguchi, B. Beschoten and C. Stampfer*  
Phys. Status Solidi B **12**, 253 (2016) (or: arXiv: 1608.02798).

## Probing electronic lifetimes and phonon anharmonicities in high-quality chemical vapor deposited graphene by magneto-Raman spectroscopy

*C. Neumann, D. Halpaap, S. Reichardt, L. Banszerus, M. Schmitz, K. Watanabe, T. Taniguchi, B. Beschoten and C. Stampfer*  
APL **107**, 233105 (2015) (or: arXiv: 1511.08984).

**Raman spectroscopy as probe of nanometre-scale strain variations in graphene**

*C. Neumann, S. Reichardt, P. Venezuela, M. Drögeler, L. Banszerus, **M. Schmitz**, K. Watanabe, T. Taniguchi, F. Mauri, B. Beschoten, S.V. Rotkin and C. Stampfer*  
Nat. Commun. **6**, 8429 (2015).

**Graphen auf dem Weg zur Anwendung**

*L. Banszerus, **M. Schmitz**, B. Beschoten and C. Stampfer*  
Physik in unserer Zeit **6**, 269 (2015).

**Ultrahigh-mobility graphene devices from chemical vapor deposition on reusable copper**

*L. Banszerus\*, **M. Schmitz**\*, S. Engels\*, M. Goldsche, K. Watanabe, T. Taniguchi, B. Beschoten and C. Stampfer*  
Sci. Adv. **1**, e1500222 (2015).

# List of Figures

2.1	Electronic Properties - Crystal structure . . . . .	6
2.2	Electronic Properties - Band structure . . . . .	8
2.3	Electronic Properties - Ambipolar field effect . . . . .	13
2.4	Electronic Properties - hBN lattice . . . . .	15
2.5	Electronic Properties - Phonon modes . . . . .	17
2.6	Electronic Properties - Raman spectrum . . . . .	18
3.1	QHE 1 - Hall bar schematic . . . . .	23
3.2	QHE 1 - Cyclotron motion . . . . .	25
3.3	QHE 1 - LL spectrum of graphene and a c2DES . . . . .	27
3.4	QHE 1 - Degeneracy lifting . . . . .	30
3.5	QHE 1 - Graphene groundstate . . . . .	31
3.6	QHE 1 - CF formation . . . . .	33
3.7	QHE 1 - CF Pyramid . . . . .	36
3.8	QHE 1 - Point quantization . . . . .	37
3.9	QHE 1 - Original QHE Measurements . . . . .	39
4.1	QHE 2 - Localization . . . . .	45
4.2	QHE 2 - Laughlin's argument . . . . .	48
4.3	QHE 2 - Büttiker edge channels . . . . .	52
4.4	QHE 2 - Conventional temperature dependence . . . . .	56
4.5	QHE 2 - Edge reconstruction . . . . .	62
4.6	QHE 2 - Current flow . . . . .	66
4.7	QHE 2 - Plateau regimes and hot spots . . . . .	69
4.8	QHE 2 - Selfconsistent loop . . . . .	70
4.9	QHE 2 - LRSRPF . . . . .	73
5.1	CVD - Growth mechanisms . . . . .	80
5.2	CVD - Growth reactors . . . . .	83
5.3	CVD - Single crystal annealing . . . . .	85
5.4	CVD - Step bunching image . . . . .	86
5.5	CVD - Step bunching . . . . .	87

5.6	CVD - Fold formation . . . . .	88
5.7	CVD - Sapphire interface growth . . . . .	90
5.8	CVD - Transfer processes . . . . .	91
5.9	CVD - Wet and dry transfer processes . . . . .	94
5.10	CVD - Oxidation Raman spectra . . . . .	95
6.1	Fabrication - hBN exfoliation . . . . .	101
6.2	Fabrication - graphite exfoliation . . . . .	102
6.3	Fabrication - Typical exfoliation results . . . . .	103
6.4	Fabrication - CVD setup . . . . .	104
6.5	Fabrication - Enclosure folding . . . . .	104
6.6	Fabrication - CVD process diagram . . . . .	105
6.7	Fabrication - Bright- and dark field microscopy . . . . .	106
6.8	Fabrication - Bright- Humidifier . . . . .	107
6.9	Fabrication - Raman monitoring of Cu/Gr oxidation . . . . .	108
6.10	Fabrication - CVD transfer schematic . . . . .	110
6.11	Fabrication - Transfer system . . . . .	112
6.12	Fabrication - PC transfer . . . . .	115
6.13	Fabrication - Bubble removal . . . . .	118
6.14	Fabrication - Raman on stacks . . . . .	119
6.15	Fabrication - Device fabrication . . . . .	121
7.1	Measurement systems - VTI setup . . . . .	126
7.2	Measurement systems - Nijmegen setup . . . . .	127
8.1	FQHE - Low temperature magneto-transport measurements . . . . .	134
8.2	FQHE - High magnetic fields measurements . . . . .	135
8.3	FQHE - Activation gap measurements . . . . .	136
9.1	RTQHE - Device pictures . . . . .	140
9.2	RTQHE - $n^*$ and mobility . . . . .	142
9.3	RTQHE - LL spectrum and QHE in Gr . . . . .	143
9.4	RTQHE - Basic quantities . . . . .	144
9.5	RTQHE - Ensemble results . . . . .	147
9.6	RTQHE - Temperature induced breakdown . . . . .	148
9.7	RTQHE - Dissipation regimes . . . . .	154
9.8	RTQHE - Phonon limit . . . . .	155
9.9	RTQHE - Temperature activation . . . . .	156
9.10	RTQHE - Sample dependent disorder . . . . .	158
B.1	Appendix - RTQHE Activation energies D7 and D8 . . . . .	170
B.2	Appendix - RTQHE Plateau overshoots . . . . .	172

# Bibliography

- [1] L. von Mises, *Human Action: A treatise on economics* (Yale University Press, 1949).
- [2] M. N. Rothbard, *Man, Economy and State* (Van Nostrand, 1962).
- [3] M. N. Rothbard, *The Ethics of Liberty* (Humanities Pr., U.S.A., 1982).
- [4] K. S. Novoselov, A. K. Geim, S. V. Morozov, D. Jiang, Y. Zhang, S. V. Dubonos, I. V. Grigorieva, and A. A. Firsov, *Electric Field Effect in Atomically Thin Carbon Films*, Science **306**, 666 (2004).
- [5] V. Dhinakaran, M. Lavanya, K. Vigneswari, M. Ravichandran, and M. D. Vijayakumar, *Review on exploration of graphene in diverse applications and its future horizon*, Mater. Today: Proc. **27**, 824 (2020).
- [6] M. A. Al Faruque, M. Syduzzaman, J. Sarkar, K. Bilisik, and M. Naebe, *A Review on the Production Methods and Applications of Graphene-Based Materials*, Nanomaterials **11**, 2414 (2021).
- [7] X. Li, W. Cai, J. An, S. Kim, J. Nah, D. Yang, R. Piner, A. Velamakanni, I. Jung, E. Tutuc, et al., *Large-Area Synthesis of High-Quality and Uniform Graphene Films on Copper Foils*, Science **324**, 1312 (2009).
- [8] L. Banszerus, M. Schmitz, S. Engels, J. Dauber, M. Oellers, F. Haupt, K. Watanabe, T. Taniguchi, B. Beschoten, and C. Stampfer, *Ultrahigh-mobility graphene devices from chemical vapor deposition on reusable copper*, Sci. Adv. **1**, e1500222 (2015).
- [9] L. Banszerus, M. Schmitz, S. Engels, M. Goldsche, K. Watanabe, T. Taniguchi, B. Beschoten, and C. Stampfer, *Ballistic Transport Exceeding 28  $\mu\text{m}$  in CVD Grown Graphene*, Nano Lett. **16**, 1387 (2016).
- [10] K. I. Bolotin, F. Ghahari, M. D. Shulman, H. L. Stormer, and P. Kim, *Observation of the fractional quantum Hall effect in graphene*, Nature **462**, 196 (2009).
- [11] C. R. Dean, A. F. Young, P. Cadden-Zimansky, L. Wang, H. Ren, K. Watanabe, T. Taniguchi, P. Kim, J. Hone, and K. L. Shepard, *Multicomponent fractional*

- quantum Hall effect in graphene*, Nat. Phys. **7**, 693 (2011).
- [12] M. I. Katsnelson, *Graphene: Carbon in Two Dimensions* (Cambridge University Press, Cambridge, England, UK, 2012), ISBN 978-0-52119540-9.
  - [13] A. H. Castro Neto, F. Guinea, N. M. R. Peres, K. S. Novoselov, and A. K. Geim, *The electronic properties of graphene*, Rev. Mod. Phys. **81**, 109 (2009).
  - [14] I. W. Frank, D. M. Tanenbaum, A. M. van der Zande, and P. L. McEuen, *Mechanical properties of suspended graphene sheets*, Journal of Vacuum Science & Technology B: Microelectronics and Nanometer Structures Processing, Measurement, and Phenomena **25**, 2558 (2007).
  - [15] D. G. Papageorgiou, I. A. Kinloch, and R. J. Young, *Mechanical properties of graphene and graphene-based nanocomposites*, Prog. Mater. Sci. **90**, 75 (2017).
  - [16] P. R. Wallace, *The Band Theory of Graphite*, Phys. Rev. **71**, 622 (1947).
  - [17] R. Peierls, *Quelques propriétés typiques des corps solides*, Annales de l'institut Henri Poincaré **5**, 177 (1935).
  - [18] L. D. Landau, *On the theory of phase transitions. II.*, Zh. Eksp. Teor. Fiz **11**, 627 (1937).
  - [19] J. W. McClure, *Band Structure of Graphite and de Haas-van Alphen Effect*, Phys. Rev. **108**, 612 (1957).
  - [20] J. C. Slonczewski and P. R. Weiss, *Band Structure of Graphite*, Phys. Rev. **109**, 272 (1958).
  - [21] R. Saito, G. Dresselhaus, and M. S. Dresselhaus, *Physical Properties of Carbon Nanotubes* (World Scientific Publishing Company, London, England, UK, 1998), ISBN 978-1-86094-093-4.
  - [22] T. Ando, *Theory of Electronic States and Transport in Carbon Nanotubes*, J. Phys. Soc. Jpn. **74**, 777 (2005).
  - [23] F. Bloch, *Über die Quantenmechanik der Elektronen in Kristallgittern*, Z. Phys. **52**, 555 (1929).
  - [24] T. Ihn, *Semiconductor Nanostructures: Quantum States and Electronic Transport* (OUP, Oxford, England, UK, 2010), ISBN 978-0-19953442-5, URL [https://books.google.de/books/about/Semiconductor\\_Nanostructures.html?id=PAAtqPgAACAAJ&redir\\_esc=y](https://books.google.de/books/about/Semiconductor_Nanostructures.html?id=PAAtqPgAACAAJ&redir_esc=y).
  - [25] S. Reichardt, Master's thesis, RWTH Aachen University (2014).
  - [26] T. Ando, T. Nakanishi, and R. Saito, *Berry's Phase and Absence of Back Scattering in Carbon Nanotubes*, J. Phys. Soc. Jpn. **67**, 2857 (1998).
  - [27] O. Klein, *Die Reflexion von Elektronen an einem Potentialsprung nach der relativistischen Dynamik von Dirac*, Z. Phys. **53**, 157 (1929).

- [28] M. I. Katsnelson, K. S. Novoselov, and A. K. Geim, *Chiral tunnelling and the Klein paradox in graphene*, Nat. Phys. **2**, 620 (2006).
- [29] N. J. G. Couto, D. Costanzo, S. Engels, D.-K. Ki, K. Watanabe, T. Taniguchi, C. Stampfer, F. Guinea, and A. F. Morpurgo, *Random Strain Fluctuations as Dominant Disorder Source for High-Quality On-Substrate Graphene Devices*, Phys. Rev. X **4**, 041019 (2014).
- [30] S. Engels, B. Terrés, A. Epping, T. Khodkov, K. Watanabe, T. Taniguchi, B. Beschoten, and C. Stampfer, *Limitations to Carrier Mobility and Phase-Coherent Transport in Bilayer Graphene*, Phys. Rev. Lett. **113**, 126801 (2014).
- [31] S. Engels, Ph.D. thesis, RWTH Aachen University, Aachen, Germany (2015), URL <http://publications.rwth-aachen.de/record/658889>.
- [32] B. M. Victor and J. Mondragon R., *Neutrino billiards: time-reversal symmetry-breaking without magnetic fields*, Proc. R. Soc. Lond. A. **412**, 53 (1987).
- [33] Y. Zhang, Y.-W. Tan, H. L. Stormer, and P. Kim, *Experimental observation of the quantum Hall effect and Berry's phase in graphene - Nature*, Nature **438**, 201 (2005).
- [34] K. S. Novoselov, A. K. Geim, S. V. Morozov, D. Jiang, M. I. Katsnelson, I. V. Grigorieva, S. V. Dubonos, and A. A. Firsov, *Two-dimensional gas of massless Dirac fermions in graphene*, Nature **438**, 197 (2005).
- [35] G. P. Mikitik and Yu. V. Sharlai, *The Berry phase in graphene and graphite multilayers*, Low Temp. Phys. **34**, 794 (2008).
- [36] N. Ashcroft and N. Mermin, *Solid State Physics* (Saunders College Publishing, Fort Worth, 1976).
- [37] V. Ariel and A. Natan, *Electron Effective Mass in Graphene*, arXiv (2012).
- [38] C. Neumann, S. Reichardt, P. Venezuela, M. Drögeler, L. Banszerus, M. Schmitz, K. Watanabe, T. Taniguchi, F. Mauri, B. Beschoten, et al., *Raman spectroscopy as probe of nanometre-scale strain variations in graphene*, Nat. Commun. **6**, 1 (2015).
- [39] R. Ribeiro-Palau, S. Chen, Y. Zeng, K. Watanabe, T. Taniguchi, J. Hone, and C. R. Dean, *High-Quality Electrostatically Defined Hall Bars in Monolayer Graphene*, Nano Lett. **19**, 2583 (2019).
- [40] H. Overweg, H. Eggimann, X. Chen, S. Slizovskiy, M. Eich, R. Pisoni, Y. Lee, P. Rickhaus, K. Watanabe, T. Taniguchi, et al., *Electrostatically Induced Quantum Point Contacts in Bilayer Graphene*, Nano Lett. **18**, 553 (2018).
- [41] M. Eich, F. Herman, R. Pisoni, H. Overweg, A. Kurzman, Y. Lee, P. Rickhaus, K. Watanabe, T. Taniguchi, M. Sigrist, et al., *Spin and Valley States in Gate-Defined Bilayer Graphene Quantum Dots*, Phys. Rev. X **8**, 031023 (2018).
- [42] D. Adams, *The Hitchhiker's Guide to the Galaxy* (HARMONY BOOKS, 1979).

- [43] L. Banszerus, B. Frohn, A. Epping, D. Neumaier, K. Watanabe, T. Taniguchi, and C. Stampfer, *Gate-Defined Electron–Hole Double Dots in Bilayer Graphene*, Nano Lett. **18**, 4785 (2018).
- [44] L. Banszerus, S. Möller, E. Icking, K. Watanabe, T. Taniguchi, C. Volk, and C. Stampfer, *Single-Electron Double Quantum Dots in Bilayer Graphene*, Nano Lett. **20**, 2005 (2020).
- [45] L. Banszerus, B. Frohn, T. Fabian, S. Somanchi, A. Epping, M. Müller, D. Neumaier, K. Watanabe, T. Taniguchi, F. Libisch, et al., *Observation of the Spin-Orbit Gap in Bilayer Graphene by One-Dimensional Ballistic Transport*, Phys. Rev. Lett. **124**, 177701 (2020).
- [46] L. Banszerus, A. Rothstein, T. Fabian, S. Möller, E. Icking, S. Trellenkamp, F. Lentz, D. Neumaier, K. Watanabe, T. Taniguchi, et al., *Electron–Hole Crossover in Gate-Controlled Bilayer Graphene Quantum Dots*, Nano Lett. **20**, 7709 (2020).
- [47] L. Banszerus, S. Möller, C. Steiner, E. Icking, S. Trellenkamp, F. Lentz, K. Watanabe, T. Taniguchi, C. Volk, and C. Stampfer, *Spin-valley coupling in single-electron bilayer graphene quantum dots*, Nat. Commun. **12**, 1 (2021).
- [48] L. Van der Pauw, *A Method of Measuring the Resistivity and Hall Coefficient on Lamellae of Arbitrary Shape*, Philips Technical Review **20**, 220 (1958).
- [49] N. G. van Kampen, *Stochastic Processes in Physics and Chemistry* (North-Holland, Amsterdam, 1981).
- [50] H. Bluhm, T. Brückel, M. Morgenstern, G. von Plessen, and C. Stampfer, *Electrons in Solids* (De Gruyter, Berlin, Germany, 2019), ISBN 978-3-11043832-1.
- [51] C. R. Dean, A. F. Young, I. Meric, C. Lee, L. Wang, S. Sorgenfrei, K. Watanabe, T. Taniguchi, P. Kim, K. L. Shepard, et al., *Boron nitride substrates for high-quality graphene electronics*, Nat. Nanotechnol. **5**, 722 (2010).
- [52] G. Giovannetti, P. A. Khomyakov, G. Brocks, P. J. Kelly, and J. van den Brink, *Substrate-induced band gap in graphene on hexagonal boron nitride: Ab initio density functional calculations*, Phys. Rev. B **76**, 073103 (2007).
- [53] K. Watanabe, T. Taniguchi, and H. Kanda, *Direct-bandgap properties and evidence for ultraviolet lasing of hexagonal boron nitride single crystal*, Nat. Mater. **3**, 404 (2004).
- [54] A. F. Young, C. R. Dean, I. Meric, S. Sorgenfrei, H. Ren, K. Watanabe, T. Taniguchi, J. Hone, K. L. Shepard, and P. Kim, *Electronic compressibility of layer-polarized bilayer graphene*, Phys. Rev. B **85**, 235458 (2012).
- [55] A. Laturia, M. L. Van de Put, and W. G. Vandenberghe, *Dielectric properties of hexagonal boron nitride and transition metal dichalcogenides: from monolayer to bulk*, npj 2D Mater. Appl. **2**, 1 (2018).



- [56] P. Kumar, Y. S. Chauhan, A. Agarwal, and S. Bhowmick, *Thickness and Stacking Dependent Polarizability and Dielectric Constant of Graphene–Hexagonal Boron Nitride Composite Stacks*, J. Phys. Chem. C **120**, 17620 (2016).
- [57] L. Wang, I. Meric, P. Y. Huang, Q. Gao, Y. Gao, H. Tran, T. Taniguchi, K. Watanabe, L. M. Campos, D. A. Muller, et al., *One-Dimensional Electrical Contact to a Two-Dimensional Material*, Science **342**, 614 (2013).
- [58] J. Xue, J. Sanchez-Yamagishi, D. Bulmash, P. Jacquod, A. Deshpande, K. Watanabe, T. Taniguchi, P. Jarillo-Herrero, and B. J. LeRoy, *Scanning tunnelling microscopy and spectroscopy of ultra-flat graphene on hexagonal boron nitride*, Nat. Mater. **10**, 282 (2011).
- [59] R. T. Weitz and A. Yacoby, *Graphene rests easy*, Nat. Nanotechnol. **5**, 699 (2010).
- [60] J. Sonntag, J. Li, A. Plaud, A. Loiseau, J. Barjon, J. H. Edgar, and C. Stampfer, *Excellent electronic transport in heterostructures of graphene and monoisotopic boron-nitride grown at atmospheric pressure*, 2D Mater. **7**, 031009 (2020).
- [61] C. R. Dean, A. F. Young, P. Cadden-Zimansky, L. Wang, H. Ren, K. Watanabe, T. Taniguchi, P. Kim, J. Hone, and K. L. Shepard, *Multicomponent fractional quantum Hall effect in graphene*, Nat. Phys. **7**, 693 (2011).
- [62] Y. Kim, A. C. Balram, T. Taniguchi, K. Watanabe, J. K. Jain, and J. H. Smet, *Even denominator fractional quantum Hall states in higher Landau levels of graphene*, Nat. Phys. **15**, 154 (2019).
- [63] A. A. Zibrov, E. M. Spanton, H. Zhou, C. Kometter, T. Taniguchi, K. Watanabe, and A. F. Young, *Even-denominator fractional quantum Hall states at an isospin transition in monolayer graphene*, Nat. Phys. **14**, 930 (2018).
- [64] Y. Cao, V. Fatemi, S. Fang, K. Watanabe, T. Taniguchi, E. Kaxiras, and P. Jarillo-Herrero, *Unconventional superconductivity in magic-angle graphene superlattices*, Nature **556**, 43 (2018).
- [65] C. V. Raman and K. S. Krishnan, *A New Type of Secondary Radiation*, Nature **121**, 501 (1928).
- [66] A. C. Ferrari, J. C. Meyer, V. Scardaci, C. Casiraghi, M. Lazzeri, F. Mauri, S. Piscanec, D. Jiang, K. S. Novoselov, S. Roth, et al., *Raman Spectrum of Graphene and Graphene Layers*, Phys. Rev. Lett. **97**, 187401 (2006).
- [67] D. Graf, F. Molitor, K. Ensslin, C. Stampfer, A. Jungen, C. Hierold, and L. Wirtz, *Spatially Resolved Raman Spectroscopy of Single- and Few-Layer Graphene*, Nano Lett. **7**, 238 (2007).
- [68] A. Gupta, G. Chen, P. Joshi, S. Tadigadapa, and Eklund, *Raman Scattering from High-Frequency Phonons in Supported n-Graphene Layer Films*, Nano Lett. **6**, 2667 (2006).

- [69] M. Huang, H. Yan, C. Chen, D. Song, T. F. Heinz, and J. Hone, *Phonon softening and crystallographic orientation of strained graphene studied by Raman spectroscopy*, Proc. Natl. Acad. Sci. U.S.A. **106**, 7304 (2009).
- [70] T. M. G. Mohiuddin, A. Lombardo, R. R. Nair, A. Bonetti, G. Savini, R. Jalil, N. Bonini, D. M. Basko, C. Galiotis, N. Marzari, et al., *Uniaxial strain in graphene by Raman spectroscopy: G peak splitting, Grüneisen parameters, and sample orientation*, Phys. Rev. B **79**, 205433 (2009).
- [71] D. Yoon, Y.-W. Son, and H. Cheong, *Strain-Dependent Splitting of the Double-Resonance Raman Scattering Band in Graphene*, Phys. Rev. Lett. **106**, 155502 (2011).
- [72] F. Ding, H. Ji, Y. Chen, A. Herklotz, K. Dörr, Y. Mei, A. Rastelli, and O. G. Schmidt, *Stretchable graphene: a close look at fundamental parameters through biaxial straining*, Nano Lett. **10**, 3453 (2010).
- [73] D. S. Lee, V. Skákalová, R. T. Weitz, K. von Klitzing, and J. H. Smet, *Transconductance Fluctuations as a Probe for Interaction-Induced Quantum Hall States in Graphene*, Phys. Rev. Lett. **109**, 056602 (2012).
- [74] C. Stampfer, F. Molitor, D. Graf, K. Ensslin, A. Jungen, C. Hierold, and L. Wirtz, *Raman imaging of doping domains in graphene on SiO<sub>2</sub>*, Appl. Phys. Lett. **91**, 241907 (2007).
- [75] S. Pisana, M. Lazzeri, C. Casiraghi, K. S. Novoselov, A. K. Geim, A. C. Ferrari, and F. Mauri, *Breakdown of the adiabatic Born–Oppenheimer approximation in graphene*, Nat. Mater. **6**, 198 (2007).
- [76] C. Casiraghi, S. Pisana, K. Novoselov, S. Duttasinha, and A. Ferrari, *Raman Fingerprint of Charged Impurities in Graphene*, undefined (2007).
- [77] J. Yan, Y. Zhang, P. Kim, and A. Pinczuk, *Electric Field Effect Tuning of Electron-Phonon Coupling in Graphene*, Phys. Rev. Lett. **98**, 166802 (2007).
- [78] S. Reichardt, *Many-Body Perturbation Theory Approach to Raman Spectroscopy and Its Application to 2D Materials* (2018), [Online; accessed 8. Nov. 2022], URL <https://orbi.lu.uni.lu/handle/10993/35610>.
- [79] C. M. Neumann, Ph.D. thesis, RWTH Aachen University, Aachen, Germany (2017).
- [80] J. Sonntag, Ph.D. thesis, RWTH Aachen University, Aachen, Germany (2021).
- [81] P. Venezuela, M. Lazzeri, and F. Mauri, *Theory of double-resonant Raman spectra in graphene: Intensity and line shape of defect-induced and two-phonon bands*, Phys. Rev. B **84**, 035433 (2011).
- [82] A. C. Ferrari and D. M. Basko, *Raman spectroscopy as a versatile tool for studying the properties of graphene*, Nat. Nanotechnol. **8**, 235 (2013).

- [83] C. Thomsen and S. Reich, *Double Resonant Raman Scattering in Graphite*, Phys. Rev. Lett. **85**, 5214 (2000).
- [84] F. Herziger, M. Calandra, P. Gava, P. May, M. Lazzeri, F. Mauri, and J. Maultzsch, *Two-Dimensional Analysis of the Double-Resonant 2D Raman Mode in Bilayer Graphene*, Phys. Rev. Lett. **113**, 187401 (2014).
- [85] R. Geick, C. H. Perry, and G. Rupprecht, *Normal Modes in Hexagonal Boron Nitride*, Phys. Rev. **146**, 543 (1966).
- [86] F. Forster, A. Molina-Sanchez, S. Engels, A. Epping, K. Watanabe, T. Taniguchi, L. Wirtz, and C. Stampfer, *Dielectric screening of the Kohn anomaly of graphene on hexagonal boron nitride*, Phys. Rev. B **88**, 085419 (2013).
- [87] C. Metzger, S. Rémi, M. Liu, S. V. Kusminskiy, A. H. C. Neto, A. K. Swan, and B. B. Goldberg, *Biaxial strain in graphene adhered to shallow depressions*, Nano Lett. **10**, 6 (2010).
- [88] T. Ando, *Anomaly of Optical Phonon in Monolayer Graphene*, J. Phys. Soc. Jpn. **75**, 124701 (2006).
- [89] L. Banszerus, H. Janssen, M. Otto, A. Epping, T. Taniguchi, K. Watanabe, B. Beschoten, D. Neumaier, and C. Stampfer, *Identifying suitable substrates for high-quality graphene-based heterostructures*, arXiv (2016).
- [90] R. Gross and A. Marx, *Festkörperphysik* (De Gruyter Oldenbourg, Berlin, Germany, 2014), ISBN 978-3-11035870-4.
- [91] R. R. Gerhardts, J. Weis, and K. von Klitzing, in *Compendium of Quantum Physics* (Springer, Berlin, Germany, 2009), pp. 572–591, ISBN 978-3-540-70626-7.
- [92] A. W. Gauß, Ph.D. thesis (2019), URL <https://elib.uni-stuttgart.de/handle/11682/10439?mode=full>.
- [93] T. Ando, A. B. Fowler, and F. Stern, *Electronic properties of two-dimensional systems*, Rev. Mod. Phys. **54**, 437 (1982).
- [94] E. Y. Andrei, G. Li, and X. Du, *Electronic properties of graphene: a perspective from scanning tunneling microscopy and magnetotransport*, Rep. Prog. Phys. **75**, 056501 (2012).
- [95] L. Onsager, *Interpretation of the de Haas-van Alphen effect*, London, Edinburgh, and Dublin Philosophical Magazine and Journal of Science **43**, 1006 (1952).
- [96] J. W. McClure, *Diamagnetism of Graphite*, Phys. Rev. **104**, 666 (1956).
- [97] A. M. J. Schakel, *Relativistic quantum Hall effect*, Phys. Rev. D **43**, 1428 (1991).

- [98] V. P. Gusynin and S. G. Sharapov, *Unconventional Integer Quantum Hall Effect in Graphene*, Phys. Rev. Lett. **95**, 146801 (2005).
- [99] V. P. Gusynin, S. G. Sharapov, and J. P. Carbotte, *Magneto-optical conductivity in graphene*, J. Phys.: Condens. Matter **19**, 026222 (2006).
- [100] N. M. R. Peres, A. H. Castro Neto, and F. Guinea, *Dirac fermion confinement in graphene*, Phys. Rev. B **73**, 241403 (2006).
- [101] F. Guinea, A. H. Castro Neto, and N. M. R. Peres, *Electronic states and Landau levels in graphene stacks*, Phys. Rev. B **73**, 245426 (2006).
- [102] P. M. Ostrovsky, I. V. Gornyi, and A. D. Mirlin, *Theory of anomalous quantum Hall effects in graphene*, Phys. Rev. B **77**, 195430 (2008).
- [103] X. Wu, Y. Hu, M. Ruan, N. K. Madiomanana, J. Hankinson, M. Sprinkle, C. Berger, and W. A. de Heer, *Half integer quantum Hall effect in high mobility single layer epitaxial graphene*, Appl. Phys. Lett. **95**, 223108 (2009).
- [104] Y. Zhang, Z. Jiang, J. P. Small, M. S. Purewal, Y.-W. Tan, M. Fazlollahi, J. D. Chudow, J. A. Jaszczak, H. L. Stormer, and P. Kim, *Landau-Level Splitting in Graphene in High Magnetic Fields*, Phys. Rev. Lett. **96**, 136806 (2006).
- [105] Z. Jiang, Y. Zhang, Y.-W. Tan, H. L. Stormer, and P. Kim, *Quantum Hall effect in graphene*, Solid State Commun. **143**, 14 (2007).
- [106] A. J. M. Giesbers, U. Zeitler, L. A. Ponomarenko, R. Yang, K. S. Novoselov, A. K. Geim, and J. C. Maan, *Scaling of the quantum Hall plateau-plateau transition in graphene*, Phys. Rev. B **80**, 241411 (2009).
- [107] J. G. Checkelsky, L. Li, and N. P. Ong, *Zero-Energy State in Graphene in a High Magnetic Field*, Phys. Rev. Lett. **100**, 206801 (2008).
- [108] A. J. M. Giesbers, Ph.D. thesis, The Netherlands (2010), URL <https://repository.ubn.ru.nl/handle/2066/74865>.
- [109] F. Chiappini, Ph.D. thesis, The Netherlands (2017), URL <https://repository.ubn.ru.nl/handle/2066/162632>.
- [110] W. Luo and R. Côté, *Zeeman coupling and screening corrections to skyrmion excitations in graphene*, Phys. Rev. B **88**, 115417 (2013).
- [111] F. Chiappini, S. Wiedmann, K. Novoselov, A. Mishchenko, A. K. Geim, J. C. Maan, and U. Zeitler, *Lifting of the Landau level degeneracy in graphene devices in a tilted magnetic field*, Phys. Rev. B **92**, 201412 (2015).
- [112] K. Nomura and A. H. MacDonald, *Quantum Hall Ferromagnetism in Graphene*, Phys. Rev. Lett. **96**, 256602 (2006).
- [113] J. Alicea and M. P. A. Fisher, *Graphene integer quantum Hall effect in the ferromagnetic and paramagnetic regimes*, Phys. Rev. B **74**, 075422 (2006).

- [114] J. Alicea and M. P. A. Fisher, *Interplay between lattice-scale physics and the quantum Hall effect in graphene*, Solid State Commun. **143**, 504 (2007).
- [115] M. Kharitonov, *Phase diagram for the  $\nu = 0$  quantum Hall state in monolayer graphene*, Phys. Rev. B **85**, 155439 (2012).
- [116] J. Jung and A. H. MacDonald, *Theory of the magnetic-field-induced insulator in neutral graphene sheets*, Phys. Rev. B **80**, 235417 (2009).
- [117] L. Veyrat, C. Déprez, A. Coissard, X. Li, F. Gay, K. Watanabe, T. Taniguchi, Z. Han, B. A. Piot, H. Sellier, et al., *Helical quantum Hall phase in graphene on SrTiO<sub>3</sub>*, Science **367**, 781 (2020).
- [118] S. Kim, J. Schwenk, D. Walkup, Y. Zeng, F. Ghahari, S. T. Le, M. R. Slot, J. Berwanger, S. R. Blankenship, K. Watanabe, et al., *Edge channels of broken-symmetry quantum Hall states in graphene visualized by atomic force microscopy*, Nat. Commun. **12** (2021).
- [119] P. San-Jose, J. L. Lado, R. Aguado, F. Guinea, and J. Fernández-Rossier, *Majorana Zero Modes in Graphene*, Phys. Rev. X **5**, 041042 (2015).
- [120] D. C. Tsui, H. L. Stormer, and A. C. Gossard, *Two-Dimensional Magnetotransport in the Extreme Quantum Limit*, Phys. Rev. Lett. **48**, 1559 (1982).
- [121] H. L. Stormer, D. C. Tsui, and A. C. Gossard, *The fractional quantum Hall effect*, Rev. Mod. Phys. **71**, S298 (1999).
- [122] H. L. Stormer, *Nobel Lecture: The fractional quantum Hall effect*, Rev. Mod. Phys. **71**, 875 (1999).
- [123] R. B. Laughlin, *Anomalous Quantum Hall Effect: An Incompressible Quantum Fluid with Fractionally Charged Excitations*, Phys. Rev. Lett. **50**, 1395 (1983).
- [124] J. K. Jain, *Composite-fermion approach for the fractional quantum Hall effect*, Phys. Rev. Lett. **63**, 199 (1989).
- [125] B. I. Halperin, P. A. Lee, and N. Read, *Theory of the half-filled Landau level*, Phys. Rev. B **47**, 7312 (1993).
- [126] L. Landau, *Diamagnetismus der Metalle*, Z. Phys. **64**, 629 (1930).
- [127] L. Schubnikow and W. J. De Haas, *A New Phenomenon in the Change of Resistance in a Magnetic Field of Single Crystals of Bismuth*, Nature **126**, 500 (1930).
- [128] T. Ando and Y. Uemura, *Theory of Quantum Transport in a Two-Dimensional Electron System under Magnetic Fields. I. Characteristics of Level Broadening and Transport under Strong Fields*, J. Phys. Soc. Jpn. **36**, 959 (1974).
- [129] T. Ando, *Theory of Quantum Transport in a Two-Dimensional Electron System under Magnetic Fields II. Single-Site Approximation under Strong Fields*, J. Phys. Soc. Jpn. **36**, 1521 (1974).

- [130] T. Ando, *Theory of Quantum Transport in a Two-Dimensional Electron System under Magnetic Fields. III. Many-Site Approximation*, J. Phys. Soc. Jpn. **37**, 622 (1974).
- [131] T. Ando, *Theory of Quantum Transport in a Two-Dimensional Electron System under Magnetic Fields. IV. Oscillatory Conductivity*, J. Phys. Soc. Jpn. **37**, 1233 (1974).
- [132] T. Ando, Y. Matsumoto, and Y. Uemura, *Theory of Hall Effect in a Two-Dimensional Electron System*, J. Phys. Soc. Jpn. **39**, 279 (1975).
- [133] K. v. Klitzing, G. Dorda, and M. Pepper, *New Method for High-Accuracy Determination of the Fine-Structure Constant Based on Quantized Hall Resistance*, Phys. Rev. Lett. **45**, 494 (1980).
- [134] H. Störmer, D. Tsui, and A. Gossard, *Zero resistance state and origin of the quantized hall effect in two-dimensional electron systems*, Surface Science **113**, 32 (1982).
- [135] K. S. Novoselov, E. McCann, S. V. Morozov, V. I. Fal'ko, M. I. Katsnelson, U. Zeitler, D. Jiang, F. Schedin, and A. K. Geim, *Unconventional quantum Hall effect and Berry's phase of  $2\pi$  in bilayer graphene - Nature Physics*, Nat. Phys. **2**, 177 (2006).
- [136] K. S. Novoselov, Z. Jiang, Y. Zhang, S. V. Morozov, H. L. Stormer, U. Zeitler, J. C. Maan, G. S. Boebinger, P. Kim, and A. K. Geim, *Room-Temperature Quantum Hall Effect in Graphene*, Science **315**, 1379 (2007).
- [137] R. E. Prange and S. M. Girvin, *The Quantum Hall Effect* (Springer, New York, NY, New York, NY, USA, 1990).
- [138] R. E. Prange, *Quantized Hall resistance and the measurement of the fine-structure constant*, Phys. Rev. B **23**, 4802 (1981).
- [139] R. B. Laughlin, *Quantized Hall conductivity in two dimensions*, Phys. Rev. B **23**, 5632 (1981).
- [140] B. I. Halperin, *Quantized Hall conductance, current-carrying edge states, and the existence of extended states in a two-dimensional disordered potential*, Phys. Rev. B **25**, 2185 (1982).
- [141] R. Joynt and R. E. Prange, *Conditions for the quantum Hall effect*, Phys. Rev. B **29**, 3303 (1984).
- [142] D. J. Thouless, *Localisation and the two-dimensional Hall effect*, J. Phys. C: Solid State Phys. **14**, 3475 (1981).
- [143] R. E. Prange and R. Joynt, *Conduction in a strong field in two dimensions: The quantum Hall effect*, Phys. Rev. B **25**, 2943 (1982).
- [144] B. Kramer, S. Kettemann, and T. Ohtsuki, *Localization in the quantum Hall regime*, Physica E **20**, 172 (2003).

- [145] E. Abrahams, P. W. Anderson, D. C. Licciardello, and T. V. Ramakrishnan, *Scaling Theory of Localization: Absence of Quantum Diffusion in Two Dimensions*, Phys. Rev. Lett. **42**, 673 (1979).
- [146] P. W. Anderson, *Absence of Diffusion in Certain Random Lattices*, Phys. Rev. **109**, 1492 (1958).
- [147] H. Levine, S. B. Libby, and A. M. M. Pruisken, *Electron Delocalization by a Magnetic Field in Two Dimensions*, Phys. Rev. Lett. **51**, 1915 (1983).
- [148] A. M. M. Pruisken, *On localization in the theory of the quantized hall effect: A two-dimensional realization of the -vacuum*, Nucl. Phys. B **235**, 277 (1984).
- [149] A. M. M. Pruisken, *Dilute instanton gas as the precursor to the integral quantum Hall effect*, Phys. Rev. B **32**, 2636 (1985).
- [150] H. P. Wei, D. C. Tsui, and A. M. M. Pruisken, *Localization and scaling in the quantum Hall regime*, Phys. Rev. B **33**, 1488 (1986).
- [151] A. M. M. Pruisken, *Quasiparticles in the theory of the integral quantum Hall effect (I)*, Nucl. Phys. B **285**, 719 (1987).
- [152] A. M. M. Pruisken, *At the Dawn of a Unifying Theory*, J. Stat. Phys. **103**, 569 (2001).
- [153] R. Kubo, *Statistical-Mechanical Theory of Irreversible Processes. I. General Theory and Simple Applications to Magnetic and Conduction Problems*, J. Phys. Soc. Jpn. **12**, 570 (1957).
- [154] R. Kubo, H. Hasegawa, and N. Hashitsume, *Quantum Theory of Galvanomagnetic Effect. I. Basic Considerations*, J. Phys. Soc. Jpn. **14**, 56 (1959).
- [155] E. M. Kendirlik, S. Sirt, S. B. Kalkan, N. Ofek, V. Umansky, and A. Siddiki, *The local nature of incompressibility of quantum Hall effect*, Nat. Commun. **8**, 14082. (2017).
- [156] D. J. Thouless, M. Kohmoto, M. P. Nightingale, and M. Den Nijs, *Quantized Hall Conductance in a Two-Dimensional Periodic Potential*, Phys. Rev. Lett. **49**, 405 (1982).
- [157] D. J. Thouless, *Quantization of particle transport*, Phys. Rev. B **27**, 6083 (1983).
- [158] D. J. Thouless and Q. Niu, *Wavefunction scaling in a quasi-periodic potential*, J. Phys. A: Math. Gen. **16**, 1911 (1983).
- [159] D. J. Thouless, *Bandwidths for a quasiperiodic tight-binding model*, Phys. Rev. B **28**, 4272 (1983).
- [160] D. J. Thouless, *Wannier functions for magnetic sub-bands*, J. Phys. C: Solid State Phys. **17**, L325 (1984).
- [161] D. J. Thouless, *Theory of the quantized hall effect*, Surf. Sci. **142**, 147 (1984).

- [162] Q. Niu and D. J. Thouless, *Quantised adiabatic charge transport in the presence of substrate disorder and many-body interaction*, J. Phys. A: Math. Gen. **17**, 2453 (1984).
- [163] D. J. Thouless and Y.-S. Wu, *Remarks on fractional statistics*, Phys. Rev. B **31**, 1191 (1985).
- [164] Q. Niu, D. J. Thouless, and Y.-S. Wu, *Quantized Hall conductance as a topological invariant*, Phys. Rev. B **31**, 3372 (1985).
- [165] Q. Niu and D. J. Thouless, *Quantum Hall effect with realistic boundary conditions*, Phys. Rev. B **35**, 2188 (1987).
- [166] M. Büttiker, *Edge-State Physics Without Magnetic Fields*, Science **325**, 278 (2009).
- [167] M. Büttiker, Y. Imry, and R. Landauer, *Josephson behavior in small normal one-dimensional rings*, Phys. Lett. A **96**, 365 (1983).
- [168] M. Büttiker, *Four-Terminal Phase-Coherent Conductance*, Phys. Rev. Lett. **57**, 1761 (1986).
- [169] M. Büttiker, *Symmetry of electrical conduction*, IBM J. Res. Dev. **32**, 317 (1988).
- [170] M. Büttiker, *Small normal-metal loop coupled to an electron reservoir*, Phys. Rev. B **32**, 1846 (1985).
- [171] M. Büttiker, *Role of quantum coherence in series resistors*, Phys. Rev. B **33**, 3020 (1986).
- [172] M. Büttiker, *Absence of backscattering in the quantum hall effect in multiprobe conductors*, Phys. Rev. B **38**, 9375 (1988).
- [173] M. Büttiker, in *Semiconductors and Semimetals* (Elsevier, Waltham, MA, USA, 1992), vol. 35, pp. 191–277.
- [174] K. Panos, Ph.D. thesis (2014).
- [175] U. Klass, W. Dietsche, K. von Klitzing, and K. Ploog, *Image of the dissipation in gated quantum Hall effect samples*, Surf. Sci. **263**, 97 (1992).
- [176] C. W. J. Beenakker, *Edge channels for the fractional quantum Hall effect*, Phys. Rev. Lett. **64**, 216 (1990).
- [177] B. J. van Wees, G. I. Meijer, J. J. Kuipers, T. M. Klapwijk, W. v. d. Graaf, and G. Borghs, *Breakdown of the quantum Hall effect in InAs/AlSb quantum wells due to counterflowing edge channels*, Phys. Rev. B **51**, 7973 (1995).
- [178] P. G. Silvestrov and K. B. Efetov, *Charge accumulation at the boundaries of a graphene strip induced by a gate voltage: Electrostatic approach*, Phys. Rev. B **77**, 155436 (2008).



- [179] I. J. Vera-Marun, P. J. Zomer, A. Veligura, M. H. D. Guimarães, L. Visser, N. Tombros, H. J. van Elferen, U. Zeitler, and B. J. van Wees, *Quantum Hall transport as a probe of capacitance profile at graphene edges*, Appl. Phys. Lett. **102**, 013106 (2013).
- [180] N. Moreau, B. Brun, S. Somanchi, K. Watanabe, T. Taniguchi, C. Stampfer, and B. Hackens, *Upstream modes and antidots poison graphene quantum Hall effect*, Nat. Commun. **12**, 1 (2021).
- [181] N. Moreau, B. Brun, S. Somanchi, K. Watanabe, T. Taniguchi, C. Stampfer, and B. Hackens, *Quantum Hall nano-interferometer in graphene*, arXiv (2021).
- [182] N. Moreau, B. Brun, S. Somanchi, K. Watanabe, T. Taniguchi, C. Stampfer, and B. Hackens, *Contacts and upstream modes explain the electron-hole asymmetry in the graphene quantum Hall regime*, Phys. Rev. B **104**, L201406 (2021).
- [183] R. Kumar, S. K. Srivastav, C. Spånslätt, K. Watanabe, T. Taniguchi, Y. Gefen, A. D. Mirlin, and A. Das, *Observation of ballistic upstream modes at fractional quantum Hall edges of graphene*, Nat. Commun. **13**, 1 (2022).
- [184] A. Poux, Z. R. Wasilewski, K. J. Friedland, R. Hey, K. H. Ploog, R. Airey, P. Plochocka, and D. K. Maude, *Microscopic model for the magnetic-field-driven breakdown of the dissipationless state in the integer and fractional quantum Hall effect*, Phys. Rev. B **94**, 075411 (2016).
- [185] A. J. M. Giesbers, U. Zeitler, M. I. Katsnelson, L. A. Ponomarenko, T. M. Mohiuddin, and J. C. Maan, *Quantum-Hall Activation Gaps in Graphene*, Phys. Rev. Lett. **99**, 206803 (2007).
- [186] S. Ilani, J. Martin, E. Teitelbaum, J. H. Smet, D. Mahalu, V. Umansky, and A. Yacoby, *The microscopic nature of localization in the quantum Hall effect*, Nature **427**, 328 (2004).
- [187] J. Martin, N. Akerman, G. Ulbricht, T. Lohmann, K. von Klitzing, J. H. Smet, and A. Yacoby, *The nature of localization in graphene under quantum Hall conditions - Nature Physics*, Nat. Phys. **5**, 669 (2009).
- [188] S. V. Morozov, K. S. Novoselov, M. I. Katsnelson, F. Schedin, L. A. Ponomarenko, D. Jiang, and A. K. Geim, *Strong Suppression of Weak Localization in Graphene*, Phys. Rev. Lett. **97**, 016801 (2006).
- [189] J. C. Meyer, A. K. Geim, M. I. Katsnelson, K. S. Novoselov, D. Obergfell, S. Roth, C. Girit, and A. Zettl, *On the roughness of single- and bi-layer graphene membranes*, Solid State Commun. **143**, 101 (2007).
- [190] E. Stolyarova, K. T. Rim, S. Ryu, J. Maultzsch, P. Kim, L. E. Brus, T. F. Heinz, M. S. Hybertsen, and G. W. Flynn, *High-resolution scanning tunneling microscopy imaging of mesoscopic graphene sheets on an insulating surface*, Proc. Natl. Acad. Sci. U.S.A. **104**, 9209 (2007).

- [191] M. I. Katsnelson and K. S. Novoselov, *Graphene: New bridge between condensed matter physics and quantum electrodynamics*, Solid State Commun. **143**, 3 (2007).
- [192] M. F. Atiyah and I. M. Singer, *The Index of Elliptic Operators: I* on JSTOR, Ann. Of Math. **87**, 484 (1968).
- [193] M. F. Atiyah and I. M. Singer, *Dirac operators coupled to vector potentials*, Proc. Natl. Acad. Sci. U.S.A. **81**, 2597 (1984).
- [194] M. I. Katsnelson, *Graphene: carbon in two dimensions*, Mater. Today **10**, 20 (2007).
- [195] Th. Englert and K. Von Klitzing, *Analysis of  $pxx$  minima in surface quantum oscillations on (100)  $n$ -type silicon inversion layers*, Surf. Sci. **73**, 70 (1978).
- [196] Th. Englert, D. C. Tsui, A. C. Gossard, and Ch. Uihlein,  *$g$ -Factor enhancement in the 2D electron gas in GaAs/AlGaAs heterojunctions*, Surf. Sci. Lett. **113**, A22 (1982).
- [197] B. Tausendfreund and K. von Klitzing, *Analysis of quantized Hall resistance at finite temperatures*, Surf. Sci. **142**, 220 (1984).
- [198] K. v. Klitzing and G. Ebert, *Application of the Quantum Hall Effect in Metrology*, Metrologia **21**, 11 (1985).
- [199] J. P. Hirtz, Y. Guldner, A. Briggs, J. P. Vieren, P. Voisin, M. Voos, and M. Razeghi, *Temperature dependence of the quantum hall effect in  $In_{0.53}Ga_{0.47}As$ -InP heterojunctions*, vol. 177 (1983).
- [200] Y. Guldner, J. P. Hirtz, A. Briggs, J. P. Vieren, M. Voos, and M. Razeghi, *Quantum hall effect and hopping conduction in  $In_xGa_{1-x}As$ -InP heterojunctions at low temperature*, Surf. Sci. **142**, 179 (1984).
- [201] S. Washburn, R. A. Webb, E. E. Mendez, L. L. Chang, and L. Esaki, *New Shubnikov-de Haas effects in a two-dimensional electron-hole system*, Phys. Rev. B **31**, 1198 (1985).
- [202] R. J. Nicholas, R. A. Stradling, and R. J. Tidey, *Evidence for Anderson localization in Landau level tails from the analysis of two-dimensional Shubnikov—de Haas conductivity minima*, Solid State Commun. **23**, 341 (1977).
- [203] R. J. Nicholas, E. Kress-Rogers, F. Kuchar, M. Pepper, J. C. Portal, and R. A. Stradling, *Electron transport in silicon inversion layers at high magnetic fields and the influence of substrate bias*, Surf. Sci. **98**, 283 (1980).
- [204] Y. Ono, *Localization of Electrons under Strong Magnetic Fields in a Two-Dimensional System*, J. Phys. Soc. Jpn. **51**, 237 (1982).
- [205] K. I. Wysokiński and W. Brenig, *Absence of variable range hopping hall conduction?*, Z. Phys. B: Condens. Matter **54**, 11 (1983).

- [206] A. L. Efros, B. I. Shklovskii, and I. Y. Yanchev, *Impurity conductivity in low compensated semiconductors*, Phys. Status Solidi B **50**, 45 (1972).
- [207] G. Ebert, K. von Klitzing, C. Probst, E. Schuberth, K. Ploog, and G. Weimann, *Hopping conduction in the Landau level tails in GaAs-Al<sub>x</sub>Ga<sub>1-x</sub>As heterostructures at low temperatures*, Solid State Commun. **45**, 625 (1983).
- [208] K. Bennaceur, P. Jacques, F. Portier, P. Roche, and D. C. Glattli, *Unveiling quantum Hall transport by Efros-Shklovskii to Mott variable-range hopping transition in graphene*, Phys. Rev. B **86**, 085433 (2012).
- [209] T. J. B. M. Janssen, N. E. Fletcher, R. Goebel, J. M. Williams, A. Tzalenchuk, R. Yakimova, S. Kubatkin, S. Lara-Avila, and V. I. Falko, *Graphene, universality of the quantum Hall effect and redefinition of the SI system*, New J. Phys. **13**, 093026 (2011).
- [210] F. Lafont, R. Ribeiro-Palau, Z. Han, A. Cresti, A. Delvallée, A. W. Cummings, S. Roche, V. Bouchiat, S. Ducourtieux, F. Schopfer, et al., *Anomalous dissipation mechanism and Hall quantization limit in polycrystalline graphene grown by chemical vapor deposition*, Phys. Rev. B **90**, 115422 (2014).
- [211] F. Lafont, R. Ribeiro-Palau, D. Kazazis, A. Michon, O. Couturaud, C. Consejo, T. Chassagne, M. Zielinski, M. Portail, B. Jouault, et al., *Quantum Hall resistance standards from graphene grown by chemical vapour deposition on silicon carbide - Nature Communications*, Nat. Commun. **6**, 1 (2015).
- [212] B. I. Shklovskii and A. L. Efros, *Electronic properties of doped semiconductors*, Springer Ser. Solid-State Sci. **45** (1984).
- [213] A. I. Ekimov, A. L. Efros, and A. A. Onushchenko, *Quantum size effect in semiconductor microcrystals*, Solid State Commun. **56**, 921 (1985).
- [214] A. L. Efros, *Density of states of 2D electron gas and width of the plateau of IQHE*, Solid State Commun. **65**, 1281 (1988).
- [215] A. L. Efros, *Non-linear screening and the background density of 2DEG states in magnetic field*, Solid State Commun. **67**, 1019 (1988).
- [216] B. E. Kane, Ph.D. thesis, Princeton University (1988).
- [217] A. L. Efros, *Metal-non-metal transition in heterostructures with thick spacer layers*, Solid State Commun. **70**, 253 (1989).
- [218] A. L. Efros, *Homogeneous and inhomogeneous states of a two-dimensional electron liquid in a strong magnetic field*, Phys. Rev. B **45**, 11354 (1992).
- [219] A. L. Efros, F. G. Pikus, and V. G. Burnett, *Density of states of a two-dimensional electron gas in a long-range random potential*, Phys. Rev. B **47**, 2233 (1993).
- [220] A. M. Chang, *A unified transport theory for the integral and fractional quantum hall effects: Phase boundaries, edge currents, and transmission/reflection*

- probabilities*, Solid State Commun. **74**, 871 (1990).
- [221] D. B. Chklovskii, B. I. Shklovskii, and L. I. Glazman, *Electrostatics of edge channels*, Phys. Rev. B **46**, 4026 (1992).
  - [222] D. B. Chklovskii, K. A. Matveev, and B. I. Shklovskii, *Ballistic conductance of interacting electrons in the quantum Hall regime*, Phys. Rev. B **47**, 12605 (1993).
  - [223] D. Pfannkuche and J. Hajdu, *Potential and current distribution in an ideal Hall bar*, Phys. Rev. B **46**, 7032 (1992).
  - [224] S. W. Hwang, D. C. Tsui, and M. Shayegan, *Experimental evidence for finite-width edge channels in integer and fractional quantum Hall effects*, Phys. Rev. B **48**, 8161 (1993).
  - [225] N. B. Zhitenev, R. J. Haug, K. v. Klitzing, and K. Eberl, *Time-resolved measurements of transport in edge channels*, Phys. Rev. Lett. **71**, 2292 (1993).
  - [226] K. Lier and R. R. Gerhardts, *Self-consistent calculations of edge channels in laterally confined two-dimensional electron systems*, Phys. Rev. B **50**, 7757 (1994).
  - [227] J. H. Oh and R. R. Gerhardts, *Self-consistent Thomas-Fermi calculation of potential and current distributions in a two-dimensional Hall bar geometry*, Phys. Rev. B **56**, 13519 (1997).
  - [228] K. P. Weitz, Ph.D. thesis, Universität Hamburg (1999).
  - [229] P. Weitz, E. Ahlswede, J. Weis, K. v. Klitzing, and K. Eberl, *A low-temperature scanning force microscope for investigating buried two-dimensional electron systems under quantum Hall conditions*, Appl. Surf. Sci. **157**, 349 (2000).
  - [230] P. Weitz, E. Ahlswede, J. Weis, K. V. Klitzing, and K. Eberl, *Hall-potential investigations under quantum Hall conditions using scanning force microscopy*, Physica E **6**, 247 (2000).
  - [231] E. Ahlswede, P. Weitz, J. Weis, K. von Klitzing, and K. Eberl, *Hall potential profiles in the quantum Hall regime measured by a scanning force microscope*, Physica B **298**, 562 (2001).
  - [232] E. Ahlswede, J. Weis, K. V. Klitzing, and K. Eberl, *Hall potential distribution in the quantum Hall regime in the vicinity of a potential probe contact*, Physica E **12**, 165 (2002).
  - [233] E. Ahlswede, Ph.D. thesis, Universität Stuttgart (2002), URL <https://elib.uni-stuttgart.de/handle/11682/6522>.
  - [234] A. Yacoby, H. F. Hess, T. A. Fulton, L. N. Pfeiffer, and K. W. West, *Electrical imaging of the quantum Hall state*, Solid State Commun. **111**, 1 (1999).
  - [235] K. Güven and R. R. Gerhardts, *Self-consistent local equilibrium model for density profile and distribution of dissipative currents in a Hall bar under strong*

- magnetic fields*, Phys. Rev. B **67**, 115327 (2003).
- [236] A. Siddiki and R. R. Gerhardts, *Incompressible strips in dissipative Hall bars as origin of quantized Hall plateaus*, Phys. Rev. B **70**, 195335 (2004).
  - [237] A. Siddiki and R. R. Gerhardts, *Range-dependent disorder effects on the plateau-widths calculated within the screening theory of the IQHE*, Int. J. Mod. Phys B **21**, 1362 (2007).
  - [238] S. Erden Gulebaglan, G. Oylumluoglu, U. Erkaslan, A. Siddiki, and I. Sökmen, *The effect of disorder on integer quantized Hall effect*, Physica E **44**, 1495 (2012).
  - [239] N. B. Yurdasan, S. E. Gulebaglan, and A. Siddiki, *The effect of disorder on local electron temperature in quantum Hall systems*, Eur. Phys. J. B **94**, 10 (2021).
  - [240] A. Siddiki, J. Horas, J. Moser, W. Wegscheider, and S. Ludwig, *Interaction-mediated asymmetries of the quantized Hall effect*, Europhys. Lett. **88**, 17007 (2009).
  - [241] A. Siddiki, S. E. Gulebaglan, N. B. Yurdasan, G. Bilgeç, A. Yildiz, and I. Sökmen, *Evanescent incompressible strips as origin of the observed Hall resistance overshoot*, Europhys. Lett. **92**, 67010 (2011).
  - [242] J. Sailer, A. Wild, V. Lang, A. Siddiki, and D. Bougeard, *Quantum Hall resistance overshoot in two-dimensional (2D) electron gases: theory and experiment*, New J. Phys. **12**, 113033 (2010).
  - [243] E. M. Kendirlik, S. Sirt, S. B. Kalkan, W. Dietsche, W. Wegscheider, S. Ludwig, and A. Siddiki, *Anomalous resistance overshoot in the integer quantum Hall effect*, Sci. Rep. **3**, 1 (2013).
  - [244] S. E. Gulebaglan, S. B. Kalkan, S. Sirt, E. M. Kendirlik, and A. Siddiki, *The dip effect under integer quantized Hall conditions*, Eur. Phys. J. B **87**, 72 (2014).
  - [245] U. Erkaslan, G. Oylumluoglu, M. Grayson, and A. Siddiki, *The visibility of IQHE at sharp edges: experimental proposals based on interactions and edge electrostatics*, New J. Phys. **14**, 023015 (2012).
  - [246] E. Peraticos, S. Kumar, M. Pepper, A. Siddiki, I. Farrer, D. Ritchie, G. Jones, and J. Griffiths, *Hall resistance anomalies in the integer and fractional quantum Hall regime*, Phys. Rev. B **102**, 115306 (2020).
  - [247] K.-J. Friedland, A. Siddiki, R. Hey, H. Kostial, A. Riedel, and D. K. Maude, *Quantum Hall effect in a high-mobility two-dimensional electron gas on the surface of a cylinder*, Phys. Rev. B **79**, 125320 (2009).
  - [248] R. R. Gerhardts, *The effect of screening on current distribution and conductance quantisation in narrow quantum Hall systems*, Phys. Status Solidi B **245**, 378 (2008).

- [249] J. Weis and K. von Klitzing, *Metrology and microscopic picture of the integer quantum Hall effect*, Philos. Trans. Royal Soc. A **369**, 3954 (2011).
- [250] S. Kim, J. Schwenk, D. Walkup, Y. Zeng, F. Ghahari, S. T. Le, M. R. Slot, J. Berwanger, S. R. Blankenship, K. Watanabe, et al., *Edge channels of broken-symmetry quantum Hall states in graphene visualized by atomic force microscopy*, Nat. Commun. **12**, 1 (2021).
- [251] A. Uri, Y. Kim, K. Bagani, C. K. Lewandowski, S. Grover, N. Auerbach, E. O. Lachman, Y. Myasoedov, T. Taniguchi, K. Watanabe, et al., *Nanoscale imaging of equilibrium quantum Hall edge currents and of the magnetic monopole response in graphene - Nature Physics*, Nat. Phys. **16**, 164 (2020).
- [252] G. Li, A. Luican-Mayer, D. Abanin, L. Levitov, and E. Y. Andrei, *Evolution of Landau levels into edge states in graphene - Nature Communications*, Nat. Commun. **4**, 1 (2013).
- [253] F. Dahlem, Ph.D. thesis (2008), URL <https://elib.uni-stuttgart.de/handle/11682/6703>.
- [254] F. Dahlem, E. Ahlswede, J. Weis, and K. V. Klitzing, *Cryogenic scanning force microscopy of quantum Hall samples: Adiabatic transport originating in anisotropic depletion at contact interfaces*, Phys. Rev. B **82**, 121305 (2010).
- [255] K. Ikushima, H. Sakuma, S. Komiyama, and K. Hirakawa, *Imaging of Cyclotron Emission from Edge Channels in Quantum Hall Conductors*, Phys. Rev. Lett. **93**, 146804 (2004).
- [256] D. Eksi, A. Y. Tunali, and A. Siddiki, *The topological inequivalence of Hall bar versus Corbino geometries in real space*, arXiv (2022).
- [257] J. Horas, A. Siddiki, J. Moser, W. Wegscheider, and S. Ludwig, *Investigations on unconventional aspects in the quantum Hall regime of narrow gate defined channels*, Physica E **40**, 1130 (2008).
- [258] Y. Zhu, H. Ji, H.-M. Cheng, and R. S. Ruoff, *Mass production and industrial applications of graphene materials*, Natl. Sci. Rev. **5**, 90 (2018).
- [259] C. Berger, Z. Song, X. Li, X. Wu, N. Brown, C. Naud, D. Mayou, T. Li, J. Hass, A. N. Marchenkov, et al., *Electronic Confinement and Coherence in Patterned Epitaxial Graphene*, Science **312**, 1191 (2006).
- [260] W. A. de Heer, C. Berger, X. Wu, P. N. First, E. H. Conrad, X. Li, T. Li, M. Sprinkle, J. Hass, M. L. Sadowski, et al., *Epitaxial graphene*, Solid State Commun. **143**, 92 (2007).
- [261] J. Kedzierski, P.-L. Hsu, P. Healey, P. W. Wyatt, C. L. Keast, M. Sprinkle, C. Berger, and W. A. de Heer, *Epitaxial Graphene Transistors on SiC Substrates*, IEEE Trans. Electron Devices **55**, 2078 (2008).

- [262] C. Berger, Z. Song, T. Li, X. Li, A. Y. Ogbazghi, R. Feng, Z. Dai, A. N. Marchenkov, E. H. Conrad, P. N. First, et al., *Ultrathin Epitaxial Graphite: 2D Electron Gas Properties and a Route toward Graphene-based Nanoelectronics*, J. Phys. Chem. B **108**, 19912 (2004).
- [263] W. A. de Heer, C. Berger, X. Wu, M. Sprinkle, Y. Hu, M. Ruan, J. A. Stroscio, P. N. First, R. Haddon, B. Piot, et al., *Epitaxial graphene electronic structure and transport*, J. Phys. D: Appl. Phys. **43**, 374007 (2010).
- [264] J. Zhao, P. Ji, Y. Li, R. Lo, K. Zhang, H. Tian, K. Yu, L. Hao, B. Bian, X. Xiao, et al., *Ultrahigh mobility semiconducting epitaxial graphene on silicon carbide* (2023), [Online; accessed 4. May 2023].
- [265] S. Park and R. S. Ruoff, *Chemical methods for the production of graphenes*, Nat. Nanotechnol. **4**, 217 (2009).
- [266] X. Li, L. Colombo, and R. S. Ruoff, *Synthesis of Graphene Films on Copper Foils by Chemical Vapor Deposition*, Adv. Mater. **28**, 6247 (2016).
- [267] R. S. Ruoff, *Personal perspectives on graphene: New graphene-related materials on the horizon*, MRS Bull. **37**, 1314 (2012).
- [268] L. Banszerus and M. Schmitz, *Graphene Sensoring*, Jugend-forscht Arbeit (2010).
- [269] M. Wang, D. Luo, B. Wang, and R. S. Ruoff, *Synthesis of Large-Area Single-Crystal Graphene*, Trends Chem. **3**, 15 (2021).
- [270] S. Xu, L. Zhang, B. Wang, and R. S. Ruoff, *Chemical vapor deposition of graphene on thin-metal films*, Cell Rep. Phys. Sci. **2**, 100372 (2021).
- [271] G. Zhao, X. Li, M. Huang, Z. Zhen, Y. Zhong, Q. Chen, X. Zhao, Y. He, R. Hu, T. Yang, et al., *The physics and chemistry of graphene-on-surfaces*, Chem. Soc. Rev. **46**, 4417 (2017).
- [272] S. Ullah, X. Yang, H. Q. Ta, M. Hasan, A. Bachmatiuk, K. Tokarska, B. Trzebicka, L. Fu, and M. H. Rummeli, *Graphene transfer methods: A review*, Nano Res. **14**, 3756 (2021).
- [273] T. Kobayashi, M. Bando, N. Kimura, K. Shimizu, K. Kadono, N. Umez, K. Miyahara, S. Hayazaki, S. Nagai, Y. Mizuguchi, et al., *Production of a 100-m-long high-quality graphene transparent conductive film by roll-to-roll chemical vapor deposition and transfer process*, Appl. Phys. Lett. **102**, 023112 (2013).
- [274] G. Ruan, Z. Sun, Z. Peng, and J. M. Tour, *Growth of Graphene from Food, Insects, and Waste*, ACS Nano **5**, 7601 (2011).
- [275] M. Batzill, *The surface science of graphene: Metal interfaces, CVD synthesis, nanoribbons, chemical modifications, and defects*, Surf. Sci. Rep. **67**, 83 (2012).
- [276] Y. Hao, L. Wang, Y. Liu, H. Chen, X. Wang, C. Tan, S. Nie, J. W. Suk, T. Jiang, T. Liang, et al., *Oxygen-activated growth and bandgap tunability of*

- large single-crystal bilayer graphene, *Nat. Nanotechnol.* **11**, 426 (2016).
- [277] B. Srinivasan, Y. Hao, R. Hariharaputran, S. Rywkin, J. C. Hone, L. Colombo, R. S. Ruoff, and Y.-W. Zhang, *Oxygen-Promoted Chemical Vapor Deposition of Graphene on Copper: A Combined Modeling and Experimental Study*, *ACS Nano* **12**, 9372 (2018).
  - [278] S. Chatterjee, T. Abadie, M. Wang, O. K. Matar, and R. S. Ruoff, *Inside the CVD “Black Box”: A Physics-Driven Exploration of Reactor Conditions during Graphene Growth*, *ChemRxiv* (2022).
  - [279] B. Luo, M. Koleini, P. R. Whelan, A. Shivayogimath, M. Brandbyge, P. Bøggild, and T. J. Booth, *Graphene-Subgrain-Defined Oxidation of Copper*, *ACS Appl. Mater. Interfaces* **11**, 48518 (2019).
  - [280] J. Li, M. Chen, A. Samad, H. Dong, A. Ray, J. Zhang, X. Jiang, U. Schwingenschlögl, J. Domke, C. Chen, et al., *Wafer-scale single-crystal monolayer graphene grown on sapphire substrate*, *Nat. Mater.* **21**, 740 (2022).
  - [281] R. Zhang, M. Li, L. Li, Y. Fan, Q. Zhang, G. Yu, D. Geng, and W. Hu, *The way towards for ultraflat and superclean graphene*, *Nano* **3**, 485 (2022).
  - [282] F. Pizzocchero, B. S. Jessen, L. Gammelgaard, A. Andryieuski, P. R. Whelan, A. Shivayogimath, J. M. Caridad, J. Kling, N. Petrone, P. T. Tang, et al., *Chemical Vapor-Deposited Graphene on Ultraflat Copper Foils for van der Waals Hetero-Assembly*, *ACS Omega* **7**, 22626 (2022).
  - [283] X. Li, C. W. Magnuson, A. Venugopal, R. M. Tromp, J. B. Hannon, E. M. Vogel, L. Colombo, and R. S. Ruoff, *Large-Area Graphene Single Crystals Grown by Low-Pressure Chemical Vapor Deposition of Methane on Copper*, *J. Am. Chem. Soc.* **133**, 2816 (2011).
  - [284] S. Jin, M. Huang, Y. Kwon, L. Zhang, B.-W. Li, S. Oh, J. Dong, D. Luo, M. Biswal, B. V. Cunniff, et al., *Colossal grain growth yields single-crystal metal foils by contact-free annealing*, *Science* **362**, 1021 (2018).
  - [285] R. S. Ruoff and S. Jin, *Single crystalline metal foil and manufacturing method therefor* (2017), uS11078594B2, URL <https://patents.google.com/patent/US11078594B2/en>.
  - [286] R. S. Ruoff and S. Jin, *Single crystalline metal foil and manufacturing method therefor* (2021), uS20210310149A1, URL <https://patents.google.com/patent/US20210310149A1/en>.
  - [287] X. Xu, Z. Zhang, J. Dong, D. Yi, J. Niu, M. Wu, L. Lin, R. Yin, M. Li, J. Zhou, et al., *Ultrafast epitaxial growth of metre-sized single-crystal graphene on industrial Cu foil*, *Science Bulletin* **62**, 1074 (2017).
  - [288] M. Huang, M. Biswal, H. J. Park, S. Jin, D. Qu, S. Hong, Z. Zhu, L. Qiu, D. Luo, X. Liu, et al., *Highly Oriented Monolayer Graphene Grown on a Cu/Ni(111)*



- Alloy Foil*, ACS Nano **12**, 6117 (2018).
- [289] L. Sun, B. Chen, W. Wang, Y. Li, X. Zeng, H. Liu, Y. Liang, Z. Zhao, A. Cai, R. Zhang, et al., *Toward Epitaxial Growth of Misorientation-Free Graphene on Cu(111) Foils*, ACS Nano **16**, 285 (2022).
  - [290] D. Yi, D. Luo, Z.-J. Wang, J. Dong, X. Zhang, M.-G. Willinger, R. S. Ruoff, and F. Ding, *What Drives Metal-Surface Step Bunching in Graphene Chemical Vapor Deposition?*, Phys. Rev. Lett. **120**, 246101 (2018).
  - [291] G.-X. Ni, Y. Zheng, S. Bae, H. R. Kim, A. Pachoud, Y. S. Kim, C.-L. Tan, D. Im, J.-H. Ahn, B. H. Hong, et al., *Quasi-Periodic Nanoripples in Graphene Grown by Chemical Vapor Deposition and Its Impact on Charge Transport*, ACS Nano **6**, 1158 (2012).
  - [292] K. Hayashi, S. Sato, and N. Yokoyama, *Anisotropic graphene growth accompanied by step bunching on a dynamic copper surface*, Nanotechnology **24**, 025603 (2012).
  - [293] X. H. Kong, H. X. Ji, R. D. Piner, H. F. Li, C. W. Magnuson, C. Tan, A. Ismach, H. Chou, and R. S. Ruoff, *Non-destructive and rapid evaluation of chemical vapor deposition graphene by dark field optical microscopy*, Appl. Phys. Lett. **103**, 043119 (2013).
  - [294] J. H. Kang, J. Moon, D. J. Kim, Y. Kim, I. Jo, C. Jeon, J. Lee, and B. H. Hong, *Strain Relaxation of Graphene Layers by Cu Surface Roughening*, Nano Lett. **16**, 5993 (2016).
  - [295] J.-S. Yu, X. Jin, J. Park, D. H. Kim, D.-H. Ha, D.-H. Chae, W.-S. Kim, C. Hwang, and J.-H. Kim, *Structural analysis of graphene synthesized by chemical vapor deposition on copper foil using nematic liquid crystal texture*, Carbon **76**, 113 (2014).
  - [296] D. Luo, X. You, B.-W. Li, X. Chen, H. J. Park, M. Jung, T. Y. Ko, K. Wong, M. Yousaf, X. Chen, et al., *Role of Graphene in Water-Assisted Oxidation of Copper in Relation to Dry Transfer of Graphene*, Chem. Mater. **29**, 4546 (2017).
  - [297] D. Yoon, Y.-W. Son, and H. Cheong, *Negative Thermal Expansion Coefficient of Graphene Measured by Raman Spectroscopy*, Nano Lett. **11**, 3227 (2011).
  - [298] M. Wang, M. Huang, D. Luo, Y. Li, M. Choe, W. K. Seong, M. Kim, S. Jin, M. Wang, S. Chatterjee, et al., *Single-crystal, large-area, fold-free monolayer graphene*, Nature **596**, 519 (2021).
  - [299] D. Luo, M. Choe, R. A. Bizao, M. Wang, H. Su, M. Huang, S. Jin, Y. Li, M. Kim, N. M. Pugno, et al., *Folding and Fracture of Single-Crystal Graphene Grown on a Cu(111) Foil*, Adv. Mater. **34**, 2110509 (2022).
  - [300] D. Rainis, F. Taddei, M. Polini, G. León, F. Guinea, and V. I. Fal'ko, *Gauge fields and interferometry in folded graphene*, Phys. Rev. B **83**, 165403 (2011).

- [301] Y. Wu, D. Zhai, C. Pan, B. Cheng, T. Taniguchi, K. Watanabe, N. Sandler, and M. Bockrath, *Quantum Wires and Waveguides Formed in Graphene by Strain*, Nano Lett. **18**, 64 (2018).
- [302] C. Ma, X. Sun, H. Du, J. Wang, M. Tian, A. Zhao, Y. Yamauchi, and B. Wang, *Landau Quantization of a Narrow Doubly-Folded Wrinkle in Monolayer Graphene*, Nano Lett. **18**, 6710 (2018).
- [303] Z. Luo, Y. Lu, D. W. Singer, M. E. Berck, L. A. Somers, B. R. Goldsmith, and A. T. C. Johnson, *Effect of Substrate Roughness and Feedstock Concentration on Growth of Wafer-Scale Graphene at Atmospheric Pressure*, Chem. Mater. **23**, 1441 (2011).
- [304] J. Pang, A. Bachmatiuk, L. Fu, C. Yan, M. Zeng, J. Wang, B. Trzebicka, T. Gemming, J. Eckert, and M. H. Rummeli, *Oxidation as A Means to Remove Surface Contaminants on Cu Foil Prior to Graphene Growth by Chemical Vapor Deposition*, J. Phys. Chem. C **119**, 13363 (2015).
- [305] J. D. Wood, S. W. Schmucker, A. S. Lyons, E. Pop, and J. W. Lyding, *Effects of Polycrystalline Cu Substrate on Graphene Growth by Chemical Vapor Deposition*, Nano Lett. **11**, 4547 (2011).
- [306] X. Chen, B. Wu, and Y. Liu, *Direct preparation of high quality graphene on dielectric substrates*, Chem. Soc. Rev. **45**, 2057 (2016).
- [307] N. Mishra, S. Forti, F. Fabbri, L. Martini, C. McAleese, B. R. Conran, P. R. Whelan, A. Shivayogimath, B. S. Jessen, L. Buß, et al., *Wafer-Scale Synthesis of Graphene on Sapphire: Toward Fab-Compatible Graphene*, Small **15**, 1904906 (2019).
- [308] M. Chen, R. C. Haddon, R. Yan, and E. Bekyarova, *Advances in transferring chemical vapour deposition graphene: a review*, Mater. Horiz. **4**, 1054 (2017).
- [309] J. K. Langstreth, K. Kevin, and D. Roberts A., *Surface energy and the contact of elastic solids*, Proc. R. Soc. Lond. A. **324**, 301 (1971).
- [310] W. S. Leong, H. Wang, J. Yeo, F. J. Martin-Martinez, A. Zubair, P.-C. Shen, Y. Mao, T. Palacios, M. J. Buehler, J.-Y. Hong, et al., *Paraffin-enabled graphene transfer*, Nat. Commun. **10**, 1 (2019).
- [311] S. Gorantla, A. Bachmatiuk, J. Hwang, H. A. Alsalman, J. Y. Kwak, T. Seyller, J. Eckert, M. G. Spencer, and M. H. Rummeli, *A universal transfer route for graphene*, Nanoscale **6**, 889 (2013).
- [312] L. Gao, W. Ren, H. Xu, L. Jin, Z. Wang, T. Ma, L.-P. Ma, Z. Zhang, Q. Fu, L.-M. Peng, et al., *Repeated growth and bubbling transfer of graphene with millimetre-size single-crystal grains using platinum*, Nat. Commun. **3**, 1 (2012).
- [313] S. Choudhary, J. V. N. Sarma, S. Pande, S. Ababou-Girard, P. Turban, B. Lepine, and S. Gangopadhyay, *Oxidation mechanism of thin Cu films: A gateway*

- towards the formation of single oxide phase, *AIP Adv.* **8**, 055114 (2018).
- [314] B. Luo, P. R. Whelan, A. Shivayogimath, D. M. A. Mackenzie, P. Bøggild, and T. J. Booth, *Copper Oxidation through Nucleation Sites of Chemical Vapor Deposited Graphene*, *Chem. Mater.* **28**, 3789 (2016).
  - [315] D. Luo, X. Wang, B.-W. Li, C. Zhu, M. Huang, L. Qiu, M. Wang, S. Jin, M. Kim, F. Ding, et al., *The Wet-Oxidation of a Cu(111) Foil Coated by Single Crystal Graphene*, *Adv. Mater.* **33**, 2102697 (2021).
  - [316] D. Luo, M. Wang, Y. Li, C. Kim, K. M. Yu, Y. Kim, H. Han, M. Biswal, M. Huang, Y. Kwon, et al., *Adlayer-Free Large-Area Single Crystal Graphene Grown on a Cu(111) Foil*, *Adv. Mater.* **31**, 1903615 (2019).
  - [317] P. Braeuninger-Weimer, O. J. Burton, P. Zeller, M. Amati, L. Gregoratti, R. S. Weatherup, and S. Hofmann, *Crystal Orientation Dependent Oxidation Modes at the Buried Graphene-Cu Interface*, *Chem. Mater.* **32**, 7766 (2020).
  - [318] O. J. Burton, Z. C. M. Winter, K. Watanabe, T. Taniguchi, B. Beschoten, C. Stampfer, and S. Hofmann, *Putting high-index Cu on the map for high-yield, dry-transferred CVD graphene*, *arXiv* (2022).
  - [319] J. S. Lee, S. H. Choi, S. J. Yun, Y. I. Kim, S. Boandoh, J.-H. Park, B. G. Shin, H. Ko, S. H. Lee, Y.-M. Kim, et al., *Wafer-scale single-crystal hexagonal boron nitride film via self-collimated grain formation*, *Science* **362**, 817 (2018).
  - [320] L. Wang, X. Xu, L. Zhang, R. Qiao, M. Wu, Z. Wang, S. Zhang, J. Liang, Z. Zhang, Z. Zhang, et al., *Epitaxial growth of a 100-square-centimetre single-crystal hexagonal boron nitride monolayer on copper*, *Nature* **570**, 91 (2019).
  - [321] T.-A. Chen, C.-P. Chuu, C.-C. Tseng, C.-K. Wen, H.-S. P. Wong, S. Pan, R. Li, T.-A. Chao, W.-C. Chueh, Y. Zhang, et al., *Wafer-scale single-crystal hexagonal boron nitride monolayers on Cu (111)*, *Nature* **579**, 219 (2020).
  - [322] K. Y. Ma, L. Zhang, S. Jin, Y. Wang, S. I. Yoon, H. Hwang, J. Oh, D. S. Jeong, M. Wang, S. Chatterjee, et al., *Epitaxial single-crystal hexagonal boron nitride multilayers on Ni (111)*, *Nature* **606**, 88 (2022).
  - [323] B. Fallahazad, Y. Hao, K. Lee, S. Kim, R. S. Ruoff, and E. Tutuc, *Quantum Hall effect in Bernal stacked and twisted bilayer graphene grown on Cu by chemical vapor deposition*, *Phys. Rev. B* **85**, 201408 (2012).
  - [324] Z. Qi, H. Shi, M. Zhao, H. Jin, S. Jin, X. Kong, R. S. Ruoff, S. Qin, J. Xue, and H. Ji, *Chemical Vapor Deposition Growth of Bernal-Stacked Bilayer Graphene by Edge-Selective Etching with H<sub>2</sub>O*, *Chem. Mater.* **30**, 7852 (2018).
  - [325] Z. Han, R. Zhang, M. Li, L. Li, D. Geng, and W. Hu, *Recent advances in the controlled chemical vapor deposition growth of bilayer 2D single crystals*, *J. Mater. Chem. C* **10**, 13324 (2022).

- [326] M. Schmitz, S. Engels, L. Banszerus, K. Watanabe, T. Taniguchi, C. Stampfer, and B. Beschoten, *High mobility dry-transferred CVD bilayer graphene*, Appl. Phys. Lett. **110**, 263110 (2017).
- [327] M. Huang, P. V. Bakharev, Z.-J. Wang, M. Biswal, Z. Yang, S. Jin, B. Wang, H. J. Park, Y. Li, D. Qu, et al., *Large-area single-crystal AB-bilayer and ABA-trilayer graphene grown on a Cu/Ni(111) foil*, Nat. Nanotechnol. **15**, 289 (2020).
- [328] C. Liu, Z. Li, R. Qiao, Q. Wang, Z. Zhang, F. Liu, Z. Zhou, N. Shang, H. Fang, M. Wang, et al., *Designed growth of large bilayer graphene with arbitrary twist angles*, Nat. Mater. **21**, 1263 (2022).
- [329] L. Sun, Z. Wang, Y. Wang, L. Zhao, Y. Li, B. Chen, S. Huang, S. Zhang, W. Wang, D. Pei, et al., *Hetero-site nucleation for growing twisted bilayer graphene with a wide range of twist angles*, Nat. Commun. **12**, 1 (2021).
- [330] X. Zhang, Y. Li, W. Mu, W. Bai, X. Sun, M. Zhao, Z. Zhang, F. Shan, and Z. Yang, *Advanced tape-exfoliated method for preparing large-area 2D monolayers: a review*, 2D Mater. **8**, 032002 (2021).
- [331] M. Zastrow, *Meet the crystal growers who sparked a revolution in graphene electronics*, Nature **572**, 429 (2019).
- [332] J. Choi, S. Koo, M. Song, D. Y. Jung, S.-Y. Choi, and S. Ryu, *Varying electronic coupling at graphene-copper interfaces probed with Raman spectroscopy*, 2D Mater. **7**, 025006 (2020).
- [333] M. Galbiati, A. C. Stoot, D. M. A. Mackenzie, P. Bøggild, and L. Camilli, *Real-time oxide evolution of copper protected by graphene and boron nitride barriers*, Sci. Rep. **7**, 39770 (2017).
- [334] L. Banszerus, K. Watanabe, T. Taniguchi, B. Beschoten, and C. Stampfer, *Dry transfer of CVD graphene using MoS<sub>2</sub>-based stamps*, Phys. Status Solidi RRL **11**, 1700136 (2017).
- [335] S. J. Haigh, A. Gholinia, R. Jalil, S. Romani, L. Britnell, D. C. Elias, K. S. Novoselov, L. A. Ponomarenko, A. K. Geim, and R. Gorbachev, *Cross-sectional imaging of individual layers and buried interfaces of graphene-based heterostructures and superlattices*, Nat. Mater. **11**, 764 (2012).
- [336] H. Ghorbanfekr-Kalashami, K. S. Vasu, R. R. Nair, F. M. Peeters, and M. Neek-Amal, *Dependence of the shape of graphene nanobubbles on trapped substance*, Nat. Commun. **8**, 1 (2017).
- [337] P. Bampoulis, V. J. Teernstra, D. Lohse, H. J. W. Zandvliet, and B. Poelsema, *Hydrophobic Ice Confined between Graphene and MoS<sub>2</sub>*, J. Phys. Chem. C **120**, 27079 (2016).
- [338] F. Pizzocchero, L. Gammelgaard, B. S. Jessen, J. M. Caridad, L. Wang, J. Hone, P. Bøggild, and T. J. Booth, *The hot pick-up technique for batch assembly of*

- van der Waals heterostructures*, Nat. Commun. **7**, 1 (2016).
- [339] E. Khestanova, F. Guinea, L. Fumagalli, A. K. Geim, and I. V. Grigorieva, *Universal shape and pressure inside bubbles appearing in van der Waals heterostructures*, Nat. Commun. **7**, 1 (2016).
  - [340] N. Leconte, H. Kim, H.-J. Kim, D. H. Ha, K. Watanabe, T. Taniguchi, J. Jung, and S. Jung, *Graphene bubbles and their role in graphene quantum transport*, Nanoscale **9**, 6041 (2017).
  - [341] D. G. Purdie, N. M. Pugno, T. Taniguchi, K. Watanabe, A. C. Ferrari, and A. Lombardo, *Cleaning interfaces in layered materials heterostructures*, Nat. Commun. **9**, 1 (2018).
  - [342] S. Berciaud, X. Li, H. Htoon, L. E. Brus, S. K. Doorn, and T. F. Heinz, *Intrinsic Line Shape of the Raman 2D-Mode in Freestanding Graphene Monolayers*, Nano Lett. **13**, 3517 (2013).
  - [343] I. Leermakers, Ph.D. thesis, The Netherlands (2019), URL <https://repository.ubn.ru.nl/handle/2066/203011>.
  - [344] L. Banszerus, T. Sohler, A. Epping, F. Winkler, F. Libisch, F. Haupt, K. Watanabe, T. Taniguchi, K. Müller-Caspary, N. Marzari, et al., *Extraordinary high room-temperature carrier mobility in graphene-WSe<sub>2</sub> heterostructures*, arXiv (2019).
  - [345] X. Du, I. Skachko, F. Duerr, A. Luican, and E. Y. Andrei, *Fractional quantum Hall effect and insulating phase of Dirac electrons in graphene*, Nature **462**, 192 (2009).
  - [346] B. E. Feldman, B. Krauss, J. H. Smet, and A. Yacoby, *Unconventional Sequence of Fractional Quantum Hall States in Suspended Graphene*, Science **337**, 1196 (2012).
  - [347] B. E. Feldman, A. J. Levin, B. Krauss, D. A. Abanin, B. I. Halperin, J. H. Smet, and A. Yacoby, *Fractional Quantum Hall Phase Transitions and Four-Flux States in Graphene*, Phys. Rev. Lett. **111**, 076802 (2013).
  - [348] N. Petrone, C. R. Dean, I. Meric, A. M. van der Zande, P. Y. Huang, L. Wang, D. Muller, K. L. Shepard, and J. Hone, *Chemical Vapor Deposition-Derived Graphene with Electrical Performance of Exfoliated Graphene*, Nano Lett. **12**, 2751 (2012).
  - [349] H. Goldman and E. Fradkin, *Dirac composite fermions and emergent reflection symmetry about even-denominator filling fractions*, Phys. Rev. B **98**, 165137 (2018).
  - [350] R. R. Du, H. L. Stormer, D. C. Tsui, A. S. Yeh, L. N. Pfeiffer, and K. W. West, *Drastic Enhancement of Composite Fermion Mass near Landau Level Filling  $\nu = \frac{1}{2}$* , Phys. Rev. Lett. **73**, 3274 (1994).

- [351] A. S. Yeh, H. L. Stormer, D. C. Tsui, L. N. Pfeiffer, K. W. Baldwin, and K. W. West, *Effective Mass and  $g$  Factor of Four-Flux-Quanta Composite Fermions*, Phys. Rev. Lett. **82**, 592 (1999).
- [352] W. Pan, H. L. Stormer, D. C. Tsui, L. N. Pfeiffer, K. W. Baldwin, and K. W. West, *Effective mass of the four-flux composite fermion at  $\nu = 1/4$* , Phys. Rev. B **61**, R5101 (2000).
- [353] M. Onoda, T. Mizusaki, and H. Aoki, *Effective-mass staircase and the Fermi-liquid parameters for the fractional quantum Hall composite fermions*, Phys. Rev. B **64**, 235315 (2001).
- [354] W. Pan, J. S. Xia, H. L. Stormer, D. C. Tsui, C. Vicente, E. D. Adams, N. S. Sullivan, L. N. Pfeiffer, K. W. Baldwin, and K. W. West, *Experimental studies of the fractional quantum Hall effect in the first excited Landau level*, Phys. Rev. B **77**, 075307 (2008).
- [355] Md. S. Hossain, M. K. Ma, M. A. Mueed, D. Kamburov, L. N. Pfeiffer, K. W. West, K. W. Baldwin, R. Winkler, and M. Shayegan, *Geometric resonance of four-flux composite fermions*, Phys. Rev. B **100**, 041112 (2019).
- [356] A. A. Zibrov, E. M. Spanton, H. Zhou, C. Kometter, T. Taniguchi, K. Watanabe, and A. F. Young, *Even-denominator fractional quantum Hall states at an isospin transition in monolayer graphene*, Nat. Phys. **14**, 930 (2018).
- [357] Y. Kim, A. C. Balram, T. Taniguchi, K. Watanabe, J. K. Jain, and J. H. Smet, *Even denominator fractional quantum Hall states in higher Landau levels of graphene*, Nat. Phys. **15**, 154 (2018).
- [358] J. Yan and M. S. Fuhrer, *Charge Transport in Dual Gated Bilayer Graphene with Corbino Geometry*, Nano Lett. **10**, 4521 (2010).
- [359] Y. Zeng, J. I. A. Li, S. A. Dietrich, O. M. Ghosh, K. Watanabe, T. Taniguchi, J. Hone, and C. R. Dean, *High-Quality Magnetotransport in Graphene Using the Edge-Free Corbino Geometry*, Phys. Rev. Lett. **122**, 137701 (2019).
- [360] S. Chen, R. Ribeiro-Palau, K. Yang, K. Watanabe, T. Taniguchi, J. Hone, M. O. Goerbig, and C. R. Dean, *Competing Fractional Quantum Hall and Electron Solid Phases in Graphene*, Phys. Rev. Lett. **122**, 026802 (2019).
- [361] F. Schulze-Wischeler, E. Mariani, F. Hohls, and R. J. Haug, *Direct Measurement of the  $g$  Factor of Composite Fermions*, Phys. Rev. Lett. **92**, 156401 (2004).
- [362] A. J. M. Giesbers, U. Zeitler, M. I. Katsnelson, L. A. Ponomarenko, T. M. G. Mohiuddin, and J. C. Maan, *Temperature dependence of the quantum Hall effect in graphene*, Physica E **40**, 1089 (2008).
- [363] D. Vaquero, V. Clericò, M. Schmitz, J. A. Delgado-Notario, A. Martín-Ramos, J. Salvador-Sánchez, C. S. A. Müller, K. Rubi, K. Watanabe, T. Taniguchi, et al., *Phonon-mediated room-temperature quantum Hall transport in graphene*,

Nat. Commun. **14**, 1 (2023).

- [364] Y.-T. Cui, B. Wen, E. Y. Ma, G. Diankov, Z. Han, F. Amet, T. Taniguchi, K. Watanabe, D. Goldhaber-Gordon, C. R. Dean, et al., *Unconventional Correlation between Quantum Hall Transport Quantization and Bulk State Filling in Gated Graphene Devices*, Phys. Rev. Lett. **117**, 186601 (2016).
- [365] L. Pfeiffer and K. W. West, *The role of MBE in recent quantum Hall effect physics discoveries*, Physica E **20**, 57 (2003).
- [366] A. A. Ramadan, R. D. Gould, and A. Ashour, *On the Van der Pauw method of resistivity measurements*, Thin Solid Films **239**, 272 (1994).
- [367] D. Rhodes, S. H. Chae, R. Ribeiro-Palau, and J. Hone, *Disorder in van der Waals heterostructures of 2D materials*, Nat. Mater. **18**, 541 (2019).
- [368] J. A. Alexander-Webber, J. Huang, D. K. Maude, T. J. B. M. Janssen, A. Tzalenchuk, V. Antonov, T. Yager, S. Lara-Avila, S. Kubatkin, R. Yakimova, et al., *Giant quantum Hall plateaus generated by charge transfer in epitaxial graphene*, Sci. Rep. **6**, 1 (2016).
- [369] D. A. Bandurin, I. Torre, R. K. Kumar, M. B. Shalom, A. Tomadin, A. Principi, G. H. Auton, E. Khestanova, K. S. Novoselov, I. V. Grigorieva, et al., *Negative local resistance caused by viscous electron backflow in graphene*, Science **351**, 1055 (2016).
- [370] J. Crossno, J. K. Shi, K. Wang, X. Liu, A. Harzheim, A. Lucas, S. Sachdev, P. Kim, T. Taniguchi, K. Watanabe, et al., *Observation of the Dirac fluid and the breakdown of the Wiedemann-Franz law in graphene*, Science **351**, 1058 (2016).
- [371] E. H. Hwang and S. Das Sarma, *Single-particle relaxation time versus transport scattering time in a two-dimensional graphene layer*, Phys. Rev. B **77**, 195412 (2008).
- [372] T. Sohler, M. Calandra, C.-H. Park, N. Bonini, N. Marzari, and F. Mauri, *Phonon-limited resistivity of graphene by first-principles calculations: Electron-phonon interactions, strain-induced gauge field, and Boltzmann equation*, Phys. Rev. B **90**, 125414 (2014).
- [373] C.-H. Park, N. Bonini, T. Sohler, G. Samsonidze, B. Kozinsky, M. Calandra, F. Mauri, and N. Marzari, *Electron-Phonon Interactions and the Intrinsic Electrical Resistivity of Graphene*, Nano Lett. **14**, 1113 (2014).
- [374] S. V. Morozov, K. S. Novoselov, M. I. Katsnelson, F. Schedin, D. C. Elias, J. A. Jaszczak, and A. K. Geim, *Giant Intrinsic Carrier Mobilities in Graphene and Its Bilayer*, Phys. Rev. Lett. **100**, 016602 (2008).
- [375] J.-H. Chen, C. Jang, S. Xiao, M. Ishigami, and M. S. Fuhrer, *Intrinsic and extrinsic performance limits of graphene devices on SiO<sub>2</sub>*, Nat. Nanotechnol. **3**,

206 (2008).

- [376] W. Shi, S. Kahn, L. Jiang, S.-Y. Wang, H.-Z. Tsai, D. Wong, T. Taniguchi, K. Watanabe, F. Wang, M. F. Crommie, et al., *Reversible writing of high-mobility and high-carrier-density doping patterns in two-dimensional van der Waals heterostructures*, Nat. Electron. **3**, 99 (2020).
- [377] E. V. Castro, H. Ochoa, M. I. Katsnelson, R. V. Gorbachev, D. C. Elias, K. S. Novoselov, A. K. Geim, and F. Guinea, *Limits on Charge Carrier Mobility in Suspended Graphene due to Flexural Phonons*, Phys. Rev. Lett. **105**, 266601 (2010).
- [378] H. Polshyn, M. Yankowitz, S. Chen, Y. Zhang, K. Watanabe, T. Taniguchi, C. R. Dean, and A. F. Young, *Large linear-in-temperature resistivity in twisted bilayer graphene*, Nat. Phys. **15**, 1011 (2019).
- [379] D. G. Polyakov and B. I. Shklovskii, *Activated Conductivity in the Quantum Hall Effect*, Phys. Rev. Lett. **73**, 1150 (1994).
- [380] D. G. Polyakov and B. I. Shklovskii, *Universal Prefactor of Activated Conductivity in the Quantum Hall Effect*, Phys. Rev. Lett. **74**, 150 (1995).
- [381] A. M. Alexeev, R. R. Hartmann, and M. E. Portnoi, *Two-phonon scattering in graphene in the quantum Hall regime*, Phys. Rev. B **92**, 195431 (2015).
- [382] S. Wiedmann, H. J. van Elferen, E. V. Kurganova, M. I. Katsnelson, A. J. M. Giesbers, A. Veligura, B. J. van Wees, R. V. Gorbachev, K. S. Novoselov, J. C. Maan, et al., *Coexistence of electron and hole transport in graphene*, Phys. Rev. B **84**, 115314 (2011).
- [383] L. Wang, P. Makk, S. Zihlmann, A. Baumgartner, D. I. Indolese, K. Watanabe, T. Taniguchi, and C. Schönenberger, *Mobility Enhancement in Graphene by in situ Reduction of Random Strain Fluctuations*, Phys. Rev. Lett. **124**, 157701 (2020).
- [384] P. Kumaravadivel, M. T. Greenaway, D. Perello, A. Berdyugin, J. Birkbeck, J. Wengraf, S. Liu, J. H. Edgar, A. K. Geim, L. Eaves, et al., *Strong magnetophonon oscillations in extra-large graphene*, Nat. Commun. **10**, 1 (2019).
- [385] A. Usher, R. J. Nicholas, J. J. Harris, and C. T. Foxon, *Observation of magnetic excitons and spin waves in activation studies of a two-dimensional electron gas*, Phys. Rev. B **41**, 1129 (1990).
- [386] M. Gibertini, A. Tomadin, M. Polini, A. Fasolino, and M. I. Katsnelson, *Electron density distribution and screening in rippled graphene sheets*, Phys. Rev. B **81**, 125437 (2010).
- [387] M. Gibertini, A. Tomadin, F. Guinea, M. I. Katsnelson, and M. Polini, *Electron-hole puddles in the absence of charged impurities*, Phys. Rev. B **85**, 201405 (2012).



- [388] M. Schmitz, T. Ouaj, Z. Winter, K. Rubi, K. Watanabe, T. Taniguchi, U. Zeitler, B. Beschoten, and C. Stampfer, *Fractional quantum Hall effect in CVD-grown graphene*, 2D Mater. **7**, 041007 (2020).

# Acknowledgments

As Sir Isaac Newton once said, "If I have seen further, it is by standing on the shoulders of giants." In this vein, I express my profound appreciation to all the researchers whose exceptional work has built the foundation for this thesis. However, this work would not have come to fruition without the individual contributions and support of numerous people. I seize this opportunity to recognize and convey my gratitude to those who have significantly influenced my academic and personal journey.

I am deeply thankful to Prof. Dr. Christoph Stampfer, who has been my professor, supervisor, mentor, and role model for over ten years. His guidance through various stages of my personal and professional development has molded me into the individual I am today. The chance he provided for and to Luca to establish and manage a CVD lab as teenagers unveiled a realm of opportunities, and the considerable autonomy he granted me in my research over the years was invaluable. I also appreciate his immense support and active involvement in sport activities and competitions.

I gratefully acknowledge Prof. Dr. Markus Morgenstern for serving as the second examiner for my PhD thesis. His approachability and willingness to discuss physics in an affable and warm manner have been instrumental in helping me comprehend the quantum Hall effect's intricacies.

My sincere gratitude goes to Prof. Dr. Uli Zeitler for his outstanding guidance and support during my two measurement stays at HFML. His passion for explaining the facility, the physics behind the quantum Hall effect, Polynesian navigation, and the highly complex question of how to measure a resistance was both extraordinary and inspiring.

I convey my earnest gratitude to Dr. Bernd Beschoten for his priceless guidance and support over the years. He has consistently provided sound advice, and his door has always been open for me whenever I needed a sympathetic ear to discuss my concerns and anxieties at the institute.

I offer my heartfelt thanks to Prof. Dr. Afif Siddiki for elucidating his groundbreaking work on the screening picture of the quantum Hall effect. I gained substantial knowledge about the dynamics of conceptual models and information flow in science from his explanations.

I express my appreciation to Stephan, who has been my supervisor, mentor, and friend since my time as a HiWi. His guidance has taught me a great deal about

fabrication, measurements, and data analysis, which has significantly contributed to my growth as a researcher.

My gratitude extends to Ruby for her invaluable assistance and support during my measurement stays at HFML.

I thank my former master's students, Taoufiq and Ananya, for their steadfast dedication and hard work in supporting my research projects. I will always cherish Taoufiq's exceptional assistance during the measurements at HFML and the memorable time we spent together. Similarly, I am grateful to Ananya for the fascinating discussions on physics that we had and for the phenomenal Indian lunches that we shared.

I would like to express my sincere appreciation to all my colleagues at the institute, including the technical and administrative staff, as well as the mechanical workshop, for their hard work, expertise, and collaboration. Their contributions have been invaluable throughout my time here. I would like to extend special thanks to Aaron, Alex, Beate, Beatrix, Christian, Corinne, David, Eike, Felix, Frank, Guido, Hubert, Ina, Jens, Jorg, Kathrin, Lars, Lucca, Lutz, Manfred, Marco, Markus, Paul, Philipp, Raoul, Robin, Sascha, Sebastian, Tjorven, Timo, Uwe, Zach, and any others whose names I may have unintentionally omitted.

My heartfelt appreciation goes to Luca, my friend since the 5th grade, for the unforgettable adventures we have shared over more than 20 years. Despite facing highs and lows over more than two decades, our mutual passion for the captivating 2D material graphene has remained a consistent bonding element, for which I am profoundly grateful.

I convey my genuine appreciation to Bernhard, my friend since college, who introduced me to the world of road cycling and became my study partner, confidant, and adventure companion. Through countless rides and hikes, we have created indelible memories, and I am grateful for the serenity and wit he has consistently exhibited over the years. I am thankful to Philipp for his support and friendship over the years. He not only introduced me to the world of triathlon but also accompanied me on numerous long runs to the Blausteinsee and back and I cherish the lively discussions we had while running, ranging from competitive pencil sharpening to obscure medical conditions, and the many memorable board game evenings we spent together, often with the penguin reigning supreme. I offer my heartfelt appreciation to Samuel, a dear friend of mine for many years since I supervised his lab course experiment. We share a passion for cycling and board games, and we have embarked on many adventurous bike tours through the Eifel, Ardennes, and the Netherlands, enjoying countless discussions and other experiences together. The thrilling air glider ride he took me on will forever remain etched in my memory. I convey my deepest gratitude

to Alex and Sarah for their friendship and support, both in Aachen and beyond. I am grateful to Maja and Florian for becoming such close friends as the "Biber-gang" during the challenging times of enforced distance. I owe a special debt of gratitude to Florian for introducing me to the coffee-game, ensuring that I had a steady supply of excellent espresso extractions to fuel my thesis writing. I extend a special thank you to David for creating MAK and for being a friend and source of inspiration for many years and for teaching me what it means to be a "harter Hund" in training. My gratitude goes to my friend Tom, the Ehrbarer Kaufmann and Bulle von Puchheim, for establishing the ERF bike tours and guiding me towards Austrian economics and the golden shine of freedom. I sincerely appreciate all the members of MAK for their support and I deeply value the countless hours we spent together, engaging in friendly banter and laughter, whether it was in our Telegram group, during our Zoom meetings, or at our memorable training camps and gatherings. Despite the challenges we faced during the dark times of the political lockdown measures, the Bearliner, the Camel, the Cat, the Dolphin, the Duck, the Eagle, the Flamingo, the Kangaroo, the Leopard, the Monkey, the Ram, the Seal, the Squirrel, and the Tiger remained constant sources of joy and inspiration for all of us. A special shout-out goes to the creators of BibItNow browser extension, which saved me days of work collecting information on the nearly 400 references for my thesis. Thanks to ChatGPT for proofreading my thesis.

I would like to express my sincere gratitude to my former teacher, Walter Stein, for his passionate dedication to coaching and mentoring nerdy teenagers like myself in conducting and presenting research projects in his spare time, over the course of several decades.

I am profoundly grateful to my parents and my brother Peter for their unwavering support and encouragement throughout my academic journey in physics. They have always believed in me and have been there for me whenever I needed them. I am truly fortunate to have such loving and supportive parents who have instilled in me the values and education that have helped me reach where I am today.

Finally, I want to express my deepest gratitude to Sophia for her love and support throughout the many years we have known each other. Her constant presence in my life has been a source of comfort and strength, and I cannot thank her enough for being there for me through thick and thin.

# Curriculum Vitae

**Hans-Michael Schmitz**

Born	September 01, 1991 in Mechernich, Germany
Since 09/2017	PhD student of Prof. Dr. Christoph Stampfer, 2nd Institute of Physics, A, RWTH Aachen University, Germany Topic: <b>CVD-Grown Graphene in High Magnetic Fields</b>
10/2016-09/2017	Master thesis in the group of Prof. Dr. Christoph Stampfer, 2nd Institute of Physics, A, RWTH Aachen University, Germany Topic: <b>High-mobility Dry-Transferred CVD Bilayer Graphene</b>
10/2015-09/2017	Master of Science in physics (1,2 with distinction) RWTH Aachen University, Germany with a focus on experimental solid state physics
06/2015-09/2015	Bachelor thesis in the group of Prof. Dr. Christoph Stampfer, 2nd Institute of Physics, A, RWTH Aachen University, Germany Topic: <b>Growth and characterization of high quality CVD bilayer graphene</b>
10/2011-09/2015	Bachelor of Science in physics (2,5) RWTH Aachen University, Germany
07/2011	Abitur (1,8) at St. Michael-Gymnasium Bad Münstereifel, Germany

# Eidesstattliche Erklärung

**Hans-Michael Schmitz**, geboren in Mechernich, erklärt hiermit, dass diese Dissertation und die darin dargelegten Inhalte die eigenen sind und selbstständig, als Ergebnis der eigenen originären Forschung, generiert wurden.

Hiermit erkläre ich an Eides statt

1. Diese Arbeit wurde vollständig oder größtenteils in der Phase als Doktorand dieser Fakultät und Universität angefertigt;
2. Sofern irgendein Bestandteil dieser Dissertation zuvor für einen akademischen Abschluss oder eine andere Qualifikation an dieser oder einer anderen Institution verwendet wurde, wurde dies klar angezeigt;
3. Wenn immer andere eigene- oder Veröffentlichungen Dritter herangezogen wurden, wurden diese klar benannt;
4. Wenn aus anderen eigenen- oder Veröffentlichungen Dritter zitiert wurde, wurde stets die Quelle hierfür angegeben. Diese Dissertation ist vollständig meine eigene Arbeit, mit der Ausnahme solcher Zitate;
5. Alle wesentlichen Quellen von Unterstützung wurden benannt;
6. Wenn immer ein Teil dieser Dissertation auf der Zusammenarbeit mit anderen basiert, wurde von mir klar gekennzeichnet, was von anderen und was von mir selbst erarbeitet wurde;
7. Teile dieser Arbeit wurden zuvor veröffentlicht und zwar in:

- **Fractional quantum Hall effect in CVD-grown graphene**

M. Schmitz, T. Ouaj, Z. Winter, K. Rubi, T. Taniguchi, K. Watanabe, U. Zeitler, B. Beschoten and C. Stampfer  
2D Mater. **7**, 041007 (2020) (or: arXiv: 2005.08938)

- **Phonon-mediated room-temperature quantum Hall transport in graphene**

D. Vaquero, V. Clerico, M. Schmitz, J.A. Delgado-Notario, A. Martin-Ramos, J. Salvador-Sanchez, C.S.A. Müller, K. Rubi, K. Watanabe, T. Taniguchi, B. Beschoten, C. Stampfer, E. Diez, M.I. Katsnelson, U. Zeitler, S. Wiedmann and S. Pezzini  
Nat. Commun. **14**, 318 (2023)

20.01.2024



